Examining Metal-Ligand and Metal-Metal Cooperativity in Ruthenium (II) bis-(Protic N-Heterocyclic Carbene) Phosphine Complexes for CO_2 and Related Substrate Transformations

Mary Cecilia Johnson

A dissertation

submitted in partial fulfillment of the

requirements for the degree of

Doctor of Philosophy

University of Washington

2021

Reading Committee:

Brandi M. Cossairt, Chair

Alexandra Velian

Gojko Lalic

Program Authorized to Offer Degree:

Chemistry

University of Washington

Abstract

Examining Metal-Ligand and Metal-Metal Cooperativity in Ruthenium (II) bis-(Protic N-Heterocyclic Carbene) Phosphine Complexes for CO_2 and Related Substrate Transformations

Mary Cecilia Johnson

Chair of the Supervisory Committee:
Prof. Brandi M. Cossairt
Chemistry

A novel bis-(protic N-heterocyclic carbene, PNHC) phosphine ligand platform is explored to understand its role in CO_2 hydrogenation catalysis and as a supporting scaffold for bimetallic complexes. Optimized syntheses for the bis-(PNHC) phosphine ligand and its metalation with a Ru(II) metal center, as well as the synthesis and coordination chemistry of a library of complexes with varying ancillary ligands (2,2'-bipyridine, 4,4'-dibromo-2,2'-bipyridine, 4,4'-dimethoxy-2,2'-bipyridine, and bis-(diphenylphosphino)ethane) are shown. We describe the hydrogenation of CO_2 to formate catalyzed by a Ru(II) bis-(protic N-heterocyclic carbene, p-NHC) phosphine complex $[Ru(bpy)(MeCN)(P^{Ph}(p\text{-}NHC)_2)](PF_6)_2$ (**1**). Under catalytic conditions (20 μmol catalyst, 20 bar CO_2, 60 bar H_2, 5 mL THF, 140 °C, 16 hrs) the activity of **1** is limited only by the amount of K_3PO_4 present in the reaction, yielding a nearly one to one ratio

of turn over number (TON) to equivalents of K_3PO_4 (relative to **1**), with the highest TON = 8,040. Additionally, analysis of the reaction solution post-run reveals the catalyst intact with no free ligand observed. Stoichiometric studies, including examination of unique carbamate and hydride complexes as relevant intermediates, were carried out to probe the operative mechanism and understand the importance of metal-ligand cooperativity in this system. We also describe the synthesis and characterization of [Ru(bpy)(solvent)(P(Ph)(NHC)$_2$- κ^2-N,N'-M(solvent)$_2$)]2+ (M = Co(II), Zn(II)) and subsequent reactivity with hydroxide and formate. Facile inter- and intramolecular cooperation is observed and the structurally responsive NHC-Cobalt-NHC binding pocket is investigated.

TABLE OF CONTENTS

LIST OF FIGURES

LIST OF TABLES

LIST OF SCHEMES

ACKNOWLEDGEMENTS

To those who have supported me throughout graduate school –

The Cossairt lab has been a better community than any I could have hoped for going into a PhD program. While some might say it is just the right mix of people at the right time, I truly believe the lab culture is fostered from the top down. Brandi's mentorship has not only guided my development as a scientist, but also set an excellent example for how to care for and encourage those around you. I am endlessly grateful for her support, academically, professionally and personally, throughout graduate school.

To my committee – Alexandra Velian, Gojko Lalic, James Carothers, and formerly Mike Heinekey and Christine Luscombe – thank you for your insightful questions and discussions during and outside of my exams. They have pushed my science forward and inspired me as a chemist.

My lab-mates have come to feel like an ever-evolving family. They have been there without fail to celebrate the big wins, comfort and encourage in times of burn out, and troubleshoot and brainstorm in times of confusion. I am constantly inspired by the collaboration and discussion within the group, and I am humbled to work alongside so many great scientists. But most of all, Ben Glassy, Danielle Henckle, Betsy Flowers, Jenny Stein, David Ung, Michael Enright, Beth Mundy, Andrew Ritchhart, Ian Murphy, Nayon Park, Tyler Robison, Madison Monahan, Florence Dou, Forrest Eagle, Micaela Homer, Ricardo Rivera, Helen Larson, Hao Nguyen, Emily Nishiwaki, Max Friedfeld, Ding-Yuan Kuo, Sam Harvey, Hunter Ripberger: thank you for being great friends and making me laugh every day.

The inorganic division as a whole has been incredibly supportive. I have made some incredible friends, some of whom I am endlessly indebted to for all of the times they have offered

to help me proofread, brainstorm, and train me: Louise Guard, Ben Leipzig, Braden Zahora, Jon Kephart, and Zuzana Culakova – thank you!

I would also like to acknowledge all the individuals who keep the chemistry department running smoothly to enable us to perform our research, and the funding sources that allowed this work: The Camille and Henry Dreyfus Foundation, The David and Lucile Packard Foundations, the ACS Petroleum Research Fund, and the Clean Energy Institute.

To those who have supported me from the beginning –

First, I would like to thank all my friends, especially Megan who has stuck by my side through it all. Thank you for all the years of friendship – your life working at a startup closely mirrored mine in grad school, and your dedication as a friend and constant willingness to escape to the mountains with me has kept me grounded.

Most importantly, my parents and my brother have always been my number one supporters, and my time in graduate school would not have looked the same without them. To my parents, thank you for always encouraging me and believing in me. Mom, thank you for always answering the phone, for demonstrating what an excellent work ethic looks like, and for all those hours you sat with me growing up helping me with homework and teaching me how to study (and also when it is time to close the books and have some fun). Dad, thank you for encouraging me to think outside the box, and for always reminding me to embrace joy and start with a joke. So here's one for you: What do heartburn chewables and formic acid have in common? They're both a form of ant acids! Tony, thank you for always reminding me to have a good time and offering a listening ear. I am lucky to have a brother who is always honest with me and who I can count on to have my back. Mom, Dad, and Tony, your love and support mean the world to me.

Chapter 1. INTRODUCTION

1.1 Carbon Dioxide Capture and Conversion Background

The development of catalysts to achieve new and more efficient chemical conversions has been at the forefront of our advancement as a society, from the Haber-Bosch process for ammonia synthesis making fertilizer readily available to feed the planet[1,2], to improved catalytic converters in our vehicles[3,4], to controlling enantioselectivities for pharmaceutical production[5]. Today, one active area of catalyst discovery and development centers around our need to develop sustainable energy sources and storage methods as well as carbon sources for the innumerable carbon-containing products that currently are sourced from petrochemicals. The dominant alternative carbon sources being pursued are carbon dioxide (CO_2) and bio-feedstocks.

As it stands today, there are two sources of CO_2 relevant to its future treatment as a feedstock that will also play a role in emissions reduction, the first of which is point source carbon capture from industrial and power plant sources and the second is direct air capture (DAC). In 2021, the cost of CO_2 from DAC is $100 - $1000 per ton. The adoption of both of these technologies is going to take a combination of significant R&D to reduce the associated cost and energy demands as well as policy support. It is currently politically infeasible to set the price of CO_2 high enough to make DAC competitive, and as such technological developments are required to bring down the cost of production/capture and also to improve the markets for CO_2 thus making it more valuable. There is currently limited market demand for CO_2, with the primary market being in the oil and gas industry for enhanced oil recovery and sequestration. The major non-oil and gas markets are chemical production, the food and beverage industries, and supplementing greenhouses.[6]

CO_2 recycling products have a long way to go before reaching market parity with traditional production methods.[7] Figure 1.1 shows the estimated cost of production for a variety of products from thermochemical CO_2 recycling compared to the current selling price of that product. The assumptions for calculation of estimated costs are that all components are from low-carbon energy sources, meaning they consume low-carbon electricity, or renewable energy, and they assumed the H_2, CO, and/or ammonia consumed as a reactant are supplied by onsite electrochemical processes powered by renewable energy. For the products that require H_2 input, the cost associated with the H_2 is significant. One outstanding challenge for the synthesis of many of these products is that of product selectivity in the reaction, which through the unproductive consumption of starting materials leads to greater costs.

One way to improve product selectivity and therefore reduce these costs is through catalyst development. Catalysts can be designed to favor certain reaction pathways by perturbing the energetics of intermediates. The end result is that more of the chemical reactants going into

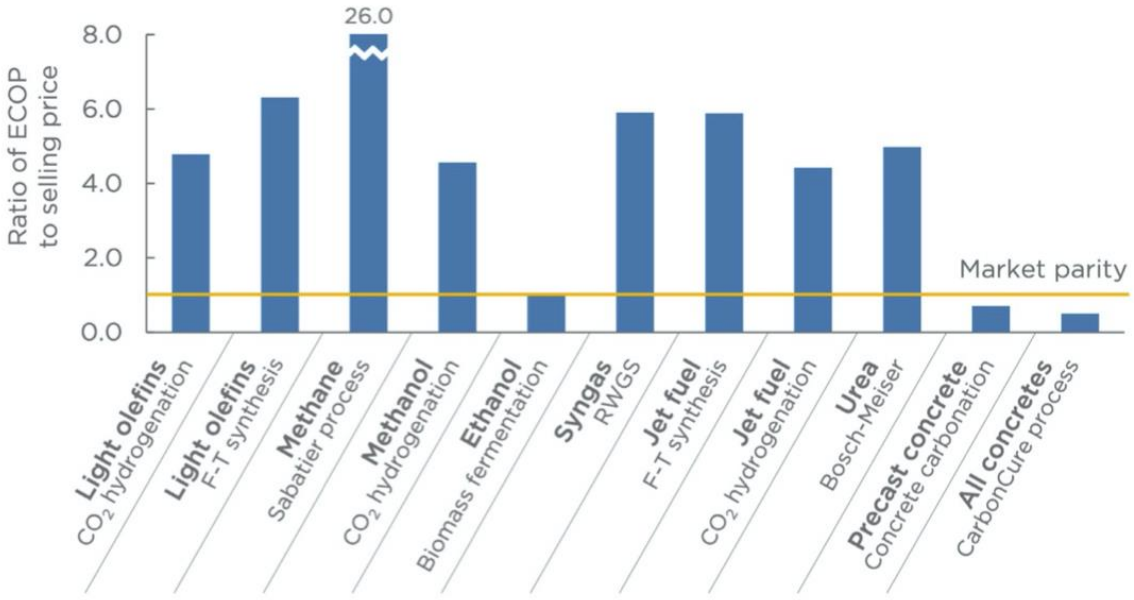

Figure 1.1. Estimated cost of production (ECOP) versus selling price of thermochemical CO_2 Recycling products, copywrite Columbia University 2021.[7]

the reaction are efficiently converted into the desired product instead of various byproducts. Improving product selectivity also means there is less need for product separation and purification, which can be intensive, and wasn't included in the cost estimation in this study. In addition to improving selectivity, other research targets for catalyst development outlined in the Basic Research Needs for Catalysis Science to Transform Energy Technologies report from the U.S. Department of Energy (2017) are for catalysts stable under industrial operating conditions and to understand and control dynamic evolution of the catalyst during the reaction.

1.2 Trends in State-of-the-Art Catalysts for Carbon Dioxide Reduction

Carbon dioxide reduction has been approached from a number of different angles, including biological and enzymatic possesses[8], organocatalysis[9–11], and thermo-[12–14], photo-[15,16] and electrocatalysis[15,17] in both homo-[13,14] and heterogeneous[12,17,18] systems. Aside from the societal impact that the identification of cheap and efficient catalysts for CO_2 reduction could have, CO_2 is a fundamentally interesting substrate given its thermodynamic stability and associated challenges with product selectivity.[12] Homogeneous organometallic systems are a useful launch pad for catalyst development from the perspective of intentional ligand design, given the precise control over reactivity and the detailed structural information available through analysis techniques like NMR and X-ray crystallography. Among state-of-the-art CO_2 hydrogenation catalysts, pincer type and tridentate facially coordinating tripodal ligands have been shown to be particularly effective.

Carbon dioxide can be converted into a variety of products including (i) C_1 products, such as carbon monoxide, formate/formic acid, methanol, and methane; (ii) C_2 and higher hydrocarbons for fuels; (iii) carboxylic acids via carboxylation of olefins; and (iv) polymers,

commonly via reaction with epoxides.[19] Common modes of activation often involve coordination to a metal center through π-coordination of the C=O bond or σ-bonding between the carbon and metal center, or less commonly σ-bonding between the oxygen and metal center (Figure 1.2).[20] Coordination and activation of CO_2 effectively increase the electron density in the CO_2 π* orbitals, lengthening and weakening the C=O π bond. The conversion of CO_2 is often facilitated by the presence of Lewis acid and amine additives. Among the roles Lewis acids play, two of the most common are to aid in the stabilization of activated CO_2 intermediates and as a counter ion to facilitate product release in the case of formate production.[21–25] Amines function as both a way to activate the substrate as well as increase the concentration of the CO_2 in solution and near the catalytic site.[26–29]

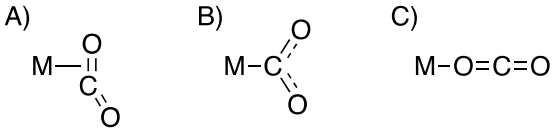

Figure 1.2. Modes of activation of CO_2 at a metal center (A) through π-coordination of the C=O bond, (B) σ-bonding between the carbon and metal center, or (C) less commonly σ-bonding between the oxygen and metal center.

1.2.1 *Pincer Ligands*

Pincer type ligands have shown to be active in CO_2 hydrogenation literature, and there are examples of where metal ligand cooperativity is both beneficial and detrimental. The reactivity with CO_2 shown by pincer supported complexes includes insertion of CO_2 into a variety of M-X bonds[30], hydrogenation to formate[25,31,32] and methanol[28,29,31,33], as well as the dehydrogenation of both formic acid[23,31,34] and methanol[22,26,27,31]. Common modes of metal ligand cooperativity observed with pincer complexes include aromatization/dearomatization[32,35–40] (Figure 1.3A) and participation of a secondary amine with a tunable protonation state[22,23,25,31,38,41] (Figure 1.3B).

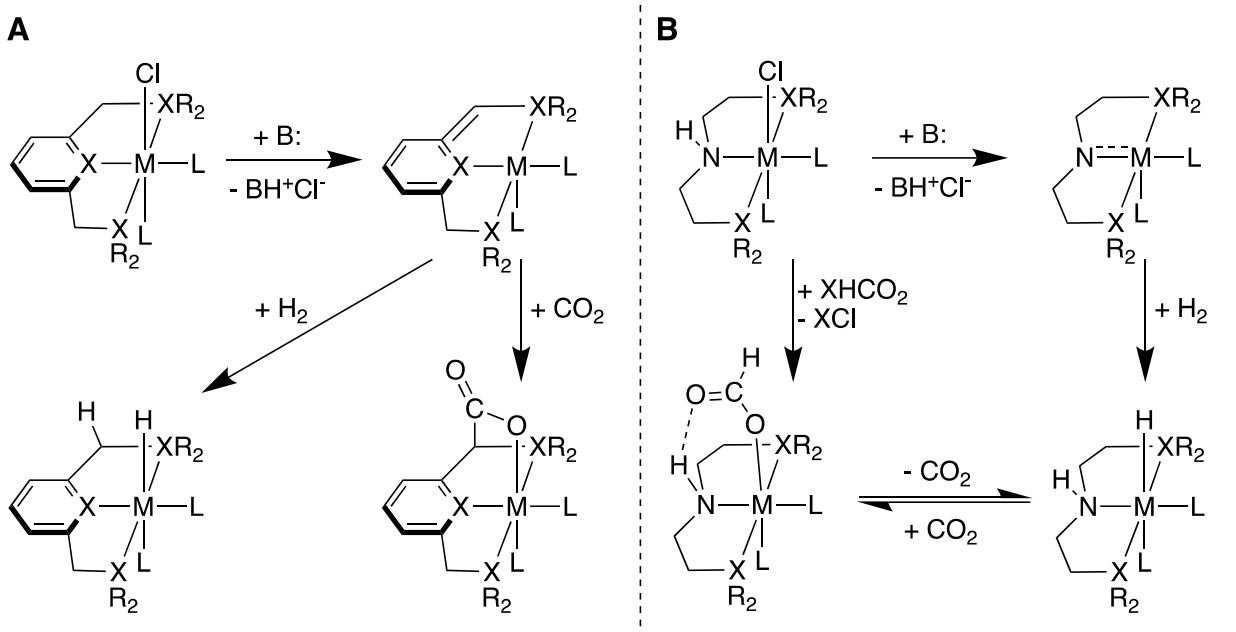

Figure 1.3. General description of metal-ligand cooperativity observed in pincer ligand supported CO_2 hydrogenation via (A) aromatization/dearomatization and (B) secondary amine protonation/deprotonation.

1.2.2 *Tridentate Facially Coordinating/Tripodal Ligands*

Other ligands that are important in the CO_2 hydrogenation literature are facially coordinating tridentate ligands. The facial coordination affords reactive sites that are cis to one another, enabling cooperative activation of substrates. Additionally, orbitals are oriented such that they facilitate back bonding interaction, thereby weakening multiple bonds and facilitating activation. In addition CO_2 hydrogenation and catalysis, the coordination chemistry of tripodal ligands has been explored for a variety of reasons, including as molecular mimics for metalloprotiens[42] and for complexation of lanthanides in self-assembled supramolecular systems[43] with applications in luminescent and light-converting devices and MRI probes, to name a few.

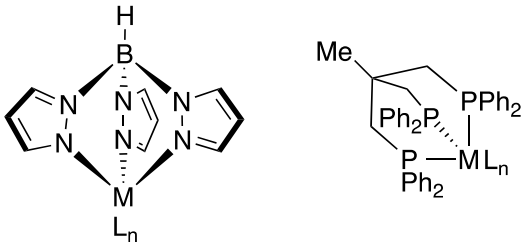

Figure 1.4. Generic representation of Tp and Triphos.

The 1,1,1-tis(diphenylphosphinomethyl)ethane (triphos) ligand and its synthetic variants are a widely studied class of tripodal ligands. When supporting a ruthenium metal center, these complexes been shown to catalyze alcohol amination[44], dehydrogenation of formic acid[45], methylation of amines[46] and imines[47] from CO_2 as a C_1 carbon source, and a variety of other hydrogenations, including the hydrogenation of amides[48,49] and lactams[50] to amines, the hydrogenation of esters[51–54] and carboxylic acids[54], and the hydrogenation of CO_2 to a variety of products including methanol[55–58] and dimethoxymethane (DMM) and other dialkoxymethane ethers which are useful formaldehyde equivalents[59–61]. A number of these ruthenium-triphos systems have also been adapted to utilize cobalt in the place of ruthenium, maintaining high catalytic activity.[62–64] Triphos is characterized by its strong sigma donating character and neutral charge, and reactivity can be tuned by altering the steric profile of the phosphine substituents[50,62,65] as well as the apical atom of the ligand[55,60,65]. As a result of the multidentate and strong sigma donating character, triphos lends catalysts high thermal stability which has been named as a factor contributing it its success in the transformation of CO_2 to methanol.[57]

Tris(pyrazolyl)borate (Tp) and its synthetic variants are another class of tripodal ligands that are characterized by their strong sigma donation, anionic charge, and facial coordination. In the case of ruthenium- and osmium-Tp complexes, the fragments are strongly hybridized such

that there is a strong bias towards 6-coordinate, octahedral complexes with the metal in the formal +2 oxidation state, which results in these complexes rarely exhibiting reactivity involving oxidative additions or associative substitutions.[66] Ruthenium-Tp complexes have been shown to catalyze hydrogenation[66–68], coupling reactions[66,69,70], hydration of nitriles[66,71], and isomerization and cyclization reactions[66]. Particularly relevant to the hydrogenation chemistry, ruthenium-Tp hydride and dihydrogen complexes have been well studied.[68] In the case of $TpRu(PPh_3)(L)(CH_3CN)$ (L = PPh_3 or CH_3CN) reaction with H_2, the $TpRu(PPh_3)(L)^+$ moiety supports an η^2–dihydrogen ligand rather than a dihydride. This observation leads to the proposition of a reaction mechanism for olefin hydrogenation that differs from the common Wilkinson catalyst mechanism which passes through a dihydride olefin intermediate. Instead, $TpRu(PPh_3)(L)(\eta^2–H_2)$ passes through a dihydrogen olefin intermediate, which is preferred as the olefin displaces L resulting in a less electron dense metal center.[68]

Furthermore, the reactivity studies of a hydride precursor, $TpRu(PPh_3)(CH_3CN)H$, with H_2 under pressure highlight another important feature of symmetric tripodal ligands in general. Under the previously stated conditions, a dihydrogen-hydride complex, $TpRu(PPh_3)(H_2)H$, is formed which exhibits a single hydride resonance in the ^1H NMR integrating to 3H which does not decoalesce down to -110ºC.[68] This rapid interconversion in part illustrates the equivalency of the reactive sites. The *cis* configuration of the open coordination sites on tridentate facially coordinating ligands allows for the activation of multiple reaction components at the metal center and for their facile interaction with one another.

The foundation these ligand systems lay, particularly in the field of CO_2 utilization, provides opportunities for further catalyst development. The incorporation of key features in these other ligand systems, for example strong sigma donation, tripodal coordination, and metal-

ligand cooperation capabilities, may deepen our understanding of the interplay of these ligand characteristics and eventually lead to a more active CO_2 reduction catalyst.

1.3 Protic N-Heterocyclic Carbenes

Protic N-heterocyclic carbenes (PNHCs) are a class of ligand characterized as strong sigma donors with an NH-wingtip adjacent to the metal center that is capable of metal ligand cooperativity. While traditional *N*-R, *N*-R substituted N-heterocyclic carbenes are prevalent throughout the literature, PNHCs are far less common. To the best of our knowledge, there are fewer than ten examples of PNHCs being used in catalysis, including the work presented within this dissertation. Stoichiometric reactivity with PNHCs, and specifically bond activation via metal-ligand cooperativity has been more broadly explored in the literature.

Metal-ligand cooperativity within p-NHC systems has been described in both the protic and the deprotonated state. When the NH-wingtip is protonated, it has been shown to participate in hydrogen bonding which leads to it functioning as a molecular recognition unit facilitating transformations for substrates containing hydrogen bonding acceptors.[72,73] When deprotonated, the ligand adopts an anionic charge and participates in bond activation and cleavage (Figure 1.5). Bond activation has been observed for CO_2[74], acetonitrile[75], and others[76], resulting in the substrate bridging between metal center and the nitrogen. Bond cleavage for X–H typically occurs via deprotonation of the substrate resulting in the reprotonation of the NH-wingtip, and has been documented for H_2[77,78] and acetylene[77]. The splitting of H_2, yielding a M–H and N–H, has make PNHCs of interest for catalyzing hydrogenation reactions, and in particular transfer hydrogenations have been pursued.[77–79] Additionally, N-alkylation[77,80], N-allylation[80], and N-carbamoylation[80] and other[76] types of N-substitutions have been observed.

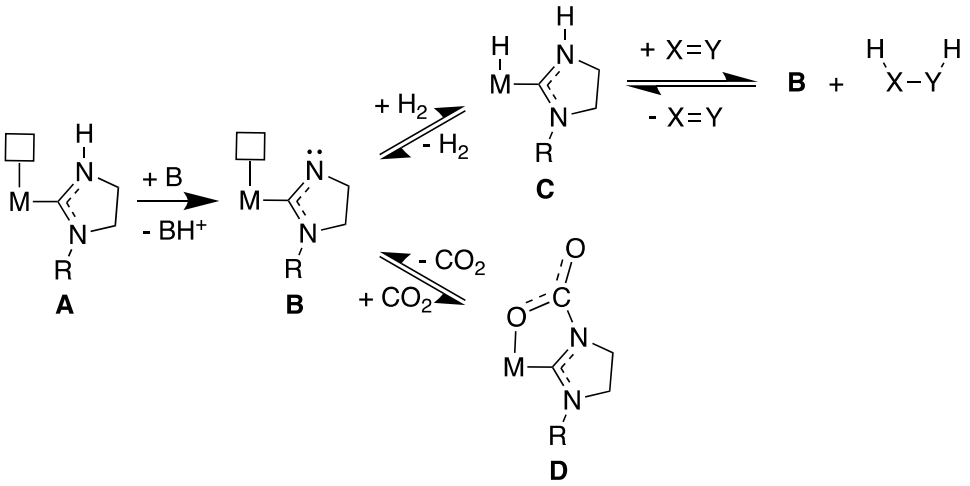

Figure 1.5. General reactivity of protic N-heterocyclic carbenes via deprotonation of **A** to **B**, with reversible splitting of H_2 to form **C**, which is then capable of hydrogenation of substrate X=Y (carbonyl or olefin) to form **B**. **B** is also capable of dehydrogenation of alcohols, as observed in transfer hydrogenation systems, and of bond activation of type **D**.

PNHCs are also capable of supporting additional metal centers at the deprotonated NH-wingtip.[76,81] It is common to observe dimerization in these systems where the sterics allow, which may occur through coordination of the deprotonated PNHC-nitrogen to a second identical metal center[82–85] or via coordination of two deprotonated PNHC-nitrogen atoms of different molecules to an added metal precursor[86]. Where sterics do not allow or through ancillary ligand choice dimerization may be avoided, in which case it is common to observe chelation either by a bis-PNHC[86,87] or by a PNHC and an additional coordinating group[88]. Notably within these systems metal-metal bonds are not observed between the metal coordinated at the PNHC-carbon and the PNHC-nitrogen.

1.4 Bimetallic Catalysis and Carbon Dioxide Reduction

Examining metalloenzymes like formic acid dehydrogenase, which interconverts formic acid and CO_2, and carbon monoxide dehydrogenase, which interconvert carbon monoxide and CO_2, provides evidence for the important role nuclearity plays in selectivity and efficiency of

these processes. Formic acid dehydrogenase operates as a monometallic Mo or W process[89], while carbon monoxide dehydrogenase operates through a Ni/Fe[90] or Cu/Mo[91] heterobimetallic pathway (Figure 1.6). With these systems as a point of reference, interest in bimetallic complexes to control selectivity for CO_2 reduction has grown.

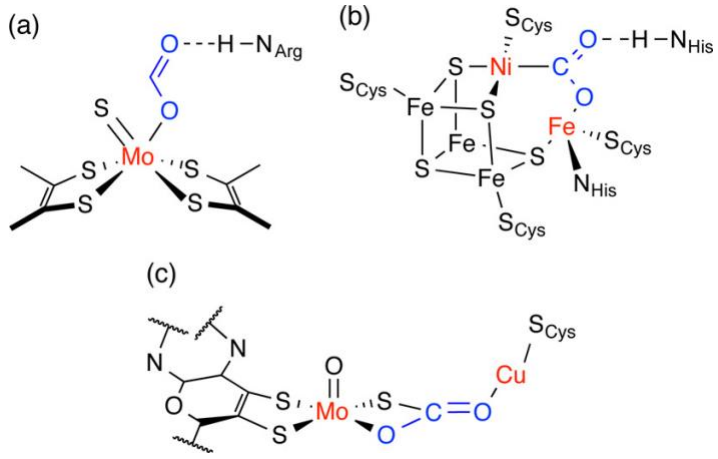

Figure 1.6. (a) Proposed monometallic CO_2 activation by a [Mo] formic acid dehydrogenase; proposed bimetallic CO_2 activation at the active sites of (b) [NiFe] and (c) [MoCu] carbon monoxide dehydrogenases.[89,91,92] Reprinted with permission from Bagherzadeh, S. and Mankad, N. *J. Am. Chem. Soc.* **2015**, 137, 34, 10898–10901. Copyright 2015 American Chemical Society.

Heterogeneous bimetallic systems have been explored for CO_2 hydrogenation catalysis to products such as CO, formate, methane, and other high value C_{2+} fuel products such as dimethyl ethers, olefins, liquid fuels, and higher alcohols.[93] Given the thermodynamic stability of CO_2 and the high barrier to C–C bond formation, such transformations are challenging, leading to issues with product selectivity in terms of carbon chain length as well as due to competitive C_1 product side reactions. The influence of a second metal on product selectivity and catalyst activity, particularly for C_{2+} products, has been demonstrated for several systems, however mechanistic details around the synergistic effects of two metals remains speculative.[93–95]

Molecular bimetallic systems provide more specific insights around metal-metal cooperation. Bimetallic cooperation has been observed in systems with two independent

monometallic complexes[96] as well as within ligand systems that support two metal centers[97]. Among the latter, bimetallic complexes supported by amino-phosphine ligands have been explored in the activation of CO_2,[98,99] as well as more broadly for carbonyl containing substrates.[100,101] These ligands support the two metal centers in a boat conformation with a flexible metal-metal bond, and experimental and computations studies suggest that this arrangement of the metal centers facilitates fast catalysis in allylic amination reactions.[102]

1.5 Summary and Outlook

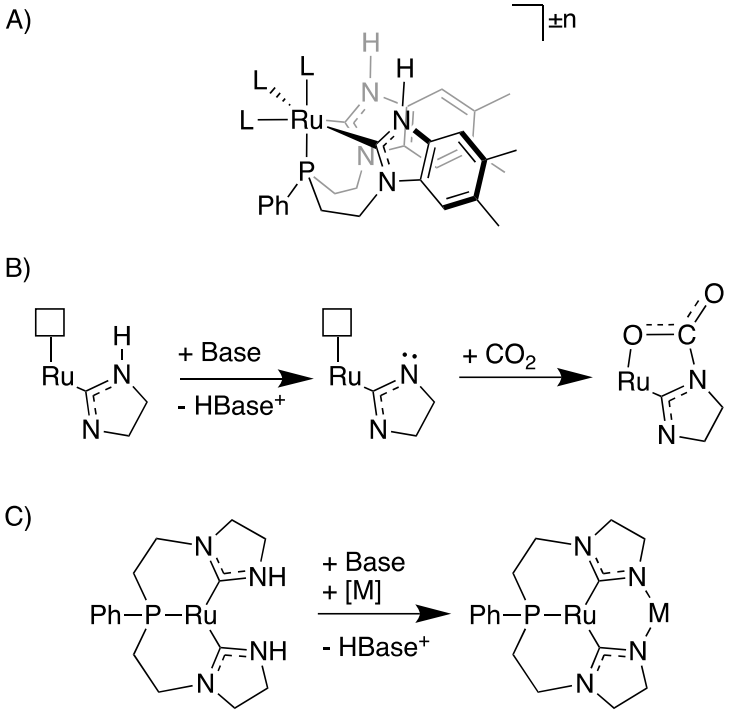

Figure 1.7. A) General representation of the tripodal bis-(protic N-heterocyclic carbene) phosphine ligand developed by the Cossairt group. B) Truncated depiction of metal ligand cooperativity for the activation of CO_2 between the ruthenium metal center one of the PNHCs.[74] C) Truncated depiction of the synthesis of the bimetallic complex supported by the bis-(PNHC), previously shown demonstrated by Flowers, *et. al.* with the ruthenium coordinated by Cp*.[87]

The bis-PNHC phosphine ligand system explored in this dissertation combines many of the features of the state-of-the-art CO_2 hydrogenation catalysts (Figure 1.7A). The tripodal coordination of the ligand allows for three facial coordination sites available for reactivity or

tuning through the exploration of ancillary ligands with different electronics, sterics, and flexibility. In chapter 1, the coordination chemistry of a series of ancillary ligands is investigated. While the bis-(PNHC) phosphine ligand is reminiscent of the geometries of triphos and Tp ligands, the different influence from the phosphine coordination versus the carbene coordination may further help tune catalyst activity and selectivity by changing the energetics of different coordination sites, versus the identical coordinating groups in traditional triphos and Tp ligands. The influence of these different binding groups at the coordination sites in the *trans* positions are illustrated in the coordination of various bidentate ancillary ligands. These factors may be further exploited by changing substituents at the phosphine or the benzimidazole backbone. Additionally, the stronger sigma donating character of the carbenes compared to the phosphine should lead to better thermal stability and a long-lived catalyst.

In addition to the tripodal coordination, the presence of the NH-wingtips adjacent to the metal center provide opportunities for metal ligand cooperativity. As observed in the pincer systems, metal ligand cooperativity can play a role in bond activation or bond breaking as well as in hydrogen bonding to stabilize high energy intermediates. Within our system the role of metal ligand cooperativity for CO_2 activation and hydrogenation is explored (Figure 1.7B). Prior work from the Cossairt group has demonstrated stoichiometric reactivity of CO_2 and formate with the bipyridine substituted ruthenium bis-PNHC phosphine complex, leading to an isolable CO_2 adduct with metal ligand cooperativity for the activation of CO_2. In chapter 2 of this work, the catalytic activity of this complex and the role of metal ligand cooperativity in the operative catalytic cycle are investigated. The splitting of H_2 between the ruthenium and deprotonated PNHC is also of interest, given the precedent for this type of metal ligand cooperativity in the

PNHC literature[77,78] and the prevalence of CO_2 insertion into M–H bonds as a step towards CO_2 hydrogenation[103].

We also anticipate that by installing a second metal center at the PNHC position we may be able to tune reactivity and achieve a different type of bond activation, for example hydrogenation to formate versus C=O bond cleavage. While the synthesis of bimetallic Ru(II)–M(II) (M = Co, Fe) complexes supported by this bis-PNHC phosphine ligand have been previously reported by the Cossairt group[87], the ruthenium was bound by Cp* thus blocking coordination sites (Figure 1.7C). The synthesis of bimetallic complexes from the bipyridine ligated ruthenium complex is explored within this dissertation, with the goal of having two coordination sites available for substrate activation to probe the synergistic effects of between the two metals.

1.6 REFERENCES

(1) Shi, L.; Yin, Y.; Wang, S.; Sun, H. Rational Catalyst Design for N_2 Reduction under Ambient Conditions: Strategies toward Enhanced Conversion Efficiency. *ACS Catal.* **2020**, *10* (12), 6870–6899. https://doi.org/10.1021/acscatal.0c01081.

(2) Liu, H.; Wei, L.; Liu, F.; Pei, Z.; Shi, J.; Wang, Z.; He, D.; Chen, Y. Homogeneous, Heterogeneous, and Biological Catalysts for Electrochemical N_2 Reduction toward NH_3 under Ambient Conditions. *ACS Catal.* **2019**, *9* (6), 5245–5267. https://doi.org/10.1021/acscatal.9b00994.

(3) *Catalytic Control of Air Pollution: Mobile and Stationary Sources*; Silver, R. G., Sawyer, J. E., Summers, J. C., Eds.; ACS Symposium Series; American Chemical Society: Washington, DC, 1992; Vol. 495. https://doi.org/10.1021/bk-1992-0495.

(4) Granger, P.; Parvulescu, V. I. Catalytic NO_x Abatement Systems for Mobile Sources: From Three-Way to Lean Burn after-Treatment Technologies. *Chem. Rev.* **2011**, *111* (5), 3155–3207. https://doi.org/10.1021/cr100168g.

(5) Magano, J.; Dunetz, J. R. Large-Scale Applications of Transition Metal-Catalyzed Couplings for the Synthesis of Pharmaceuticals. *Chem. Rev.* **2011**, *111* (3), 2177–2250. https://doi.org/10.1021/cr100346g.

(6) Meckling, J.; Biber, E. A Policy Roadmap for Negative Emissions Using Direct Air Capture. *Nat. Commun.* **2021**, *12* (1), 2051. https://doi.org/10.1038/s41467-021-22347-1.

(7) Bhardwaj, A.; Mccormick, D. C.; Friedmann, D. J. OPPORTUNITIES AND LIMITS OF CO2 RECYCLING IN A CIRCULAR CARBON ECONOMY: 76.

(8) Appel, A. M.; Bercaw, J. E.; Bocarsly, A. B.; Dobbek, H.; DuBois, D. L.; Dupuis, M.; Ferry, J. G.; Fujita, E.; Hille, R.; Kenis, P. J. A.; Kerfeld, C. A.; Morris, R. H.; Peden, C. H. F.; Portis, A. R.; Ragsdale, S. W.; Rauchfuss, T. B.; Reek, J. N. H.; Seefeldt, L. C.; Thauer, R. K.; Waldrop, G. L. Frontiers, Opportunities, and Challenges in Biochemical and Chemical Catalysis of CO_2 Fixation. *Chem. Rev.* **2013**, *113* (8), 6621–6658. https://doi.org/10.1021/cr300463y.
(9) Pramudita, R. A.; Motokura, K. Transformative Reduction of Carbon Dioxide through Organocatalysis with Silanes. *Green Chem.* **2018**, *20* (21), 4834–4843. https://doi.org/10.1039/C8GC02052C.
(10) Frogneux, X.; Blondiaux, E.; Thuéry, P.; Cantat, T. Bridging Amines with CO_2 : Organocatalyzed Reduction of CO_2 to Aminals. *ACS Catal.* **2015**, *5* (7), 3983–3987. https://doi.org/10.1021/acscatal.5b00734.
(11) Fiorani, G.; Guo, W.; Kleij, A. W. Sustainable Conversion of Carbon Dioxide: The Advent of Organocatalysis. *Green Chem.* **2015**, *17* (3), 1375–1389. https://doi.org/10.1039/C4GC01959H.
(12) De, S.; Dokania, A.; Ramirez, A.; Gascon, J. Advances in the Design of Heterogeneous Catalysts and Thermocatalytic Processes for CO_2 Utilization. *ACS Catal.* **2020**, *10* (23), 14147–14185. https://doi.org/10.1021/acscatal.0c04273.
(13) Sordakis, K.; Tang, C.; Vogt, L. K.; Junge, H.; Dyson, P. J.; Beller, M.; Laurenczy, G. Homogeneous Catalysis for Sustainable Hydrogen Storage in Formic Acid and Alcohols. *Chem. Rev.* **2017**. https://doi.org/10.1021/acs.chemrev.7b00182.
(14) Wang, W.-H.; Himeda, Y.; Muckerman, J. T.; Manbeck, G. F.; Fujita, E. CO_2 Hydrogenation to Formate and Methanol as an Alternative to Photo- and Electrochemical CO_2 Reduction. *Chem. Rev.* **2015**, *115* (23), 12936–12973. https://doi.org/10.1021/acs.chemrev.5b00197.
(15) Kumaravel, V.; Bartlett, J.; Pillai, S. C. Photoelectrochemical Conversion of Carbon Dioxide (CO_2) into Fuels and Value-Added Products. *ACS Energy Lett.* **2020**, *5* (2), 486–519. https://doi.org/10.1021/acsenergylett.9b02585.
(16) Li, K.; Peng, B.; Peng, T. Recent Advances in Heterogeneous Photocatalytic CO_2 Conversion to Solar Fuels. *ACS Catal.* **2016**, *6* (11), 7485–7527. https://doi.org/10.1021/acscatal.6b02089.
(17) Chen, C.; Zhang, Z.; Li, G.; Li, L.; Lin, Z. Recent Advances on Nanomaterials for Electrocatalytic CO_2 Conversion. *Energy Fuels* **2021**, *35* (9), 7485–7510. https://doi.org/10.1021/acs.energyfuels.1c00448.
(18) Jiang, X.; Nie, X.; Guo, X.; Song, C.; Chen, J. G. Recent Advances in Carbon Dioxide Hydrogenation to Methanol via Heterogeneous Catalysis. *Chem. Rev.* **2020**, *120* (15), 7984–8034. https://doi.org/10.1021/acs.chemrev.9b00723.
(19) Burkart, M. D.; Hazari, N.; Tway, C. L.; Zeitler, E. L. Opportunities and Challenges for Catalysis in Carbon Dioxide Utilization. *ACS Catal.* **2019**, 7937–7956. https://doi.org/10.1021/acscatal.9b02113.
(20) Vogt, M.; Nerush, A.; Diskin-Posner, Y.; Ben-David, Y.; Milstein, D. Reversible CO_2 Binding Triggered by Metal–Ligand Cooperation in a Rhenium(I) PNP Pincer-Type Complex and the Reaction with Dihydrogen. *Chem Sci* **2014**, *5* (5), 2043–2051. https://doi.org/10.1039/C4SC00130C.
(21) Silvia, J. S.; Cummins, C. C. Binding, Release, and Functionalization of CO2 at a Nucleophilic Oxo Anion Complex of Titanium. *Chem. Sci.* **2011**, *2* (8), 1474. https://doi.org/10.1039/c1sc00215e.

(22) Bielinski, E. A.; Förster, M.; Zhang, Y.; Bernskoetter, W. H.; Hazari, N.; Holthausen, M. C. Base-Free Methanol Dehydrogenation Using a Pincer-Supported Iron Compound and Lewis Acid Co-Catalyst. *ACS Catal.* **2015**, *5* (4), 2404–2415. https://doi.org/10.1021/acscatal.5b00137.
(23) Bielinski, E. A.; Lagaditis, P. O.; Zhang, Y.; Mercado, B. Q.; Würtele, C.; Bernskoetter, W. H.; Hazari, N.; Schneider, S. Lewis Acid-Assisted Formic Acid Dehydrogenation Using a Pincer-Supported Iron Catalyst. *J. Am. Chem. Soc.* **2014**, *136* (29), 10234–10237. https://doi.org/10.1021/ja505241x.
(24) Heimann, J. E.; Bernskoetter, W. H.; Hazari, N.; Mayer, J. M. Acceleration of CO_2 Insertion into Metal Hydrides: Ligand, Lewis Acid, and Solvent Effects on Reaction Kinetics. *Chem. Sci.* **2018**, *9* (32), 6629–6638. https://doi.org/10.1039/C8SC02535E.
(25) Zhang, Y.; MacIntosh, A. D.; Wong, J. L.; Bielinski, E. A.; Williard, P. G.; Mercado, B. Q.; Hazari, N.; Bernskoetter, W. H. Iron Catalyzed CO_2 Hydrogenation to Formate Enhanced by Lewis Acid Co-Catalysts. *Chem Sci* **2015**, *6* (7), 4291–4299. https://doi.org/10.1039/C5SC01467K.
(26) Kothandaraman, J.; Goeppert, A.; Czaun, M.; Olah, G. A.; Prakash, G. K. S. Conversion of CO_2 from Air into Methanol Using a Polyamine and a Homogeneous Ruthenium Catalyst. *J. Am. Chem. Soc.* **2016**, *138* (3), 778–781. https://doi.org/10.1021/jacs.5b12354.
(27) Kothandaraman, J.; Kar, S.; Sen, R.; Goeppert, A.; Olah, G. A.; Prakash, G. K. S. Efficient Reversible Hydrogen Carrier System Based on Amine Reforming of Methanol. *J. Am. Chem. Soc.* **2017**, *139* (7), 2549–2552. https://doi.org/10.1021/jacs.6b11637.
(28) Rezayee, N. M.; Huff, C. A.; Sanford, M. S. Tandem Amine and Ruthenium-Catalyzed Hydrogenation of CO_2 to Methanol. *J. Am. Chem. Soc.* **2015**, *137* (3), 1028–1031. https://doi.org/10.1021/ja511329m.
(29) Lane, E. M.; Zhang, Y.; Hazari, N.; Bernskoetter, W. H. Sequential Hydrogenation of CO_2 to Methanol Using a Pincer Iron Catalyst. *Organometallics* **2019**, acs.organomet.9b00413. https://doi.org/10.1021/acs.organomet.9b00413.
(30) Schmeier, T. J.; Nova, A.; Hazari, N.; Maseras, F. Synthesis of PCP-Supported Nickel Complexes and Their Reactivity with Carbon Dioxide. *Chem. – Eur. J.* **2012**, *18* (22), 6915–6927. https://doi.org/10.1002/chem.201103992.
(31) Bernskoetter, W. H.; Hazari, N. Reversible Hydrogenation of Carbon Dioxide to Formic Acid and Methanol: Lewis Acid Enhancement of Base Metal Catalysts. *Acc. Chem. Res.* **2017**, *50* (4), 1049–1058. https://doi.org/10.1021/acs.accounts.7b00039.
(32) Huff, C. A.; Sanford, M. S. Catalytic CO_2 Hydrogenation to Formate by a Ruthenium Pincer Complex. *ACS Catal.* **2013**, *3* (10), 2412–2416. https://doi.org/10.1021/cs400609u.
(33) Huff, C. A.; Sanford, M. S. Cascade Catalysis for the Homogeneous Hydrogenation of CO_2 to Methanol. *J. Am. Chem. Soc.* **2011**, *133* (45), 18122–18125. https://doi.org/10.1021/ja208760j.
(34) Curley, J. B.; Smith, N. E.; Bernskoetter, W. H.; Hazari, N.; Mercado, B. Q. Catalytic Formic Acid Dehydrogenation and CO_2 Hydrogenation Using Iron $PN^R P$ Pincer Complexes with Isonitrile Ligands. *Organometallics* **2018**. https://doi.org/10.1021/acs.organomet.8b00534.
(35) Vogt, M.; Gargir, M.; Iron, M. A.; Diskin-Posner, Y.; Ben-David, Y.; Milstein, D. A New Mode of Activation of CO2 by Metal–Ligand Cooperation with Reversible C□C and M□O Bond Formation at Ambient Temperature. *Chem. – Eur. J.* **2012**, *18* (30), 9194–9197. https://doi.org/10.1002/chem.201201730.
(36) Zou, Y.-Q.; Chakraborty, S.; Nerush, A.; Oren, D.; Diskin-Posner, Y.; Ben-David, Y.; Milstein, D. Highly Selective, Efficient Deoxygenative Hydrogenation of Amides Catalyzed by a

Manganese Pincer Complex via Metal–Ligand Cooperation. *ACS Catal.* **2018**, 8014–8019. https://doi.org/10.1021/acscatal.8b02902.
(37) Feller, M.; Gellrich, U.; Anaby, A.; Diskin-Posner, Y.; Milstein, D. Reductive Cleavage of CO_2 by Metal–Ligand-Cooperation Mediated by an Iridium Pincer Complex. *J. Am. Chem. Soc.* **2016**, *138* (20), 6445–6454. https://doi.org/10.1021/jacs.6b00202.
(38) Gunanathan, C.; Milstein, D. Bond Activation and Catalysis by Ruthenium Pincer Complexes. *Chem. Rev.* **2014**, *114* (24), 12024–12087. https://doi.org/10.1021/cr5002782.
(39) Huff, C. A.; Kampf, J. W.; Sanford, M. S. Role of a Noninnocent Pincer Ligand in the Activation of CO_2 at (PNN)Ru(H)(CO). *Organometallics* **2012**, *31* (13), 4643–4645. https://doi.org/10.1021/om300403b.
(40) Huff, C. A.; Kampf, J. W.; Sanford, M. S. Reversible Carbon–Carbon Bond Formation between Carbonyl Compounds and a Ruthenium Pincer Complex. *Chem. Commun.* **2013**, *49* (64), 7147. https://doi.org/10.1039/c3cc43517b.
(41) Schmeier, T. J.; Dobereiner, G. E.; Crabtree, R. H.; Hazari, N. Secondary Coordination Sphere Interactions Facilitate the Insertion Step in an Iridium(III) CO_2 Reduction Catalyst. *J. Am. Chem. Soc.* **2011**, *133* (24), 9274–9277. https://doi.org/10.1021/ja2035514.
(42) Walleck, S.; Glaser, T. A Dinucleating Ligand System with Varying Terminal Donors to Mimic Diiron Active Sites. *Isr. J. Chem.* **2020**, *60* (10–11), 1019–1031. https://doi.org/10.1002/ijch.201900097.
(43) Hamacek, J.; Vuillamy, A. Controlling the Structures of Lanthanide Complexes in Self-Assemblies with Tripodal Ligands. *Eur. J. Inorg. Chem.* **2018**, *2018* (10), 1155–1166. https://doi.org/10.1002/ejic.201701075.
(44) Nakagawa, N.; Derrah, E. J.; Schelwies, M.; Rominger, F.; Trapp, O.; Schaub, T. Triphos Derivatives and Diphosphines as Ligands in the Ruthenium-Catalysed Alcohol Amination with NH_3. *Dalton Trans.* **2016**, *45* (16), 6856–6865. https://doi.org/10.1039/C5DT04870B.
(45) Mellone, I.; Peruzzini, M.; Rosi, L.; Mellmann, D.; Junge, H.; Beller, M.; Gonsalvi, L. Formic Acid Dehydrogenation Catalysed by Ruthenium Complexes Bearing the Tripodal Ligands Triphos and NP_3. *Dalton Trans* **2013**, *42* (7), 2495–2501. https://doi.org/10.1039/C2DT32043F.
(46) Li, Y.; Sorribes, I.; Yan, T.; Junge, K.; Beller, M. Selective Methylation of Amines with Carbon Dioxide and H2. *Angew. Chem. Int. Ed.* **2013**, *52* (46), 12156–12160. https://doi.org/10.1002/anie.201306850.
(47) Beydoun, K.; Ghattas, G.; Thenert, K.; Klankermayer, J.; Leitner, W. Ruthenium-Catalyzed Reductive Methylation of Imines Using Carbon Dioxide and Molecular Hydrogen. *Angew. Chem. Int. Ed.* **2014**, *53* (41), 11010–11014. https://doi.org/10.1002/anie.201403711.
(48) Núñez Magro, A. A.; Eastham, G. R.; Cole-Hamilton, D. J. The Synthesis of Amines by the Homogeneous Hydrogenation of Secondary and Primary Amides. *Chem. Commun.* **2007**, No. 30, 3154. https://doi.org/10.1039/b706635j.
(49) Coetzee, J.; Dodds, D. L.; Klankermayer, J.; Brosinski, S.; Leitner, W.; Slawin, A. M. Z.; Cole-Hamilton, D. J. Homogeneous Catalytic Hydrogenation of Amides to Amines. *Chem. - Eur. J.* **2013**, *19* (33), 11039–11050. https://doi.org/10.1002/chem.201204270.
(50) Meuresch, M.; Westhues, S.; Leitner, W.; Klankermayer, J. Tailor-Made Ruthenium-Triphos Catalysts for the Selective Homogeneous Hydrogenation of Lactams. *Angew. Chem.* **2016**, *128* (4), 1414–1417. https://doi.org/10.1002/ange.201509650.

(51) Teunissen, H. T.; Elsevier, C. J. Ruthenium Catalysed Hydrogenation of Dimethyl Oxalate to Ethylene Glycol. *Chem. Commun.* **1997**, No. 7, 667–668. https://doi.org/10.1039/a700862g.
(52) Teunissen, H. T. Homogeneous Ruthenium Catalyzed Hydrogenation of Esters to Alcohols‡. *Chem. Commun.* **1998**, No. 13, 1367–1368. https://doi.org/10.1039/a801807c.
(53) van Engelen, M. C.; Teunissen, H. T.; de Vries, J. G.; Elsevier, C. Suitable ligands for homogeneous ruthenium-catalyzed hydrogenolysis of esters https://reader.elsevier.com/reader/sd/pii/S1381116903004278?token=59E35B9837870AB5EA7078982A205F48552C13E0F92712C7CA2FDA20D13E848B27F584B47E9643AA309E65184EC16DDB&originRegion=us-east-1&originCreation=20211027220638 (accessed 2021 -10 -27). https://doi.org/10.1016/S1381-1169(03)00427-8.
(54) Li, Y.; Topf, C.; Cui, X.; Junge, K.; Beller, M. Lewis Acid Promoted Ruthenium(II)-Catalyzed Etherifications by Selective Hydrogenation of Carboxylic Acids/Esters. *Angew. Chem.* **2015**, *127* (17), 5285–5289. https://doi.org/10.1002/ange.201500062.
(55) Schieweck, B. G.; Jürling-Will, P.; Klankermayer, J. Structurally Versatile Ligand System for the Ruthenium Catalyzed One-Pot Hydrogenation of CO_2 to Methanol. *ACS Catal.* **2020**, *10* (6), 3890–3894. https://doi.org/10.1021/acscatal.9b04977.
(56) Erickson, J. D.; Preston, A. Z.; Linehan, J. C.; Wiedner, E. S. Enhanced Hydrogenation of Carbon Dioxide to Methanol by a Ruthenium Complex with a Charged Outer-Coordination Sphere. *ACS Catal.* **2020**, *10* (13), 7419–7423. https://doi.org/10.1021/acscatal.0c02268.
(57) Wesselbaum, S.; Moha, V.; Meuresch, M.; Brosinski, S.; Thenert, K. M.; Kothe, J.; Stein, T. vom; Englert, U.; Hölscher, M.; Klankermayer, J.; Leitner, W. Hydrogenation of Carbon Dioxide to Methanol Using a Homogeneous Ruthenium–Triphos Catalyst: From Mechanistic Investigations to Multiphase Catalysis. *Chem Sci* **2015**, *6* (1), 693–704. https://doi.org/10.1039/C4SC02087A.
(58) Wesselbaum, S.; vom Stein, T.; Klankermayer, J.; Leitner, W. Hydrogenation of Carbon Dioxide to Methanol by Using a Homogeneous Ruthenium-Phosphine Catalyst. *Angew. Chem. Int. Ed.* **2012**, *51* (30), 7499–7502. https://doi.org/10.1002/anie.201202320.
(59) Thenert, K.; Beydoun, K.; Wiesenthal, J.; Leitner, W.; Klankermayer, J. Ruthenium-Catalyzed Synthesis of Dialkoxymethane Ethers Utilizing Carbon Dioxide and Molecular Hydrogen. *Angew. Chem. Int. Ed.* **2016**, *55* (40), 12266–12269. https://doi.org/10.1002/anie.201606427.
(60) Seibicke, M.; Siebert, M.; Siegle, A. F.; Gutenthaler, S. M.; Trapp, O. Application of Hetero-Triphos Ligands in the Selective Ruthenium-Catalyzed Transformation of Carbon Dioxide to the Formaldehyde Oxidation State. *Organometallics* **2019**, *38* (8), 1809–1814. https://doi.org/10.1021/acs.organomet.9b00107.
(61) Konrath, R.; Sekine, K.; Jevtovikj, I.; Paciello, R. A.; Hashmi, A. S. K.; Schaub, T. Performance Enhancing Additives for Reusable Ruthenium-Triphos Catalysts in the Reduction of CO_2 to Dimethoxymethane. *Green Chem.* **2020**, *22* (19), 6464–6470. https://doi.org/10.1039/D0GC02528C.
(62) Schieweck, B. G.; Klankermayer, J. Tailor-Made Molecular Cobalt Catalyst System for the Selective Transformation of Carbon Dioxide to Dialkoxymethane Ethers. *Angew. Chem. Int. Ed.* **2017**, *56* (36), 10854–10857. https://doi.org/10.1002/anie.201702905.
(63) Schneidewind, J.; Adam, R.; Baumann, W.; Jackstell, R.; Beller, M. Low-Temperature Hydrogenation of Carbon Dioxide to Methanol with a Homogeneous Cobalt Catalyst. *Angew. Chem. Int. Ed.* **2017**, *56* (7), 1890–1893. https://doi.org/10.1002/anie.201609077.

(64) Korstanje, T. J.; van der Vlugt, J. I.; Elsevier, C.; de Bruin, B. Hydrogenation of Carboxylic Acids with a Homogeneous Cobalt Catalyst. *Science* **2016**, *350* (6258), 298–302. https://doi.org/10.1126/science.aac9655.
(65) Siebert, M.; Seibicke, M.; Siegle, A. F.; Kräh, S.; Trapp, O. Selective Ruthenium-Catalyzed Transformation of Carbon Dioxide: An Alternative Approach toward Formaldehyde. *J. Am. Chem. Soc.* **2019**, *141* (1), 334–341. https://doi.org/10.1021/jacs.8b10233.
(66) Becker, E.; Pavlik, S.; Kirchner, K. The Organometallic Chemistry of Group 8 Tris(Pyrazolyl)Borate Complexes. In *Advances in Organometallic Chemistry*; Elsevier, 2008; Vol. 56, pp 155–197. https://doi.org/10.1016/S0065-3055(07)56003-X.
(67) Yin, C.; Xu, Z.; Yang, S.-Y.; Ng, S. M.; Wong, K. Y.; Lin, Z.; Lau, C. P. Promoting Effect of Water in Ruthenium-Catalyzed Hydrogenation of Carbon Dioxide to Formic Acid. *Organometallics* **2001**, *20* (6), 1216–1222. https://doi.org/10.1021/om000944x.
(68) Lau, C.; Ng, S.; Jia, G.; Lin, Z. Some Ruthenium Hydride, Dihydrogen, and Dihydrogen-Bonded Complexes in Catalytic Reactions. *Coord. Chem. Rev.* **2007**, *251* (17–20), 2223–2237. https://doi.org/10.1016/j.ccr.2006.12.001.
(69) Arikawa, Y.; Asayama, T.; Moriguchi, Y.; Agari, S.; Onishi, M. Reversible N−N Coupling of NO Ligands on Dinuclear Ruthenium Complexes and Subsequent N_2O Evolution: Relevance to Nitric Oxide Reductase. *J. Am. Chem. Soc.* **2007**, *129* (46), 14160–14161. https://doi.org/10.1021/ja0763504.
(70) Foley, N. A.; Lail, M.; Lee, J. P.; Gunnoe, T. B.; Cundari, T. R.; Petersen, J. L. Comparative Reactivity of TpRu(L)(NCMe)Ph (L = CO or PMe_3): Impact of Ancillary Ligand L on Activation of Carbon−Hydrogen Bonds Including Catalytic Hydroarylation and Hydrovinylation/Oligomerization of Ethylene. *J. Am. Chem. Soc.* **2007**, *129* (21), 6765–6781. https://doi.org/10.1021/ja068542p.
(71) Leung, C. W.; Zheng, W.; Zhou, Z.; Lin, Z.; Lau, C. P. Mechanism of Catalytic Hydration of Nitriles with Hydrotris(Pyrazolyl)Borato (Tp) Ruthenium Complexes. *Organometallics* **2008**, *27* (19), 4957–4969. https://doi.org/10.1021/om800474w.
(72) Meier, N.; Hahn, F. E.; Pape, T.; Siering, C.; Waldvogel, S. R. Molecular Recognition Utilizing Complexes with NH,NR-Stabilized Carbene Ligands. *Eur. J. Inorg. Chem.* **2007**, *2007* (9), 1210–1214. https://doi.org/10.1002/ejic.200601258.
(73) Hahn, F. E.; Naziruddin, A. R.; Hepp, A.; Pape, T. Synthesis, Characterization, and H-Bonding Abilities of Ruthenium(II) Complexes Bearing Bidentate NR,NH-Carbene/Phosphine Ligands †. *Organometallics* **2010**, *29* (21), 5283–5288. https://doi.org/10.1021/om100388w.
(74) Norris, M. R.; Flowers, S. E.; Mathews, A. M.; Cossairt, B. M. H_2 Production Mediated by CO_2 via Initial Reduction to Formate. *Organometallics* **2016**, *35* (17), 2778–2781. https://doi.org/10.1021/acs.organomet.6b00595.
(75) Wang, X.; Chen, H.; Li, X. Ir(III)-Induced C-Bound to N-Bound Tautomerization of a N-Heterocyclic Carbene. *Organometallics* **2007**, *26* (18), 4684–4687. https://doi.org/10.1021/om700498w.
(76) Kuwata, S.; Hahn, F. E. Complexes Bearing Protic N-Heterocyclic Carbene Ligands. *Chem. Rev.* **2018**. https://doi.org/10.1021/acs.chemrev.8b00176.
(77) Miranda-Soto, V.; Grotjahn, D. B.; DiPasquale, A. G.; Rheingold, A. L. Imidazol-2-Yl Complexes of Cp*Ir as Bifunctional Ambident Reactants. *J. Am. Chem. Soc.* **2008**, *130* (40), 13200–13201. https://doi.org/10.1021/ja804713u.

(78) Miranda-Soto, V.; Grotjahn, D. B.; Cooksy, A. L.; Golen, J. A.; Moore, C. E.; Rheingold, A. L. A Labile and Catalytically Active Imidazol-2-Yl Fragment System. *Angew. Chem. Int. Ed.* **2011**, *50* (3), 631–635. https://doi.org/10.1002/anie.201005100.
(79) Chang, W.; Gong, X.; Wang, S.; Xiao, L.-P.; Song, G. Acceptorless Dehydrogenation and Dehydrogenative Coupling of Alcohols Catalysed by Protic NHC Ruthenium Complexes. *Org. Biomol. Chem.* **2017**, *15* (16), 3466–3471. https://doi.org/10.1039/C7OB00542C.
(80) Johnson, L. K.; Angelici, R. J. Synthesis of Aminooxycarbene Complexes of Iron with N-Alkyl, -Allyl, and -Carbamoyl Groups. *Inorg. Chem.* **1987**, *26* (7), 973–976. https://doi.org/10.1021/ic00254a002.
(81) Evans, K. J.; Mansell, S. M. Functionalised N-Heterocyclic Carbene Ligands in Bimetallic Architectures. *Chem. – Eur. J.* **2020**, chem.201905510. https://doi.org/10.1002/chem.201905510.
(82) Jin, H.; Kluth, P.; Hahn, F. E. Synthesis of Complexes with Protic NH,NR-NHC Ligands by Oxidative Addition of N-Alkyl-2-Iodoimidazoles to [M(PPh3)4] (M = Pd, Pt) Complexes. *Eur. J. Inorg. Chem.* **2017**, *2017* (20), 2774–2781. https://doi.org/10.1002/ejic.201700403.
(83) He, F.; Danopoulos, A. A.; Braunstein, P. Trifunctional PNHC, Imine, Pyridine Pincer-Type Iridium(III) Complexes: Synthetic, Structural, and Reactivity Studies. *Organometallics* **2016**, *35* (2), 198–206. https://doi.org/10.1021/acs.organomet.5b00926.
(84) Rong, M. K.; Chirila, A.; Franciolus, D.; Lutz, M.; Nieger, M.; Ehlers, A. W.; Slootweg, J. C.; Lammertsma, K. Protic NHC Iridium Complexes with β-H Reactivity–Synthesis, Acetonitrile Insertion, and Oxidative Self-Activation. *Organometallics* **2019**, acs.organomet.9b00584. https://doi.org/10.1021/acs.organomet.9b00584.
(85) Bente, S.; Kampert, F.; Tan, T. T. Y.; Hahn, F. E. Site-Selective Metallation of Dicarbene Precursors. *Chem. Commun.* **2018**, *54* (91), 12887–12890. https://doi.org/10.1039/C8CC08440H.
(86) Tegethoff, M.; Roelfes, F.; Schulte to Brinke, C.; Tan, T. T. Y.; Kampert, F.; Jin, G.-X.; Hahn, F. E. Synthesis of Heterobimetallic Complexes by Coordination of Rhodium(III) and Iridium(III) Poly-N,O-NHC Complexes to Silver(I), Copper(II), and Zinc(II). *Organometallics* **2018**. https://doi.org/10.1021/acs.organomet.8b00252.
(87) Flowers, S. E.; Cossairt, B. M. Mono- and Dimetalation of a Tridentate Bisimidazole-Phosphine Ligand. *Organometallics* **2014**, *33* (17), 4341–4344. https://doi.org/10.1021/om500592u.
(88) Hahn, F. E.; Hein, P.; Lügger, T. Synthesis of Heterobimetallic Metal Derivatives: A Carbene Complex as Chelate Ligand. *Z. Für Anorg. Allg. Chem.* **2003**, *629* (7–8), 1316–1321. https://doi.org/10.1002/zaac.200300078.
(89) Reda, T.; Plugge, C. M.; Abram, N. J.; Hirst, J. Reversible Interconversion of Carbon Dioxide and Formate by an Electroactive Enzyme. *Proc. Natl. Acad. Sci.* **2008**, *105* (31), 10654–10658. https://doi.org/10.1073/pnas.0801290105.
(90) Breglia, R.; Arrigoni, F.; Sensi, M.; Greco, C.; Fantucci, P.; De Gioia, L.; Bruschi, M. First-Principles Calculations on Ni,Fe-Containing Carbon Monoxide Dehydrogenases Reveal Key Stereoelectronic Features for Binding and Release of CO_2 to/from the C-Cluster. *Inorg. Chem.* **2021**, *60* (1), 387–402. https://doi.org/10.1021/acs.inorgchem.0c03034.
(91) Dobbek, H.; Gremer, L.; Kiefersauer, R.; Huber, R.; Meyer, O. Catalysis at a Dinuclear [CuSMo(AO)OH] Cluster in a CO Dehydrogenase Resolved at 1.1-Å Resolution. 6.
(92) Jeoung, J.-H.; Dobbek, H. Carbon Dioxide Activation at the Ni,Fe-Cluster of Anaerobic Carbon Monoxide Dehydrogenase. *Science* **2007**, *318* (5855), 1461–1464. https://doi.org/10.1126/science.1148481.

(93) Ye, R.-P.; Ding, J.; Gong, W.; Argyle, M. D.; Zhong, Q.; Wang, Y.; Russell, C. K.; Xu, Z.; Russell, A. G.; Li, Q.; Fan, M.; Yao, Y.-G. CO2 Hydrogenation to High-Value Products via Heterogeneous Catalysis. *Nat. Commun.* **2019**, *10* (1), 5698. https://doi.org/10.1038/s41467-019-13638-9.
(94) Wang, W.; Jiang, X.; Wang, X.; Song, C. Fe–Cu Bimetallic Catalysts for Selective CO_2 Hydrogenation to Olefin-Rich C_{2}^{+} Hydrocarbons. *Ind. Eng. Chem. Res.* **2018**, *57* (13), 4535–4542. https://doi.org/10.1021/acs.iecr.8b00016.
(95) Liu, L.; Fan, F.; Jiang, Z.; Gao, X.; Wei, J.; Fang, T. Mechanistic Study of Pd–Cu Bimetallic Catalysts for Methanol Synthesis from CO_2 Hydrogenation. *J. Phys. Chem. C* **2017**, *121* (47), 26287–26299. https://doi.org/10.1021/acs.jpcc.7b06166.
(96) Bagherzadeh, S.; Mankad, N. P. Catalyst Control of Selectivity in CO_2 Reduction Using a Tunable Heterobimetallic Effect. *J. Am. Chem. Soc.* **2015**, *137* (34), 10898–10901. https://doi.org/10.1021/jacs.5b05692.
(97) Buchwalter, P.; Rosé, J.; Braunstein, P. Multimetallic Catalysis Based on Heterometallic Complexes and Clusters. *Chem. Rev.* **2015**, *115* (1), 28–126. https://doi.org/10.1021/cr500208k.
(98) Krogman, J. P.; Foxman, B. M.; Thomas, C. M. Activation of CO_2 by a Heterobimetallic Zr/Co Complex. *J. Am. Chem. Soc.* **2011**, *133* (37), 14582–14585. https://doi.org/10.1021/ja2071847.
(99) Krogman, J. P.; Bezpalko, M. W.; Foxman, B. M.; Thomas, C. M. Synthesis, Structure, and Reactivity of an Anionic Zr–Oxo Relevant to CO_2 Reduction by a Zr/Co Heterobimetallic Complex. *Inorg. Chem.* **2013**, *52* (6), 3022–3031. https://doi.org/10.1021/ic302473j.
(100) Zhang, H.; Wu, B.; Marquard, S. L.; Litle, E. D.; Dickie, D. A.; Bezpalko, M. W.; Foxman, B. M.; Thomas, C. M. Investigation of Ketone C═O Bond Activation Processes by Heterobimetallic Zr/Co and Ti/Co Tris(Phosphinoamide) Complexes. *Organometallics* **2017**, *36* (18), 3498–3507. https://doi.org/10.1021/acs.organomet.7b00445.
(101) Zhou, W.; Marquard, S. L.; Bezpalko, M. W.; Foxman, B. M.; Thomas, C. M. Catalytic Hydrosilylation of Ketones Using a Co/Zr Heterobimetallic Complex: Evidence for an Unusual Mechanism Involving Ketyl Radicals. *Organometallics* **2013**, *32* (6), 1766–1772. https://doi.org/10.1021/om301194g.
(102) Walker, W. K.; Kay, B. M.; Michaelis, S. A.; Anderson, D. L.; Smith, S. J.; Ess, D. H.; Michaelis, D. J. Origin of Fast Catalysis in Allylic Amination Reactions Catalyzed by Pd–Ti Heterobimetallic Complexes. *J. Am. Chem. Soc.* **2015**, *137* (23), 7371–7378. https://doi.org/10.1021/jacs.5b02428.
(103) Jessop, P. G.; Ikariya, T.; Noyori, R. Homogeneous Hydrogenation of Carbon Dioxide. 14.

Chapter 2. SYNTHESIS OF MONOMETALLIC RUTHENIUM (II) BIS-(PNHC) PHOSPHINE COMPLEXES

2.1 INTRODUCTION

The synthesis of protic N-heterocyclic carbenes (PNHCs) has been achieved via the formal tautomerization of azoles, N-protonation of C-azolyls, N-deprotection of N-Masked NHC complexes, nucleophilic substitution, and cyclization or annulation.[1] The tautomerization of azoles has been shown to be acid/base-induced as well as chelation-assisted. The presence of Brønsted acid or base often functions to lower the kinetic barrier for tautomerization, and in some cases deprotonation of the carbon in N-coordinated azoles induces rearrangement, followed by N-protonation.[1] Interestingly, chelation-assisted tautomerization does not require the presence of acid or base for the reaction to take place. Typically, the first step of chelation-assisted tautomerization is the coordination of the ligand through the coordinating groups attached to the azole moiety, and in cases where the ligand backbone is flexible, this often leads to an isolable complex with partial chelation and a dangling azole group. The tautomerization then takes place either at high temperature or due to chloride abstraction.[1]

The mechanisms for chelation assisted tautomerization are still under investigation. One proposed mechanism is redox tautomerization, whereby the C-H of the azole undergoes oxidative addition to form the metal-carbene and a metal-hydride bond, followed by reductive elimination of the hydride resulting in the metal with its original oxidation state and the PNHC ligand. Alternatively, a redox-neutral mechanism proceeds via deprotonation of the azole C-H with stepwise or concerted metalation to form the carbene, followed by reprotonation to form the

PNHC.[1] It has been postulated that the redox mechanism is preferred for low-valent metals while the redox-neutral mechanism is preferred for mid- to high-valent metals.

PNHC-phosphine chelating ligands are among the literature precedent for chelation-assisted tautomerization. This body of literature is dominated by bidentate ligands containing a diphenylphosphine tethering group linked to the PNHC through an ethyl linker. Building upon this motif, and motivated by chemistry observed with tridentate facially coordinating ligands, our group has developed a bis-(PNHC) phenylphosphine ligand (**L**).[2–4] This bis-PNHC phosphine ligand has been studied in systems supporting a ruthenium (II) metal center ligated by bipyridine (**1**) and Cp* (**2**) ancillary ligands, as well as in a coordinatively unsaturated system (**3**), shown in Figure 2.1. Ligation for each of these systems proceeds first through coordination of the phosphine to the ruthenium, and in the case of **2** and **3** dimer formation is observed at room temperature through the coordination of the benzimidazole nitrogen to a second ruthenium center.[2,4] For complex **3**, chloride abstraction at room temperature is required to promote dimerization.[4] For complex **1**, the synthesis was carried out with the protonation of the benzimidazole nitrogen atoms such that the dimerization was prohibited.[3] In all three cases, PNHC formation was observed with the application of high temperature, between 100 ºC and 175 ºC.

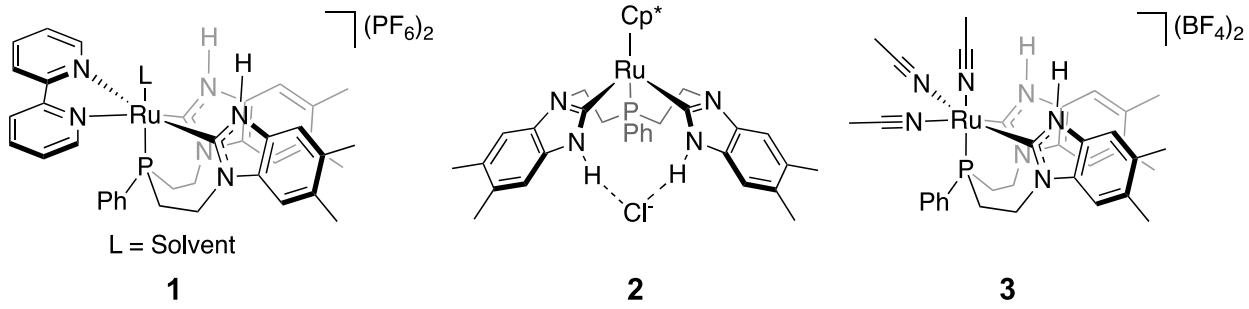

Figure 2.1. Previously characterized Ruthenium bis-(PNHC) phosphine complexes.[2–4]

In addition to the metalation of **L**, the influence of ancillary ligands is of interest. In the system studied here, in addition to steric and electronic effects at the metal center, it was anticipated that changing the electron donating strength of the ancillary ligands would influence the Brønsted acidity of the NH-wingtips and ultimately the cooperative reactivity of the complex with small molecules. Furthermore, exploring the coordination of ancillary ligands with complex **3**, versus installing the ancillary ligand prior to metalation of **L** as was done for **1** and **2**, could provide a generalizable platform for a wide library of PNHC complexes. This approach also provides insight on the electronics at the various coordination sites, i.e. *trans* to the carbenes versus the phosphine, which could help to inform future catalyst design when thinking about catalysis with the coordinatively unsaturated complex.

Herein, the metalation of this bis-PNHC phosphine ligand is explored, including the investigation of acid/base-induced tautomerization versus chelation-assisted thermally driven tautomerization, and a one-pot synthesis is developed. A small library of complexes bearing different bidentate ancillary ligands is then investigated, and the coordination of said ancillary ligands is investigated with **3**.

2.2 Results and Discussion

2.2.1 *Ligand Synthesis*

The synthesis of bis-(*N*-ethyl-5,6-dimethylbenzimidazole)phenylphosphine (**L**) has been optimized though a number of iterations based on previously published procedures.[2,3] Common challenges with this synthesis are pushing the equilibrium towards completion and oxidation of the phosphine.[i] Through application ^{1}H-coupled ^{31}P NMR, it is evident that the original synthesis, involving the addition of 2 equivalents of strong base (KOtBu or n-BuLi) followed by the addition of 2 equivalents of *N*-ethylchloro-5,6-dimethylbenzimidazole (bim), yields a mixture

Scheme 2.1. Competing reactions hindering the synthesis of **L**.

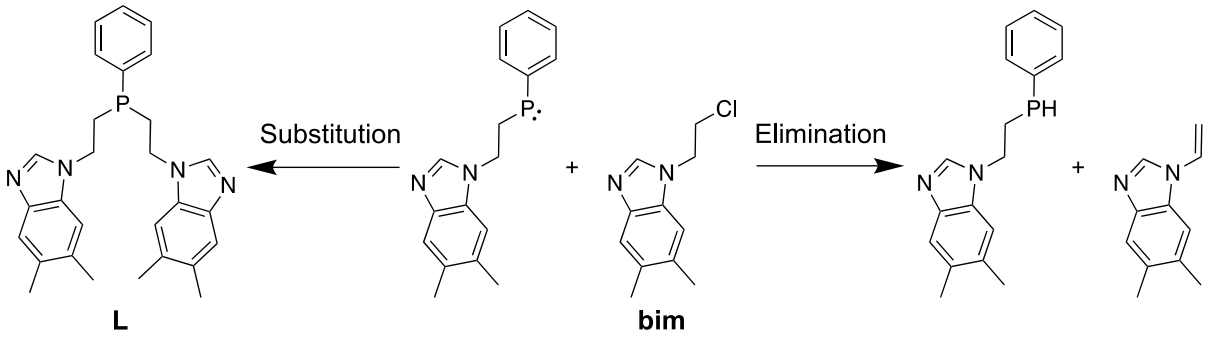

of doubly substituted phenylphosphine and singly substituted and reprotonated phenylphosphine. The reprotonation of the phenylphosphine likely arises from competition of phenylphosphine as a nucleophile in the substitution reaction at the 1-chloro-ethyl moiety of bim, versus elimination at this position with phenylphosphine acting as a base and yielding the vinyl analog of the ligand arm (Scheme 2.1). This hypothesis is supported by the requirement of additional equivalents of base to push the reaction to completion, as well as the prior procedure[2] that uses the vinyl analog of the ligand arm as the precursor.

The optimized synthesis is carried out by the addition of 1 equivalent of n-BuLi followed by 1 equivalent of bim to reach the singly substituted (bim)(H)P(Ph). These steps are then repeated with an additional 1 equivalent of n-BuLi and 1 equivalent of bim to yield the doubly substituted R_2PPh (**L**). Tracking by ^{1}H-coupled ^{31}P NMR shows clean conversion (Scheme 2.2, Figure 2.2).

Scheme 2.2. Optimized synthesis of **L** including characteristic ^{1}H-coupled ^{31}P NMR signals.

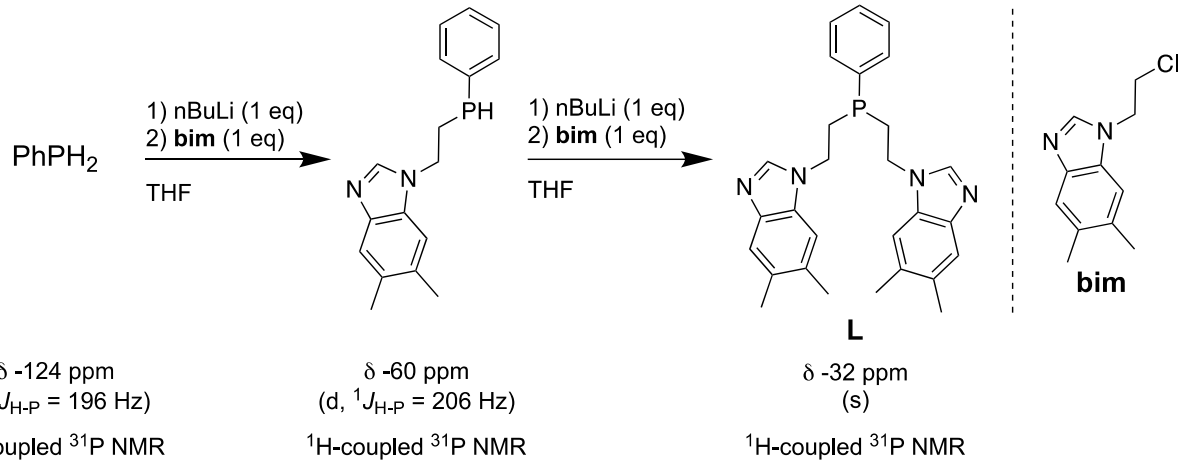

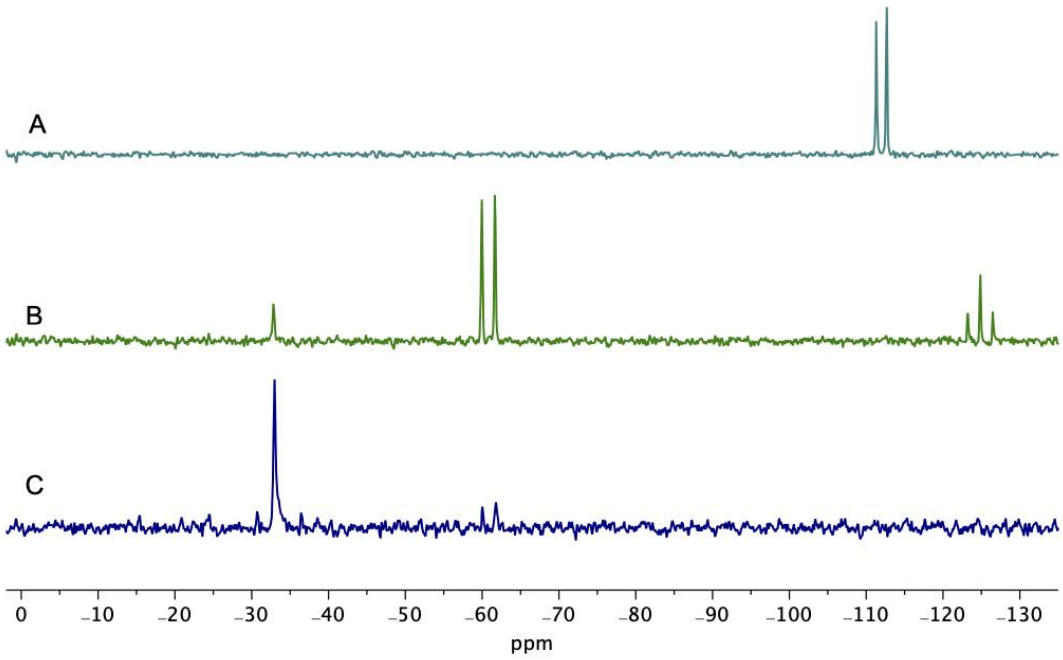

Figure 2.2. Ligand (**L**) synthesis tracking by ^{1}H-coupled ^{31}P NMR (121 MHz, THF, 298 K). (A) $PhPH_2$ with 1 equivalent of nBuLi indicates clean mono-deprotonation of $PhPH_2$ (***δ*** -112 ppm, d, $^{1}J_{H\text{-}P}$ = 166.7 Hz) (B) After addition of 1 equivalent of bim, indicating a major product of PhP(H)(R) (***δ*** -60 ppm, d, $^{1}J_{H\text{-}P}$ = 206.1 Hz), with minor products being reprotonated $PhPH_2$ (***δ*** -124 ppm, t, $^{1}J_{H\text{-}P}$ = 196.8 Hz) and fully converted **L** (***δ*** -32 ppm, s). (C) After the second addition of nBuLi and bim, showing near full conversion to **L**.

2.2.2 *Metalation of the Ligand*

Prior work from the Cossairt group has demonstrated the metalation of **L** or close analogs of **L** with a variety of ruthenium (II) precursors, yielding bipyridine (**1**), Cp* (**2**), and coordinatively unsaturated (**3**) complexes supported by the tripodal bis-(PNHC) phosphine ligand (Figure 2.1).[2–4] The routes to metalation for each of these vary to some degree, yet observed commonalities open the possibility of a generalizable one-pot synthesis and general understanding of the metalation of **L**.

For the synthesis of **2** $[RuCp^*Cl]_4$ was reacted with **L** in DCM, and after 10 minutes a dimer formed with the phosphine coordinated to one ruthenium and the open nitrogen of one benzimidazole ligand arms coordinated to a second ruthenium. Each ruthenium is coordinated to one phosphine and one benzimidazole nitrogen in addition to Cp* and chloride. This complex is then isolated, dissolved in DMSO and heated at 100 ºC for 30 hours, in which time the chloride is displaced and the benzimidazoles undergo thermally driven tautomerization or C-H activation at the C(1) position to yield the bis-(PNHC).[2]

The synthesis of **3** is ultimately achieved in a one pot synthesis by reacting $[Ru(C_6H_6)Cl_2]_2$ and **L** in N-methyl-2-pyrrolidone (NMP) and heating at 170 ºC for 1 hour, followed by removal of volatiles and addition of $AgBF_4$ in CH_3CN, yielding **3** in 93% yield. On route to the one pot synthesis, coordination through the phosphine is first observed at room temperature and if the chlorides are abstracted prior to heating, then dimer formation is observed. Unlike the reaction pathway to **2**, prolonged heating of the dimers in this case lead to the eventual decomposition into multiple species.[4]

The synthesis of **1** was designed in a way that avoids dimerization but involves multiple steps.[3] The original synthesis for **1** was carried out by protonating the open nitrogen positions on

the benzimidazole arms of **L** with trifluoromethanesulfonic acid, which effectively blocks coordination through the nitrogen position, then heating at reflux upon addition of the [Ru(bpy)(C_6H_6)OTf]OTf precursor in ethanol. This reaction led to substitution of the inner sphere triflate with **L** bound through the phosphine and the outer sphere triflate was exchanged with hexaflorophosphate, yielding [Ru(C_6H_6)(bpy)(PPh(RH^+)$_2$)](PF_6)$_4$. This complex was isolated before being heated at 155 °C in ethylene glycol and trimethylamine, yielding **1** (Scheme 2.3, route A).[3] As has been observed with the syntheses of **2** and **3**, the elevated temperature is purposed to be responsible for the PNHC forming step. This, therefore, calls into question the necessity of the trimethylamine and the initial protonation of the benzimidazole. The NH wingtip is a more acidic proton than the benzimidazole C(1) proton, and the NH would be

Scheme 2.3. One-pot synthesis of **1**.

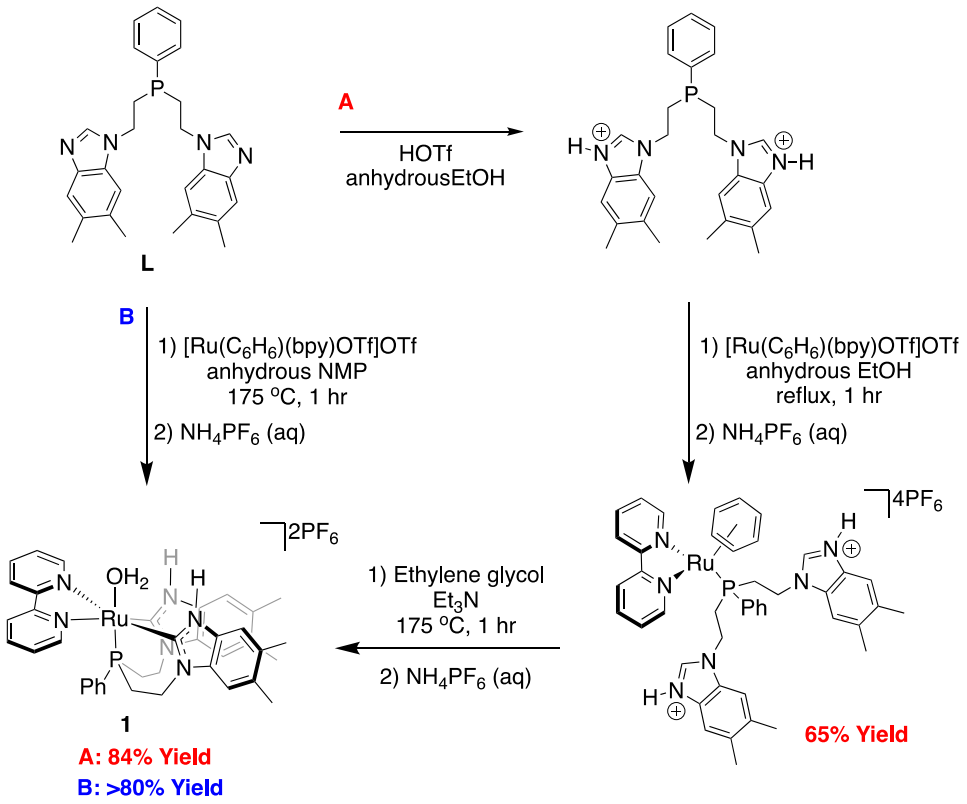

deprotonated by the trimethylamine prior to the formation of the metal-carbene bond, thus leaving this step open to dimerization during this step in any case.

This consideration led to the development of a new synthetic scheme for **1**, which eliminates the protonation and isolation steps (Scheme 2.3, route B). The synthesis is carried out by the direct reaction of [Ru(bpy)(C_6H_6)OTf][OTf] with P^{Ph}(1-*N*-ethyl-5,6-dimethylbenzimidazole)$_2$ (**L**) in N-methyl-2-pyrrolidone (NMP). The reaction proceeds first through the coordination of the phosphine to the ruthenium, followed by the thermally driven tautomerization of the benzimidazoles to the desired PNHC complex in >80% isolated yield. The desired product is evident based up the ^{31}P NMR peak at 41 ppm as well as the appearance of the ^{1}H NMR peak around 10.7 ppm corresponding to the NH wingtip of the PNHC and the disappearance of the imidazole C(1) proton around 8 ppm in the ^{1}H NMR of **L**.

Thermally driven tautomerization or C-H activation resulting in PNHC formation has previously been observed for chelating ligands containing a PNHC moiety in the literature, including the synthesis of **2**.[2,12,13] Base promoted tautomerization is another method for PNHC formation. For example, in the presence of a suitable metal precursor, the addition of a slight excess of KOtBu to deprotonate the imidazole at the C1 position, followed by addition of NH_4PF_6 to protonate the N-H wingtips generates the desired PNHC complex.[14,15] This method was explored as an alternative route to synthesize **3**. A slight excess of KOtBu was added to Ru(C_6H_6)Cl_2($PPhR_2$) in CD_2Cl_2 followed by addition of NH_4PF_6 to protonate the tautomerized PNHC, following literature precedent.[14] Rather than PNHC formation, which would be evident in the ^{1}H NMR by the NH peak around 11 ppm, the appearance of new multiplets in the olefinic region between 6.0 and 6.3 ppm indicates deprotonation of the ethylene linkers. Additionally, after the addition of KOtBu the two imidazole arms become inequivalent as indicated by the

appearance of several aromatic peaks in the ^{1}H NMR spectrum between 7.1 and 8.0 ppm and at least five peaks between 2.3 and 2.5 ppm which correspond to the benzimidazole methyl substituents (Figure 2.3). The addition of NH_4PF_6 simplifies the ^{1}H NMR spectrum to reveal a major product similar to the starting material, most notably with the absence of the resonance that would indicate protonation of the PNHC NH-wingtip between 10 and 12.5 ppm. (Figure 2.3C).[4] Additionally, many minor products persist, as is evidence by the broad baseline peaks in the aromatic region and the lower intensity peaks in the methyl region. Thus, base promoted tautomerization is not an option for metalation of **L**, primarily due to the ligand backbone's sensitivity to deprotonation.

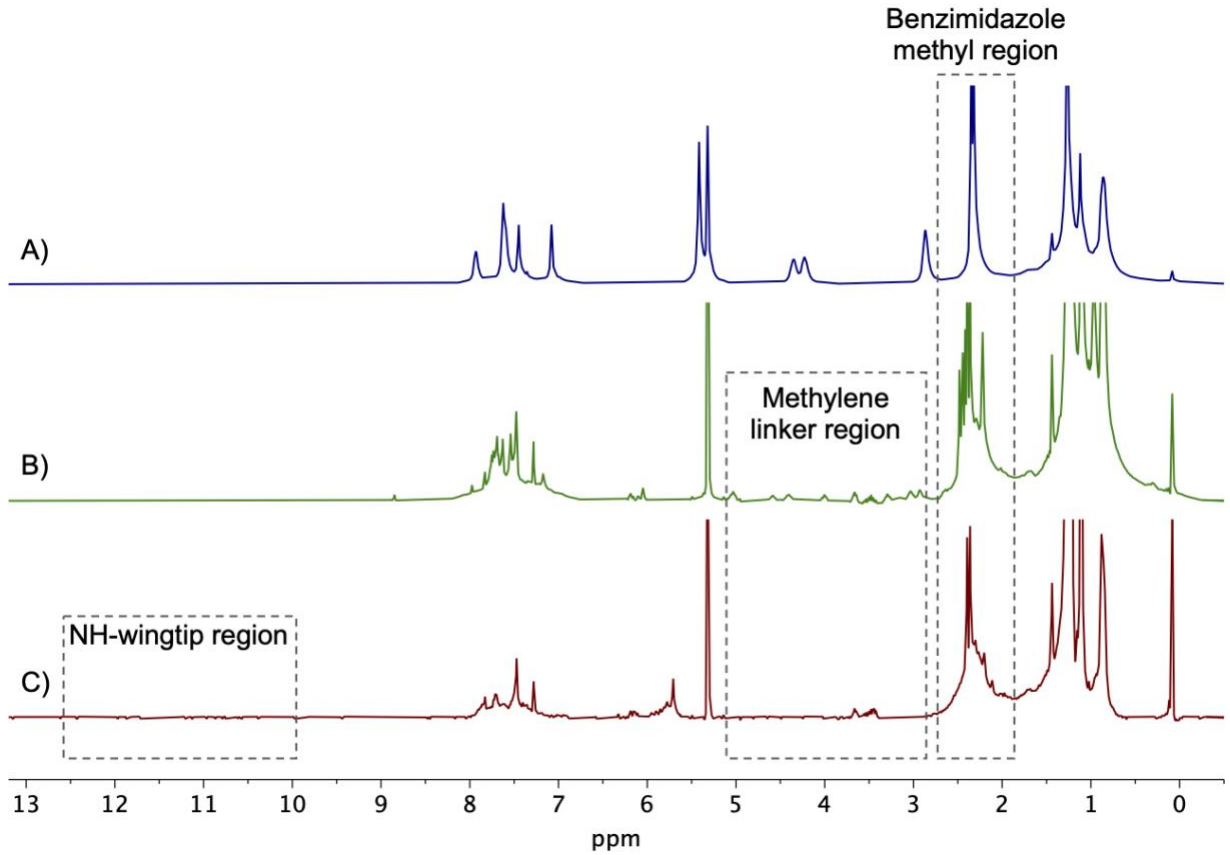

Figure 2.3. ^{1}H NMR (298 K, 499.7 MHz) in CD_2Cl_2 of $Ru(C_6H_6)Cl_2(PPhR_2)$ (A) with the addition of KOtBu (B), and the subsequent addition of NH_4PF_6 (C). Key regions include the NH-wingtip region, highlighting the absence of the peak which would indicate protonation of the PNHC NH-wingtip, the methylene linker region, and the benzimidazole methyl backbone region.

2.2.3 *Ancillary Ligand Library*

Of the three complexes previously characterized, the bipyridine ancillary ligand coordinated *trans* to the PNHC moieties in **1** is of initial interest for further reactivity and catalytic studies as it isolates the reactive coordination site adjacent to the PNHC moieties allowing for controlled investigation of metal-ligand cooperativity. A series of 4,4'-disubstituted bipyridine ligated complexes were synthesized to probe the influence on the PNHCs and overall reactivity with varying electron donating and withdrawing properties. The one-pot synthesis of **1** was easily adapted to include the substituted bipyridine ruthenium precursors (Scheme 2.4).

Scheme 2.4. Synthesis of **1a-c**, 4,4'-disubstituted bipyridine complexes.

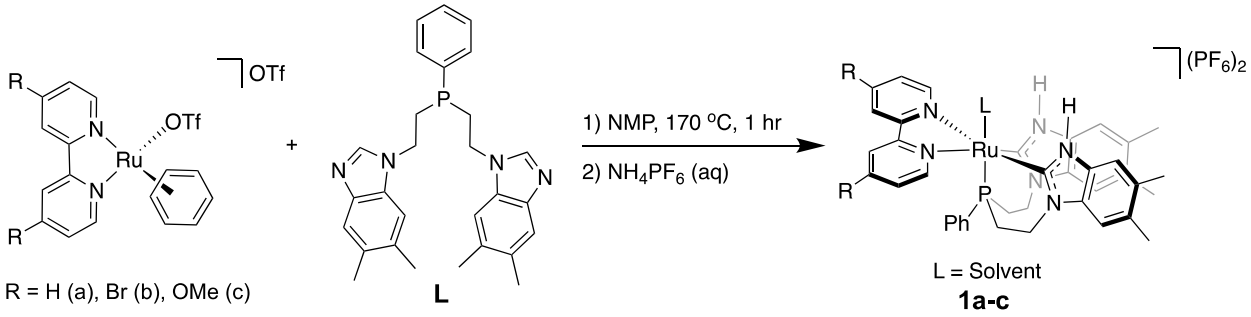

Table 2.1. Hammett Constants for the 4,4'-disubstituted bipyridine complexes.[16]

Substituent	Hammett Constants (para-effect)
-OMe	-0.268
-H	0.000
-Br	+0.232

Negative Values indicate electron donating character.

The coordinatively unsaturated complex **3** poses a unique opportunity to investigate the coordination of bidentate ligands to the metal center already supported by **L**. In addition to interest in bipyridine as an ancillary ligand, other properties of bidentate ligands that are of

interest are the rigidity of the backbone and the steric bulk. As such, the coordination of bipyridine and 1,2-bis-(diphenylphosphino)ethane (dppe) to **3** are investigated.

When unsubstituted bipyridine is added to **3** in acetonitrile at room temperature, four species are present as evidenced by ^{31}P NMR (Scheme 2.5, Figure 2.4). Over the course of many days with heating at 50 ºC one major product is identified as the bipyridine ligated complex with one pyridine coordinated *trans* to a PNHC and one *trans* to the phosphine (**4**). The ^{31}P NMR shows only one phosphorus containing species in solution, and the unsymmetric coordination of the bipyridine ligand is evident in the ^{1}H NMR by the appearance of two singlets at 9.86 ppm and 9.37 ppm each integrating to 1, corresponding to the inequivalent NH groups of the PNHCs. Additionally, the methyl groups on the benzimidazole backbone of **L** appear as four singlets at 2.44 ppm, 2.42 ppm, 2.38 ppm, and 2.32 ppm each integrating to roughly 3 (Figure 2.5). The coordination of 4,4'-dibromobipyridine with **3** was also investigated, however after treating the reaction under the same conditions as the unsubstituted bipyridine, one major product was not observed for 4,4-dibromobipyridine.

Scheme 2.5. In Situ coordination of bipyridine to **3**.

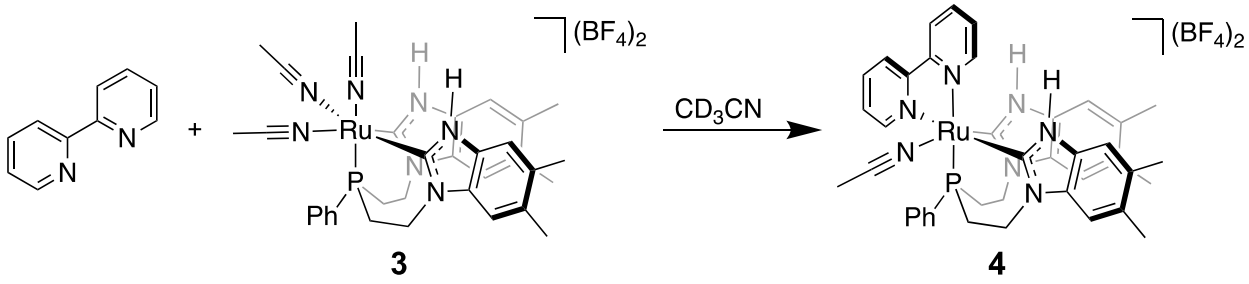

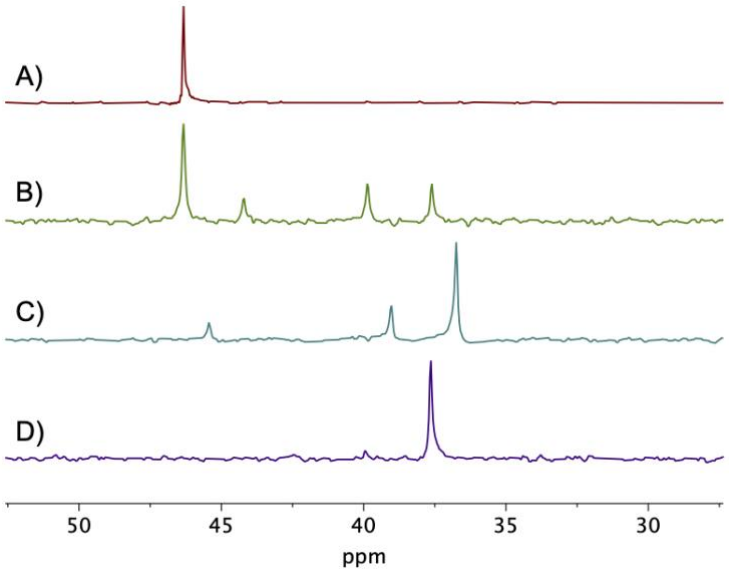

Figure 2.4. ^{31}P NNMR (121 MHz, 298K, CD_3CN) of the reaction of the coordinatively unsaturated complex **3** (A) with bipyridine after two days at room temperature and two hours at 40ºC (B), after an additional five days at room temperature (C), and after reaching one major product with continued heating at 50ºC overnight (D).

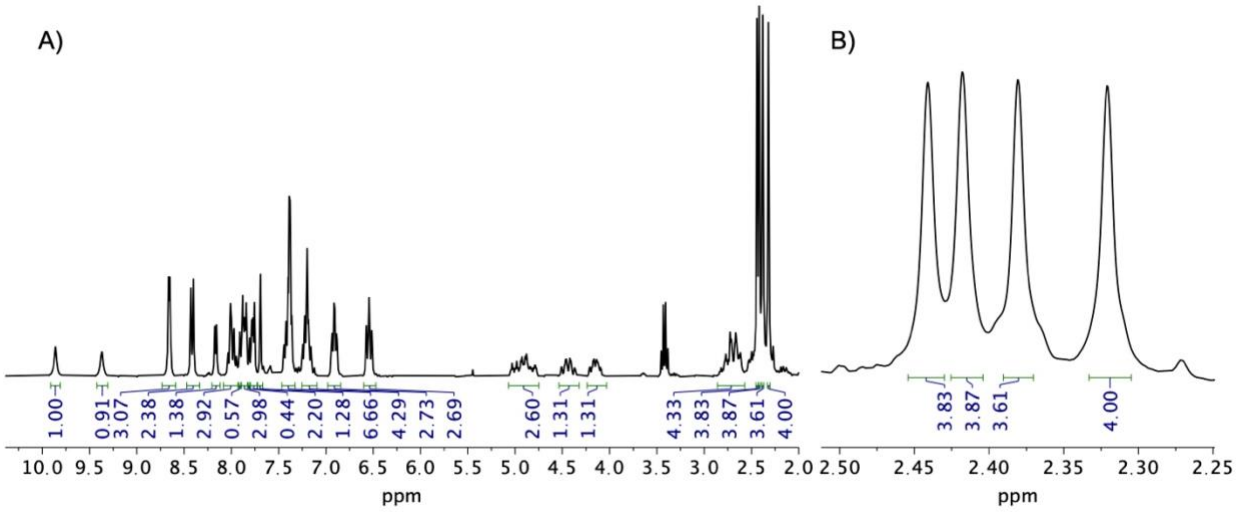

Figure 2.5. ^{1}H NMR (301 MHz, 298K, CD_3CN) of **4**. A) Full spectrum. B) Methyl region.

Scheme 2.6. Synthesis of **5**.

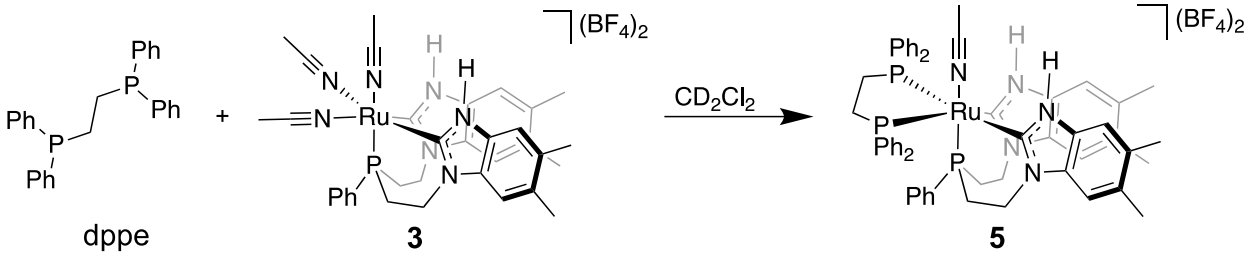

The reaction between dppe and **3** was carried out in dichloromethane and one major product, complex **5**, was observed after 17 hours at room temperature (Scheme 2.6). The coordination of dppe *trans* to the PNHCs is evident in the ^{31}P NMR by two signals, one doublet at 40 ppm and a triplet at 26 ppm, both with a $J_{P\text{-}P}$ = 26.4 Hz indicating that they are coupled to one another. The doublet corresponds to the two symmetric dppe phosphines coupling to the phosphine in **L**. The triplet corresponds to the phosphine in **L** coupled to the two chemically identical phosphines in dppe (Figure 2.6). This assignment was confirmed by X-ray crystallography (Figure 2.7).

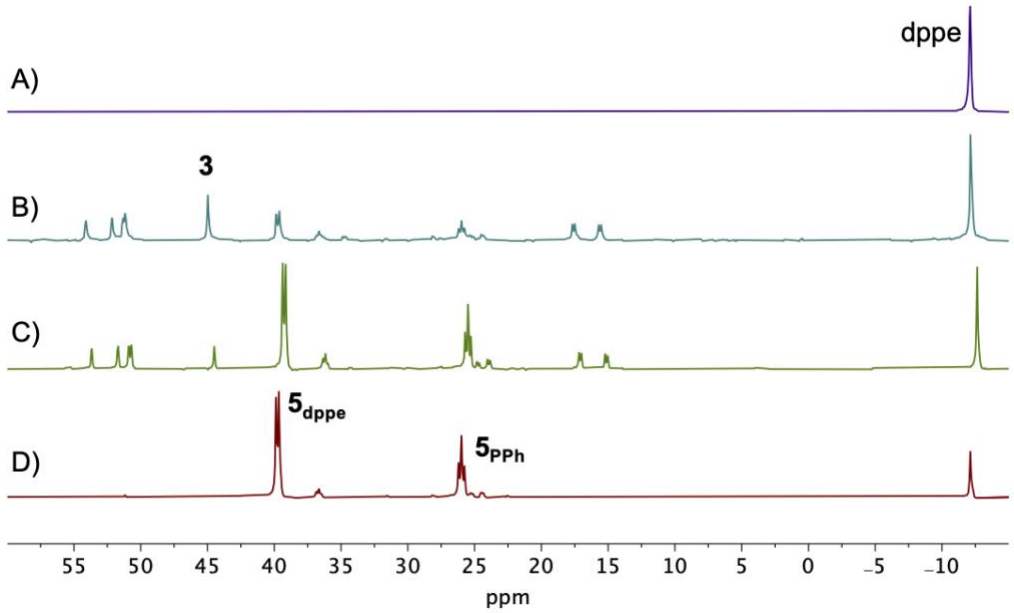

Figure 2.6. ^{31}P NMR (121 MHz, 298K, CD_2Cl_2) of the reaction between dppe (A) and **3** after 15 minutes at room temperature (B), 90 minutes at room temperature (C), and after reaching complete conversion to **5** (δ 40 ppm (d, J = 26.4 Hz) and 26 ppm (t, J = 26.4 Hz)) after 17 hours at room temperature (D).

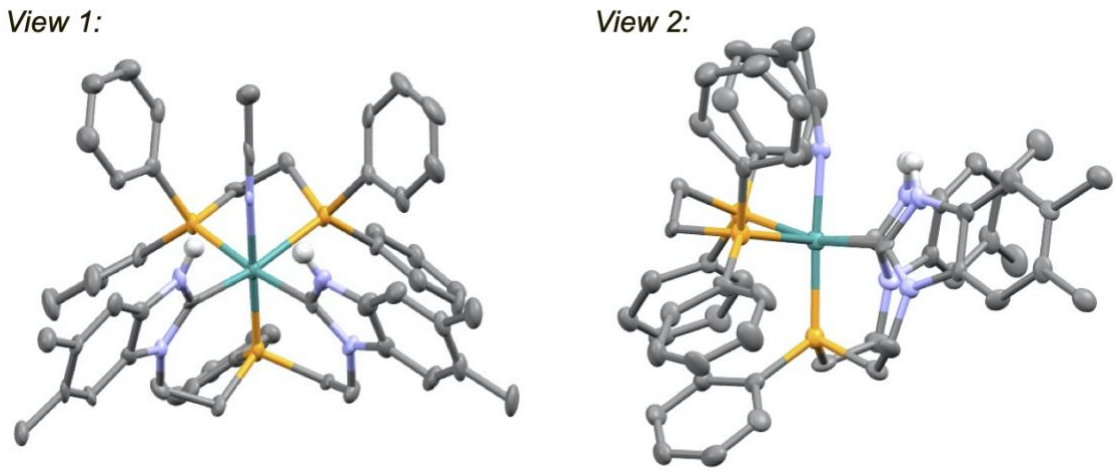

Figure 2.7. Crystal structure of **5** from two viewpoints. Two PF_6^- anions, one dichloromethane molecule, and all hydrogens, with the exception of the NH-wingtips, were excluded for clarity.

When **5** is dissolved in acetonitrile and heated at 60 ºC for 2 hours, isomerization takes place yielding a structure equivalent to **4**, with one dppe phosphine remaining coordinated *trans* to a PNHC and one coordinating trans to the phosphine of **L**. This coordination environment is evident in the ^{31}P NMR, with three doublets of doublets coupled to one another at 46 ppm ($J_{P\text{-}P}$ = 11.3 Hz, 26.5 Hz), 43 ppm ($J_{P\text{-}P}$ = 11.5 Hz, 22.0 Hz), and 25 ppm ($J_{P\text{-}P}$ = 22.4 Hz, 26.3 Hz) (Figure 2.8). It is hypothesized that due to the *trans* effect of the strongly sigma donating carbenes there is increased lability at those positions. In dichloromethane, a non-coordinating solvent, the substitution of the acetonitrile *trans* to the PNHCs with dppe is more favorable than displacing the acetonitrile trans to the phosphine of **L**. However, when placed in acetonitrile the equilibrium favors a more loosely coordinated solvent molecule trans to the PNHC. Displacement of dppe from **5** is also observed when dissolved in pyridine.

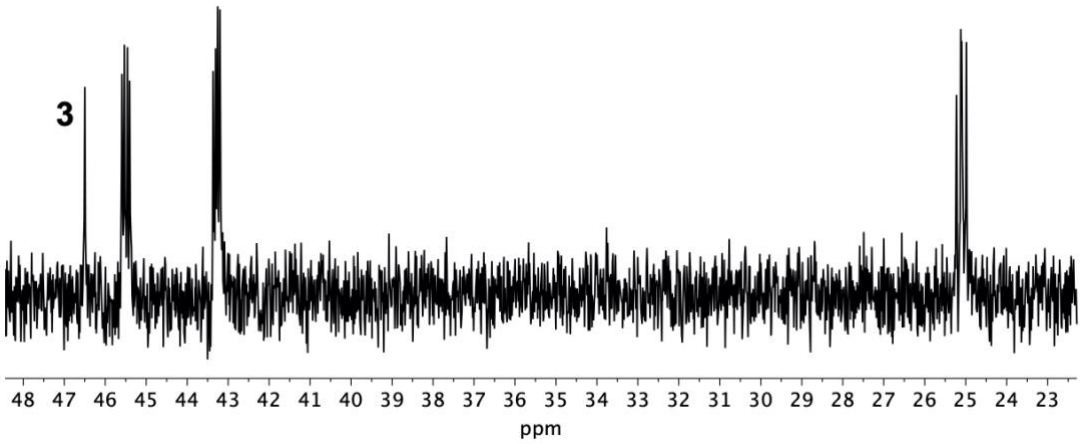

Figure 2.8. ^{31}P NMR (202 MHz, 298K, CD_3CN) showing isomerization of **5**, as evidenced by the precense three doublets of doublets coupled to one another at 46 ppm ($J_{P\text{-}P}$ = 11.3 Hz, 26.5 Hz), 43 ppm ($J_{P\text{-}P}$ = 11.5 Hz, 22.0 Hz), and 25 ppm ($J_{P\text{-}P}$ = 22.4 Hz, 26.3 Hz).

2.2.4 *Characterization*

The deprotonated species is of interest due its involvement in CO_2 activation to produce a carbamate species,[3] as well as its ability to support a second metal center.[2] To better understand the electronics at the metal center in the deprotonated state, ^{13}CO was first added at the open position of **1**. While the ^{1}H NMR spectrum remains essentially unchanged, the peak in the ^{31}P NMR spectrum shifts from a singlet at 43 ppm in **1** to a doublet at 11 ppm in **1-^{13}CO**. The coupling corresponds to the ^{13}CO substituent *trans* to the phosphine which appears as a doublet at 193 ppm in the ^{13}C NMR spectrum, and the *J* coupling for both is 93 Hz. In addition to the IR

Scheme 2.7. Deprotonation and possible resonance structures of deprotonated **1-^{13}CO**, with red indicating localization of anionic charge.

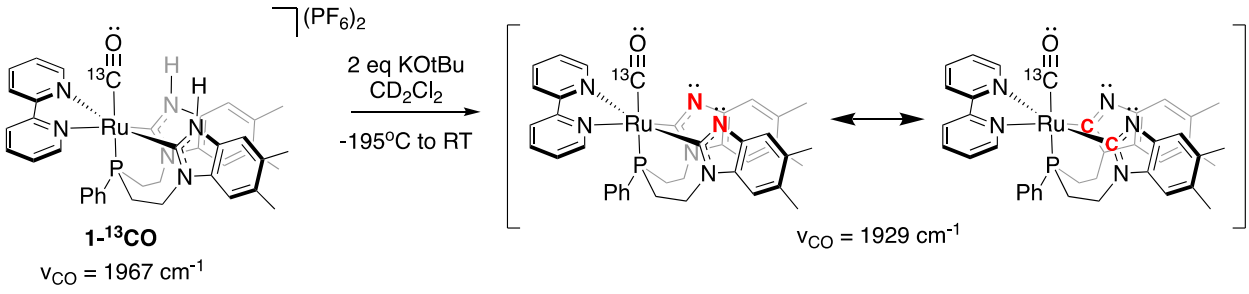

activity, the coupling from the ^{13}CO in the ^{31}P NMR spectrum is a convenient spectroscopic handle for identifying the persistence of bound ^{13}CO during subsequent reactivity studies.

Successful deprotonation was carried out using two equivalents of KOtBu and was evident by ^{1}H NMR by the disappearance of the NH wingtip peak at 10.5 ppm in CD_2Cl_2 while the rest of the complex remains equivalent (Figure 2.9). By IR spectroscopy, a decrease in the ν_{CO} stretch from 1967 cm^{-1} for protonated **1-^{13}CO** to 1929 cm^{-1} for deprotonated **1-^{13}CO** indicates that the increased electron density on the benzimidazole nitrogen atoms is being donated to the metal center, resulting in increased back bonding in the CO pi* orbitals (Figure 2.10). This suggests that the anionic character may be localized on the carbene rather than the nitrogen (Scheme 2.7).

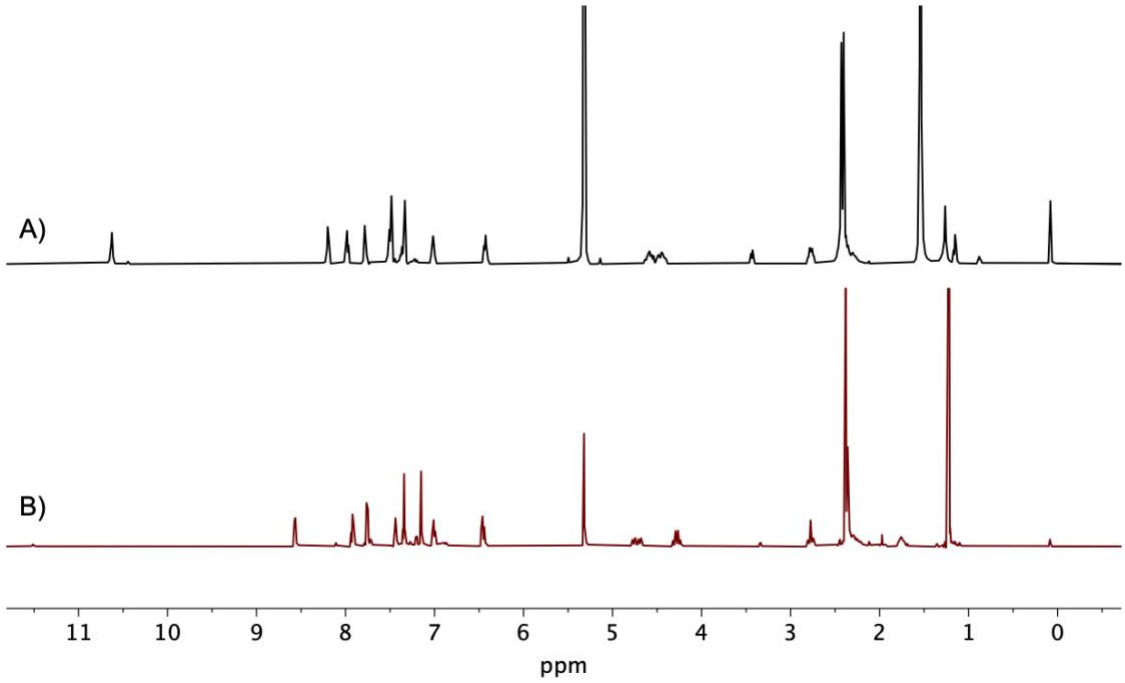

Figure 2.9. ^{1}H NMR (CD_2Cl_2, 500 MHz, 298 K) of **1-^{13}CO** (A) and **1-^{13}CO** with deprotonated NH-wingtips (B).

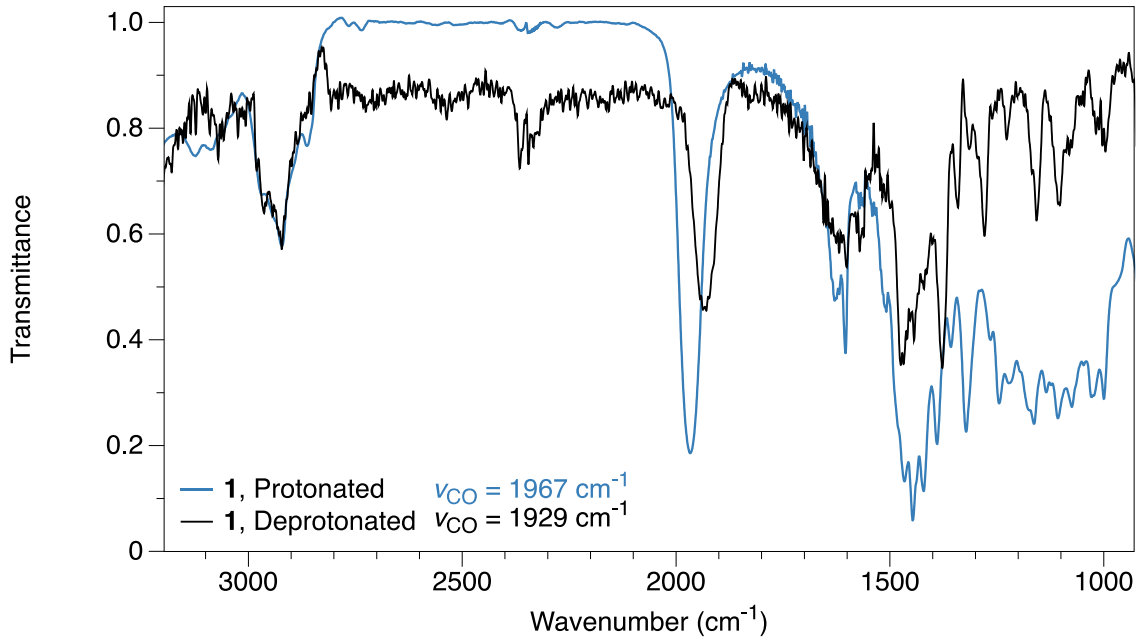

Figure 2.10. FT-IR data comparing the ν_{CO} for **1-^{13}CO** with protonated and deprotonated PNHCs.

This information provides a better understanding of how the electronics between the ruthenium and the deprotonated NH wingtip may interact with CO_2, since CO_2 is known to be activated between ruthenium and the deprotonated NH wingtip. By altering the substitution on the bipyridine ligand we will be able to fully screen how different electron withdrawing and donating substituents effect the electronic environment at the site of activation.

Cyclic voltammetry can supplement the insights about electron density at the metal center gained by investigating the redox potentials of the complexes in the ancillary ligand library as the electron donating and withdrawing groups are varied. Studying complexes **1a-c** using cyclic voltammetry shows the anticipated shifts in the $Ru^{II/III}$ redox couple (Figure 2.11, Table 3.2) corresponding to the more electron withdrawing bromo-substituted **1b** with an $E_{1/2}$ of 0.77 V vs $Fc^{+/0}$ and a $\Delta E_{1/2}$ of +0.05 V compared to **1a**, and the more electron donating methoxy-substituted **1c** with an $E_{1/2}$ of 0.71 V vs $Fc^{+/0}$ and a $\Delta E_{1/2}$ of -0.01 V compared to **1a**. The coordinatively unsaturated complex **3** gave an $E_{1/2}$ of 0.79 V vs $Fc^{+/0}$, more oxidative than the

couple for **1b**. This indicates that the more electron rich the metal center is, the more easily oxidized it is, and hence it should be more capable of reducing a substrate. In addition to **1a** having the isolated reactive site adjacent to the PNHCs, it is more reducing than **3,** further motivating the selection of **1a** as the catalyst for thorough investigation of its reactivity.

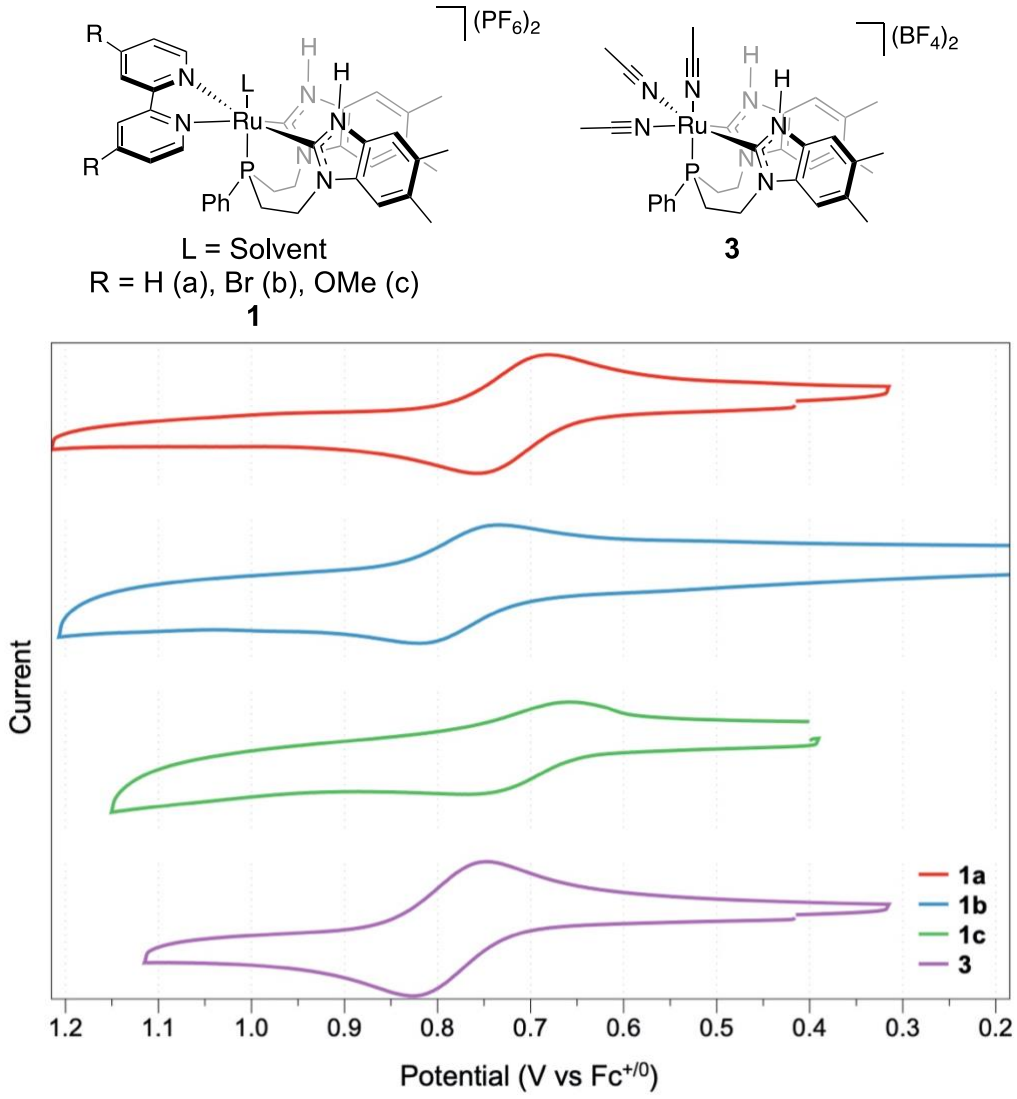

Figure 2.11. Cyclic Voltammograms for complexes **1a-c** and **3**.

Table 2.2. Electrochemical Characterization of **1a-c** and **3**.

Compound	**$E_{1/2}$** (V vs $Fc^{+/0}$)	**ΔE** (vs **1**)
1a	0.72	0
1b	0.77	0.05 V
1c	0.71	-0.01 V
3	0.79	0.07 V

1.0 mM **1**, 0.2 M (N^tBu_4)(PF_6) in CH_3CN, 500 mV/s, Glassy Carbon (working), Pt (counter), Ag (pseudo reference).

The influence that the electron density at the metal center has on the pKa of the PNHCs is demonstrated by comparing the reactivity of K_3PO_4 with both **1** and **3**. Complex **1** was dissolved in THF-d_8 and stirred for 1.5 hours at room temperature. There are two distinct peaks at 10.9 and 11.0 ppm in the ^{1}H NMR corresponding to two different environments for the NH wingtips (Figure 2.12). Typically, the NH wingtips appear as a single peak at 10.7 ppm in acetonitrile or 10.5 ppm in DCM. It is proposed that THF partially exchanges with the acetonitrile ligand. This is supported in the ^{31}P NMR, with the appearance of a second peak nearly overlapping with the original at 54.6 ppm and 52.9 ppm (Figure 2.13). With the addition of K_3PO_4 (13 equivalents) and stirring at room temperature for 1 hour, there is a complete disappearance of peaks corresponding to the NH wingtips, a shifting in the methyl region, and a shifting of the aromatic peaks with new peaks present in the ^{1}H NMR. The ^{31}P NMR shows a major peak at 47.9 ppm, corresponding to the deprotonated species (Figure 2.12 and 2.13).

Complex **3** was dissolved in THF-d_8 and stirred for 1.5 hours at room temperature. After 1.5 hours at room temperature in THF, **3** appears unchanged by ^{1}H NMR, with the distinct NH wingtip peak at 11.4 ppm, four sharp aromatic peaks, and two methyl groups on the ligand at 2.32 and 2.34 ppm. After stirring in THF at room temperature overnight, the spectrum is largely

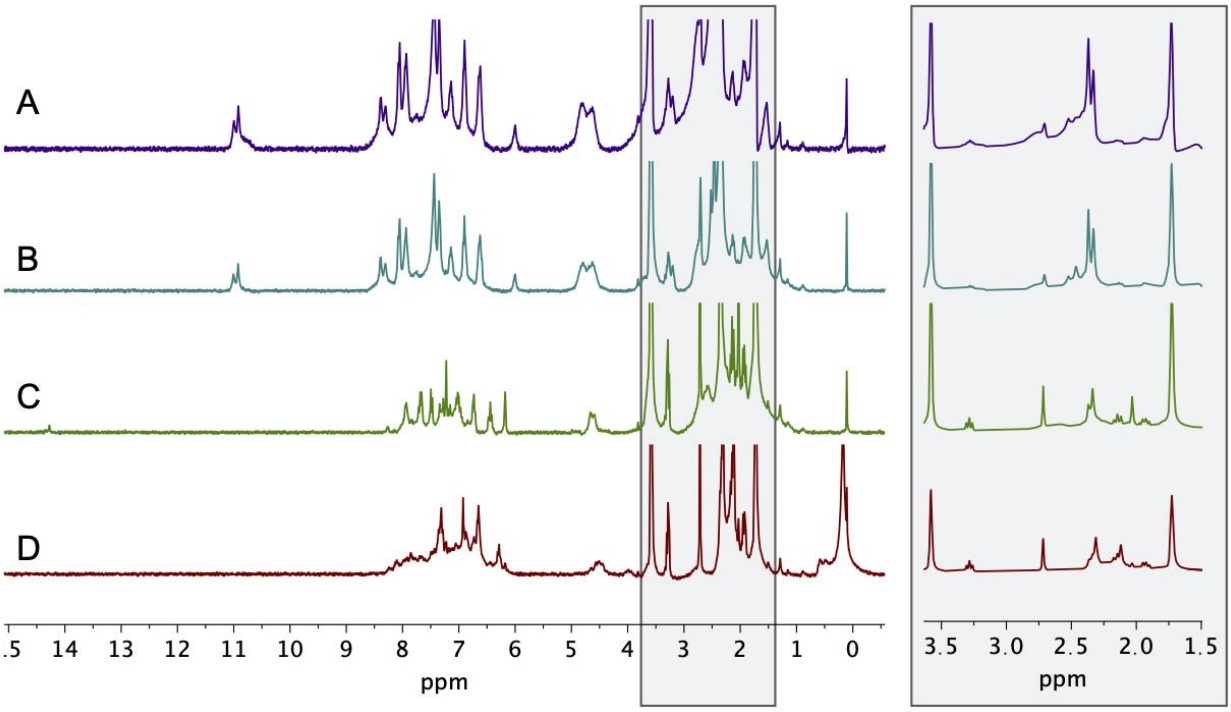

Figure 2.12. ^{1}H NMR, 300 MHz, THF-d_8, 298K. Progression of reaction between complex **1** and excess K_3PO_4, showing **1** in THF-d_8 after 90 minutes (A) and overnight (B), followed by the reaction with excess K_3PO_4 after 1 hour at room temperature (C) and after heating for 90 minutes at 100 ºC (D).

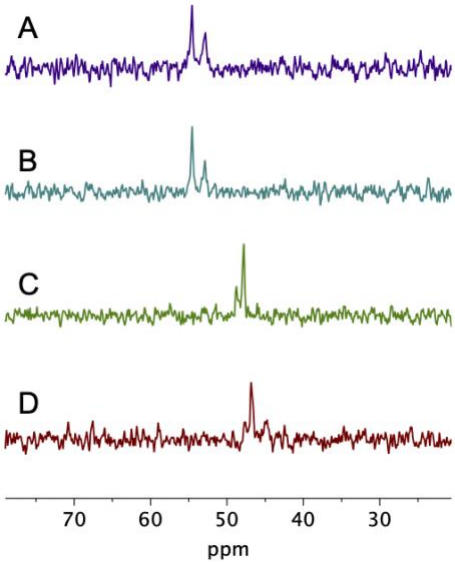

Figure 2.13. ^{31}P NMR, 121.48 MHz, THF-d_8, 298K. Progression of reaction between complex **1** and excess K_3PO_4, showing **1** in THF-d_8 after 90 minutes (A) and overnight (B), followed by the reaction with excess K_3PO_4 after 1 hour at room temperature (C) and after heating for 90 minutes at 100 ºC (D).

unchanged with the exception of the broadening of the aromatic peaks and the methyl group peaks. The addition of K_3PO_4 (10 equivalents) does not deprotonate the NH wingtips after 1 hour of stirring at room temperature. Rather, two additional peaks appear in the ^1H NMR at 11.2 and 10.7 ppm, each integrating to half that of the NH wingtip peak at 11.4 ppm. The aromatic region now consists of a sharp multiplet, two broad singlets, and four sharper singlets, and there are now at least five peaks corresponding to the methyl groups on the ligand backbone (Figure 2.14). Likely there are multiple species in solution, however solubility challenges prevented collection of meaningful ^{31}P NMR data. It is interesting that for complex **1** the K_3PO_4 readily deprotonates the NH wingtips, while for complex **2** there is only partial deprotonation and/or some other reactivity or coordination. This suggests that the ancillary ligands may have some influence over the pKa of the NH wingtips.

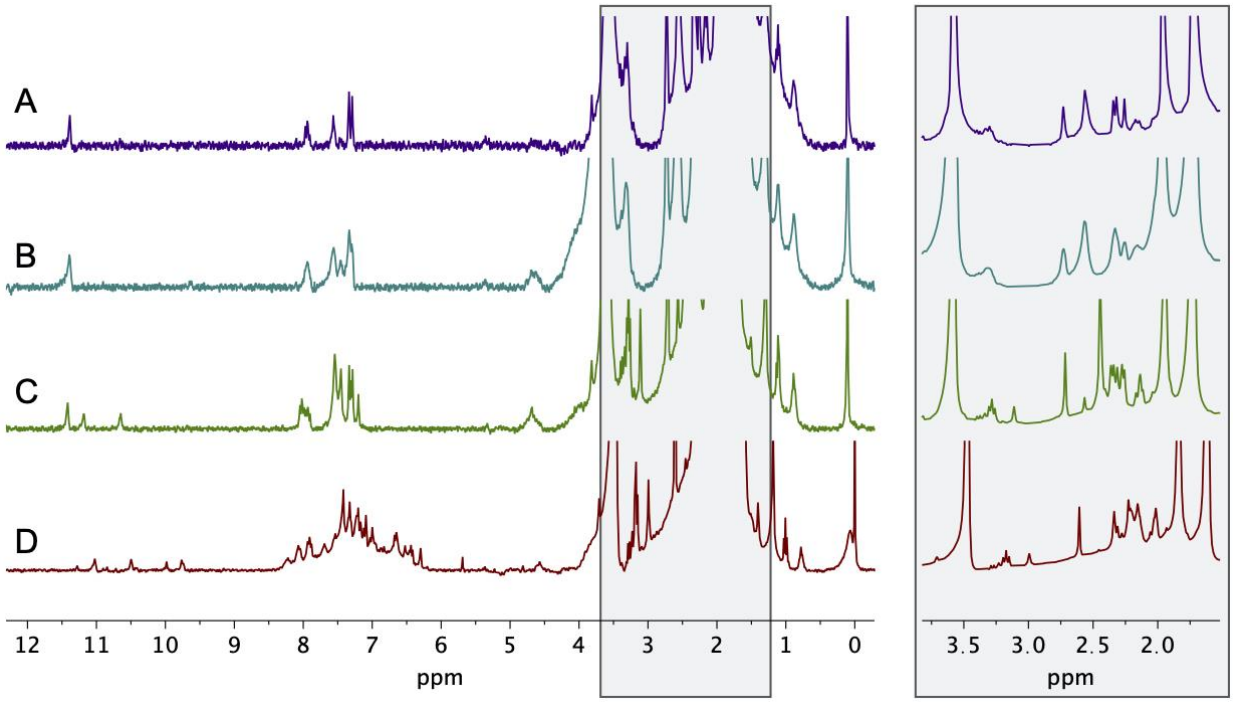

Figure 2.14. ^1H NMR, 300 MHz, THF-d_8, 298K. Progression of reaction between complex **2** and excess K_3PO_4, showing **2** in THF-d_8 after 90 minutes (A) and overnight (B), followed by the reaction with excess K_3PO_4 after 1 hour at room temperature (C) and after heating for 90 minutes at 100 ºC (D).

2.2.5 *Methylation of the NH-Wingtips*

Scheme 2.8. Methylation of **1**

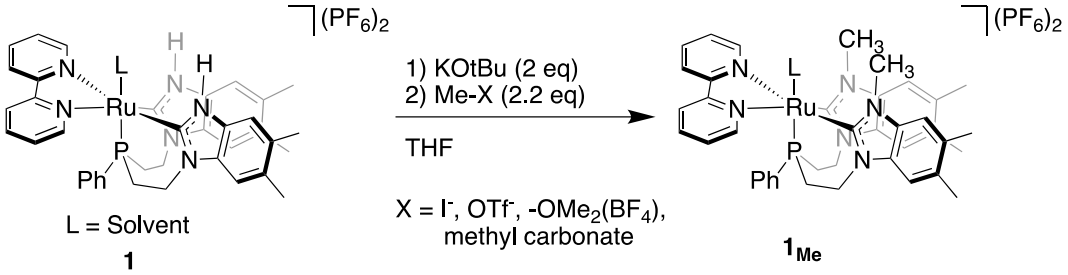

One way to determine whether the PNHCs are involved in metal-ligand cooperativity (MLC) in a catalytic reaction is by blocking those active sites. Methylation of PNHCs has been demonstrated in the literature for mono-PNHC phosphine ligands and are achieved by reaction of the deprotonated PNHC complex with a strong methyl donor, such as MeOTf.[17]

The synthesis of compound **1-Me** via methylation of the NH wingtips in **1** was pursued, first by deprotonation by 2 equivalents of KOtBu at reduced temperature, followed by the addition of a methyl donor, such as dimethyl carbonate, Me_3OBF_4, MeI, and MeOTf (Scheme 2.8). Methylation was shown to be unselective, and full methylation of the NH wingtips was not observed.

Of the methylating agents screened, dimethyl carbonate is the mildest. Following deprotonation, reaction with dimethyl carbonate leads to partial reactivity, with the ^{31}P NMR suggesting a significant amount of the deprotonated intermediate remaining unreacted by the persistence of the signal at 46 ppm (Figure 2.15). Additionally, a peak at 0.95 ppm is present after reaction with dimethyl carbonate. The ^{1}H NMR suggests one major species, however the signal to noise is poor due to swamping of the signal by the excess dimethyl carbonate.

The choice of Me_3OBF_4, which is a stronger methylating agent than dimethyl carbonate and roughly equivalent to the strength of MeI, did show reactivity with the deprotonated

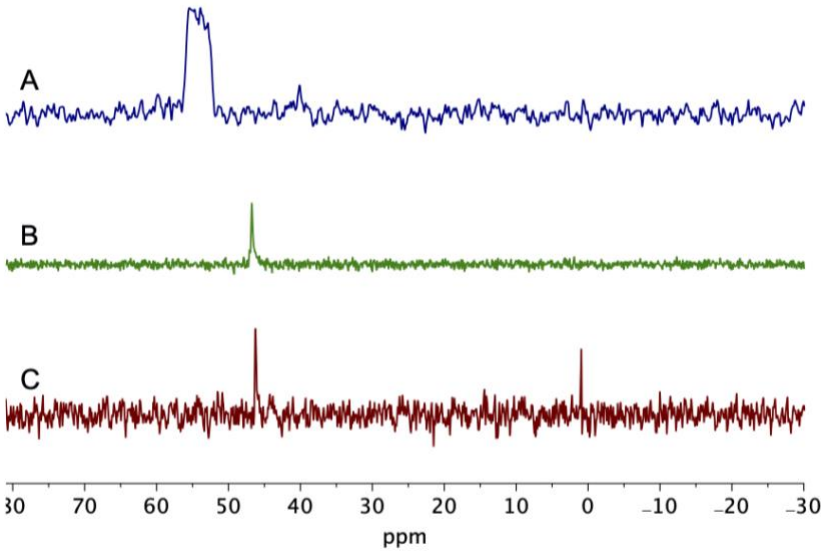

Figure 2.15. ^{31}P NMR (121 MHz, THF-d_8, 298K) data for the reaction between **1** (A) and dimethyl carbonate for the synthesis of **1-Me**. (B) Deprotonation by KOtBu. (C) Reaction of the deprotonated intermediate with dimethyl carbonate.

intermediate, however many species were formed with no major product (Figure 2.16). After 17 hours at room temperature two major species are dominant by ^{31}P NMR at 56 and 54 ppm (Figure 2.16E, right). It is proposed that these two species are at different states of methylation. Concentrating this sample and redissolving in deuterated acetonitrile leads to the formation of many new signals in the ^{31}P NMR (Figure 2.17A). As a strategy to force the reaction to one major product a third equivalent of Me_3OBF_4 was added, targeting the complex with both NH wingtips methylated as well as the metal center. This addition, however, did not greatly alter the product distribution, as evidence by the ^{1}H and ^{31}P NMR (Figure 2.17B).

Methyl iodide was tested in excess (10 equivalents) with the goal of pushing the methylation of **1** to completion. Initial reactions with CD_3I suggested methyl incorporation, evidenced by ^{2}H NMR (Figure 2.18), and by ^{31}P NMR prior to work up there was only one major phosphorus containing species (Figure 2.19). The ^{1}H NMR however did suggest multiple products or unsymmetric coordination environments, including minor species containing resonances at 11.3 and 11.7 ppm, consistent with the NH wingtip resonances (Figure 2.19C).

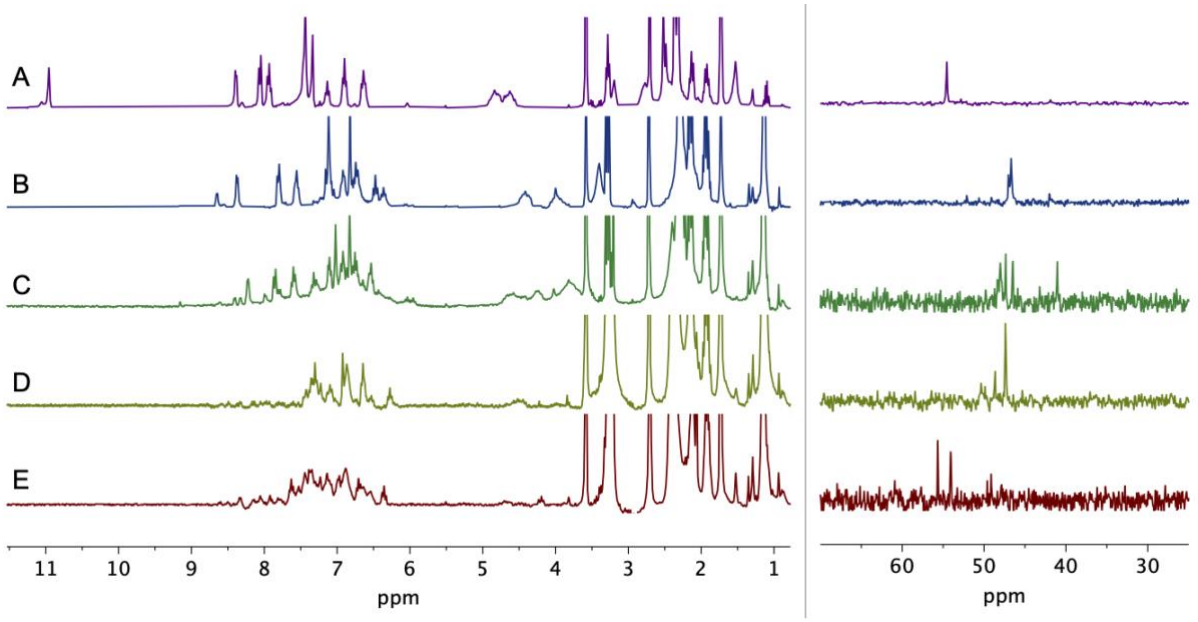

Figure 2.16. ^{1}H NMR (left; 301 MHz, CD_3CN, 298K) and ^{31}P NMR (right; 121 MHz, THF-d8, 298K) data for the reaction between **1** (A) and Me_3OBF_4 for the synthesis of **1-Me**. (B) Deprotonation by KOtBu. (C) Reaction of the deprotonated intermediate with Me_3OBF_4 after 10 minutes (C), 4 hours (D), and 17 hours (E) at room temperature.

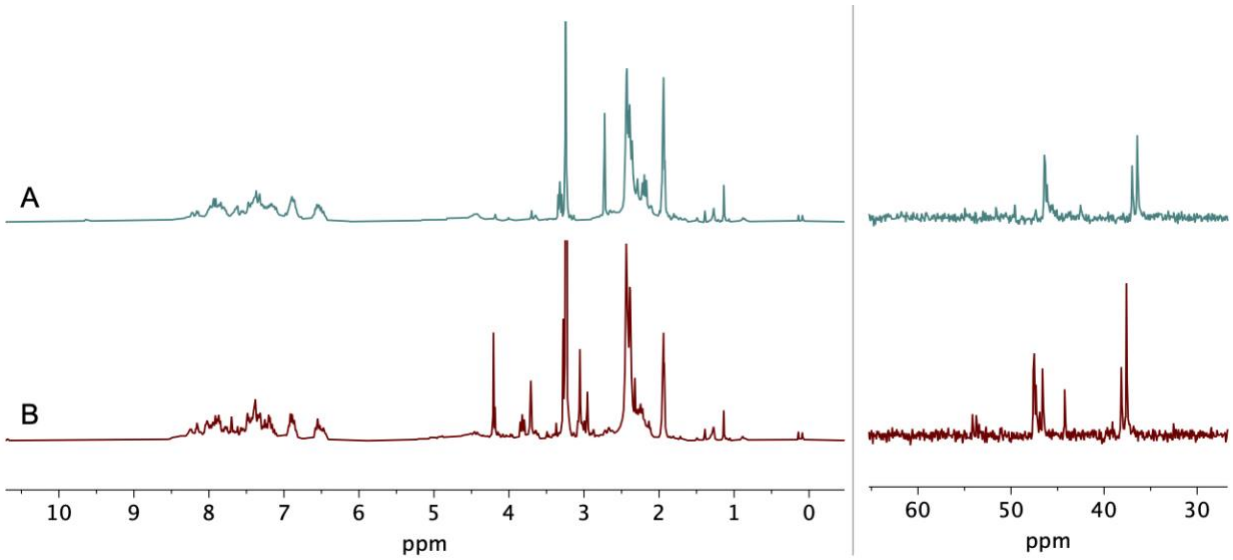

Figure 2.17. ^{1}H (left; 301 MHz, CD_3CN, 298K) and ^{31}P NMR (right; 121 MHz, CD_3CN, 298K) of the reaction between the deprotonated intermediate of **1** with Me_3OBF_4 after concentrating and redissolving in CD_3CN (A) and after the addition of a third equivalent of Me_3OBF_4 (B).

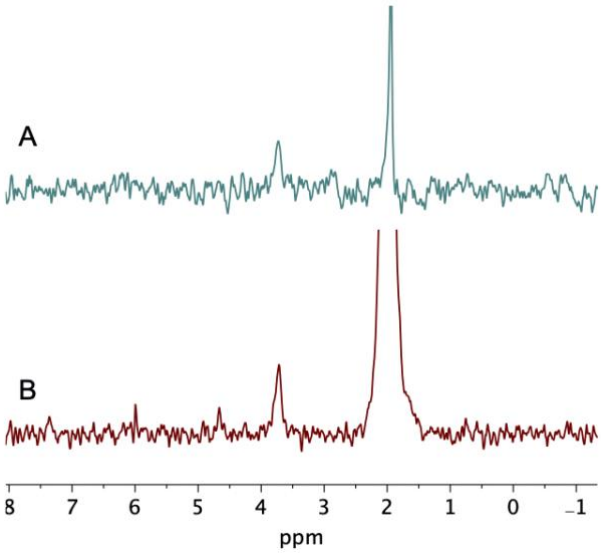

Figure 2.18. ^{2}H NMR (76 MHz, CH_3CN, 298K) following reaction between **1**, KOtBu, and CD_3I. A) CD_3CN peak at 1.94 ppm, and deuterated methyl product peak at 3.73 ppm. Unreacted CD_3I is expected approximately at 2.16 ppm. B) Sample spiked with CD_3CN.

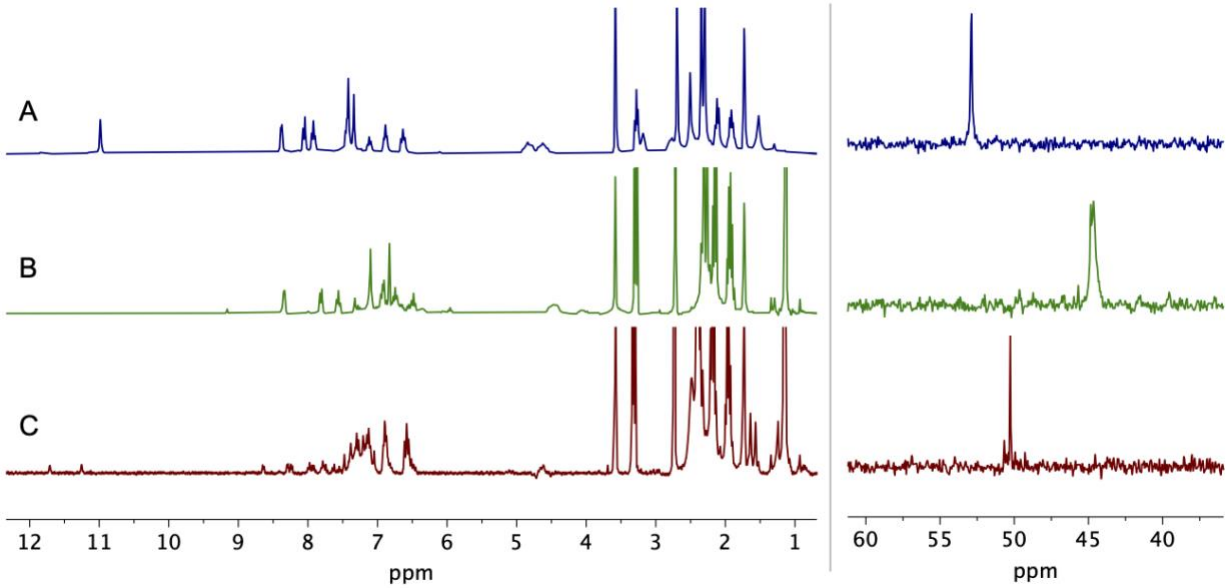

Figure 2.19. ^{1}H (left; 301 MHz, THF-d_8, 298K) and ^{31}P NMR (right; 121 MHz, THF-d_8, 298K) data for the reaction between **1** and CD_3I for the synthesis of **6.** A) Complex **1**. B) Deprotonation by KOtBu. C) Reaction of the deprotonated intermediate with CD_3I.

Upon recrystallization from acetonitrile and diethyl ether, a sample suitable for X-ray diffraction was obtained and revealed a mixture of co-crystallized species. Both species showed acetonitrile activated with the solvent nitrogen coordinated to the ruthenium and a deprotonated NH-wingtip coordinated to the carbon of the nitrile group. The other ligand arm in the crystal

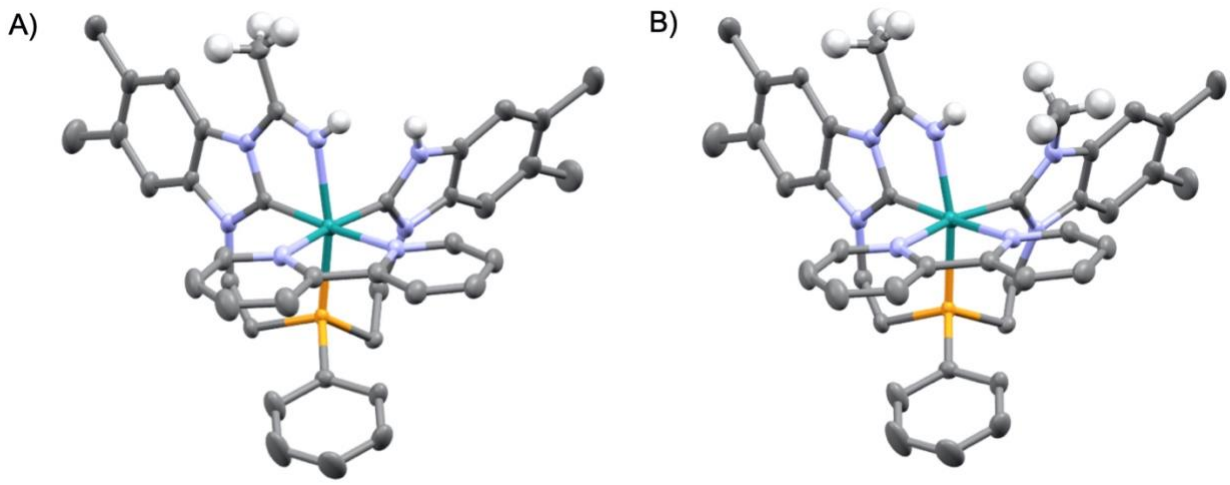

Figure 2.20. Crystal structure showing activation of acetonitrile between the ruthenium and one arm of the ligand with the other arm of the ligand showing disorder, with a protonated nitrogen appearing in 80% of the molecules (A) and a methylated nitrogen appearing in the remaining 20% of the molecules (B). The structure was crystalized with one iodide anion and one diiodine molecule. The iodide, iodine, and all hydrogen atoms with the exception of the acetonitrile hydrogens, the NH wingtip and the hydrogens of the methylated nitrogen, are excluded for clarity.

structure is disordered, with a protonated nitrogen in 80% of the molecules and a methylated nitrogen appearing in the remaining 20% (Figure 2.20). This result was consistent with NMR data obtained for replicate runs, where after two days at room temperature with CH_3I, two major products are observed by ^{31}P NMR and there are two peaks consistent with the NH wingtips at 11.5 and 11.9 ppm. The product distribution remains unchanged after heating at 50 ºC for 2 and a half hours, as well as after addition of a mild base, K_3PO_4, in large excess (15 equivalents) to attempt to deprotonate the NH-wingtip positions. K_3PO_4 was previously shown to deprotonate **1** but not **3**, illustrating the dependence of the wingtip pKa on the chemical and electronic environment of the complex. In the product formed here, K_3PO_4 is not a strong enough base to deprotonate the NH wingtip positions. Using nBuLi in the place of KOtBu for the deprotonation showed one major species while monitoring the reaction in situ by ^{31}P and ^{1}H NMR, however there is no clear signal corresponding to the incorporation of methyl by ^{1}H NMR. Upon work up

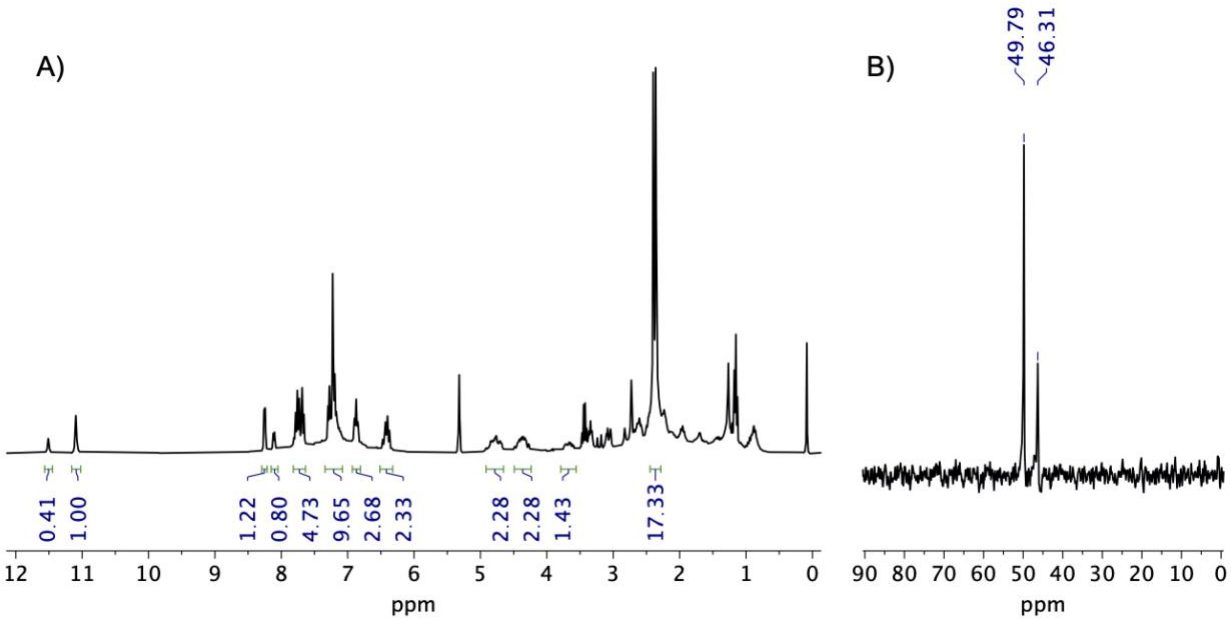

Figure 2.21. (A) ^{1}H (301 MHz, CD_2Cl_2, 298K) and (B) ^{31}P NMR (121 MHz, CD_2Cl_2, 298K) data for the reaction of **1** deprotonated with nBuLi and reacted with CH_3I.

by concentrating, crashing out with diethyl ether, and collecting the resultant powder, NMR in CD_2Cl_2 shows the conversion into a species containing two ^{1}H NMR resonances at 11.1 and 11.5 ppm, consistent with the protonation of the NH wingtips (Figure 2.21).

Given the vast excess of CH_3I that was used and only partial methylation observed, CH_3OTF, a stronger methylating agent, was used in slight excess (2.2 equivalents). The reactivity was not selective, with multiple species apparent in the ^{31}P NMR after 10 minutes at room temperature and no significant change after 24 hours at room temperature. Additionally, by ^{1}H NMR the peaks consistent with the NH wingtips are present after 10 minutes and there are no resonances that would suggest methyl incorporation (Figure 2.22).

Due to the challenges faced with selectivity in the direct methylation of **1**, the synthesis of the methylated ligand ($\mathbf{L_{CH3}}$) prior to metalation was also pursued. The methylated ligand arm (bim_{CH3}) was successfully synthesized by refluxing bim in acetonitrile for 24 hours in the

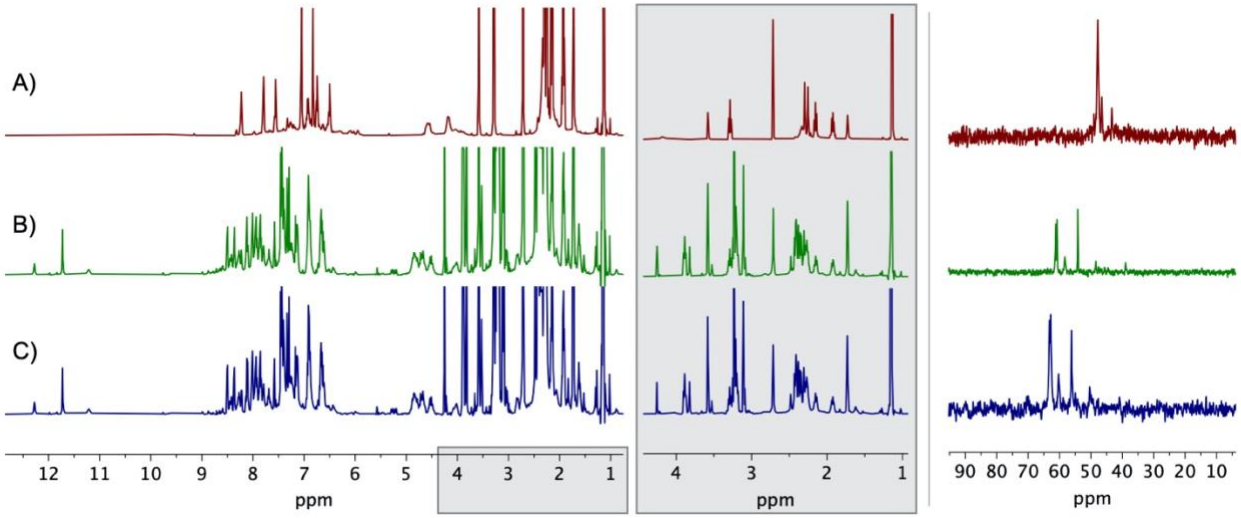

Figure 2.22. ^{1}H (left; 500 MHz, THF-d_8, 298K) and ^{31}P NMR (right; 202 MHz, THF-d_8, 298K) data for the reaction between **1** and CH_3OTf for the synthesis of **6**. (A) Deprotonation by KOtBu. (B) Reaction of the deprotonated intermediate with CH_3OTf after 10 minutes at room temperature and (C) after 24 hours at room temperature.

presence of two equivalents of MeI. The product bim_{CH3} was isolated in >99% yield (Scheme 2.9, Figure 2.23). The synthesis of L_{CH3} was attempted by two methods. The first method was single deprotonation and substitution of the $PhPH_2$ with bim_{CH3} carried out in THF, followed by a repetition of these steps for the second substitution. The reaction was monitored by ^{1}H-coupled ^{31}P NMR, with characteristic resonances appearing as a doublet at -60 ppm with a coupling constant of 214.42 Hz, suggested as the singly substituted phosphine, and a singlet at -27 ppm, suggested as corresponding to the doubly substituted $\mathbf{L_{CH3}}$. Following the second addition of nBuLi and R_{CH3}, the species appearing at -27 ppm is dominant, however an insoluble white precipitate crashes out of solution and upon work up and being dissolved in CD_3CN the product distribution is largely the species with the ^{31}P NMR resonance at -60 ppm. As CD_3CN readily dissolved the insoluble species in THF, the synthesis was attempted in CH_3CN however the deprotonation of the $PhPH_2$ in this solvent lead to an undesired byproduct. Running the synthesis in THF and heating at 65 ºC overnight similarly, did not yield the desired product, and multiple

Scheme 2.9. Synthesis of the methylated ligand arm, bim_{CH3}.

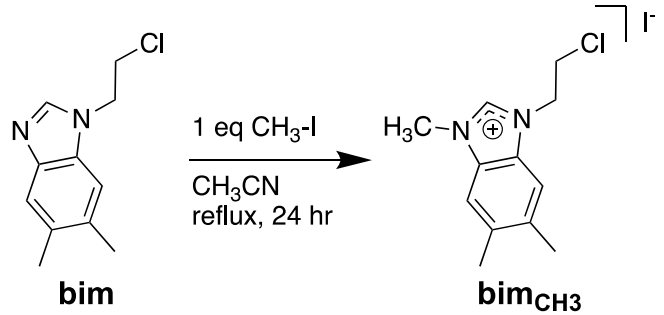

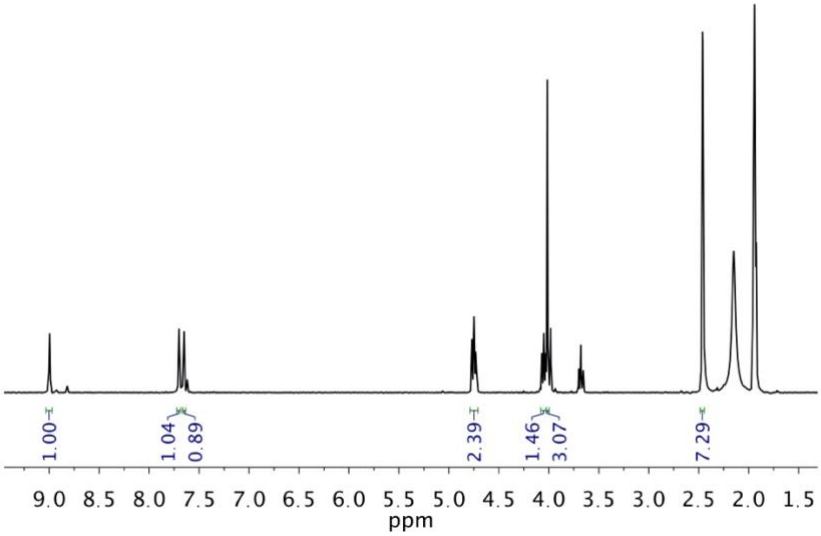

Figure 2.23. ^1H NMR characterization of bim_{CH3} (CD_3CN, 300 MHz, 298K).

methods for work up and purification, including filtration, air free work up, and recrystallization, did not yield a single product.

The methylation of the NH-wingtips, both pre- and post-metalation of the ligand, proved significantly more challenging than described in the literature for single arm, mono-PNHC, analogs of **L**. For the direct methylation of the PNHCs in **1**, it is hypothesized that the bis-PNHC enables unexpected reactivity rendering the methylation at those sites unstable/reactive. This may be due to the charge distribution of the deprotonated intermediate, as this species already has a negative charge and is not a strong nucleophile. Perhaps in the analogous mono-PNHC systems where alkylation does take place, the presence of only one carbene is more nucleophilic, where in the bis-PNHC system not only is there the negative charge of the ligand but also the

increased electron density from the two strongly sigma donating carbenes. Similarly, the charge is likely responsible for the instability of $\mathbf{L_{CH3}}$.

2.3 CONCLUSIONS

A one-pot synthesis for the metalation of **L** to yield a tripodal bis-(PNHC) phosphine ruthenium complex has been developed, and a library of bidentate ancillary ligands, including substituted bipyridines and dppe, have been isolated and characterized. Coordination of bipyridine and dppe with **3** was explored, and coordination trans to the carbenes appears to be favored in non-coordinating solvents. The pKa of the NH-wingtips of the PNHCs appear to be influenced by the ancillary ligand, with clean deprotonation observed of **1** with K_3PO_4 but multiple products of various protonation states being observed with **3** and K_3PO_4. Finally, the methylation of the NH-wingtips was pursued in order to probe metal-ligand cooperativity by comparting the N-H versus N-Me complexes in catalysis and substrate activation, but the full methylation proved unfavorable.

2.4 EXPERIMENTAL

2.4.1 *General Considerations*

All manipulations were carried out under an N_2 atmosphere, either in a glovebox or using Schlenk technique, unless otherwise noted. THF, CH_2Cl_2, Et_2O, and CH_3CN were purchased from Fisher Scientific and dried on a solvent purification system. N-methyl-2-pyrrolidinone (NMP, anhydrous, 99.5%), 2,2'-bipyridine (bpy), 4,4'-dimethoxy-2,2'-bipyridine (97%), 1,2-bis-(diphenylphosphino)ethane (dppe), ammonium hexafluorophosphate (NH_4PF_6, 99.98% trace metals basis), KOtBu, nBuLi (1.6 M in hexanes solution, anhydrous), dimethyl carbonate (99%, anhydrous), Me_3OBF_4, MeI (99%), and MeOTf (98%, 10g ampules) were purchased from

Sigma-Aldrich and dried as necessary. 4,4'-dibromo-2,2'-bipyridine was purchased from TCI America and dried overnight. Deuterated NMR solvents were purchased from Cambridge Isotope Lab Inc. Unless manipulations were performed in air, all NMR solvents were dried over CaH_2, vacuum transferred, and stored in the glovebox over molecular sieves. THF-d_8 was purchased in ampules and used without further purification. ^{1}H, ^{13}C, and ^{31}P NMR were recorded on either a Bruker AV300, Bruker AV301, Bruker AV 500, or Bruker AV700 spectrometer. $[Ru(C_6H_6)(bpy)(OTf)](OTf)$ and 1-*N*-(chloroethyl)-5,6-dimethylbenzimidazole were synthesized according to literature procedures, and the procedure for the ruthenium precursors were easily adapted for the 4,4'-disubstituted-2,2'-bipyridine library.[3]

Cyclic voltammetry was carried out using an Epsilon Potentiostat (BASi) in an N_2 glovebox. The electrolyte solution was 0.2 M tetrabutylammonium hexafluorophosphate in CH_3CN, with a glassy carbon working electrode, platinum counter electrode, and a Ag wire pseudo reference electrode in a Vycor-fritted compartment. The tetrabutylammonium hexafluorophosphate electrolyte was recrystallized two times in EtOH and dried overnight under vacuum at 100 ºC. Glass carbon electrodes with a diameter of 3.0 mm were polished using 1.0, 0.3, and 0.05 micron polishing powder followed by 5 minute sonication cycles in deionized water. All CVs were referenced to a ferrocene internal standard added after the experiment.

2.4.2 *Synthesis and Characterization*

Modified Synthesis of P^{Ph}(1-*N*-ethyl-5,6-dimethylbenzimidazole)$_2$ (L). In a glovebox, a round bottom flask equipped with a magnetic stir bar was charged with phenyl phosphine as a 10% w/w solution in hexanes (3.8 g of solution, 3.4 mmol $PhPH_2$, 1 eq) and 40 mL of anhydrous THF. The reaction mixture was then chilled in the glovebox liquid nitrogen coldwell for 15 minutes. A 1.6 M nBuLi solution in hexanes was titrated three times with diphenylacetic acid

before addition of nBuLi (2.31 mL, 3.7 mmol, 1.1 eq) to the chilled $PhPH_2$ while stirring. The reaction mixture turned yellow and was stirred for 10 minutes at room temperature. The reaction mixture was then chilled in the cold well for 15 minutes, along with 1-*N*-(chloroethyl)-5,6-dimethylbenzimidazole ($EtClbimMe_2$; 786 mg, 3.7 mmol, 1.1 eq) in 20 mL THF. The $EtClbimMe_2$ was added to the reaction mixture while thawing and the mixture is stirred for 1 hr at room temperature. This process was then repeated for a second addition of 1 equivalent of nBuLi and 1 equivalent of $EtClbimMe_2$. The crude reaction mixture can be monitored by ^1H-coupled ^{31}P NMR to confirm complete conversion to product, with diagnostic peaks being δ -32 (s), -60 (d, $^1J_{H\text{-}P}$ = 206 Hz), -124 (t, $^1J_{H\text{-}P}$ = 196 Hz) ppm corresponding to L, HP^{Ph}(1-*N*-ethyl-5,6-dimethylbenzimidazole), and $PhPH_2$ respectively. The reaction is removed to air for work up following the previously published procedure and characterization data is consistent.[3] (Yield = 50%).

Modified Synthesis of [Ru(4,4'-di-X-2,2'-bpy)(H_2O)(P^{Ph}(PNHC)$_2$)](PF_6)$_2$ (X = H, Br, OMe) (1). The previously published synthesis of 1 involved multiple steps.[3] The synthesis has been modified, and a one pot synthesis was carried out by adding L (105.1 mg, 0.2313 mmol) to [Ru(C_6H_6)(4,4'-di-X-bpy)(OTf)](OTf) (0.2313 mmol; X = H, Br, OMe) in anhydrous NMP (3.75 mL). The reaction was heated at 175 °C for 1 hr, before cooling to room temperature and adding to an aqueous solution of excess NH_4PF_6. The resulting precipitate was collected on a medium porosity frit. Product is isolated as a red-brown air stable powder. (Yield 99%). Characterization is consistent with previously published data, however it was found that taking an NMR spectrum in a coordinating solvent gives significantly more clarity due to well-defined coordination of solvent in the open coordination site.

[Ru(bpy)(H$_2$O)(P^{Ph}(PNHC)$_2$)](PF$_6$)$_2$ (X = H) (1a). ^{1}H NMR (CD$_3$CN, 500 MHz) δ 10.65 (s, 2H), 8.24 (d, 2H, *J* = 5.19 Hz), 7.92-7.83 (m, 4H), 7.40-7.37 (m, 2H), 7.35 (s, 2H), 7.29 (s, 2H), 7.18 (t, 1H, *J* = 7.53 Hz), 6.87 (td, 2H, *J* = 7.69 Hz, 2.29 Hz), 6.47 (dd, 2H, *J* = 9.91 Hz, 7.67 Hz), 4.68-4.52 (m, 2H), 4.34-4.18 (m, 2H), 2.60-2.51 (m, 4H), 2.40 (s, 6H), 2.38 (s, 6H). ^{31}P{^{1}H} NMR (CD$_3$CN, 202 MHz) δ 44.4. ^{13}C{^{1}H} NMR (CD$_3$CN, 126 MHz) δ 192.14 (d, J_{CP} = 15.62 Hz), 156.62, 153.33, 138.69, 134.91, 133.60, 133.26, 132.44, 132.36, 130.39, 129.55, 129.47, 128.75, 128.68, 127.49, 124.17, 111.76, 110.74, 42.76, 24.11, 23.84, 20.32, 20.07.

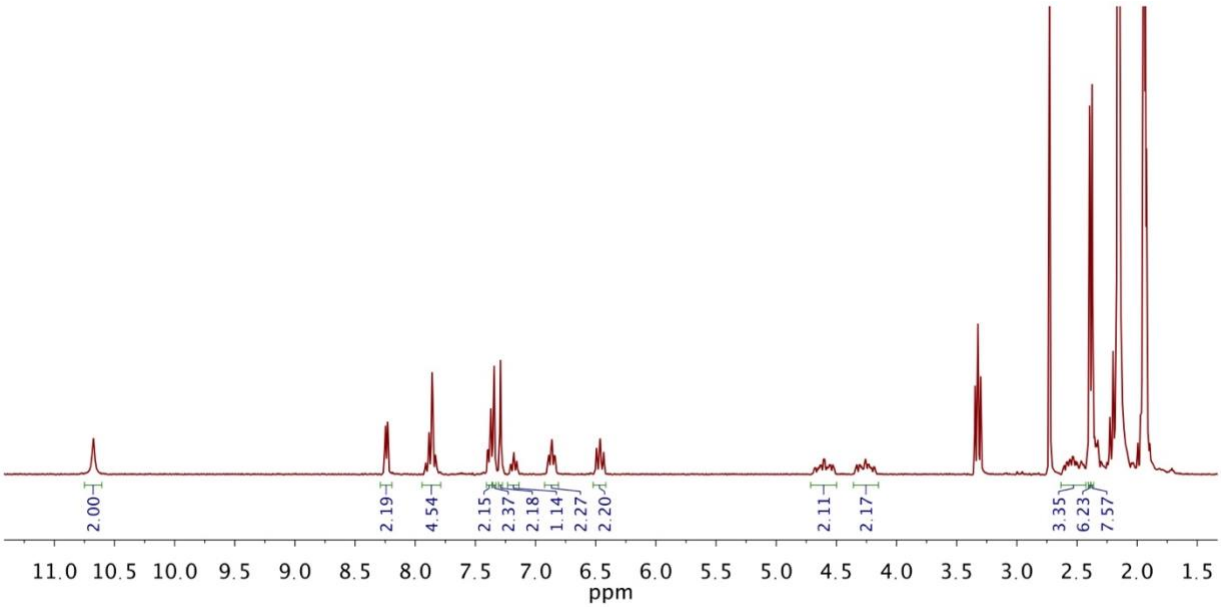

Figure 2.24. ^{1}H NMR (300 MHz, CD$_3$CN, 298 K) of complex **1a**.

[Ru(4,4'-dibromo-2,2'-bpy)(H$_2$O)(P^{Ph}(PNHC)$_2$)](PF$_6$)$_2$ (1b). ^{1}H NMR (CD$_3$CN, 301 MHz) δ 10.65 (s, 2H), 8.08 (d, 2H), 8.06 (d, 2H), 7.59 (dd, 2H), 7.35 (s, 2H), 7.29 (s, 2H), 6.99 (td, 2H), 6.54 (dd, 2H), 4.54 (m, 2H), 4.21 (m, 2H), 2.62-2.47 (m, 4H), 2.39 (s, 6H), 2.37 (s, 6H). ^{31}P{^{1}H} NMR (CD$_3$CN, 121 MHz) δ 47.7. ^{13}C NMR (176 MHz, CD$_3$CN) δ 156.69, 153.87, 134.89, 133.74, 133.25, 132.41, 131.08, 130.65, 129.55, 128.90, 128.02, 111.99, 110.69, 66.28, 42.81, 24.08, 23.89, 20.32, 20.07, 15.63.

[Ru(4,4'-dimethoxy-2,2'-bpy)(H_2O)(P^{Ph}(PNHC)$_2$)](PF_6)$_2$ (1c). ^{1}H NMR (CD_3CN, 500 MHz) δ 10.62 (s, 2H), 7.97 (d, 2H), 7.33 (s, 4H), 7.27 (s, 2H), 7.23 (t, 1H), 6.95 (td, 2H), 6.91 (dd, 2H), 6.55 (t, 2H), 4.56 (m, 4H), 4.20 (m, 4H), 3.92 (s, 6H), 2.39 (s, 6H), 2.37 (s, 6H). ^{31}P{^{1}H} NMR (CD_3CN, 121 MHz) δ 44.7. ^{13}C NMR (176 MHz, CD_3CN) δ 192.96 (d, J = 15.46), 175.30, 167.93, 158.04, 153.99, 134.82, 133.55, 133.09, 132.28, 130.37, 129.42 (d, J = 8.12), 129.05 (d, J = 8.15), 118.26, 113.52, 111.58, 110.72, 110.62, 57.37, 49.77, 42.67, 31.12, 29.55, 24.21, 24.01, 20.26, 20.00, 18.35.

Synthesis of [Ru(bpy)(^{13}CO)(P^{Ph}(PNHC)$_2$)](PF_6)$_2$ (1-^{13}CO). A round bottom flask containing **1** in CH_2Cl_2 was fitted with a sparge tube connected to a lecture bottle of ^{13}CO gas purchased from Sigma Aldrich. The solution was degassed three times and put under static vacuum before opening the lecture bottle to introduce ^{13}CO at -78 °C. The solution was allowed to thaw and stirred overnight. The reaction flask was then vented and concentrated. ^{1}H NMR (CD_2Cl_2, 500 MHz) δ 10.54 (s, 2H), 8.12 (d, 2H), 7.90 (t, 2H), 7.70 (d, 2H), 7.44-7.40 (m, 5H), 7.25 (s, 2H), 6.94 (t, 2H), 6.35 (t, 2H), 4.55-4.46 (m, 2H), 4.42-4.33 (m, 2H), 2.70-2.66 (m, 2H), 2.35 (s, 6H), 2.32 (s, 6H), 2.30-2.27 (m, 2H). ^{31}P{^{1}H} NMR (CD_2Cl_2, 202 MHz) δ 10.8 (d, J = 93 Hz). ^{13}C NMR (CD_2Cl_2, 125 MHz) δ 193.6 (d, J = 93 Hz), 180.7, 163.0, 155.8, 152.9, 139.6, 134.8, 133.9, 133.4, 132.8, 129.9, 128.0, 124.3, 112.8, 110.2, 75.4, 42.3, 20.6, 20.3. FTIR (KBr) ν_{13CO} = 1967 cm^{-1}.

Synthesis of [Ru(bpy)(CO)(P^{Ph}(PNHC)$_2$)](PF_6)$_2$ (1-CO). A round bottom flask of **1** in CH_2Cl_2 was sparged for five minutes with CO from a gas cylinder through a schlenk line. ^{1}H NMR (CD_2Cl_2, 700 MHz) δ 11.30 (s, 2H), 8.14 (d, 2H), 7.89 (t, 2H), 7.71 (d, 2H), 7.42 (t, 3H), 7.32 (s, 2H), 7.27 (s, 2H), 6.93 (t, 2H), 6.36 (t, 2H), 4.47-4.43 (m, 4H), 2.34 (s, 6H), 2.31 (s, 6H), 2.29-2.25 (m, 4H). ^{31}P{^{1}H} NMR (CD_2Cl_2, 202 MHz) δ 10.4. ^{13}C NMR (CD_2Cl_2, 125 MHz) δ.180.7,

175.1, 155.4, 152.6, 139.2, 134.1, 133.3, 133.2, 132.6, 131.1, 129.6, 129.5, 128.1, 128.0, 127.5, 126.3, 123.9, 112.1 110.0, 49.4, 42.0, 29.7, 24.1, 23.8, 20.0, 19.9, 19.8. FTIR (solution cell) ν_{CO} = 2023 cm^{-1}.

Synthesis of $[Ru(CH_3CN)_3(P^{Ph}(PNHC)_2)](BF_4)_2$ (3). In a N_2 glovebox, a 100 ml thick-walled Schlenk tube equipped with a stir bar was charged with dichloro(benzene)ruthenium(II) dimer (0.182 g, 0.363 mmol, 1 eq) and L (0.334 mg, 0.734 mmol, 2 eq), and NMP (10 ml). The reaction mixture was allowed to stir at room temperature for at least an hour. The Schlenk tube was sealed, removed from the glove box, connected to the Schlenk line, and heated outside the box at 170 °C for one hour. The volatiles were then removed under reduced pressure, at 100 °C on the Schlenk line, over the course of four hours. The Schlenk tube was brought into the glove box and acetonitrile (10 ml) and AgBF4 (0.284 g, 1.45 mmol, 4 eq) were added to the reaction mixture. The solution immediately became gray and cloudy. The resultant mixture was stirred for 1 hr before being filtered through Celite and the captured solids were washed with acetonitrile (3 x 5 ml). The volume of the extracts was reduced by half under reduced pressure, and the product was precipitated from solution with diethyl ether (30 ml). The resulting precipitate was collected on a frit and was washed with diethyl ether (3 x 15 ml), and dried overnight under reduced pressure. The product was collected as a white powder (0.583 g, 93% yield).

High quality crystals suitable for X-ray diffraction were grown by slow diffusion of diethyl ether into the CD_3CN solution at -35°C. ^1H NMR (700 MHz, CD_2Cl_2) δ 10.78 (s, 2H, N-H), 7.85 (dd, J = 10.2, 7.7 Hz, 2H, Ph-H), 7.64 (td, J = 7.8, 2.1 Hz, 2H, Ph-H), 7.61 – 7.56 (m, 1H, Ph-H), 7.39 (s, 2H, Ar-H), 7.11 (s, 2H, Ar-H), 4.39 (dddd, J = 19.3, 13.2, 10.0, 2.5 Hz, 2H, -CH_2), 4.25 (dddd, J = 26.2, 14.2, 7.3, 3.2 Hz, 2H, -CH_2), 2.71 (tdd, J = 12.9, 7.1, 3.7 Hz, 2H, -CH_2), 2.62 (s,

3H, NCCH3), 2.35 (s, 6H, -CH3), 2.33 (s, 6H, -CH3), 2.22 (s, 6H NCCH3), 2.14 (tdd, J = 13.0, 9.6, 6.0 Hz, 2H, -CH2). $^{31}P\{^{1}H\}$ NMR (202 MHz, CD_3CN) δ 44.73 . ^{13}C NMR (176 MHz, CD_3CN) δ 189.05, 188.95, 134.87, 134.63, 134.07, 133.39, 133.11, 132.41, 131.90, 131.85, 131.44, 129.79, 129.74, 124.69, 118.31, 111.88, 110.58, 26.73, 26.53, 20.29, 20.04. Anal. Calc. for $B_2C_{34}F_8H_{40}N_4PRu$: C, 47.91; H, 4.73; N, 11.5. Found: C, 47.09; H, 4.65; N, 11.35 %.

[Ru(bpy)(CH3CN)(P^{Ph}(PNHC)2)](BF4)2 (4). [Ru(CH3CN)3(P^{Ph}(PNHC)2)](BF4)2 (**3**) (68.1 mg, 0.0799 mmol, 1 eq) and 2,2'-bipyridine (bpy) (mg, mmol, 1.2 eq) are separately dissolved in dichloromethane and frozen. The solution of bpy is added to **3** while thawing and stirred at room temperature overnight. The solution is then concentrated to 1 mL and **4** is crashed out of solution with the addition of Et2O and collected on a frit. ^{1}H NMR (301 MHz, CD_3CN) δ 9.86 (s, 1H), 9.37 (s, 1H), 8.17 (d, *J* = 5.52 Hz, 1H), 8.05-7.93 (m, 3H), 7.91 (d, *J* = 1.84 Hz, 1H), 7.81 (d, *J* = 1.53 Hz, 1H), 7.80-7.74 (m, 2H), 7.69 (s, 1H), 7.26-7.14(m, 4H), 6.91 (td, *J* = 7.83 Hz, 2.26 Hz, 2H), 6.59-6.50 (m, 2H), 5.06-4.75 (m, 2H), 4.53-4.34 (m, 1H), 4.23-4.07 (m, 1H), 2.85-2.59 (m, 4H), 2.44 (s, 3H), 2.42 (s, 3H), 2.38 (s, 3H), 2.32 (s, 3H). $^{31}P\{^{1}H\}$ NMR (121 MHz, CD_3CN) δ 38.

[Ru(dppe)(CH3CN)(P^{Ph}(PNHC)2)](BF4)2 (5). [Ru(CH3CN)3(P^{Ph}(PNHC)2)](BF4)2 (**3**) (68.1 mg, 0.0799 mmol, 1 eq) and 1,2-bis(diphenylphosphino)ethane (dppe) (38.2 mg, 0.0959 mmol, 1.2 eq) are separately dissolved in dichloromethane and frozen. The solution of dppe is added to **3** while thawing and stirred at room temperature overnight. The solution is then concentrated to 1 mL and **5** is crashed out of solution with the addition of Et2O and collected on a frit as a grey-purple powder. High quality crystals suitable for X-ray diffraction were grown by layering 0.5 mL diethyl ether and 0.5 mL of a 16 mM solution of **5** in dichloromethane. ^{1}H NMR (700 MHz, CD_2Cl_2) δ 10.98 (s, 2H), 7.62 (s, 2H), 7.45-7.39 (m, 5H), 7.33-7.28 (m, 10H), 7.27 (s, 2H), 7.17

(t, *J* = 8.0 Hz, 5H), 7.08 (q, *J* = 9.0 Hz, 5H), 4.55-4.47 (m, 2H), 4.45-4.36 (m, 2H), 2.96-2.85 (m, 2H), 2.75-2.65 (m, 2H), 2.51-2.44 (m, 4H), 2.42 (s, 12H). $^{31}P\{^{1}H\}$ NMR (202 MHz, CD_2Cl_2) δ 40 (d, J_{PP} = 26.4 Hz), 26 (t, J_{PP} = 26.4 Hz).

1-*N*-chloroethyl-2-*N*-methyl-5,6-dimethylbenzimidazolium iodide (bim_{CH3}). In air, methyl iodide (180 µL, 2.28 g/mL, 2.886 mmol) is added dropwise to a stirring solution of 1-*N*-(chloroethyl)-5,6-dimethylbenzimidazole (502 mg, 2.405 mmol) in THF, chilled in a dry ice/acetone bath. The reaction mixture was stirred at 40 ºC for 3 hours. Diethyl ether was added to the reaction mixture and the resulting suspension was stirred for 12 hours at room temperature. The reaction mixture was filtered, and the precipitate was washed with diethyl ether (3 x 5 mL) and dried under vacuum. ^{1}H NMR (301 MHz, CD_3CN) δ 9.09 (s, 1H), 7.72 (s, 1H), 7.65 (s, 1H), 4.77 (t, *J* = 5.59 Hz, 2H), 4.06 (t, *J* = 5.55 Hz, 2H), 4.02 (s, 3H), 2.46 (s, 6H).

2.4.3 *Crystallographic Information*

Table 3.3. Crystallographic information for complex **5**.

Empirical formula	C57 H60 Cl2 F12 N5 P5 Ru	
Formula weight	1369.92	
Temperature	100(2) K	
Wavelength	0.71073 Å	
Crystal system	Monoclinic	
Space group	P 2_1/n	
Unit cell dimensions	a = 14.873(6) Å	α= 90°.
	b = 20.764(7) Å	β= 91.306(15)°.
	c = 19.236(7) Å	γ = 90°.
Volume	5939(4) $Å^3$	
Z	4	
Density (calculated)	1.532 Mg/m^3	
Absorption coefficient	0.569 mm^{-1}	
F(000)	2792	
Crystal size	0.260 x 0.050 x 0.030 mm^3	
Theta range for data collection	1.443 to 26.370°.	
Index ranges	-18<=h<=18, -25<=k<=25, 0<=l<=24	
Reflections collected	23933	
Independent reflections	12142 [R(int) = 0.2302]	

Completeness to theta = 25.000°	100.0 %
Refinement method	Full-matrix least-squares on F^2
Data / restraints / parameters	12142 / 57 / 766
Goodness-of-fit on F^2	0.710
Final R indices [I>2sigma(I)]	R1 = 0.0668, wR2 = 0.1205
R indices (all data)	R1 = 0.2301, wR2 = 0.1740
Largest diff. peak and hole	1.196 and -1.081 e.$Å^{-3}$

Table 3.4. Crystallographic data for the structures provided targeting the synthesis of **6**, revealing partial methylation and acetonitrile activation.

Empirical formula	C40.22 H41.78 D0.68 I2 N7 P Ru	
Formula weight	1010.48	
Temperature	100(2) K	
Wavelength	0.71073 Å	
Crystal system	Monoclinic	
Space group	P 21/c	
Unit cell dimensions	a = 11.0950(5) Å	α= 90°.
	b = 27.3604(14) Å	β= 93.405(2)°.
	c = 13.1385(7) Å	γ = 90°.
Volume	3981.3(3) $Å^3$	
Z	4	
Density (calculated)	1.686 Mg/m^3	
Absorption coefficient	2.023 mm^{-1}	
F(000)	1991	
Crystal size	0.190 x 0.150 x 0.050 mm^3	
Theta range for data collection	1.489 to 28.372°.	
Index ranges	-14<=h<=14, -36<=k<=36, -17<=l<=17	
Reflections collected	19653	
Independent reflections	9941 [R(int) = 0.0208]	
Completeness to theta = 25.000°	99.7 %	
Refinement method	Full-matrix least-squares on F^2	
Data / restraints / parameters	9941 / 40 / 526	
Goodness-of-fit on F^2	1.147	
Final R indices [I>2sigma(I)]	R1 = 0.0382, wR2 = 0.0772	
R indices (all data)	R1 = 0.0516, wR2 = 0.0817	
Largest diff. peak and hole	1.256 and -1.126 e.$Å^{-3}$	

2.5 REFERENCES

(1) Kuwata, S.; Hahn, F. E. Complexes Bearing Protic N-Heterocyclic Carbene Ligands. *Chem. Rev.* **2018**. https://doi.org/10.1021/acs.chemrev.8b00176.
(2) Flowers, S. E.; Cossairt, B. M. Mono- and Dimetalation of a Tridentate Bisimidazole-Phosphine Ligand. *Organometallics* **2014**, *33* (17), 4341–4344. https://doi.org/10.1021/om500592u.

(3) Norris, M. R.; Flowers, S. E.; Mathews, A. M.; Cossairt, B. M. H $_2$ Production Mediated by CO $_2$ via Initial Reduction to Formate. *Organometallics* **2016**, *35* (17), 2778–2781. https://doi.org/10.1021/acs.organomet.6b00595.
(4) Flowers, S. E.; Johnson, M. C.; Pitre, B. Z.; Cossairt, B. M. Synthetic Routes to a Coordinatively Unsaturated Ruthenium Complex Supported by a Tripodal, Protic Bis(N-Heterocyclic Carbene) Phosphine Ligand. *Dalton Trans.* **2018**. https://doi.org/10.1039/C7DT04333C.
(5) Kovács, T.; Urbanics, A.; Csatlós, F.; Binder, J.; Falk, A.; Uhlig, F.; Keglevich, G. A Study on the Deoxygenation of Phosphine Oxides by Different Silane Derivatives. *Curr. Org. Synth.* **2016**, *13* (1), 148–153.
(6) Kovács, T.; Urbanics, A.; Csatlós, F.; Keglevich, G. A Study on the Deoxygenation of Trialkyl-, Dialkyl-Phenyl- and Alkyl-Diphenyl Phosphine Oxides by Hydrosilanes. *Heteroat. Chem.* **2017**, *28* (4), e21376. https://doi.org/10.1002/hc.21376.
(7) Petit, C.; Favre-Reguillon, A.; Albela, B.; Bonneviot, L.; Mignani, G.; Lemaire, M. Mechanistic Insight into the Reduction of Tertiary Phosphine Oxides by Ti(O *i* Pr) $_4$ /TMDS. *Organometallics* **2009**, *28* (22), 6379–6382. https://doi.org/10.1021/om900747b.
(8) Li, Y.; Das, S.; Zhou, S.; Junge, K.; Beller, M. General and Selective Copper-Catalyzed Reduction of Tertiary and Secondary Phosphine Oxides: Convenient Synthesis of Phosphines. *J. Am. Chem. Soc.* **2012**, *134* (23), 9727–9732. https://doi.org/10.1021/ja301764m.
(9) Li, Y.; Lu, L.-Q.; Das, S.; Pisiewicz, S.; Junge, K.; Beller, M. Highly Chemoselective Metal-Free Reduction of Phosphine Oxides to Phosphines. *J. Am. Chem. Soc.* **2012**, *134* (44), 18325–18329. https://doi.org/10.1021/ja3069165.
(10) Keglevich, G.; Kovács, T.; Csatlós, F. The Deoxygenation of Phosphine Oxides under Green Chemical Conditions: Deoxygenation of Phosphine Oxides under Green Chemical Conditions. *Heteroat. Chem.* **2015**, *26* (3), 199–205. https://doi.org/10.1002/hc.21249.
(11) Buonomo, J. A.; Eiden, C. G.; Aldrich, C. C. Chemoselective Reduction of Phosphine Oxides by 1,3-Diphenyl-Disiloxane. *Chem. - Eur. J.* **2017**, *23* (58), 14434–14438. https://doi.org/10.1002/chem.201703875.
(12) Miranda-Soto, V.; Grotjahn, D. B.; Cooksy, A. L.; Golen, J. A.; Moore, C. E.; Rheingold, A. L. A Labile and Catalytically Active Imidazol-2-Yl Fragment System. *Angew. Chem. Int. Ed.* **2011**, *50* (3), 631–635. https://doi.org/10.1002/anie.201005100.
(13) Toda, T.; Yoshinari, A.; Ikariya, T.; Kuwata, S. Protic N-Heterocyclic Carbene Versus Pyrazole: Rigorous Comparison of Proton- and Electron-Donating Abilities in a Pincer-Type Framework. *Chem. - Eur. J.* **2016**, *22* (46), 16675–16683. https://doi.org/10.1002/chem.201602552.
(14) Ruiz, J.; Perandones, B. F. Base-Promoted Tautomerization of Imidazole Ligands to N-Heterocyclic Carbenes and Subsequent Transmetalation Reaction. *J. Am. Chem. Soc.* **2007**, *129* (30), 9298–9299. https://doi.org/10.1021/ja073144n.
(15) Ruiz, J.; Sol, D.; Van der Maelen, J. F.; Vivanco, M. Base-Promoted Transmetalation Reactions of Protic N-Heterocyclic Carbenes and Acyclic Diamino Carbenes from Mn ^{I} to Au ^{I} : A Mechanistic Study. *Organometallics* **2017**, *36* (5), 1035–1041. https://doi.org/10.1021/acs.organomet.7b00009.
(16) Hansch, Corwin.; Leo, A.; Taft, R. W. A Survey of Hammett Substituent Constants and Resonance and Field Parameters. *Chem. Rev.* **1991**, *91* (2), 165–195. https://doi.org/10.1021/cr00002a004.

(17) Miranda-Soto, V.; Grotjahn, D. B.; DiPasquale, A. G.; Rheingold, A. L. Imidazol-2-Yl Complexes of Cp*Ir as Bifunctional Ambident Reactants. *J. Am. Chem. Soc.* **2008**, *130* (40), 13200–13201. https://doi.org/10.1021/ja804713u.

Chapter 3. REACTIVITY AND CATALYTIC CO_2 HYDROGENATION BY MONOMETALLIC RUTHENIUM BIS-(PROTIC N-HETEROCYCLIC CARBENE) PHOSPHINE LIGATED COMPLEXES

Significant portions of the following chapter have previously been published. Reprinted (adapted) with permission from Johnson, M. C., *et. al. Inorg. Chem.* **2021**, 60, 8, 5996–6003.

3.1 INTRODUCTION

Protic N-heterocyclic carbene (p-NHC) ligated organometallic complexes are of interest in small molecule activation and catalysis due to the potential for metal-ligand cooperativity facilitated by the proximity of the NH wingtip to the transition metal center. Additionally, the strong sigma donor character of p-NHCs makes them useful supporting ligands for reduction chemistry, particularly in hydrogenative catalytic transformations. While NHCs are a thoroughly studied ligand platform, the catalytic properties of the protic analogs have been less thoroughly examined. To the best of our knowledge, there are fewer than ten catalytic studies using p-NHCs, six of which are focused on hydrogenation or dehydrogenation catalysis. Three of these involve the direct hydrogenation of imines,[1] alkenes,[2] and carbonyls,[3] one is concerned with acceptorless dehydrogenation and dehydrogenative coupling,[4] and two focus on transfer hydrogenation-dehydrogenation of carbonyls[5,6] and alkenes.[6] In direct hydrogenation it has been proposed that p-NHCs are involved in the initial activation of H_2 between the metal center and the deprotonated NH-wingtip,[1] used as a molecular recognition unit for substrates via hydrogen

bonding,[2] or simply a spectator.[3] In these three cases, high yields are achieved, though relatively high catalyst loadings result in the highest turnover number (TON) being less than 40.[3]

The catalytic system studied herein was designed with two principal concepts in mind. First, two p-NHCs are installed *cis* to one another with nearly parallel NH-wingtips. The aim here is to increase the number of protons proximal to the site where hydrogenation occurs or to potentially act as a second site for metal-ligand cooperativity. Additionally, the strong sigma donating character and tris-chelating nature of the bis-carbene phosphine platform should endow this system with high thermal stability resulting in prolonged catalyst lifetimes. Previous work with this ligand platform examined stoichiometric reactivity with CO_2, formate, and bicarbonate.[7] Each of these reagents ultimately yields a carbamate complex (**6**), with the oxygen bound to the ruthenium metal center and the carbon bound through the deprotonated NH-wingtip. When formate is treated with the starting $[Ru(bpy)(MeCN)(P^{Ph}(p\text{-}NHC)_2)](PF_6)_2$ complex, **1**, the reaction proceeds through a dimeric formate-bridged intermediate before liberating H_2 gas and yielding **6**.

This observed stoichiometric activation of CO_2, as well as the tripodal geometry and strong sigma donor character of the ligand combine many common features of successful CO_2 hydrogenation catalysts. Leitner and coworkers reported the first homogeneous catalyzed direct hydrogenation of CO_2 to methanol using a ruthenium 1,1,1-tris(diphenylphosphinomethyl)ethane ("triphos") precatalyst.[8] The facial coordination of the triphos ligand increases the favorability of

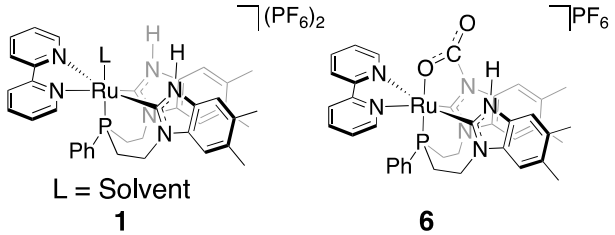

Figure 3.1. Catalyst **1** and the CO_2 adduct **6**.

hydride transfer to the carboxylate units and the high thermal stability of the ruthenium triphos complex is necessary for catalyst longevity under the harsh conditions required for the reaction to proceed. Additionally, several research groups have reported CO_2 activation between the metal center and the ligand framework, particularly with pincer ligands.[9–14] In these systems, CO_2 activation via metal-ligand cooperativity is reversible, and the so-formed CO_2 adducts are generally regarded as off-cycle catalytic intermediates. By examining CO_2 hydrogenation with our ruthenium bis-p-NHC phosphine complex (**1**), which combines tridentate facial coordination and strong sigma donating character, we aim to understand whether the dynamic proton binding and metal-ligand cooperation environment of the p-NHCs will be a benefit for efficient catalysis.

In this work, we evaluated complex **1** as a CO_2 hydrogenation catalyst. We observed a linear dependence between catalyst turnover and equivalents of base (relative to catalyst), with turnovers as high as 8,040 measured using 0.2 mM of catalyst. Identification of catalyst speciation following catalytic runs supports the hypothesis that the tridentate and strongly sigma donating p-NHC phosphine ligand creates a robust and long-lived catalyst and that catalysis is limited solely by the consumption of K_3PO_4. Mechanistic investigations were carried out and the reactivity of **1** with H_2 was investigated, which in the presence of base forms a unique hydride bridged dimer (**7**) with two symmetric hydrogen bonding pairs, each containing one p-NHC of opposing monomer units. Both **6** and **7** were investigated as possible catalytic intermediates, revealing details about the importance of metal-ligand cooperativity in the hydrogenation of CO_2.

3.2 Results and Discussion

3.2.1 *General Catalyst Screening*

In order to probe the catalytic activity of **1** for the hydrogenation of CO_2 to formate**,** a series of additives were screened at a ratio of 100 equivalents relative to catalyst **1** (4 mM in THF) using 20:60 bar CO_2:H_2 at 140 °C for 16 hours, as summarized in Table 3.1. The additives screened were tailored based on our knowledge of the stoichiometric reactivity of **1** with CO_2 and literature precedent, so basic conditions, as well as Lewis acids were used. The latter has been shown to stabilize relevant activated CO_2 and formate intermediates, thus facilitating catalysis (Table 3.1).[16,17]

With 100 equivalents of K_3PO_4, a TON of 92 was observed. When KPF_6 was used, the TON was suppressed to 4, indicating the important role of base for catalysis to proceed at an appreciable rate. When 100 equivalents of water were added in addition to 100 equivalents of K_3PO_4, catalysis was suppressed to a TON of 37, likely due to the equilibrium between K_3PO_4 and K_2PO_4H. The presence of water would shift the equilibrium towards K_2PO_4H, thereby inhibiting the catalysis that requires the deprotonation of the ligand or an intermediate. Additionally, the requirement for basic conditions was expected to be necessary since formic acid production is thermodynamically uphill from H_2 and CO_2, but the reaction becomes favorable in the presence of base to yield formate.[18] Amine bases also show decreased TONs compared to K_3PO_4. This allows us to hypothesize that the Brønsted basic and Lewis acidic properties of K_3PO_4 are complementary in the operative catalytic cycle.

Changing the ratio of CO_2 to H_2 while keeping the total pressure constant did not materially influence TON (Table 3.2, entries 1 and 3 at 80 bar and entries 2 and 4 at 40 bar). Decreasing the total pressure from 80 bar to 40 bar did cause a decrease catalytic activity by

roughly 10 TON (Table 3.2, entries 1 and 2). The higher catalytic activity associated with higher total pressures are attributed to more forcing catalytic conditions.

Table 3.5. Screening Additives

Cat	Additive (100 eq) [a]	TON [b]
1	K_3PO_4	92 [c]
1	DBU	23
1	KPF_6	4
1	K_3PO_4 + H_2O [d]	37

Conditions: 20 µmol catalyst, THF (5 mL), 16 hr, 140 °C, CO_2:H_2 (20:60 bar). [a] eq. rel. to catalyst. [b] Work up: centrifuge. [c] experiment run in triplicate. [d] 100 eq of K_3PO_4 and 100 eq of H_2O.

Table 3.6. Summary of catalytic results with variable total and partial pressures of CO_2 and H_2.

Entry	Cat.	Cat. µmol	CO_2:H_2 (bar)	Additive[a]	TON[b]
1	**1**	20	20:60	K_3PO_4 (100 eq)	92
2	**1**	20	10:30	K_3PO_4 (100 eq)	79
3	**1**	20	5:75	K_3PO_4 (100 eq)	89
4	**1**	20	20:20	K_3PO_4 (100 eq)	80
5	**1**	20	0:60	K_3PO_4 (100 eq)	2
6	**1**	20	20:0	K_3PO_4 (100 eq)	0.5

Conditions: THF (5 mL), 16 hr, 140 °C. [a] eq. rel. to catalyst. [b] Work up: centrifuge.

One hypothesis being considered for these bis-(p-NHC) phosphine ligated complexes was that the electron donating and withdrawing properties of the ancillary ligand may influence their catalytic activity. Screening the library of 4,4'-bis-substituted bipyridine ligated complexes revealed that under the catalytic conditions screened, the ancillary ligand had no significant influence (Table 3.3). Catalyst **1** was selected as the system of interest over **3** to pursue the

Table 3.7. Ancillary ligand library screening.

Cat	TON [a]
1a	92
1b	92
1c	94
3	92

Conditions: 20 μmol catalyst, THF (5 mL), 100 eq K_3PO_4, 16 hr, 140 °C, CO_2:H_2 (20:60 bar). [a] Work up: centrifuge. [c] experiment run in triplicate. [d] 100 eq of K_3PO_4 and 100 eq of H_2O.

remainder of the catalytic study in order to isolate the single reactive site on the ruthenium metal center adjacent to p-NHC moieties.

When K_3PO_4 was used as an additive in variable equivalents relative to **1**, nearly stoichiometric equivalents of product to base were observed (Table 3.4 and Figure 3.2). When 9,900 equivalents of K_3PO_4 were added, 8,040 equivalents of formate were produced. A control experiment revealed a slow background reaction with K_3PO_4 in the absence of catalyst, but by comparing molar equivalents of product formed to base we observe a 13-fold increase with catalyst (Table 3.4). This well documented background reaction is attributed to formate being thermodynamically downhill from CO_2 and H_2, and under the forcing conditions used here the reaction is able to proceed at a measurable rate.[18,19] Screening for higher TONs was prohibited by the physical constraints of the reactors and the insoluble nature of the K_3PO_4 and potassium formate product. Because the TONs correlate with the equivalents of K_3PO_4 present, we sought further evidence that the TON was being limited solely by the consumption of K_3PO_4.

Examination of the change in pressure over the course of the reaction shows a steady decrease in pressure corresponding to the consumption of CO_2 and H_2. After a period of time, for example after 5 hours with 1000 eq K_3PO_4, the change in pressure reaches a plateau, indicating an abrupt end to the reaction at approximately 1000 TON (Figure 3.3). This observation suggests that the change in pressure can be used to estimate turnover frequencies, which in the case of 1000 eq of K_3PO_4 is 193 h^{-1}. In addition, Na_3PO_4 was screened as an additive at 1000 eq relative to catalyst, and the reaction proceeds at a significantly slower rate than in the presence of 1000 eq K_3PO_4, with a TON = 550 and a TOF = 34 hr^{-1} (Table 3.5 and Figure 3.4). Quantification following the use of Na_3PO_4 was challenging due to the nature of the product, which formed a partially soluble gel in D_2O. In the presence of some gel, quantification by NMR using the dimethylformamide internal standard showed a TON = 550. The sample was then transferred into a J Young tube and heated at 85 °C for 48 hours. Analysis by NMR following heating showed a TON = 4,057. While quantification was challenging, the results are on the order of magnitude expected relative to K_3PO_4 and it was not pursued further.

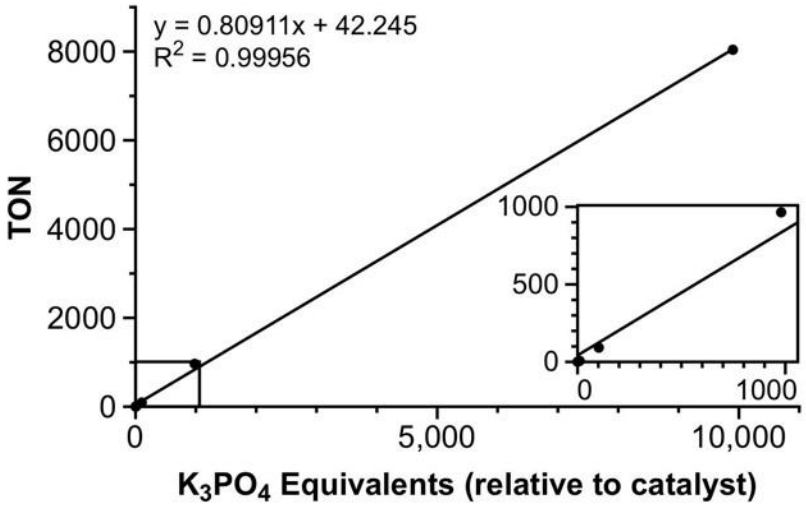

Figure 3.2. Linear relationship between equivalents of K_3PO_4 and TON with catalyst **1**.

Table 3.8. Screening equivalents of K_3PO_4 and control experiment

[Cat]	Eq K_3PO_4 (mmol K_3PO_4)	TON (mmol Prod.)	Molar Ratio[e]
4 mM	10[c] (0.2)	7 (0.14)	0.70
4 mM	100[c] (2.0)	92 (1.83)	0.92
4 mM[a]	980[c] (19.8)	965 (19.49)	0.98
0.2 mM[b]	9,900[c,d] (9.9)	8,040 (8.04)	0.81
0	- (2.0)	- (0.14)	0.07

Conditions: catalyst **1**, THF (5 mL), 140 °C, 16 hr, 20 bar CO_2, 60 bar H_2. [a] THF (7mL). [b] 500 µL of a 2.0 mM catalyst solution in THF. [c] Experiments were run in triplicate. [d] At 0.2 mM the reaction rate decreased and was run for 4 days. [e] The molar ratio of formate product to K_3PO_4 additive was used as a metric to compare the role of the catalyst versus the control run in the absence of catalyst.

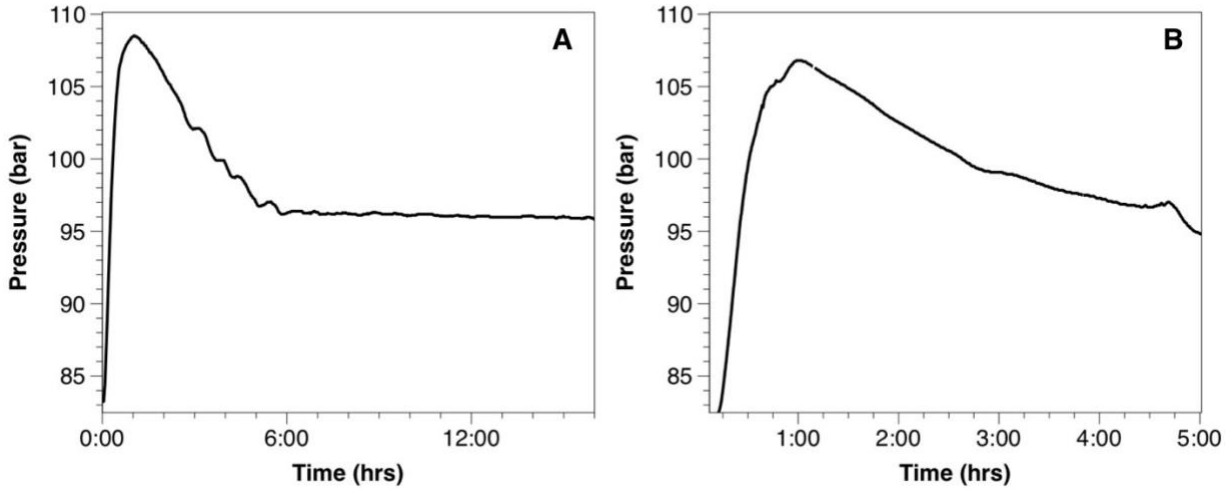

Figure 3.3. Representative pressure change data logged for catalysis using 1,000 eq of K_3PO_4 relative to catalyst over 16 hours with a total pressure change of 12 bar (A) and 5 hours with a total pressure change of 11 bar (B).

Table 3.9. Impact of alkali metal on catalysis.

Additive	TON	TOF (hr^{-1})
K_3PO_4	965	193
Na_3PO_4	550 (4057[a])	34 (253[a])

Conditions: Cat. **1** (20 µmol), 1,000 eq Additive, THF (7 mL), 16 hr, 20 bar CO_2, 60 bar H_2,140 °C.
[a] After heating to fully solubilize the gel formed in D_2O.

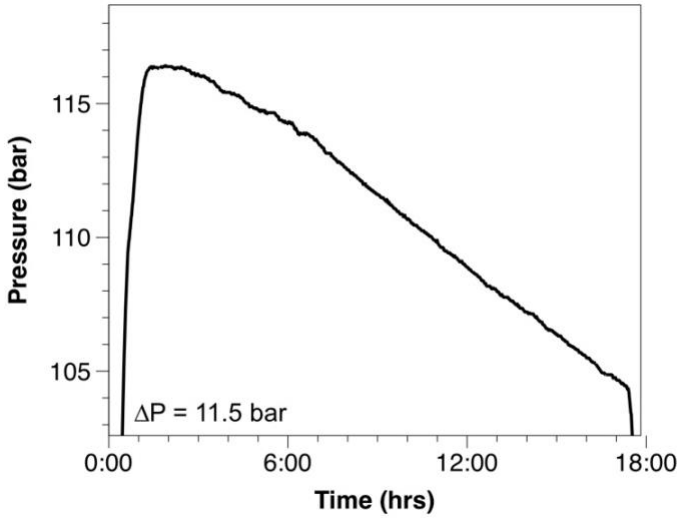

Figure 3.4. Pressure change data logged for catalysis using 1,000 eq of Na_3PO_4 with a total pressure change of 11.5 bar over the course of 16 hours (20 µmol **1**, 7 mL THF, 20 bar CO_2, 60 bar H_2, 140 °C).

3.2.2 *Catalyst Speciation*

In order to probe the fate of **1**, the reaction mixtures were analyzed following catalytic runs and work up by centrifugation of the reaction mixture to separate the insoluble (phosphate and formate) components, which were then dissolved in D_2O after the organics were decanted away. In the aqueous portion we routinely observed an orange precipitate settle out of solution. This orange precipitate was assigned as **6** via NMR spectroscopy, with a ^{31}P NMR resonance at 45 ppm and a ^{1}H NMR spectrum that overlays exactly with independently synthesized **6** (Figures 3.5 and 3.6). This assignment was confirmed by X-ray crystallography (Figure 3.7). When the organic portion was analyzed, two peaks were observed in the ^{31}P NMR spectrum at 25 ppm and

50 ppm in CD_2Cl_2. We propose that the peak at 50 ppm corresponds to the starting catalyst **1** with the open coordination site either bound by solvent (THF) or formate (Figure 3.8A). We have previously reported the independently synthesized formate bridged dimer with a ^{31}P NMR shift of 52 ppm in CD_2Cl_2 (Figure 3.8B).[7] We hypothesize that the peak at 25 ppm corresponds to a complex with the carbenes no longer coordinated to the metal center, Ru-PR_3, possibly due to non-innocent reactivity of H_2 with the p-NHCs, yielding the uncoordinated benzimidazole arms (Figure 3.8A). The Ru-PR_3 complex was previously isolated en route to the complete metalation of the ligand via thermally driven tautomerization and is bound solely through the phosphine of **L**. It is characterized by a ^{31}P NMR shift of 24 ppm in CD_3CN (Figure 3.8B).[7] These species are depicted in Figure 3.9A.

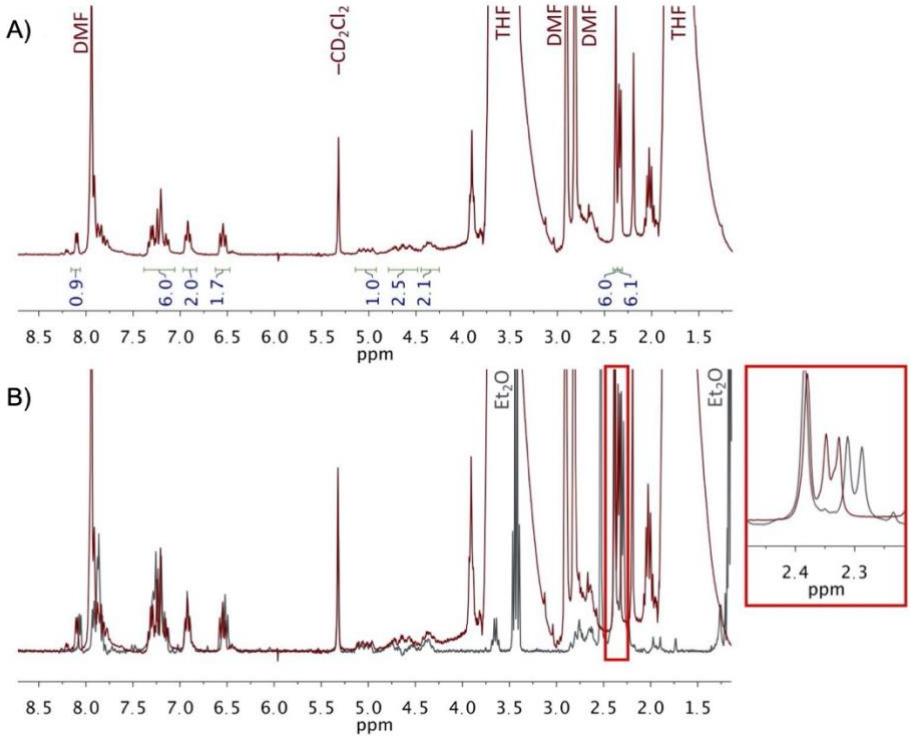

Figure 3.5. (A) ^1H NMR (CD_2Cl_2, 300 MHz, 298K) of **6** isolated from catalytic reaction run under standard conditions. DMF is from use as an internal standard for product quantification prior to catalyst isolation. (B) ^1H NMR (CD_2Cl_2, 300 MHz, 298K) of **6** isolated from catalytic reaction (red) overlain with ^1H NMR (CD_2Cl_2, 300 MHz, 298K) of independently synthesized **6**.

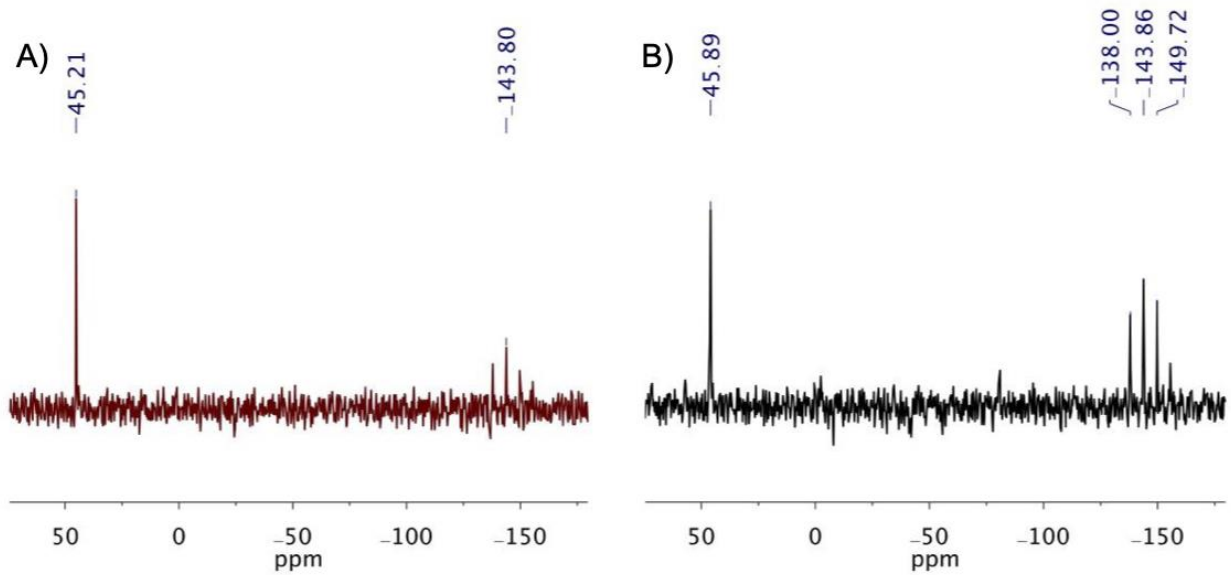

Figure 3.6. (A) ^{31}P NMR (CD_2Cl_2, 121 MHz, 298K) of **6** isolated from catalytic reaction run under standard conditions. (B) ^{31}P NMR (CD_2Cl_2, 121 MHz, 298K) of independently synthesized **6**.

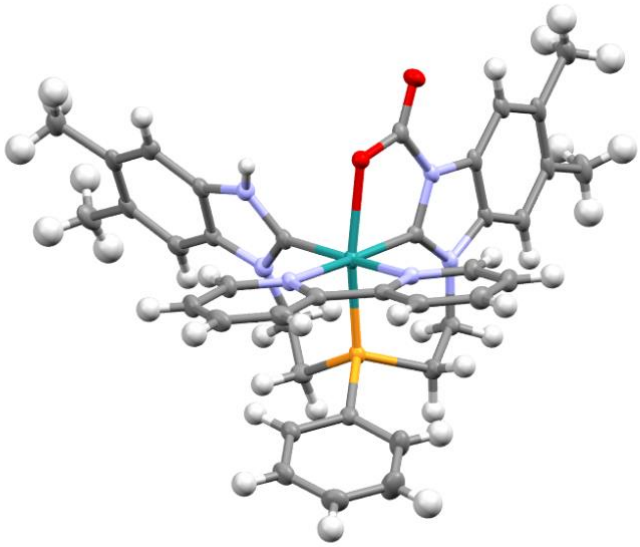

Figure 3.7. Molecular structure of **6** with thermal ellipsoids shown at 50% probability with hydrogen atoms removed for clarity, in addition to two dichloromethane molecules, one dimethyl sulfoxide molecules, and one hexafluorophosphate anion.

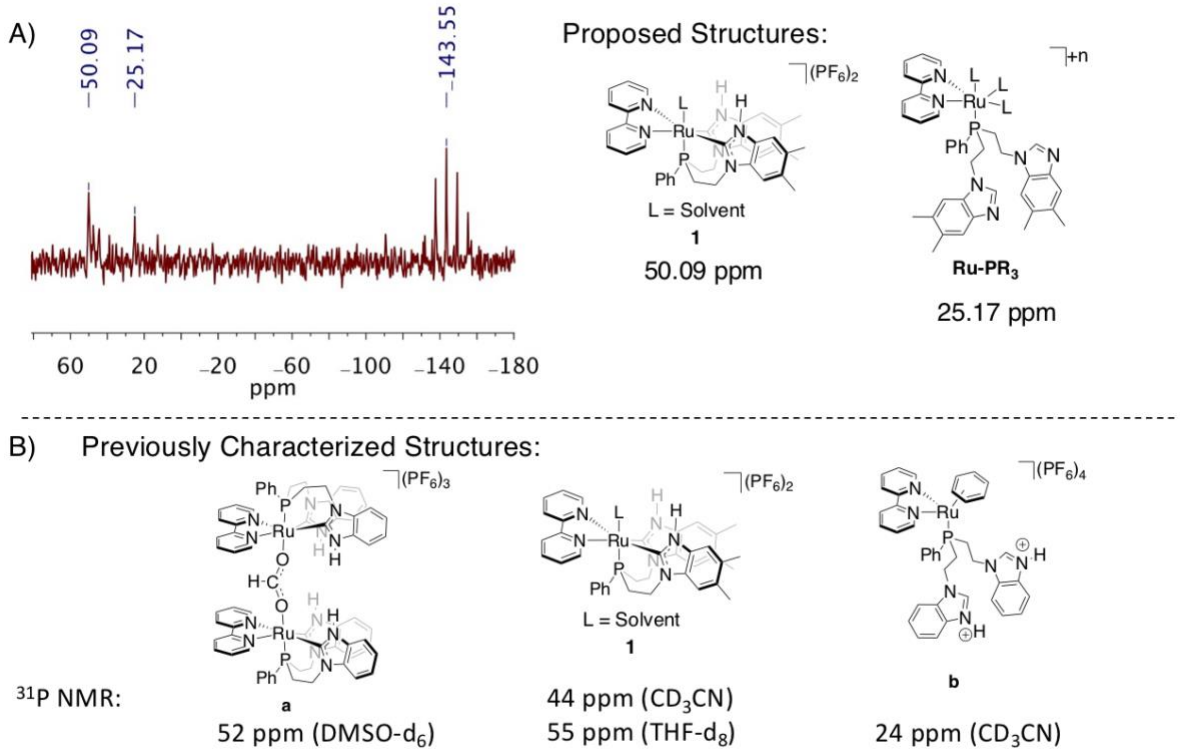

Figure 3.8. (A) ^{31}P NMR (CD_2Cl_2, MHz, 298K) and proposed structures for the peak at 50.09 ppm and at 25.17 ppm. The signal at -143.55 ppm corresponds to $(PF_6)^-$. (B) ^{31}P NMR data for previously characterized complexes **a**, **1**, and **b** used to predict structures in part A.[1]

When **1** is treated under standard catalytic conditions in THF with 100 equivalents of K_3PO_4 and the vessel is charged with 20 bar CO_2, the only ^{31}P NMR signals observed are at 45 ppm and 50, 52, and 54 ppm, the latter of which are likely due to different binding environments at the open coordination site of **1** (Scheme 3.1 and Figure 3.10). When this is repeated using 60 bar H_2, the only peaks observed in the ^{31}P NMR are at 52 ppm and 25 ppm, confirming that the peak at 25 ppm is due to reactivity with the H_2 (Scheme 3.2 and Figure 3.11). Notably in all of these experiments, we do not observe any free ligand or intractable solids that would indicate ruthenium decomposition, supporting the claim of the robust nature of **1** as a catalyst. These results are summarized in Figure 3.8B.

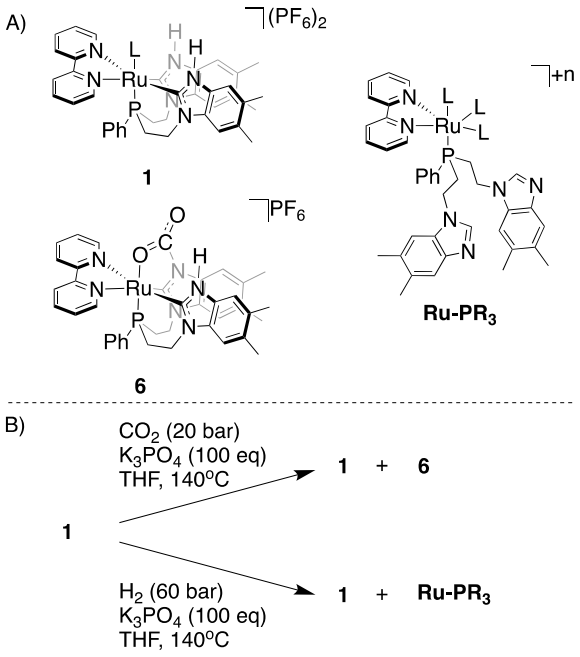

Figure 3.9. A) Major catalyst speciation products following catalysis. B) Catalyst speciation distribution observed under conditions with only CO_2 or only H_2.

Scheme 3.1. Speciation of **1** following standard catalytic conditions with only CO_2 and no H_2.

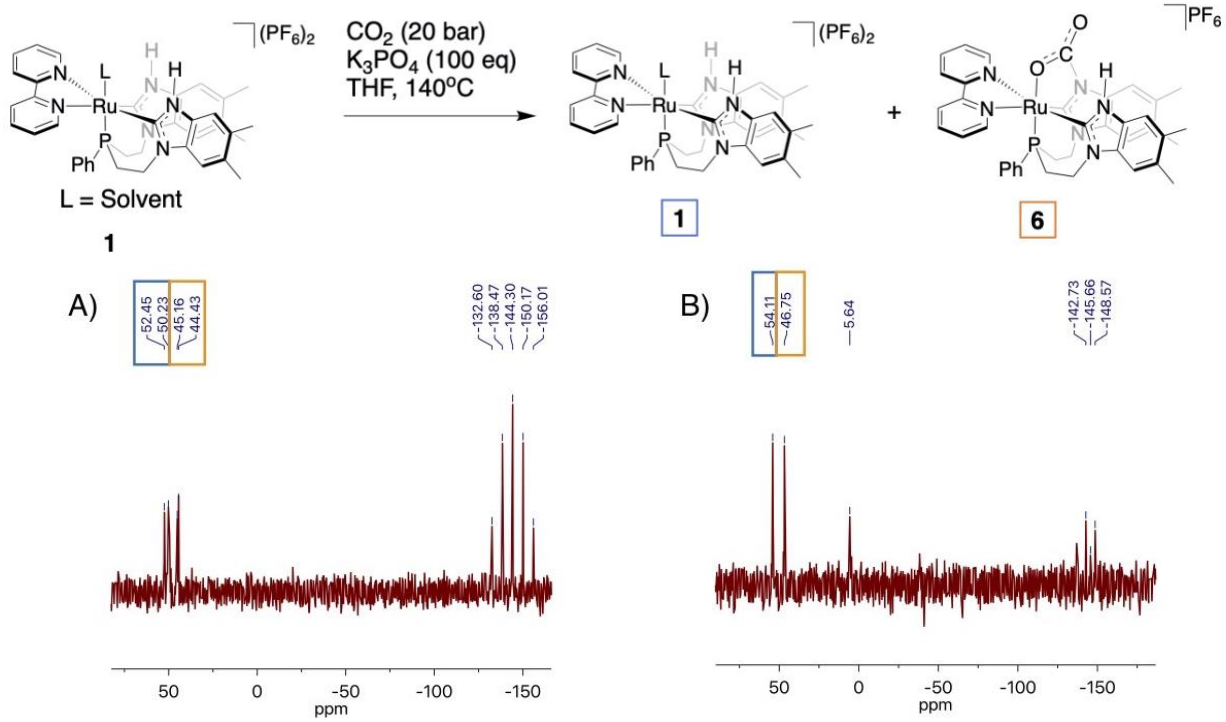

Figure 3.10. Catalyst speciation under standard catalytic conditions charging only with CO_2. Characterization by ^{31}P NMR (CD_2Cl_2, 121.48 MHz, 298K) of (A) the concentrated organic portion following work up and (B) the concentrated aqueous portion following work up, with the peak at 5 ppm corresponding to K_3PO_4.

Scheme 3.2. Speciation of **1** following standard catalytic conditions with only H_2 and no CO_2.

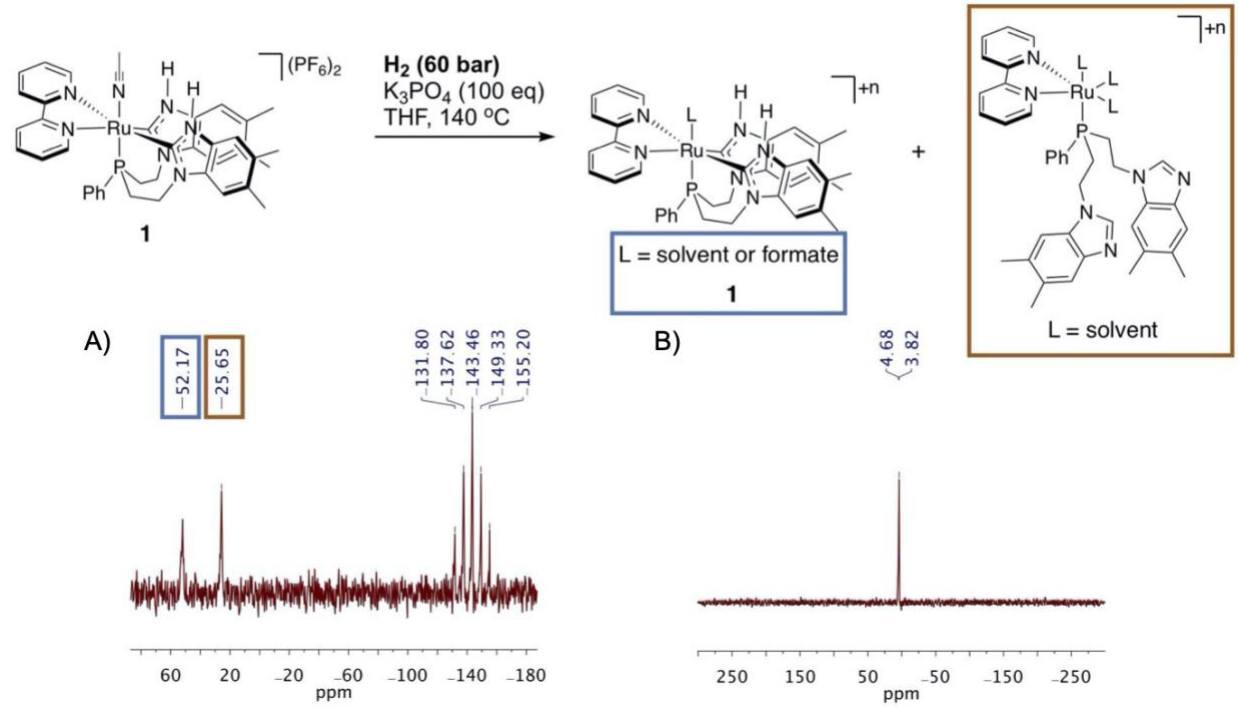

Figure 3.11. Catalyst speciation under standard catalytic conditions charging only with H_2. Characterization by ^{31}P NMR (CD_2Cl_2, 121.48 MHz, 298K) of (A) the concentrated organic portion following work up and (B) the concentrated aqueous portion following work up, with the peak at 5 ppm corresponding to K_3PO_4.

3.2.3 *Mechanistic Investigation*

Deprotonation of the NH-wingtips is expected to play a central role in catalysis through metal ligand cooperation. Two pathways are plausible following the initial deprotonation; either reaction with hydrogen to form a hydride complex (**7**) or reactivity with CO_2 to form the carbamate complex (**6**) (Figure 3.12). These pathways have been investigated and will be discussed in detail. In the PNHC literature there are a number of examples of hydrogen being split between the metal center and a deprotonated NH-wingtip.[5,20] In our system we have previously reported the facile formation of **6** via activation of CO_2 between the metal center and the deprotonated NH-wingtip,[7] reminiscent of CO_2 activation through metal ligand cooperativity in pincer ligand chemsitry.[9–13]

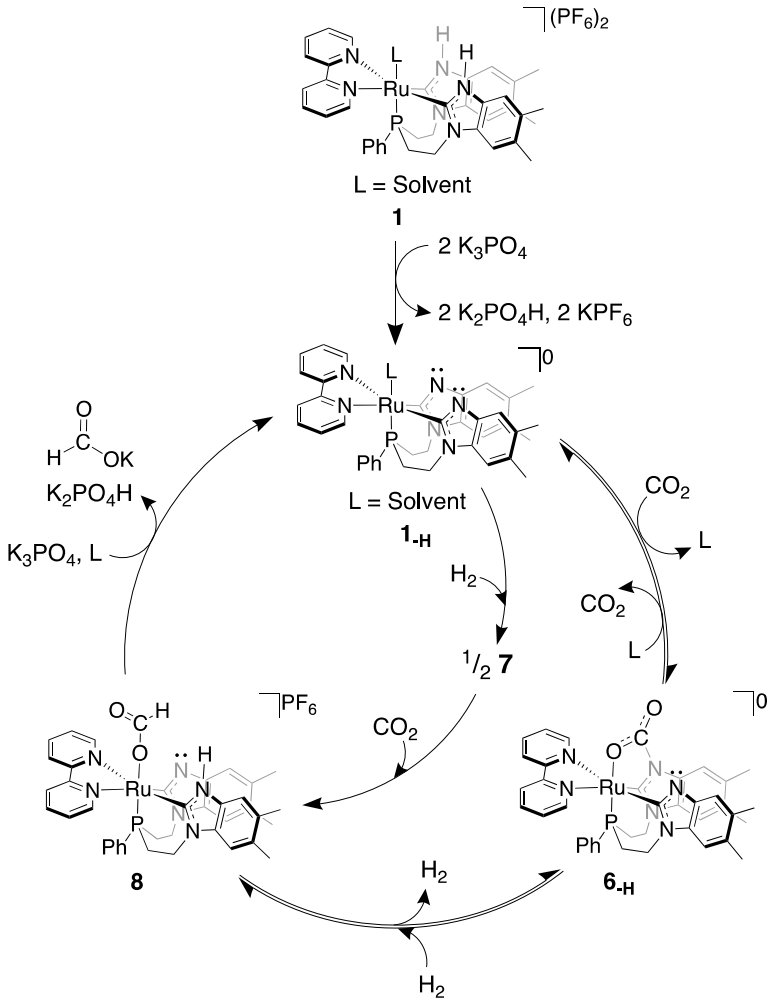

Figure 3.12. Proposed catalytic pathways for the hydrogenation of CO_2 to formate by **1**.

When 13 equivalents of K_3PO_4 were added to a solution of complex **1** in THF-d_8 and stirred at room temperature for 1 hour, there was a complete disappearance of peaks corresponding to the NH-wingtips, a shifting in the methyl region, and a shifting of the aromatic peaks. The ^{31}P NMR spectrum showed a shift from 54 ppm to 48 ppm. Together, these results indicate complete deprotonation of the NH-wingtips to form the doubly deprotonated species (**1**$_{-H}$**)**. Upon heating at 100 °C for 1.5 hours, the ^{31}P NMR spectrum shows the persistence of the peak corresponding to the deprotonated species, suggesting that **1**$_{-H}$ remains stable in THF with excess K_3PO_4.

When **6** was treated in the same manner as above, little change was observed. With the addition of K_3PO_4 there was a disappearance of the ^1H NMR peak corresponding to the NH-wingtip, but no change in the remainder of the spectrum, suggesting that there is an equilibrium occurring between the phosphate and the PNHC. Heating at 100 °C for 1.5 hours also shows no significant transformation, which is corroborated by ^{31}P NMR spectroscopy. This suggests that the pKa of the phosphate conjugate acid is close to that of the NH-wingtip in **6**.

When a sample of **6** with ^{13}C labeled CO_2 incorporated was dissolved in THF-d_8 and pressurized with 8 bar H_2 no reaction was observed, even after heating to 100 °C for 24 hours (Scheme 3.3 and Figure 3.13). When this was repeated in the presence of excess K_3PO_4 a reaction occurs at elevated temperatures. Tracking by ^{31}P NMR spectroscopy, we began to see a new peak form at 32 ppm after 1 hr at 100 °C. After an extended period of time at room temperature we see the peak at 32 ppm persist, a gradual loss of signal at 45 ppm (**6**) and the appearance of a new peak at 51 ppm, likely corresponding to complex **1** (Scheme 3.3 and Figure 3.14). Additionally, by ^1H NMR spectroscopy we see the peaks corresponding to the methyl groups on the benzimidazole shift (Figure 3.15). Simultaneously, a solid precipitated from the solution. The precipitate was isolated and evaluated by ^1H NMR spectroscopy in D_2O. A doublet appears at 8.45 ppm with a $^1J_{CH}$ = 194 Hz, which is evidence of formate with the ^{13}C labeled CO_2 incorporated (Figure 3.16). This coupling constant is consistent with that of $H^{13}CO_2Na$ taken independently in D_2O.

Scheme 3.3. Treatment of ^{13}C labeled **6** with H_2 gas with and without K_3PO_4.

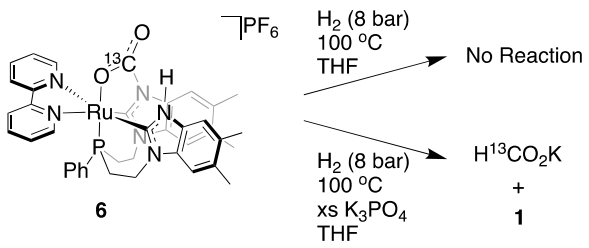

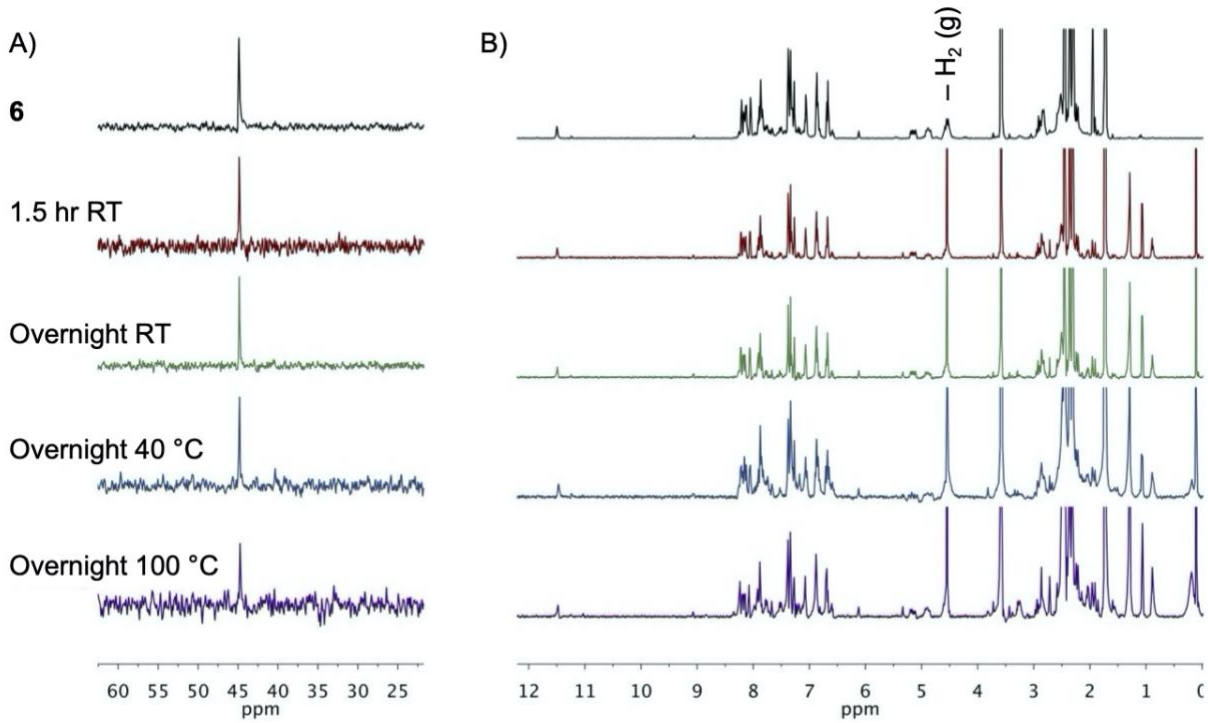

Figure 3.13. Reactivity of ^{13}C labeled **6** with H_2. (A) ^{3} NMR (THF-d_8, 121.48 MHz, 298K) of 1-$^{13}CO_2$ with the peak at -44.8 ppm remaining unchanged. (B) ^{1}H NMR (THF-d_8, 300.10 MHz, 298K) of 1-$^{13}CO_2$ with H_2 gas (4.45 ppm) remaining unchanged over the course of the reaction.

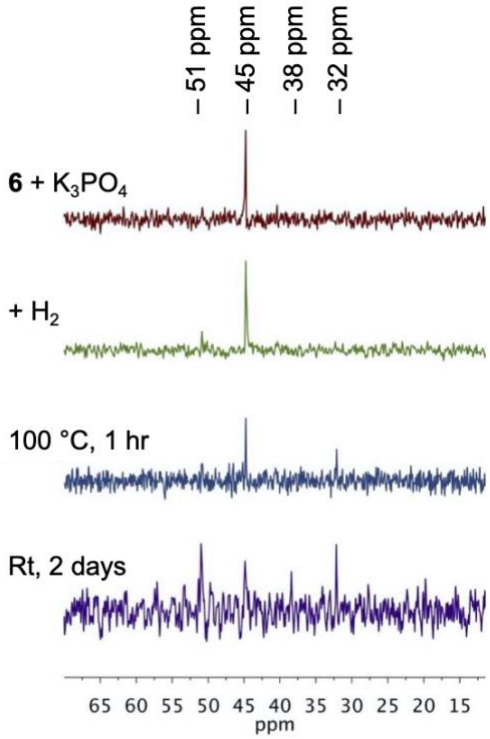

Figure 3.14. ^{31}P NMR (THF-d_8, 202.29 MHz, 298K) of **6** tracking changes in the reaction with H_2 and K_3PO_4.

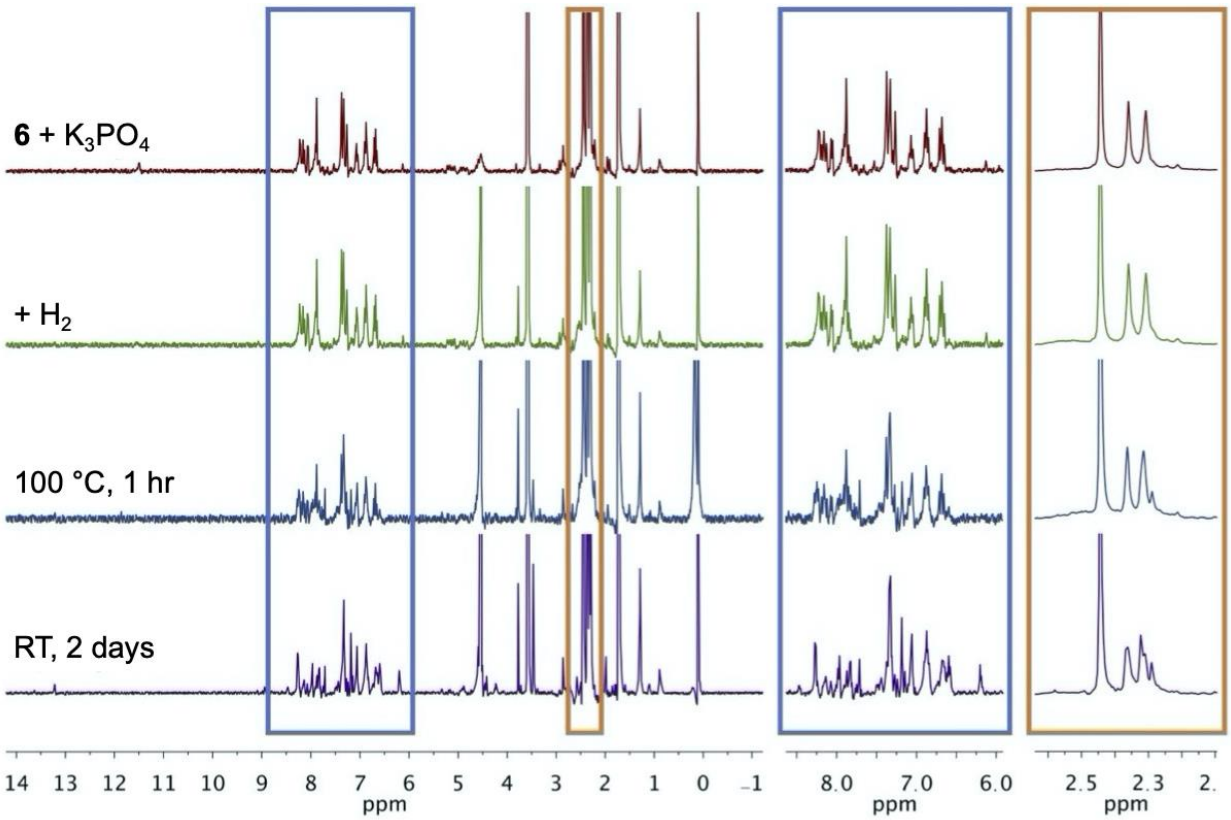

Figure 3.15. ^{1}H NMR (THF-d_8, 499.72 MHz, 298K) of **6** tracking changes in the reaction with H_2 and K_3PO_4, with the aromatic region (blue) and the benzimidazole methyl group region (orange) highlighted.

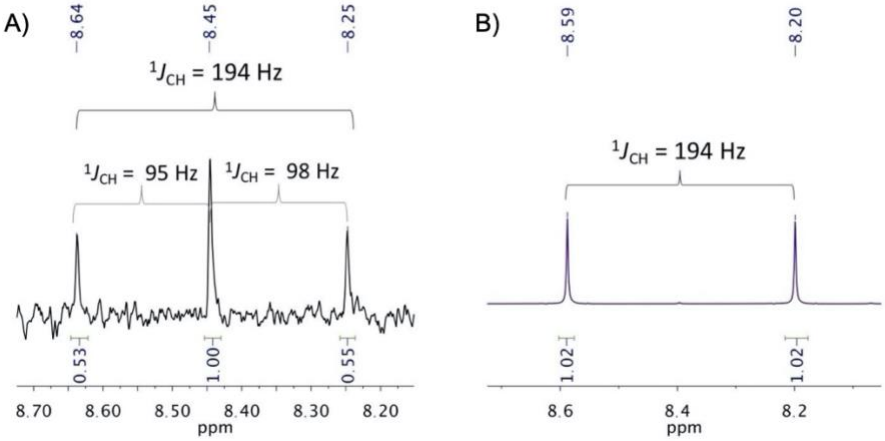

Figure 3.16. (A) ^{1}H NMR (D_2O, 499.7 MHz, 298K) of the precipitate formed after reaction of **6** with H_2 and K_3PO_4. The *J* coupling constants suggest that the observed peaks are not a triplet, but rather a singlet at 8.45 ppm and a doublet at 8.44 ppm with a $^{1}J_{CH}$ constant of 194 MHz, which is consistent with the $^{1}J_{CH}$ of $H^{13}CO_2^-$. (B) ^{1}H NMR (D_2O, 499.7 MHz, 298K) of $H^{13}CO_2Na$ taken independently.

The observation that K_3PO_4 is required for the reactivity of **6** with H_2 reveals that the role of the K_3PO_4 is not limited to the deprotonation of the NH-wingtips. Once CO_2 is bound, the potassium could be required as a Lewis acid to (I) aid in the dissociation of the charge balanced potassium formate product and/or (II) stabilize the activated CO_2 and weaken or break the ruthenium-oxygen bond and provide an open site for hydrogen activation.[16,17] Alternatively, the phosphate may be necessary to help with the activation of the H_2. Previous reports have illustrated the deprotonation of the metal-bound hydrogen directly,[19,21] or, specifically in p-NHC literature, activation of hydrogen between the metal center and the deprotonated NH-wingtip has been observed.[1,5,20]

Scheme 3.4. Temperature dependence for catalytic CO_2 hydrogenation.

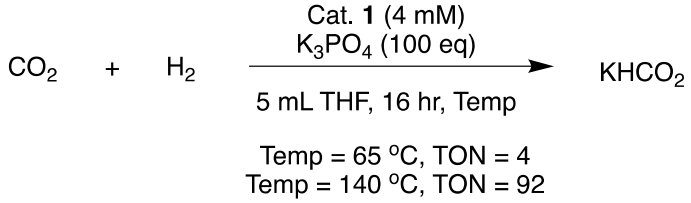

Table 3.10. Screening catalytic precursors.

Catalyst	Eq of K_3PO_4	TON
1	100	92
1	1000	965
6	100	99
7	1000	981

Conditions: 20 µmol catalyst, THF (5 mL), 16 hr, 140 °C, CO_2:H_2 (20:60 bar).

To probe the dissociation of CO_2, ^{13}C labeled **6** was heated in THF-d_8 to 105 °C and monitored by NMR spectroscopy. After heating, a small amount of free $^{13}CO_2$ at 125.8 ppm was observed in the ^{13}C NMR spectrum in addition to the peak corresponding to **6** at 156.4 ppm, confirming gradual dissociation of $^{13}CO_2$ at elevated temperature, though the equilibrium lies towards coordinated CO_2 (Figure 3.17). When ^{13}C labeled **6** was heated only to 90 °C no free

$^{13}CO_2$ is observed by ^{13}C NMR spectroscopy, indicating that the CO_2 is only labile above 90 °C (Figure 3.18). Notably, when the standard catalytic conditions were changed to decrease the temperature from 140 °C to 65 °C, we saw a corresponding decrease in TON from 92 to 4 (Scheme 3.4). When the run at 65 °C was analyzed for catalyst speciation, a significant amount of **6** was identified by the characteristic ^{31}P NMR peak at 45 ppm. Together, these data support the hypothesis that high temperature is required for labilizing CO_2 in **6**, which is likely important for catalysis to proceed. Attempts at methylation of the NH-wingtip to block the coordination of CO_2 and directly validate the role of metal ligand cooperativity in the CO_2 activation pathway observed here have been made, however the synthesis has so far been unsuccessful. It should be noted that when independently synthesized **6** is used as the precatalyst, catalytic activity is maintained (Table 3.6).

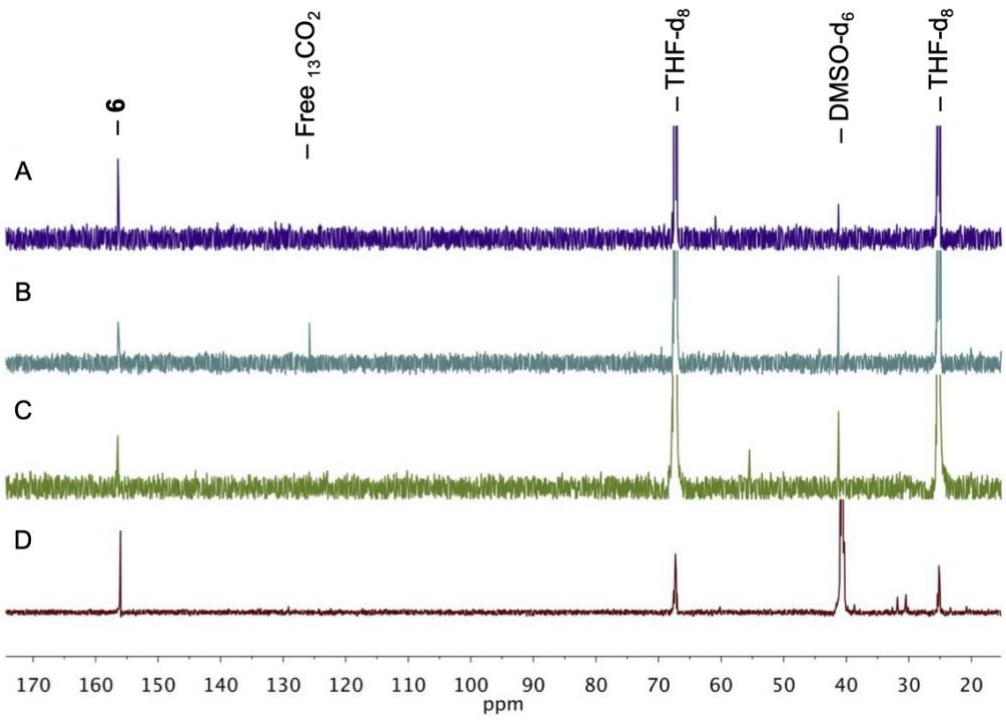

Figure 3.17. (A) ^{13}C NMR (THF-d_8, 176.02 MHz, 298K) of ^{13}C labeled **6** before heating to 105°C. (B) ^{13}C NMR (THF-d_8, 176.02 MHz, 298K) of ^{13}C labeled **6** after heating to 105°C and cooling back to 25°C. (C) ^{13}C NMR (THF-d_8, 176.02 MHz, 298K) of supernatant above orange crystals that formed at room temperature. (D) ^{13}C NMR (DMSO-d_6, 176.02 MHz, 298K) of isolated orange crystals.

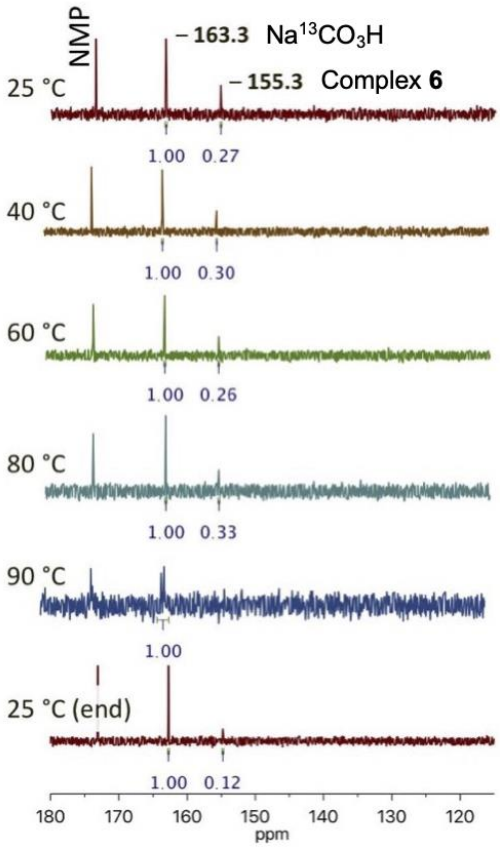

Figure 3.18. Variable Temperature ^{13}C NMR (CD_2Cl_2, 176.02 MHz, 298K) of ^{13}C labeled **6** in 2,5-dimethyltetrahydrofuran, NMP, and CD_2Cl_2. T1 was estimated to be 8.658 seconds and d1 was set to be 43.3 seconds.

Additionally, the coordination of **6** was probed using cyclic voltammetry (Figure 3.19). At a scan rate of 1000 mV/s in acetonitrile, a single oxidation feature is observed, with two returning reduction features, indicating that there is an equilibrium process occurring in the oxidized state. As scan rate is decreased, a second oxidation feature comes more prominent and the more oxidatively shifted reduction becomes more prominent, providing further evidence of an equilibrium process. The proposed process, shown in Figure 3.19, proceeds when **6** (A) is oxidized (C) and the Ru–O bond is broken due to the loss of electron density, forming the Ru^{III}-pendant carbamate (D). The reduction features observed are D to B at the more oxidative potential and C to A at the more reductive potential. Performing this experiment in non-

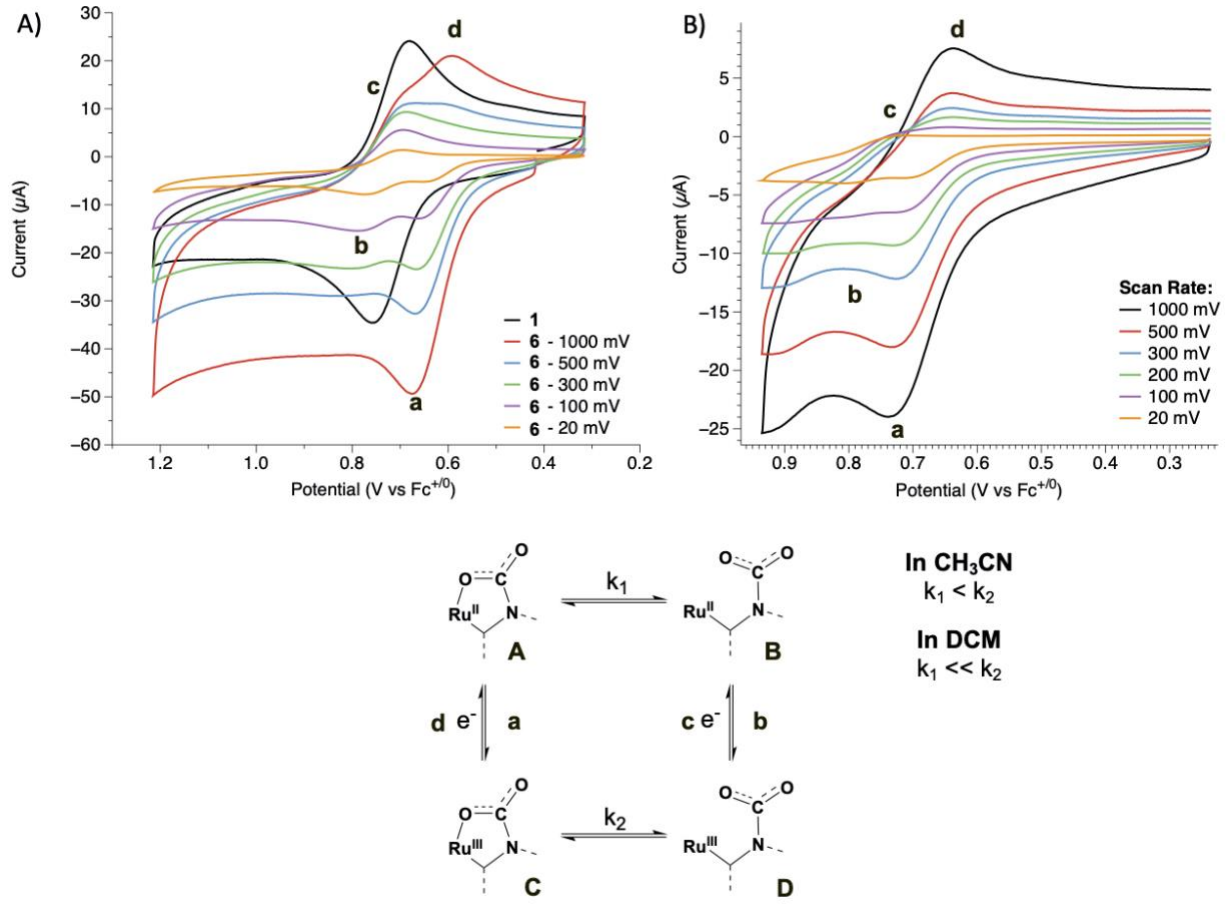

Figure 3.19. Cyclic voltammetry performed on **6** at different scan rates in (A) coordinating and (B) non-coordinating solvent, revealing an equilibrium between full coordination of CO_2 of types A and C and activation at only the PNHC-nitrogen of types B and D. A) 0.2 M $(NtBu_4)PF_6$ in CH_3CN, Glassy Carbon (working), Pt (counter), Ag (pseudo reference). B) 0.2 M $(NtBu_4)PF_6$ in DCM, Glassy Carbon (working), Pt (counter), Ag (pseudo reference).

coordinating solvent (DCM) shows a much slower equilibrium process occurring, which is expected as coordinating solvent would help to stabilize the metal center in B and D.

Based on these results, **6** has been shown to be catalytically relevant. Formate has been observed in situ via NMR spectroscopy following reactivity **6** with H_2 in the presence of K_3PO_4, indicating that the CO_2 in **6** is capable of being incorporated into the product. The coordinated CO_2 becomes labile around 100 °C, which is likely a contributing factor for the high temperatures required for catalytic activity. We can conclude that the formation of **6** does not

inhibit catalysis under our standard conditions. Another possible catalytic route is through reactivity first with H_2. The insertion of CO_2 into a metal-hydride bond is a common pathway for the hydrogenation of CO_2.[18]

Following literature precedent,[5,20] the hydride complex, **7**, was targeted by deprotonation of **1** with either stoichiometric KOtBu or excess K_3PO_4, followed by reaction with an atmosphere of hydrogen gas. Over the course of ten days the reaction between $\mathbf{1}_{\text{-}\mathbf{H}}$ and H_2 reached completion (Scheme 3.5). A triplet in the ^1H NMR spectrum at -9.3 ppm (with a J_{PH} coupling constant of 37 Hz) indicates the formation of a hydride *trans* to two equivalent phosphine ligands (Figure 3.20B). This is further confirmed by $^1H\{^{31}P\}$ NMR spectroscopy; the resonance at -9.3 ppm is observed as a singlet. This suggests the formation of a hydride-bridged dimer. Additionally, a peak is present at 20.2 ppm in the ^1H NMR spectrum. This strongly deshielded peak is suggestive of a proton hydrogen bonded between two nitrogen atoms of the p-NHCs (*vide infra*). The four distinct peaks corresponding to the methyl groups of the benzimidazole backbone indicate that the ligand arms are in two distinct environments. This assignment has been confirmed by X-ray crystallography (Figure 3.20A). In addition to confirming the hydride-centered dimer, only one PF_6^- counterion was observed, indicating an overall charge of +1 for **7**. This is consistent with two of the four p-NHCs being deprotonated and is supported by the integration observed in the ^1H NMR for the hydride peak at -9.3 ppm (1 hydrogen) and the peak at 20.2 ppm (2 hydrogens).

Scheme 3.5. Synthesis of **7**.

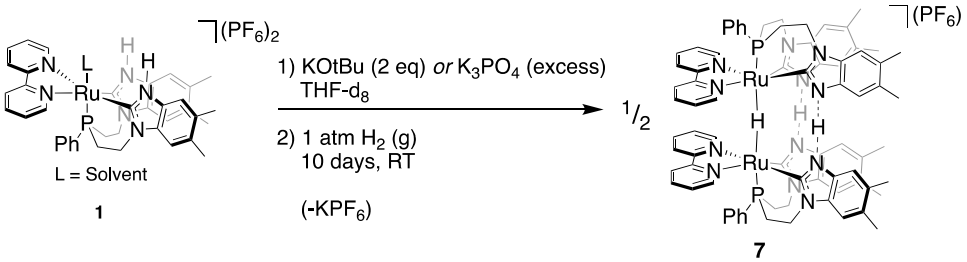

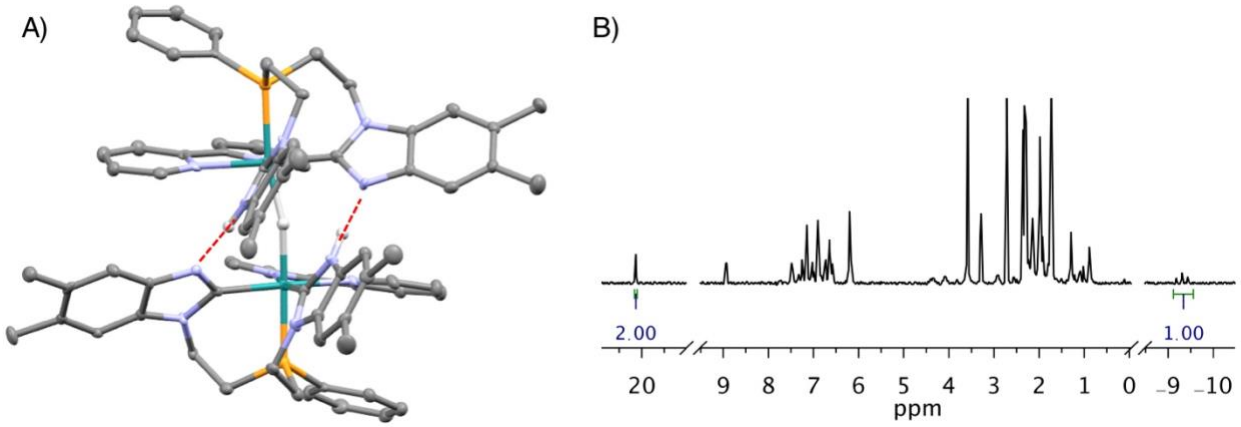

Figure 3.20. A) Molecular structure of **7** with thermal ellipsoids shown at 50% probability. Solvent of crystallization (THF), PF_6^- counter ion, and all hydrogen atoms except the metal-bound hydride and the ligand N-H protons are removed for clarity. Electron density was observed between the associated nitrogen atoms and the disorder model was used to place the N-H protons in ideal geometry at half-site occupancy. B) ^{1}H NMR (THF-d_8, 300 MHz, 298 K) spectrum of **7**, with integrations for the hydride peak at -9.3 ppm (J_{PH} = 37 Hz) and the N-H protons at 20.2 ppm.

To further corroborate the assignment of **7** as a dimer in solution, DOSY NMR spectra of **1** and of **7** were obtained (Figures 3.21 and 3.22). A comparison of the diffusion coefficients of **1** and **7** are consistent with the assignment of **7** as a dimer. Using the Stokes-Einstein relation,

$$D = \frac{kT}{6\pi r\eta}$$

where,

$$r = \left(\frac{3(MW)}{4\pi N\rho}\right)^{1/3}$$

and D = diffusion coefficient, k = Boltzman Constant, T = temp (K), η = solvent viscosity, MW = molecular weight, N = Avogadro's Number, r = molecule radius, and ρ = density, we find that,

$$D \propto \frac{1}{MW^{1/3}}$$

and,

$$D^3 \propto \frac{1}{MW}$$

Based on this relationship, the known molecular weights of **1** and **7**, and the experimental diffusion coefficient of **1**, the diffusion coefficient of **7** was estimated:

$$\frac{(D_1)^3}{(D_3)^3} = \frac{\left({}^1/_{MW_1}\right)}{\left({}^1/_{MW_3}\right)}$$

$$\frac{(6.5 \times 10^{-6})^3}{(D_3)^3} = \frac{\left({}^1/_{1019.76}\right)}{\left({}^1/_{1567.59}\right)}$$

$$\frac{2.75 \times 10^{-16}}{(D_3)^3} = 1.5$$

$$D_3 = 5.68 \times 10^{-6}$$

The DOSY spectrum of **7** is complicated by overlapping peaks and minor peak misalignment. However, determining the diffusion coefficient based on the peaks that are solitary and well aligned gives a diffusion coefficient that is consistent with the calculated estimated diffusion coefficient for the dimer structure.

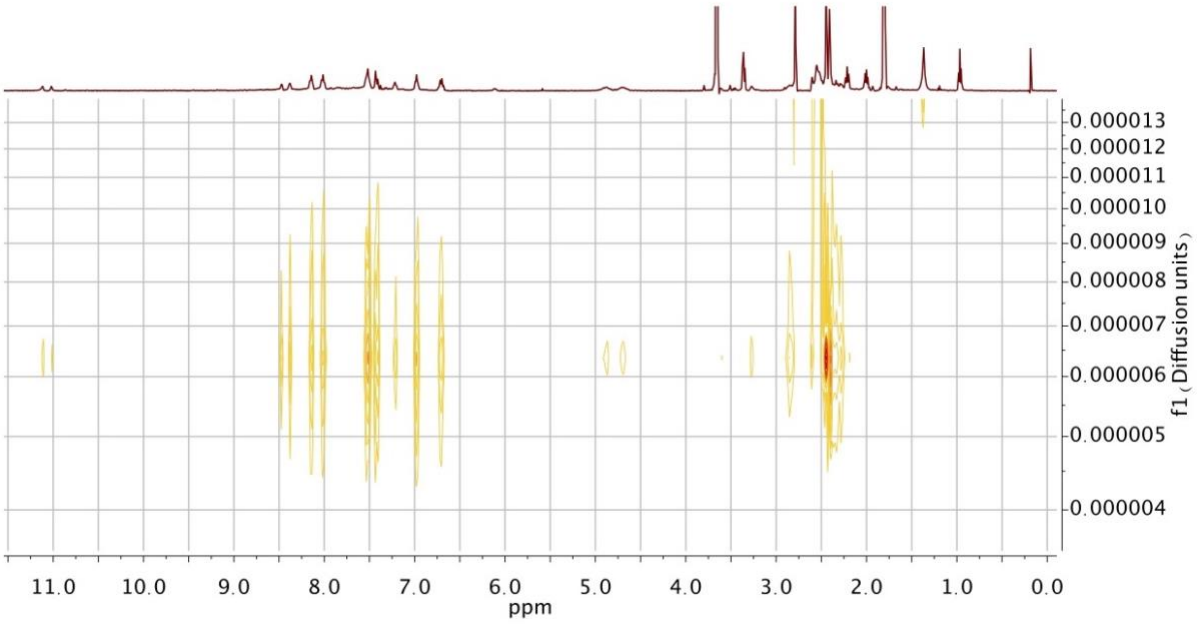

Figure 3.21. DOSY spectra of complex **1** in THF-d_8 at 298K. The diffusion coefficient is found to be 6.5 x 10^{-6} cm^2/s.

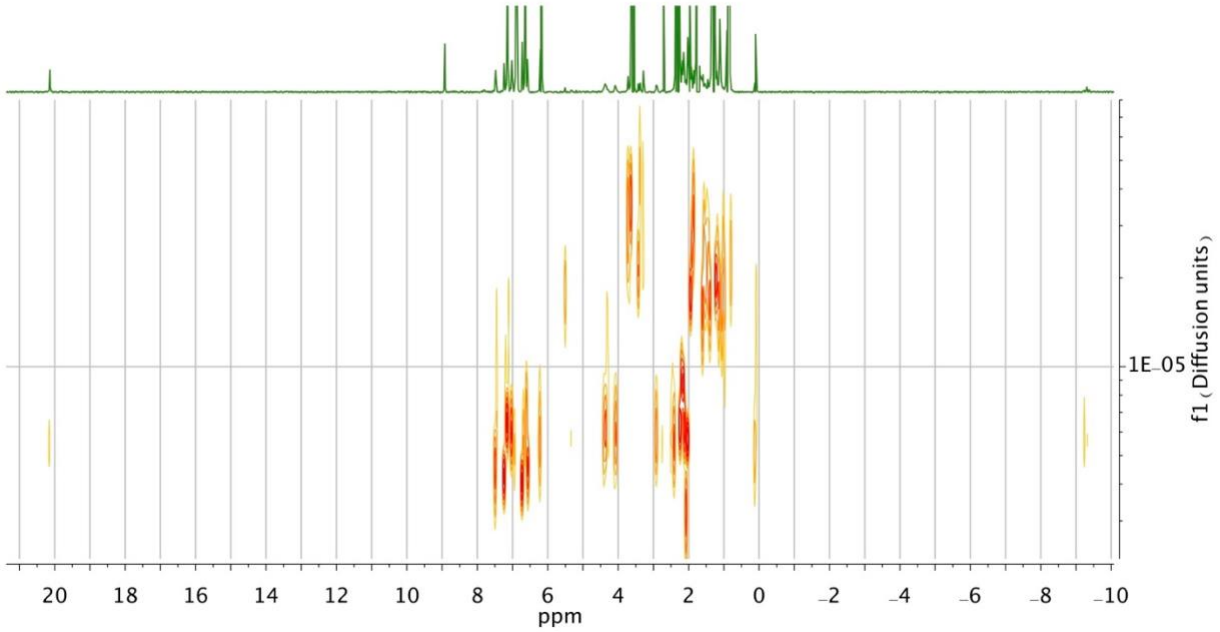

Figure 3.22. DOSY spectra of complex **7** in THF-d_8 at 298K. The diffusion coefficient is found to be 5.5 x 10^{-6} cm^2/s.

Chemical shifts around 20 ppm in diamagnetic ^{1}H NMR spectra are not common. However, it is known within the p-NHC literature that the addition of a hydrogen bonding acceptor causes the resonance corresponding to the NH-wingtip to shift downfield.[2,22] Furthermore, hydrogen bonding in proteins has been studied by ^{1}H NMR spectroscopy, and characteristic chemical shifts are associated with different types of hydrogen bonding. It is observed that symmetrical hydrogen bonds, referred to as single-well hydrogen bonds, have characteristic ^{1}H NMR shifts of 20-22 ppm.[23,24] Single-well hydrogen bonds are the strongest type of hydrogen bonds, and the proton lies linearly and equidistant between the heteroatoms. In strong hydrogen bonding, the bond between hydrogen and the heteroatom is longer relative to the normal covalent length and shorter than the normal hydrogen bonding length. The typical heteroatom separation for N---H---N in a single well hydrogen bond is 2.6 to 2.7 Å.[24] In the case of **7**, the distance between both sets of nitrogen atoms that are oriented towards one another is 2.7 Å, which is consistent with the literature and further supports the claim of two protons

hydrogen bonded in these positions. This leads to an environment where the proton is uniquely deshielded.[24]

Complex **7** can also be synthesized as a minor product through reaction with NaH, as has been demonstrated in an analogous system containing one p-NHC ligand.[4,5] When NaH is added incrementally to **1**, the evolution of hydrogen gas is first observed by the appearance of a singlet at 4.54 ppm in the ^{1}H NMR spectrum in THF-d_8, along with a decrease in intensity (for 1 equivalent NaH) and eventual disappearance (2 equivalents) of the NH-wingtip peak. The presence of **7** is first indicated by the peak at 20.1 ppm in the ^{1}H NMR with the addition of 1 equivalent of NaH. With the addition of the second equivalent of NaH, the hydride triplet at -9.3 ppm begins to grow in, and with the addition of a third equivalent the peaks at 20.1 and -9.3 ppm persist and the ^{31}P NMR peak at 38 ppm indicates that **7** is one of three major products.

Previous reports of reactivity between PNHC complexes with both H_2 gas and NaH involve systems containing a bidentate phosphine PNHC ligand with Cp or Cp* supporting ligands.[4,5,20] In these reports, the hydride resonance appears as a doublet with $^{2}J_{HP}$ ranging from 28.4 Hz to 36.5 Hz, indicating a terminal hydride *trans* to a phosphorus atom. Additionally, the NH-wingtips in these systems are observed in their typical ^{1}H NMR regions. The differences in reactivity observed in the present system, primarily the formation of a bridging hydride and the symmetrical hydrogen bonding, may be in part explained by the lack of steric congestion at the metal center. The bipyridine ligand leads to a relatively flat and open face in **1**, which may enable the formation of the dimer **7**. In addition, the dimer is further stabilized by p-p stacking between the two center benzimidazole rings, between the bipyridine rings, and between the phenyl and bipyridine rings, as is evident from the X-ray crystallography (Figures 3.23 and

3.24). These stabilizing forces may contribute to the differences in reactivity observed between the system studied presently and the analogous literature examples.[4,5]

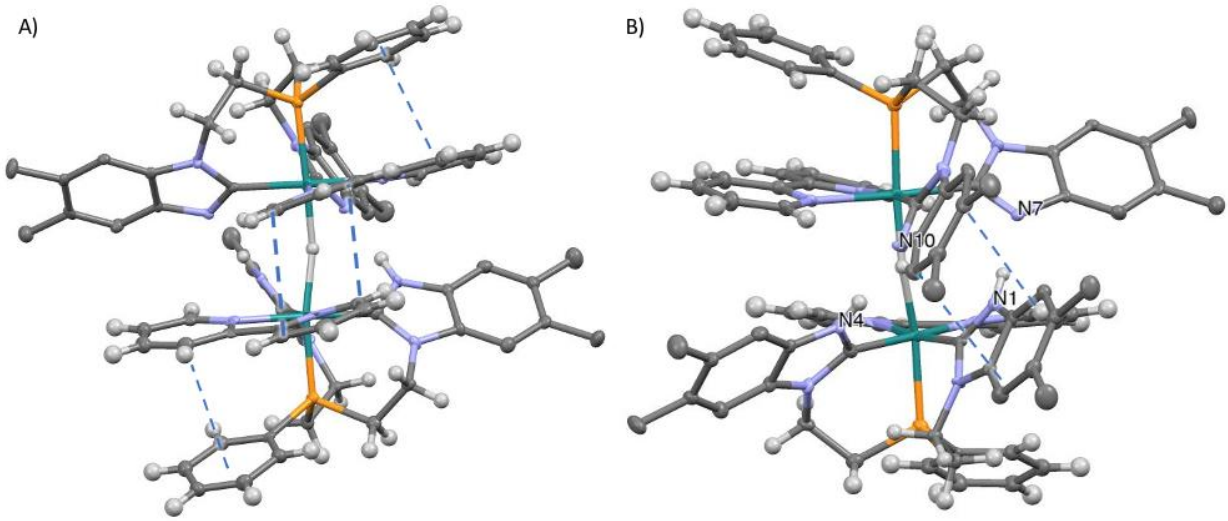

Figure 3.23. Regions of p-p stacking are illustrated, highlighted by blue dotted lines. A) Crystal structure of **7** from the perspective showing the bipyridine rings and the phenyl rings. B) Crystal structure of **7** from the perspective showing the central benzimidazole ligand arms.

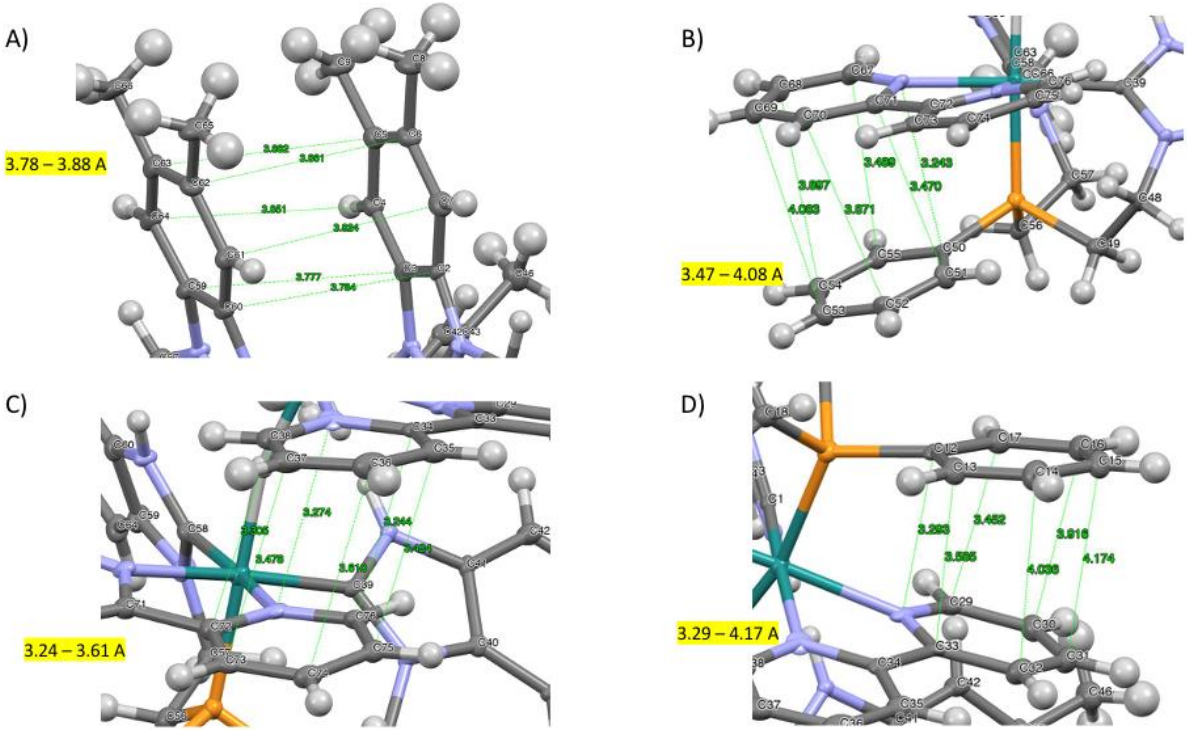

Figure 3.24. Distances between pi-pi stacking aromatic rings in **7** are shown for (A) the central benzimidazole ligand arms, (B) one pair of phenyl ring and bipyridine ring, (C) two bipyridine rings, and (D) the second pair of phenyl ring and bipyridine ring.

When **1** was exposed to hydrogen gas in the absence of base, no reaction occurred after an extended period of time (4 days) at room temperature. Heating at 60 °C for 2 hours and 20 minutes showed partial decomposition of the PF_6^- counter ion to $PO_2F_2^-$, evident by ^{31}P NMR spectroscopy by the presence of a triplet at -13 ppm ($^1J_{PF}$ = 971 Hz) which is consistent with the literature.[25] Upon cooling, this triplet disappeared, and the proton NMR is restored to its previous state, indicating a reversible reaction (Figure 3.25).

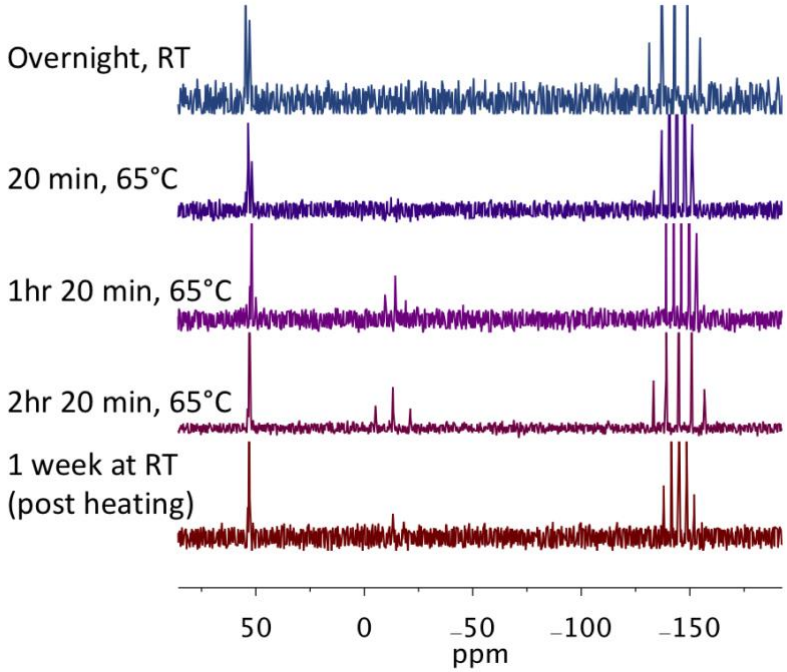

Figure 3.25. ^{31}P NMR data (THF-d_8, 121.48 MHz, 298 K) showing to decomposition of the PF_6 anion at -144.99 ppm (*sept*, $^1J_{P\text{-}F}$ = 716 Hz) to PO_2F_2 anion at -13 ppm (*t*, $^1J_{PF}$ = 971 Hz).

The reaction of **7** and CO_2 first leads to the full disappearance of the peak at 20.1 ppm, indicating that the symmetrical hydrogen bond has been disrupted. Additionally, there is a shifting of the hydride peak from -9.3 ppm to -9.7 ppm and a gradual decline in peak intensity, suggesting the consumption of the hydride (Figure 3.26 and 3.27). After 4 hours at room temperature there is a small peak growing in at 11.5 ppm, which is consistent with a typical NH-wingtip signal. After 24 hours, the signal for the peak at 11.5 ppm has increased and there is a

small peak at 13.2 ppm, which is consistent with the formate bound complex previously identified by our group.[7] The formate bound complex has been observed in the solid state as a formate bridged dimer.[7] This suggests that one possible catalytic pathway involves the insertion of CO_2 into the Ru-H-Ru bond. The reaction of **7** with $^{13}CO_2$ led to the formation of a precipitate. The precipitate was dissolved in DMSO-d_6 and characterized by NMR spectroscopy as **6**, which is consistent with our previous study of the formate dimer complex which is capable of liberating hydrogen gas to yield **6**.[7] When **7** was isolated and used as the precatalyst, it showed comparable catalytic activity to **1** (Table 3). As such, both **6** and **7** are viable precatalysts. When catalytic speciation was evaluated following the run with **7**, peaks at 38 ppm and 24 ppm in the ^{31}P NMR are revealed, consistent with previously identified catalyst speciation (Figure 3.9).

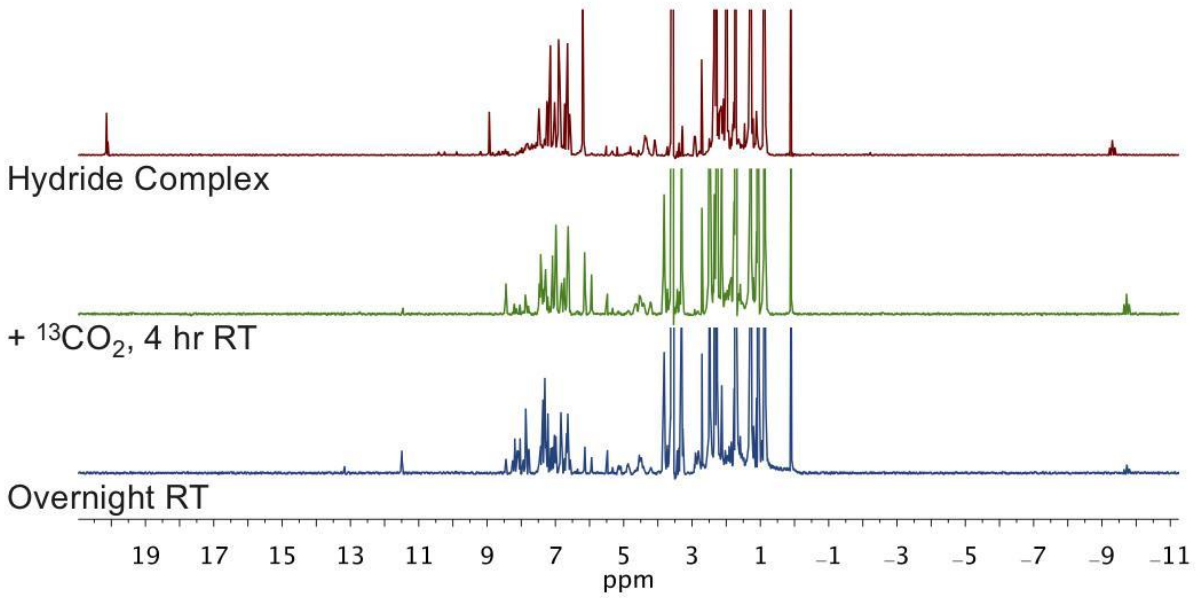

Figure 3.26. ^{1}H NMR of the reaction of **7** with $^{13}CO_2$.

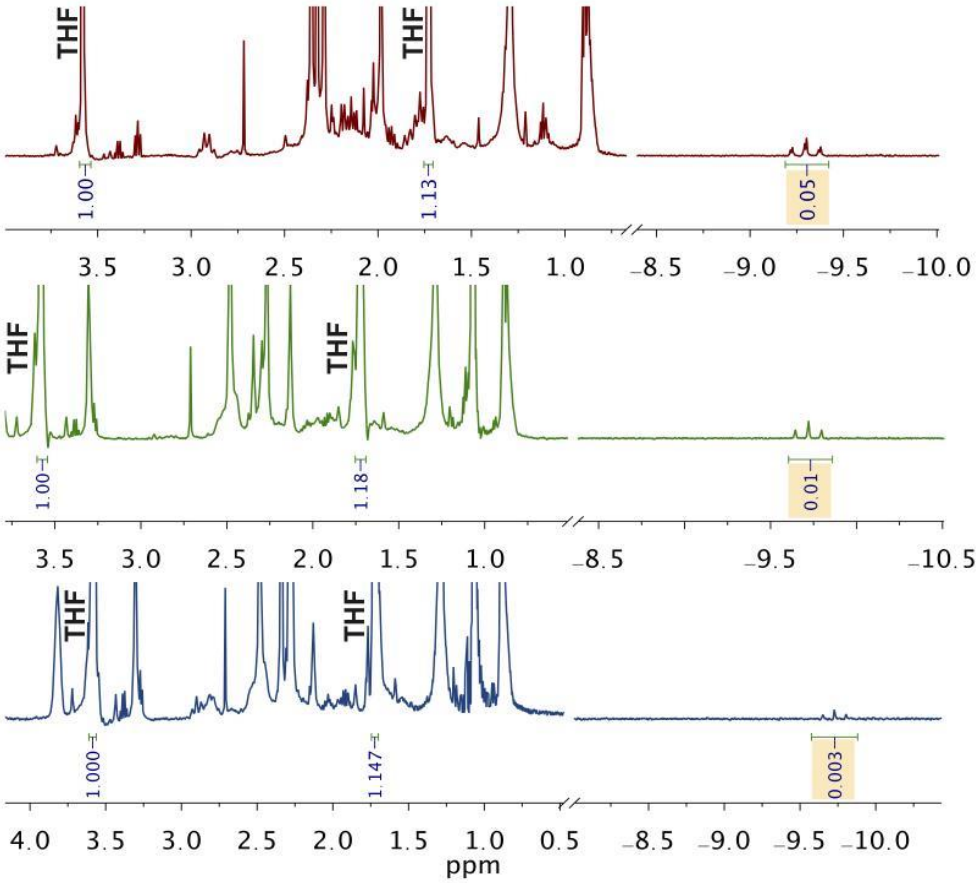

Figure 3.27. Integration of the hydride peak referenced to the solvent confirming the decreasing concentration of **7**.

Given the insights gained from the stoichiometric studies, it is proposed that the reaction proceeds first through the deprotonation of the NH-wingtips, converting **1** to **1-H** (Figure 3.12). K_3PO_4 is also required for the extrusion of formate from the catalyst, likely due to the Lewis acidic properties of K^+. Complex **6** is readily formed from the addition of CO_2 to **1-H** and is isolated from the reaction mixture following catalysis indicating that it is likely a resting state on the catalytic cycle or an easily accessible off cycle species. Complex **6** becomes labile around 100 °C, which is likely a contributing factor for the required high temperatures to achieve appreciable catalytic turnover. When **6** is treated with H_2 gas in the presence of K_3PO_4, potassium formate is formed with incorporation of the coordinated CO_2 into the product. Deprotonation of the NH-wingtips is also required for **1** to react with H_2 gas, forming the hydride

bridged dimer **7**. When **7** is treated with CO_2 there is evidence by ^1H NMR spectroscopy of the formation of the formate coordinated complex, in addition to the formation of **6**. This is consistent with the known reactivity of the formate complex, which releases H_2 gas to form **6**, and thus indicating this is a reversible step in the catalytic cycle.[7] Based on the stoichiometric studies, it is observed that **6** forms far more readily than **7**, with the latter transformation reaching completion over the course of 7 days. In addition, the prevalence of **6** as the product in a number of stoichiometric transformations, as well as its isolation as a dominant product post-catalysis, supports its existence as a low energy resting state. Based on these observations, we propose that catalysis likely proceeds through **6** as the dominant pathway, however both pathways are feasible especially under the catalytic conditions. Studying the catalytic speciation following the conclusion of the reaction shows no significant catalyst degradation, with all the isolated species on or readily accessible from the catalytic cycle and no evidence of free ligand or ruthenium decomposition. This, along with the linear dependence of TON on the molar equivalence of K_3PO_4, suggests an incredibly robust and long-lived catalyst.

3.3 CONCLUSIONS

Complex **1** has been demonstrated to be a robust catalyst for the hydrogenation of CO_2 to formate, limited only by the consumption of stoichiometric K_3PO_4, achieving a TON of 8,040. In our p-NHC system, stoichiometric base also contributes to the formation of **6** and **7**, both of which have been shown to be relevant to the catalytic cycle. The TONs are only limited by the consumption of K_3PO_4, as is evident by the lack of catalyst decomposition observed by studying the catalyst speciation, as well as the linear dependence of TON on the molar equivalence of K_3PO_4. It is proposed that the strong sigma donation of PNHCs lends to the stability of the

catalyst. The hydrogenation of CO_2 to formate likely proceeds though **6** as the dominant pathway, though under the catalytic conditions both proposed pathways are likely operative.

3.4 EXPERIMENTAL

3.4.1 *General Information*

All manipulations were carried out under an N_2 atmosphere, either in a glovebox or using Schlenk technique, unless otherwise noted. THF, CH_2Cl_2, Et_2O, and CH_3CN were purchased from Fisher Scientific and dried on a solvent purification system. N-methyl-2-pyrrolidinone (NMP, anhydrous, 99.5%), 2,5-dimethyltetrahydrofuran (mixture of *cis* and *trans* 96%, dried over CaH_2 and stored in glovebox), ammonium hexafluorophosphate (NH_4PF_6, 99.98% trace metals basis), mesitylene, *N*,*N*-dimethylformamide (DMF), 1,8-diazabicyclo[5.4.0]undec-7-ene (DBU, 98%), potassium hexafluorophosphate (KPF_6), $NaH^{13}CO_2$, tribasic potassium phosphate (K_3PO_4), and iodomethane (99%) were purchased from Sigma-Aldrich. CO_2 (Research 5.0 grade) and H_2 (Research 5.0 grade) were purchased from Airgas Inc. Deuterated NMR solvents were purchased from Cambridge Isotope Lab Inc. Unless manipulations were performed in air, all NMR solvents were dried over CaH_2, vacuum transferred, and stored in the glovebox over molecular sieves. THF-d_8 was purchased in ampules and used without further purification. ^1H, ^{13}C, and ^{31}P NMR were recorded on either a Bruker AV300, Bruker AV301, Bruker AV 500, or Bruker AV700 spectrometer. All DOSY spectra were collected on a Bruker AV 500 spectrometer in THF-d_8 at 298 K using a basic STE DOSY pulse sequence. The gradient dimension was acquired over 32 evenly spaced data points from 5% to 95% gradient strength at 16 scans each. Scans were run using a T1 delay of 30 s and a DOSY gradient pulse Δ delay of 150 ms.

[Ru(C_6H_6)(bpy)(OTf)](OTf) and 1-*N*-(chloroethyl)-5,6-dimethylbenzimidazole were

synthesized according to literature procedures.[1] For studies involving complex **6** that was independently synthesized, **1** was treated with sodium formate or ^{13}C labeled sodium formate according to the literature.[1] Modifications have been made to the literature procedure of **1** and P^{Ph}(1-*N*-ethyl-5,6-dimethylbenzimidazole)$_2$ (**L**) and the new preparation will be discussed in the synthesis section.

3.4.2 *Synthesis and Characterization*

Synthesis of μ-H[Ru(bpy)(P^{Ph}(p-NHC)(NHC)](PF$_6$) (7). In a glovebox, complex **1** (95 mg, 0.0932 mmol) and K_3PO_4 (99 mg, 0.4664 mmol) were dissolved in THF (3 mL). The reaction mixture was degassed and stirred under an atmosphere of H_2 (g) for 11 days. The reaction mixture was then filtered through a PTFE syringe filter and stirred with Et_2O (5 mL) for 5 minutes. The precipitate was allowed to settle, and the supernatant was decanted off, concentrated and washed with pentane. The product was isolated from the supernatant as a dark brown powder. Yield: 34% (51 mg). ^1H NMR (THF-d$_8$, 300 MHz, 298 K) δ 20.13 (s, 2H), 8.93 (d, *J* = 5.52, 2H), 7.48 (t, *J* = 7.67, 2 H), 7.15 (s, 4 H), 7.05-7.00 (m, 2H), 6.92 (s, 1H), 6.90 (s, 2H), 6.87 (s, 2H), 6.74 (d, *J* = 5.37, 2H), 6.67-6.56 (m, 8H), 6.20 (m, 10H), 4.48-4.24 (m, 2H), 4.18-4.00 (m, 2H), 3.00-2.84 (m, 2H), 2.36 (s, 6H), 2.33 (s, 6H), 2.29 (s, 6H), 1.98 (s, 6H), -9.33 (t, $^2J_{PH}$ = 37.57, 1H). $^{13}C\{^1H\}$ NMR (THF-d$_8$, 125 MHz, 298 K) δ 179.18, 162.10, 156.37, 154.78, 153.38, 151.96, 144.60, 144.38, 137.34, 136.62, 135.59, 134.81, 134.54, 133.27, 133.07, 129.41, 128.18, 127.94, 125.88, 124.56, 123.40, 122.08, 114.59, 111.61, 108.40, 50.78, 48.55, 43.80, 42.71, 29.94, 21.03, 20.03, 19.80. $^{31}P\{^1H\}$ NMR (THF-d$_8$, 121 MHz, 298K) δ 38.3. Crystals suitable for X-Ray diffraction were obtained through slow vapor diffusion of pentane into THF.

Elemental Analysis – Predicted (Actual, sample 1; Actual, sample 2): C, 58.23 (52.40; 56.66); H

4.95 (4.71; 4.52); N 10.72 (8.96; 9.76); Actual values are consistently low due to persistent salt impurity. There are no proton containing impurities present in the corresponding ^{1}H NMR spectra.

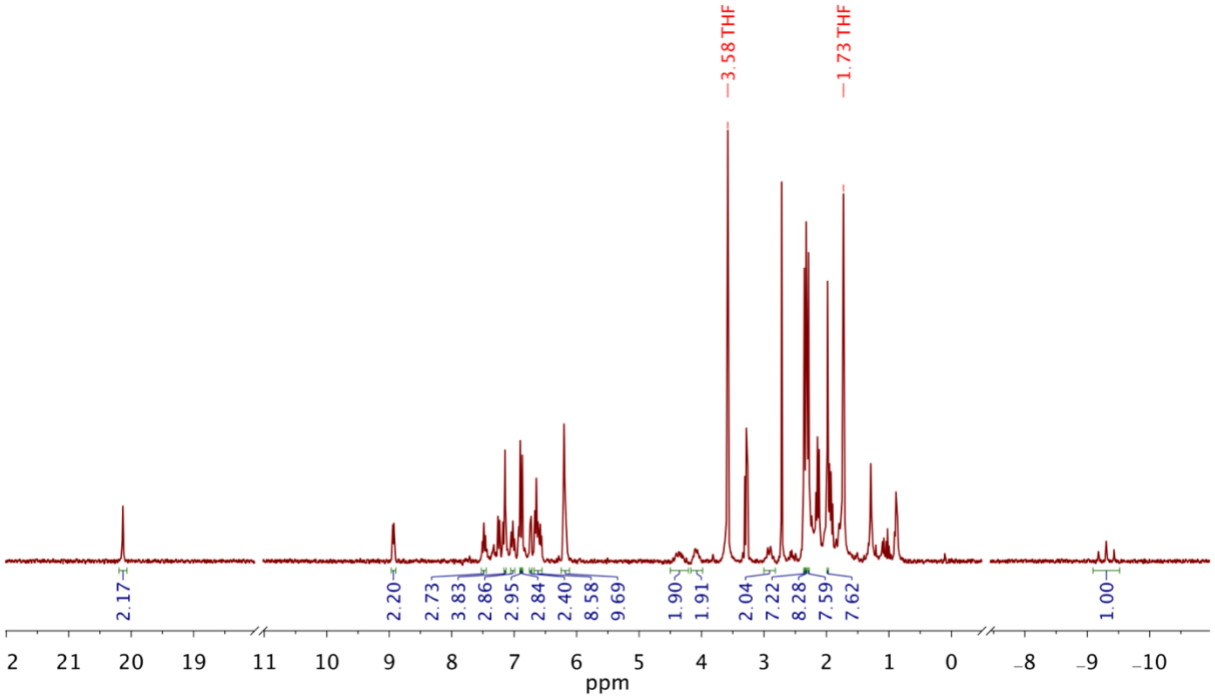

Figure 3.28. ^{1}H NMR spectrum (300 MHz, THF-d$_8$, 298K) of compound **3**.

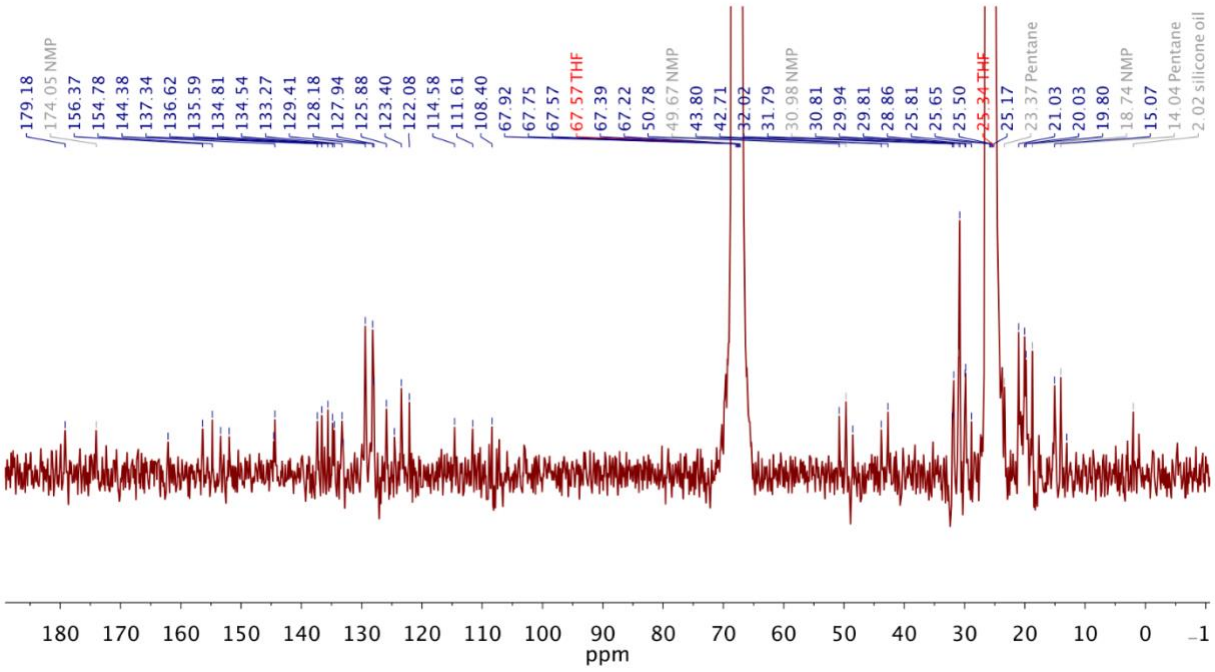

Figure 3.29. ^{13}C NMR spectrum (125 MHz, THF-d$_8$, 298K) of compound **3**.

3.4.3 *Catalysis*

Catalytic experiments were carried out in three 50 mL Parr Instrument Company's Micro Benchtop Reactors Model 4590 with PTFE flat gaskets, mounted with moveable heads. Reactors are equipped with teflon coated impellers for stirring, which are operated by an overhead magnetic drive, and the base of the reactors are equipped with removable teflon liners. Temperature is controlled and monitored by an internal thermocouple and is additionally monitored by a secondary external thermocouple inserted into the wall of the ceramic fiber heater. A stark difference between the external and internal temperatures was discovered, so the internal thermocouple is used to set and maintain the temperature and the external thermocouple is used as a safety measure. The system is operated by a 4848 reactor controller and SpecView version 3 software with data logging.

Reactors were assembled under inert conditions in the glovebox. Standard conditions were 20 µmol of catalyst, 100 equivalents of K_3PO_4 as the additive, 5 mL THF, 20 bar CO_2, and 60 bar H_2 at 140 °C for 16 hours. Changes to standard conditions are stated when appropriate.

Reactions were worked up under air. The contents of the reactor, the THF solution and any precipitate due to remaining K_3PO_4 or potassium formate product, were transferred to a centrifuge tube and centrifuged. The resulting pellet and supernatant were then separated and analyzed separately for product. The pellet was dissolved in D_2O and dimethylformamide was added as an internal standard. To the supernatant, mesitylene was added as an internal standard and the solution was spiked with DMSO-d_6 for instrument locking. These were analyzed by NMR.

Catalyst speciation was determined by concentrating both the organic and aqueous portions and separately dissolving in CD_2Cl_2 for analysis by NMR spectroscopy. Successful

recrystallization of the aqueous catalyst specie was from slow vapor diffusion of Et_2O into CD_2Cl_2.

3.4.4 *Mechanistic Studies*

A. Reactivity of **1** with K_3PO_4.

A J Young tube was charged with **1** (4 mg, 4 µmol) in 0.3 mL THF-d_8 and analyzed by ^1H and ^{31}P NMR after 1 hr at room temperature. K_3PO_4 (11 mg, 52.8 µmol) was then added directly to the tared J Young Tube, rotated overnight at room temperature to promote mixing of the minimally soluble K_3PO_4 and the solution, and then analyzed by ^1H and ^{31}P NMR. The reaction mixture was then heated at 100 °C and analyzed by ^1H and ^{31}P NMR at the 1 hr and the 2.5 hr marks.

B. Reactivity of ^{13}C Labeled **6** with K_3PO_4.

A J Young tube was charged with ^{13}C labeled **6** (4 mg, 4 µmol) in 0.3 mL THF-d_8 and analyzed by ^1H and ^{31}P NMR after 1 hr at room temperature. K_3PO_4 (19 mg, 89.5 µmol) was then added directly to the tared J Young Tube, rotated overnight at room temperature to promote mixing of the minimally soluble K_3PO_4 and the solution, and then analyzed by ^1H and ^{31}P NMR. The reaction mixture was then heated at 100 °C and analyzed by ^1H and ^{31}P NMR at the 1 hr and the 2.5 hr marks.

C. Reactivity of ^{13}C Labeled **6** with 8 bar H_2 at 100°C (no K_3PO_4).

A J Young tube was charged with ^{13}C labeled **6** (2 mg, 2 µmol) in 0.3 mL THF-d_8, degassed, and sealed under static vacuum. The tube was then charged with 8 bar H_2 and rotated to promote mixing of the solution and headspace. The reaction was analyzed after 1.5 hr at room temperature by ^1H, ^{13}C, and ^{31}P NMR and after rotating overnight at room temperature by ^1H and ^{31}P NMR. The reaction was then heated at 40 °C overnight and analyzed by ^1H and ^{31}P NMR, and then heated to 100 °C overnight and analyzed by ^1H and ^{31}P NMR. Analysis by ^{13}C NMR

was not carried out after the 1.5 hr mark due to low signal to noise and no observed change in the ^{1}H and ^{31}P NMR spectra rendered long scan times for ^{13}C NMR unnecessary.

D. Reactivity of ^{13}C Labeled **6** with 8 bar H_2 and K_3PO_4 at 100°C.

A J Young tube was charged with ^{13}C labeled **6** (2 mg, 2 µmol) and K_3PO_4 (8 mg, 38 µmol) in 0.5 mL THF-d_8, degassed, and sealed under static vacuum. The tube was then charged with 8 bar H_2 and rotated to promote mixing of the reaction mixture and the headspace. During the course of the reaction, changes were monitored by ^{1}H and ^{31}P NMR. Data was collected before pressurization with H_2, after pressurization with H_2 after 1 hr at room temperature, and after heating for 1 hr at 100 °C. After 2 days at room temperature the reaction mixture was analyzed by ^{1}H, ^{13}C, and ^{31}P NMR. The reaction mixture contained both solution and precipitate in the J Young tube, and the supernatant was decanted away from the precipitate which was then dissolved in D_2O and analyzed by ^{1}H and ^{13}C NMR.

E. Dissociation of $^{13}CO_2$ from ^{13}C Labeled **6** at 105°C.

A J Young tube was charged with ^{13}C labeled 2 (10 mg, 11 µmol) in 0.3 mL THF-d_8. Variable temperature ^{1}H and ^{13}C NMR was performed between 25 °C and 105 °C in increasing ten-degree intervals with an equilibration time of 5 minutes at each temperature. Signal was lost about the boiling point of THF-d_8. The sample was then cooled to 25 °C in the instrument and ^{1}H and ^{13}C NMR spectra were collected. After three days, orange crystals had formed in the J Young tube. The supernatant was decanted away from the crystals which were dissolved in DMSO-d_6. The supernatant and crystals were both analyzed by ^{1}H and ^{13}C NMR.

F. Variable Temperature NMR of ^{13}C Labeled **6** from 25°C to 90°C.

A J Young tube was charged with ^{13}C labeled **6** (19.6 mg, 22 µmol) in 500 µL 2,5-dimethyltetrahydrofuran (boiling point = 90 °C) and 160 µL NMP to aid with solubility. The tube was spiked with CD_2Cl_2. A capillary of $Na^{13}CO_3H$ in H_2O was used as an internal standard.

T1 measurements were performed to allow for proper integration of the ^{13}C NMR of 1-$^{13}CO_2$ and the internal standard, and T1 was found to be 8.65 seconds and d1 was set as 43.3 seconds. Variable temperature ^{13}C NMR was run at 25, 40, 60, 80 and 90°C with a 15 minutes equilibration time at each temperature.

G. Reactivity of **7** with $^{13}CO_2$.

A J Young tube was charged with **7** (10 mg, 6.4 µmol) in 0.3 mL THF-d_8, degassed, and filled with an atmosphere of $^{13}CO_2$ (g). The reaction was monitored by ^{1}H, ^{13}C and ^{31}P NMR spectroscopy for 24 hours. The solution was then decanted away from the resulting orange precipitate which was analyzed in DMSO-d_6 by NMR spectroscopy.

H. Reactivity of **1** with H_2 and no K_3PO_4 (Decomposition of PF_6^-)

A J Young tube was charged with **1** (10 mg, 0.0098 mmol) in THF-d8, degassed, and filled with an atmosphere of H_2 gas. After four days at room temperature and no observed reaction, the J Young tube was heated at 60 C for 2 hours and 20 minutes.

3.4.5 *Crystallographic Information*

Table 3.11. Crystallographic Information for Complex **2** (isolated from catalytic reaction mixture).

Empirical formula	C42.76 H47.28 Cl4 F6 N6 O2.88 P2 Ru S0.88	
Formula weight	1138.30	
Temperature	100(2) K	
Wavelength	0.71073 Å	
Crystal system	Triclinic	
Space group	P -1	
Unit cell dimensions	a = 12.9626(8) Å	α= 101.694(4)°.
	b = 13.0497(8) Å	β= 91.240(4)°.
	c = 15.3431(10) Å	γ = 108.197(3)°.
Volume	2404.3(3) $Å^3$	
Z	2	
Density (calculated)	1.572 Mg/m^3	
Absorption coefficient	0.722 mm^{-1}	
F(000)	1158	
Crystal size	0.290 x 0.150 x 0.080 mm^3	
Theta range for data collection	1.361 to 28.335°.	

Index ranges	-17<=h<=17, -17<=k<=17, -19<=l<=20
Reflections collected	22939
Independent reflections	11791 [R(int) = 0.0322]
Completeness to theta = 25.000°	99.4 %
Absorption correction	Semi-empirical from equivalents
Max. and min. transmission	0.746 and 0.698
Refinement method	Full-matrix least-squares on F^2
Data / restraints / parameters	11791 / 9 / 629
Goodness-of-fit on F^2	1.040
Final R indices [I>2sigma(I)]	R1 = 0.0416, wR2 = 0.0967
R indices (all data)	R1 = 0.0598, wR2 = 0.1055
Largest diff. peak and hole	1.208 and -1.099 e.Å^{-3}

Table 3.12. Crystallographic Information for Complex **3**.

Empirical formula	C92 H109 F6 N12 O4 P3 Ru2	
Formula weight	1855.96	
Temperature	100(2) K	
Wavelength	0.71073 Å	
Crystal system	Triclinic	
Space group	P -1	
Unit cell dimensions	a = 12.9219(12) Å	α= 82.215(4)°.
	b = 13.0307(11) Å	β= 83.087(4)°.
	c = 27.997(2) Å	γ = 66.365(4)°.
Volume	4267.6(6) Å^3	
Z	2	
Density (calculated)	1.444 Mg/m^3	
Absorption coefficient	0.483 mm^{-1}	
F(000)	1928	
Crystal size	0.090 x 0.060 x 0.050 mm^3	
Theta range for data collection	1.472 to 25.350°.	
Index ranges	-15<=h<=15, -15<=k<=15, -33<=l<=33	
Reflections collected	31252	
Independent reflections	15635 [R(int) = 0.1327]	
Completeness to theta = 25.000°	100.0 %	
Refinement method	Full-matrix least-squares on F^2	
Data / restraints / parameters	15635 / 905 / 1107	
Goodness-of-fit on F^2	0.948	
Final R indices [I>2sigma(I)]	R1 = 0.0571, wR2 = 0.0926	
R indices (all data)	R1 = 0.1504, wR2 = 0.1193	
Largest diff. peak and hole	0.729 and -0.737 e.Å^{-3}	

3.5 REFERENCES

(1) Aznarez, F.; Iglesias, M.; Hepp, A.; Veit, B.; Sanz Miguel, P. J.; Oro, L. A.; Jin, G.-X.; Hahn, F. E. Iridium(III) Complexes Bearing Chelating Bis-NHC Ligands and Their Application in the Catalytic Reduction of Imines: Iridium(III) Complexes Bearing Chelating Bis-NHC Ligands and Their Application in the Catalytic Reduction of Imines. *Eur. J. Inorg. Chem.* **2016**, *2016* (28), 4598–4603. https://doi.org/10.1002/ejic.201600922.

(2) Meier, N.; Hahn, F. E.; Pape, T.; Siering, C.; Waldvogel, S. R. Molecular Recognition Utilizing Complexes with NH,NR-Stabilized Carbene Ligands. *Eur. J. Inorg. Chem.* **2007**, *2007* (9), 1210–1214. https://doi.org/10.1002/ejic.200601258.

(3) Mühlen, C.; Linde, J.; Rakers, L.; Tan, T. T. Y.; Kampert, F.; Glorius, F.; Hahn, F. E. Synthesis of Iron(0) Complexes Bearing Protic NHC Ligands: Synthesis and Catalytic Activity. *Organometallics* **2019**, *38* (12), 2417–2421. https://doi.org/10.1021/acs.organomet.9b00260.

(4) Chang, W.; Gong, X.; Wang, S.; Xiao, L.-P.; Song, G. Acceptorless Dehydrogenation and Dehydrogenative Coupling of Alcohols Catalysed by Protic NHC Ruthenium Complexes. *Org. Biomol. Chem.* **2017**, *15* (16), 3466–3471. https://doi.org/10.1039/C7OB00542C.

(5) Miranda-Soto, V.; Grotjahn, D. B.; Cooksy, A. L.; Golen, J. A.; Moore, C. E.; Rheingold, A. L. A Labile and Catalytically Active Imidazol-2-Yl Fragment System. *Angew. Chem. Int. Ed.* **2011**, *50* (3), 631–635. https://doi.org/10.1002/anie.201005100.

(6) Gomez-Lopez, J. L.; Chávez, D.; Parra-Hake, M.; Royappa, A. T.; Rheingold, A. L.; Grotjahn, D. B.; Miranda-Soto, V. Synthesis and Reactivity of Bis(Protic N-Heterocyclic Carbene)Iridium(III) Complexes. *Organometallics* **2016**, *35* (18), 3148–3153. https://doi.org/10.1021/acs.organomet.6b00501.

(7) Norris, M. R.; Flowers, S. E.; Mathews, A. M.; Cossairt, B. M. H_2 Production Mediated by CO_2 via Initial Reduction to Formate. *Organometallics* **2016**, *35* (17), 2778–2781. https://doi.org/10.1021/acs.organomet.6b00595.

(8) Wesselbaum, S.; Moha, V.; Meuresch, M.; Brosinski, S.; Thenert, K. M.; Kothe, J.; Stein, T. vom; Englert, U.; Hölscher, M.; Klankermayer, J.; Leitner, W. Hydrogenation of Carbon Dioxide to Methanol Using a Homogeneous Ruthenium–Triphos Catalyst: From Mechanistic Investigations to Multiphase Catalysis. *Chem Sci* **2015**, *6* (1), 693–704. https://doi.org/10.1039/C4SC02087A.

(9) Vogt, M.; Gargir, M.; Iron, M. A.; Diskin-Posner, Y.; Ben-David, Y.; Milstein, D. A New Mode of Activation of CO2 by Metal–Ligand Cooperation with Reversible C-C and M-O Bond Formation at Ambient Temperature. *Chem. – Eur. J.* **2012**, *18* (30), 9194–9197. https://doi.org/10.1002/chem.201201730.

(10) Vogt, M.; Nerush, A.; Diskin-Posner, Y.; Ben-David, Y.; Milstein, D. Reversible CO_2 Binding Triggered by Metal–Ligand Cooperation in a Rhenium(I) PNP Pincer-Type Complex and the Reaction with Dihydrogen. *Chem Sci* **2014**, *5* (5), 2043–2051. https://doi.org/10.1039/C4SC00130C.

(11) Zhang, Y.; MacIntosh, A. D.; Wong, J. L.; Bielinski, E. A.; Williard, P. G.; Mercado, B. Q.; Hazari, N.; Bernskoetter, W. H. Iron Catalyzed CO_2 Hydrogenation to Formate Enhanced by Lewis Acid Co-Catalysts. *Chem Sci* **2015**, *6* (7), 4291–4299. https://doi.org/10.1039/C5SC01467K.

(12) Huff, C. A.; Kampf, J. W.; Sanford, M. S. Role of a Noninnocent Pincer Ligand in the Activation of CO_2 at (PNN)Ru(H)(CO). *Organometallics* **2012**, *31* (13), 4643–4645.

https://doi.org/10.1021/om300403b.
(13) Huff, C. A.; Sanford, M. S. Catalytic CO_2 Hydrogenation to Formate by a Ruthenium Pincer Complex. *ACS Catal.* **2013**, *3* (10), 2412–2416. https://doi.org/10.1021/cs400609u.
(14) Gunanathan, C.; Milstein, D. Bond Activation and Catalysis by Ruthenium Pincer Complexes. *Chem. Rev.* **2014**, *114* (24), 12024–12087. https://doi.org/10.1021/cr5002782.
(15) Flowers, S. E.; Johnson, M. C.; Pitre, B. Z.; Cossairt, B. M. Synthetic Routes to a Coordinatively Unsaturated Ruthenium Complex Supported by a Tripodal, Protic Bis(N-Heterocyclic Carbene) Phosphine Ligand. *Dalton Trans.* **2018,** ***47***, 1276-1283. https://doi.org/10.1039/C7DT04333C.
(16) Silvia, J. S.; Cummins, C. C. Binding, Release, and Functionalization of CO2 at a Nucleophilic Oxo Anion Complex of Titanium. *Chem. Sci.* **2011**, *2* (8), 1474. https://doi.org/10.1039/c1sc00215e.
(17) Heimann, J. E.; Bernskoetter, W. H.; Hazari, N. Understanding the Individual and Combined Effects of Solvent and Lewis Acid on CO_2 Insertion into a Metal Hydride. *J. Am. Chem. Soc.* **2019**, *141* (26), 10520-10529. https://doi.org/10.1021/jacs.9b05192.
(18) Jessop, P. G.; Ikariya, T.; Noyori, R. Homogeneous Hydrogenation of Carbon Dioxide. *Chem. Rev*. **1995**, *95* (2), 261-272. https://doi.org/10.1021/cr00034a001
(19) Schmeier, T., Dobereiner, G., Crabtree, R., Hazari, N. Secondary Coordination Sphere Interactions Facilitate the Insertion Step in an Iridium(III) CO_2 Reduction Catalyst. *J. Am. Chem. Soc.* **2011**, 133, 24, 9274–9277. https://doi.org/10.1021/ja2035514.
(20) Miranda-Soto, V.; Grotjahn, D. B.; DiPasquale, A. G.; Rheingold, A. L. Imidazol-2-Yl Complexes of Cp*Ir as Bifunctional Ambident Reactants. *J. Am. Chem. Soc.* **2008**, *130* (40), 13200–13201. https://doi.org/10.1021/ja804713u.
(21) Chinn, M. S.; Heinekey, D. M. Dihydrogen Complexes of Ruthenium. 2. Kinetic and Thermodynamic Considerations Affecting Product Distribution. *J. Am. Chem. Soc.* **1990**, *112* (13), 5166–5175. https://doi.org/10.1021/ja00169a026.
(22) Hahn, F. E.; Naziruddin, A. R.; Hepp, A.; Pape, T. Synthesis, Characterization, and H-Bonding Abilities of Ruthenium(II) Complexes Bearing Bidentate NR,NH-Carbene/Phosphine Ligands †. *Organometallics* **2010**, *29* (21), 5283–5288. https://doi.org/10.1021/om100388w.
(23) Ishikita, H.; Saito, K. Proton Transfer Reactions and Hydrogen-Bond Networks in Protein Environments. *J. R. Soc. Interface* **2014**, *11* (91), 20130518. https://doi.org/10.1098/rsif.2013.0518.
(24) Frey, P. A. Review: Strong Hydrogen Bonding in Molecules and Enzymatic Complexes. *Magn. Reson. Chem.* **2001**, *39* (S1), S190–S198. https://doi.org/10.1002/mrc.953.
(25) Christe, K., Dixon, D., Schrobilgen, G., Wilson, W. Tetrafluorophosphate Anion. *J. Am. Chem. Soc.* **1997**, *119*, 3918-392.

Chapter 4. BIMETALLIC COORDINATION

4.1 INTRODUCTION

Bimetallic cooperation for small molecule activation has been of interest across fields of chemistry, from bioinorganic to homo- and heterogeneous catalysis. As discussed in the introduction (Chapter 1.4), the formic acid dehydrogenase metalloenzymes selectively and efficiently interconverts CO_2 and formic acid in either a Ni/Fe or a Mo/Cu system. One of the challenges posed by CO_2 conversion to C_1 and C_{2+} products is that of product selectivity. The thermodynamic stability of CO_2 renders it relatively inert in comparison with the desired products, which can be overcome by reaction with a higher energy reactant like H_2, changing conditions such as solvent to make the product more thermodynamically favorable, and/or through external energy inputs to help overcome high activation energy barriers.[1] Understanding of the relative thermodynamics and kinetics of the desired reaction pathway is critical for tuning parameters to avoid competitive byproducts. One way that the field of heterogeneous catalysis has tackled issues of selectivity for many reaction types is through the deployment of bimetallic systems. One example comes from a heterogeneous Fischer-Tropsch chemistry, which is a chemical reaction between carbon monoxide and hydrogen, commonly referred to as syngas, to produce hydrocarbons. When a cobalt-based catalyst is used, hydrocarbons of broad molecular weight distribution result and the catalyst is difficult to regenerate. With the incorporation of 0.15% ruthenium the catalytic activity and selectivity for C_{5+} products was improved. Additionally, ruthenium promoted cleansing of the cobalt surface was observed by hydrogenolysis of the carbonaceous residues and reduction of surface oxygen species under

hydrogen at low temperatures.[2] Synergistic effects have also been observed between cobalt and ruthenium for the homologation of methanol and the hydroformylation of olefins.[3]

Molecular bimetallic systems afford greater control and detailed insights, which provides the opportunity to systematically probe metal-metal cooperativity. In addition to metal choice, factors such as binding geometry and metal-metal bonding abilities play an important role in observed reactivity. One common class of ligands supporting bimetallic complexes are phosphineamides. The Thomas group has demonstrated a tris-phosphineamide bridged Zr/Co complex capable of the cleavage of the C=O bond of CO_2, which results in a Zr–O–Co bridging oxo and a cobalt carbonyl.[4,5] The electronic disparity between Zr and Co is anticipated to enhance the bridging oxo reactivity, and treatment with various electrophiles results in the interruption of the Zr–O–Co bridging to form a terminal zirconium oxo stabilized by coordination of the electrophile.[4,5] One of the persistent challenges in this system is liberation of CO from the cobalt.

Phosphineamide bridged bimetallics have also been explored for other metal systems and reactivity, including a Ti/Pd system which catalyzes allylic amination.[6] In this study, a monometallic Pd complex and two bimetallic Ti/Pd complexes with the metal centers in different orientations relative to one another are examined. In the first bimetallic complex, the metal centers are in a “boat” conformation with the metals at the apical positions, allowing for metal-metal bonding. In the second, half of the boat is flatted such that the metal-metal interaction is interrupted. It is determined that the boat conformation and the flexibility associated with the phosphineamide ligands play important roles in allowing metal-metal interactions, which in turn increase the rate of catalysis.

Scheme 4.1. Synthesis of the bis-(PNHC) phosphine supported bimetallic complexes. Reprinted (adapted) with permission from Flowers, S.E and Cossairt, B. M. *Organometallics* **2014**, 33, 17, 4341–4344. Copyright 2014 American Chemical Society.

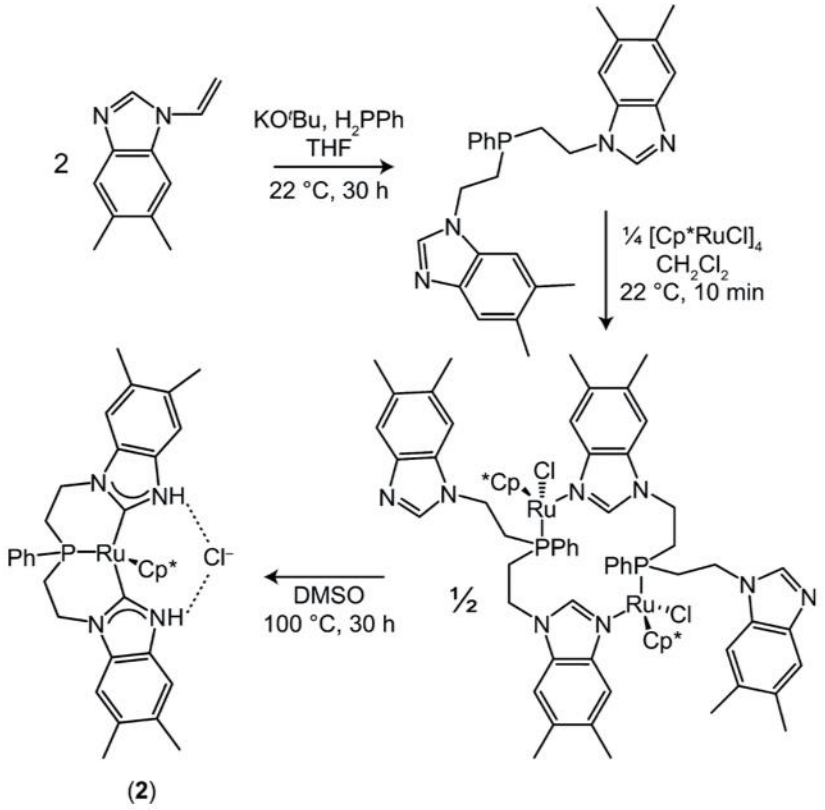

Prior work from our group has demonstrated the synthesis of bimetallic complexes supported by the bis-PNHC phosphine ligand, **L**.[7] With Ru(II)-Cp* coordinated at the bis-carbene phosphine position, the PNHCs were deprotonated by a strong base and metaled with the addition of MCl_2 (M = Fe, Co), forming a neutral product with one inner sphere chloride (Scheme 4.1). In this system, the coordination of the metals forms a half boat conformation, with the flattening of the ring likely due in part to the steric hinderance of the Cp*. While N-metalation of PNHCs has been demonstrated in the literature[8–15], N-metalation and chelation of neighboring PNHCs in this manor is uncommon, and to the best of our knowledge has only been observed in one other study.[14] Typically in N-metalated PNHC bimetallics, dimerization or oligomerization occurs enabled by low steric profile and ligand flexibility.[8]

In addition to the Cp* flattening the boat conformation between the two metal centers in in the bis-PNHC phosphine (**L**) system, it is also blocking the coordination sites at the ruthenium, essentially rendering it a metalloligand. By adopting bipyridine as an ancillary ligand in the place of Cp* an open coordination site will be made available adjacent to the PNHCs. The reduction of steric bulk on this face of the complex should allow for greater flexibility to investigate metal-metal cooperation. As previously discussed, ruthenium and cobalt are known to have complementary properties in bimetallic systems. To supplement the exploration of N-metalation of Co(II), Zn(II) will be pursued. While Zn(II) and Co(II) have approximately the same ionic radii, Zn(II) is redox inactive and diamagnetic. Both Co and Zn are gaining popularity as first row transition metal catalysts for CO_2 hydrogenation[16–23], and have even been shown to exhibit reactivity with CO_2 in ligand systems reminiscent of the κ^2-N,N' binding pocket studied herein, such as β-diketiminate.[19,24] The influence of the ancillary ligand selection and the repercussions of opening the additional coordination site on the ruthenium are explored.

4.2 Results and Discussion

4.2.1 *Synthesis*

Preliminary results for the synthesis of the ruthenium-cobalt complex (**10**) revealed that the coordination of cobalt at the deprotonated bis-(p-NHC) position can be quite dynamic and is sensitive to the reaction conditions. Crystal structures obtained from initial synthesis and exploratory reactivity studies revealed the cobalt metal center coordinated in the p-NHC pocket in a variety of geometries, including octahedrally, tetrahedrally, and in a pseudo-paddlewheel environment (Figure 4.1).

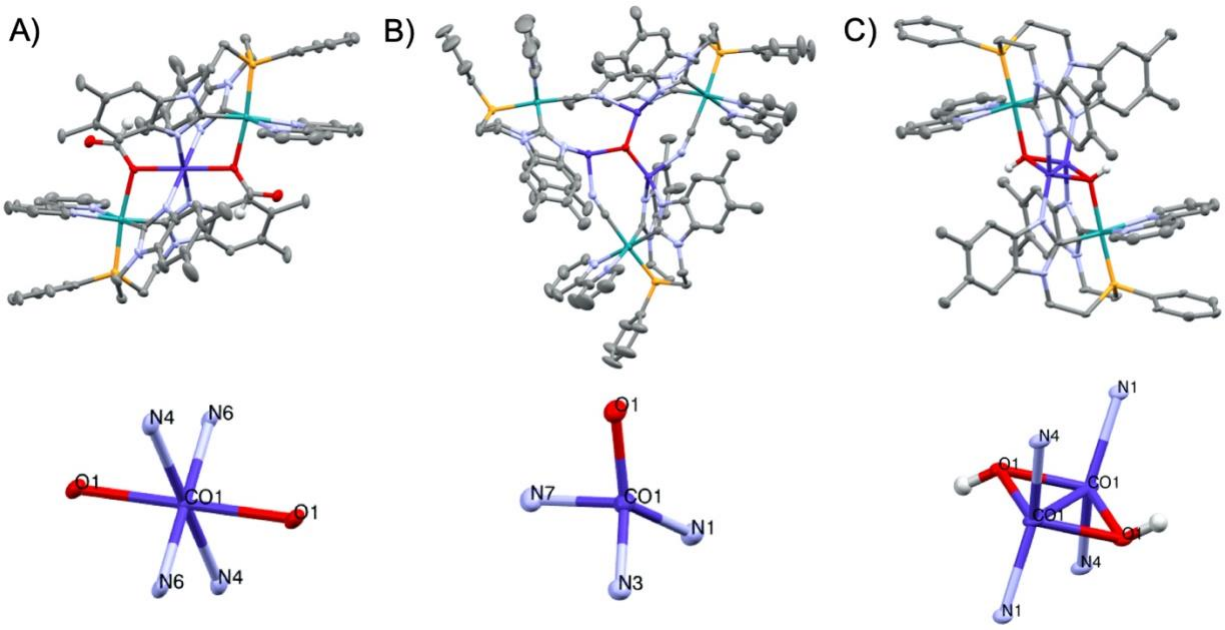

Figure 4.1. Cobalt coordination in crystal structures.

Notably, in every observed cobalt coordination environment there is dimerization (Figure 4.1, A and C) or trimerization (Figure 4.1, B) in the solid state, enabled by the open coordination position on the ruthenium and the vastly changed steric profile of the bipyridine ligand versus the Cp* ligand previously studied.[7] Additionally, the bipyridine changes the orientation of **L**, forcing the NH-wingtips into a more parallel position than the Cp* complex . This can be observed in the monometallic precursors, complexes **1** and **2** (Figure 4.2). In the analysis of bond lengths for these structures (Table 4.1), one of the largest differences is in the distance between the NH-wingtip nitrogen atoms. In **1**, the distance between these positions (N3 and N5, Figure 4.3) is 4.195 Å, while in **2**, the distance is a much shorter 3.415 Å (N2 and N4, Figures 4.2). When Fe is installed in **2** (Complex **9-Fe**, Figure 4.3) very little rearrangement of the ligand is required, with the largest changes occurring as the carbene-Ru-carbene bond angle decreases from 92.62º to 90.35º and the PNHC-nitrogen distance decreases to 3.233 Å, a change of 0.2 Å.

When Co is installed in **1**, we see two primary behaviors for coordination. First is the κ^2N,N'-Co chelation by PNHC-nitrogen atoms of the same **L**, as seen in the Figure 4.1, A and B. Both complexes were formed after reaction of **10** with formate and will be referred to as **12-dimer** and **12-trimer**. Significantly more rearrangement of **L** is required for the conversion of **1** to **12-trimer** than is required for the synthesis of **9-Fe** from **2**. While the distance between the PNHC-nitrogen atoms in **1** is 4.195 Å, in **12-trimer** the distance is decreased by a whole angstrom to 3.101 Å. The carbene-Ru-carbene bond angle is also decreased from 92.12º in **1** to 88.34º in **12-trimer**.

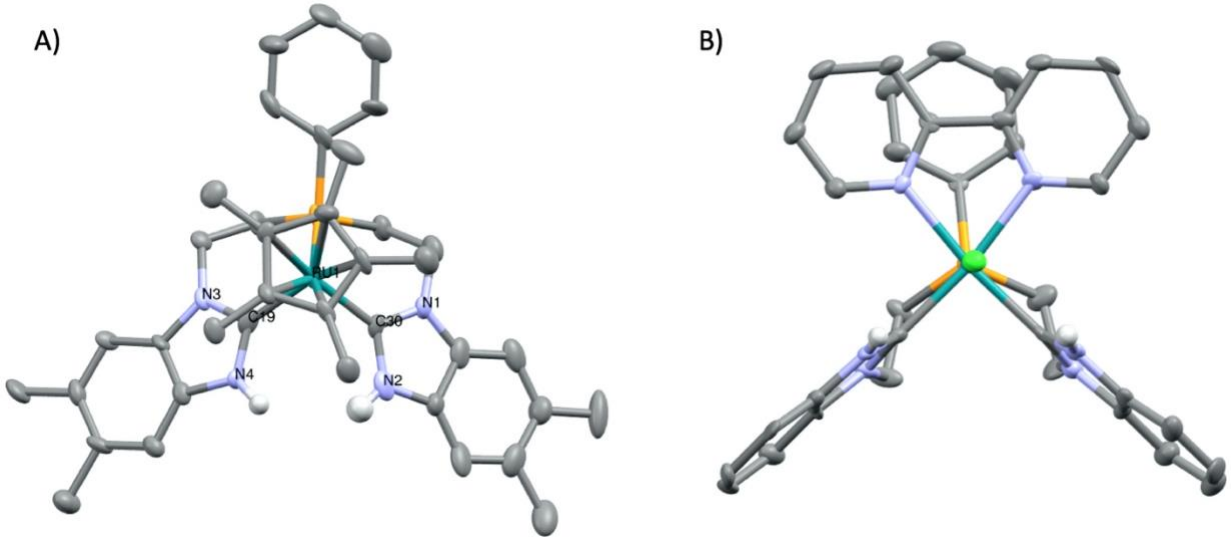

Figure 4.2. Top down view of complexes **1** (B) and **2** (A) showing the impact of changing the ruthenium ancillary ligand from Cp* (A) to bipyridine (B), resulting in the orientation of the PNHC NH-wingtips changing from pointing towards one another to being parallel. (A) All hydrogen atoms, except for the PNHC NH-wingtips, one THF, one diethyl ether, and one chloride hydrogen bound to the NH-wingtips were excluded for clarity. (B) All hydrogen atoms, except for the PNHC NH-wingtips, and one chloride hydrogen bound to the NH-wingtips were excluded for clarity.

On the other hand, Co coordination has also been observed in a pseudo-paddlewheel environment, where the Co is coordinated by two PNHC-nitrogen atoms, one each from different **L**, resulting in di-ruthenium/di-cobalt complex with the two cobalt atoms at the center (Figure

4.1C and Figure 4.4). This structure has been isolated in duplicate following the deprotonation and metalation of **1** and will be referred to as **10-dimer**. In this arrangement, the PNHC-nitrogen atoms within one **L** are spaced at 4.223 Å, only a 0.1 Å difference from **1**, and the **10-dimer** carbene-Ru-carbene bond angle is 93.85º, only 1º greater than that in **1**. Similar paddlewheel structures have been observed in the literature, containing a $(Co_2)^{+4}$ core with a bond order of zero and a Co-Co distance between 2.6893(12) and 2.861(5) Å, which is consistent with the observed Co-Co distance in **10-dimer** (2.793Å).[25]

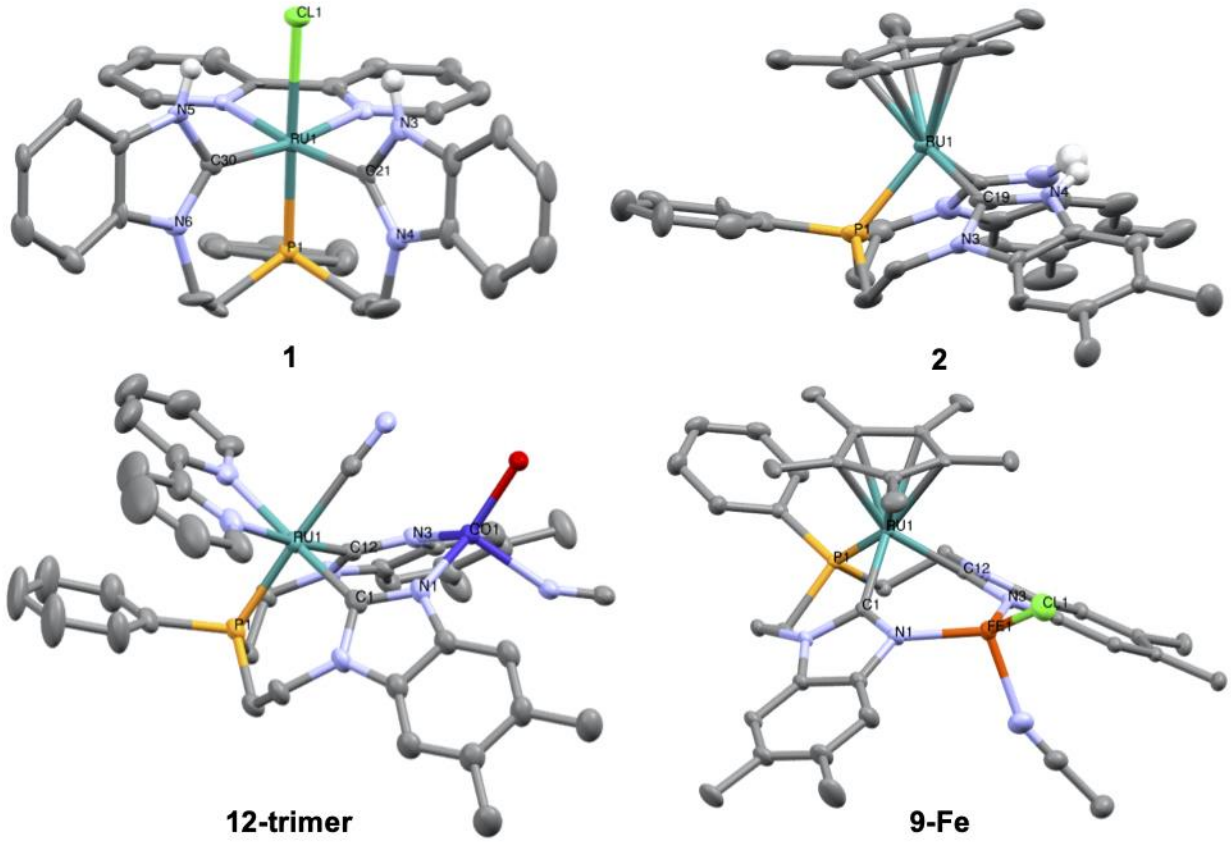

Figure 4.3. Crystal structures obtained for **1**, **2**, **9-Fe**, and **12-trimer** with numbering scheme shown for reference to Table 4.1. A truncated image of **12-trimer** is shown, focusing on the coordination of one subunit. In all structures, all hydrogen atoms, except for the PNHC NH-wingtips where present were excluded for clarity. For **1**, one chloride hydrogen bound to the NH-wingtips was excluded. For **2**, one THF, one diethyl ether, and one chloride hydrogen bound to the NH-wingtips were excluded. For **9-Fe**, on acetonitrile solvent molecule is excluded. For **10-trimer**, disordered DMSO and diethyl ether, and one chloride were excluded.

Given these insights, it can be concluded that the selection of the ancillary ligand is important not only for providing an open reactive coordination site on the ruthenium to probe synergistic metal-metal effects in reactivity, but also for providing accessibility for metalation at the PNHC-nitrogen position by controlling the orientation of the NH-wingtips relative to one another. The energetic barrier and probable strain associated with the ligand rearrangement from **1** to the κ^2N,N'-Co chelation binding motif may explain the dynamic structures dependent on solvent and concentration observed over the course of synthesizing and characterizing **10** (*vide infra*).

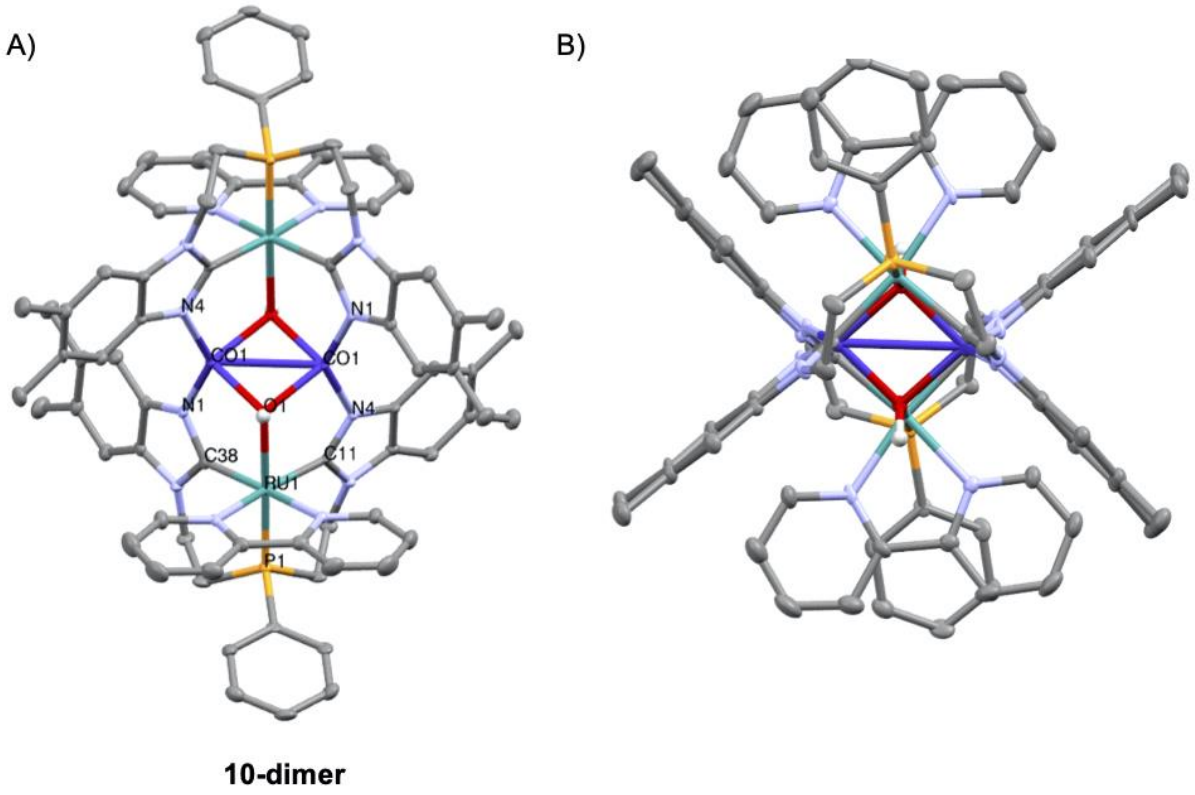

Figure 4.4. Crystal Structures obtained for **10-dimer** with numbering scheme shown in (A) for reference to Table 4.1. B) Top down view of **10-dimer** illustrating the parallel orientation of the benzimidazole ligand arms. All hydrogen atoms, except for hydroxide protons, and two PF_6^- anions and two THF solvent molecules were excluded for clarity.

Table 4.13. Selected Bond Lengths and Bond Angles for Complexes **1**[a], **2**[b], **9-Fe**[a], **10-trimer**[a], and **10-dimer**[c].

Selected Bond	Bond Length (Å)	Selected Angle	Bond Angle (º)
Complex **1**			
Ru1–C30	2.024	C30-Ru1-C21	92.12
Ru1–C21	2.010	Ru1-C30-N5	123.39
C30-N5	1.353	Ru1-C21-N3	121.14
C21-N3	1.365	C30-Ru1-P1	92.69
C30-C21	2.905		
N5-N3	4.195		
Complex **2**			
Ru1–C19	2.029	C30-Ru1-C19	92.62
Ru1–C30	2.029	Ru1-C30-N2	127.65
C19-N4	1.357	Ru1-C19-N4	126.24
C30-N2	1.378	C30-Ru1-P1	87.77
C30-C19	2.935	C19-Ru1-P1	89.07
N4-N2	3.415		
Complex **9-Fe**			
Ru1–C1	2.035	C1-Ru1-C12	90.35
Ru1–C12	2.041	Ru1-C1-N1	124.97
N1-Fe1	2.002	C1-N1-Fe1	116.81
N3-Fe1	2.001	N1-Fe1-N3	107.77
N1-N3	3.233	P1-Ru1-C1	89.42
C1-C12	2.891		
Ru1-Fe1	3.579		
Complex **10-dimer**			
Ru1-C11	2.034	C38-Ru1-C11	93.85
Ru1-C38	2.041	Ru1-C11-N4	121.28
Ru1-Co1	3.453	C11-N4-Co1	120.04
Ru1-O1	2.217	P1-Ru1-C11	121.28
C11-N4	1.370	O1-Ru1-C1	89.46
N4-Co1	1.952	Ru1-O1-Co1	109.99
Co1-O1	1.995	Co1-O1-Co1	89.08
Co1-Co1	2.793	N1-Co1-N4	136.91
C11-C38	2.976		
N1-N4 (same L)	4.223		
N1-N4 (different L)	3.626		
Complex **12-trimer**			
Ru1-C1	2.029	C1-Ru-C12	88.34
Ru1-C12	2.030	Ru1-C1-N1	125.58
C1-N1	1.357	C1-N1-Co1	121.08
N1-Co1	2.005	P1-Ru1-C1	89.77

(Table 4.1 Continued)			
C12-N3	1.355	N1-Co1-N3	101.07
N3-Co1	2.012		
C1-C12	2.828		
N1-N3	3.101		
Ru1-Co1	3.645		

[a] Reference Figure 4.3 for numbering scheme. [b] Reference Figure 4.2A and Figure 4.3 for numbering scheme. [c] Reference Figure 4.4 for numbering scheme.

When the synthesis is carried out in DMSO, full conversion to a paramagnetic complex **10** is observed (Scheme 4.2). Given the variety of coordination environments observed crystallographically, 0.5, 1, and 2 equivalents of $CoCl_2$ were screened. With 0.5 equivalents many minor products were observed with no major species. With an additional 0.5 equivalent added (1 equivalent total) a major species emerged. The addition of another single equivalent of $CoCl_2$ (2 equivalents total), showed no immediate change in the product distribution (Figure 4.7). Over the course of 20 days at room temperature all peaks coalesced into the major species previously stated, which remained stable in solution through six weeks at room temperature. This suggests that the coordination of a single cobalt per PNHC binding pocket is the thermodynamic preference. Furthermore, carrying out the synthesis with 1 equivalent of $CoCl_2$ and heating at 75 ºC for 24 hours yielded the same major species (Figure 4.8). The ^{1}H NMR spectrum is also consistent with respect to the previously published Cp* equivalent, **9-Co** (Figures 4.5 and 4.6).

Scheme 4.2. Synthesis of **10**.

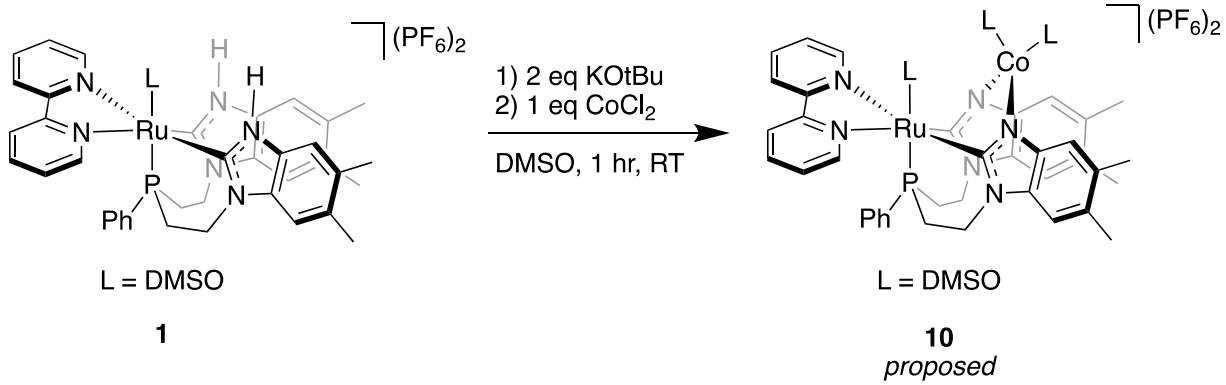

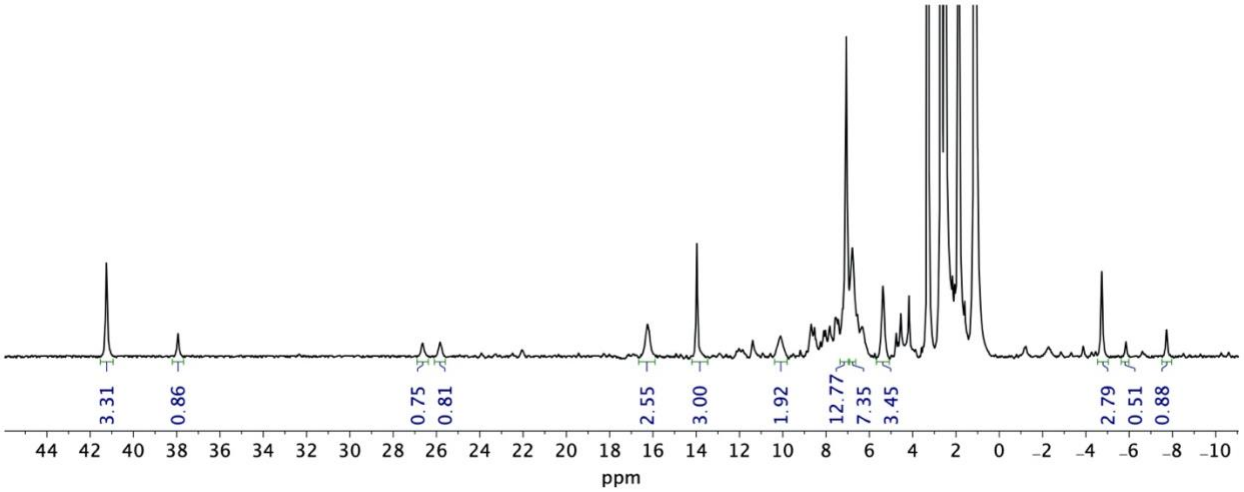

Figure 4.5. ^{1}H NMR (500 MHz, 298k, DMSO-d_6) of **10**.

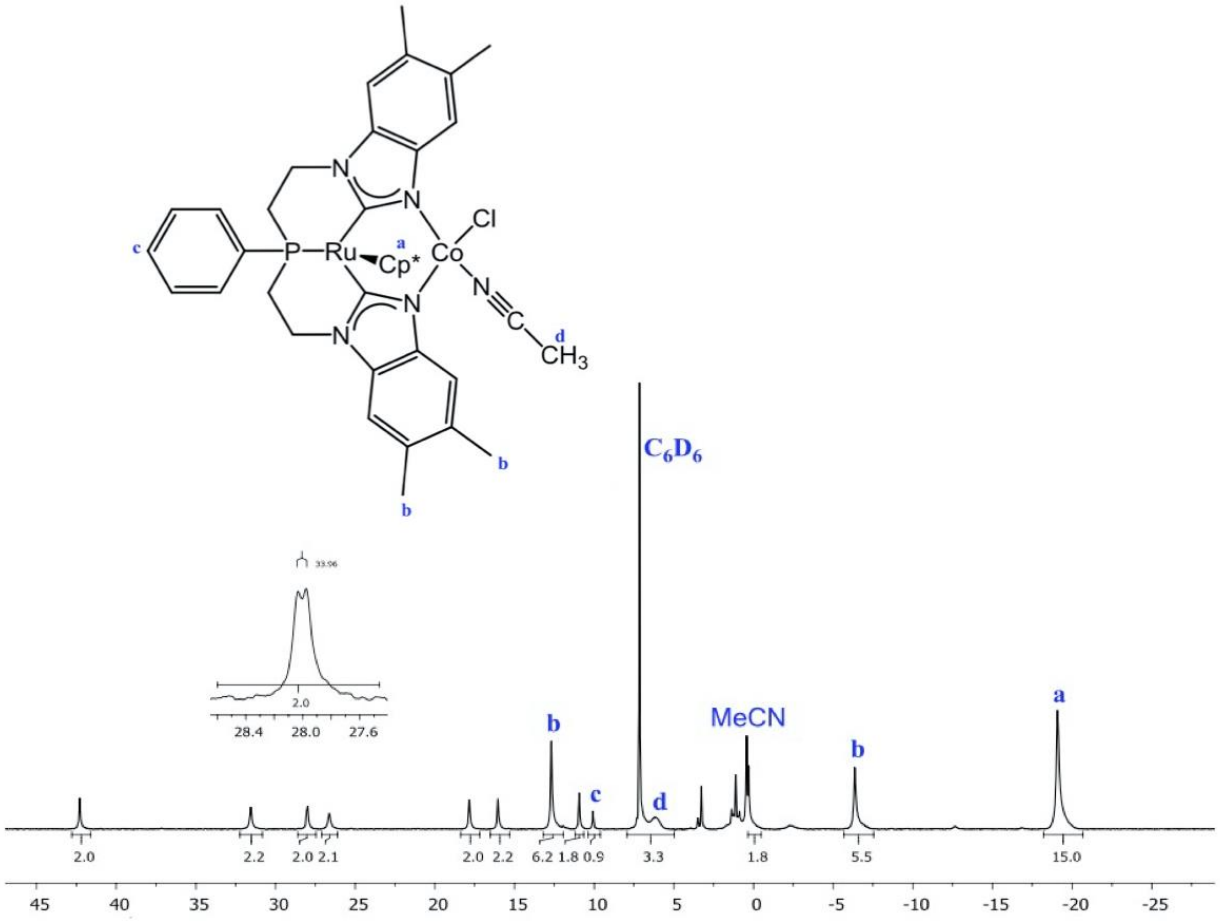

Figure 4.6. ^{1}H NMR (500 MHz, 298k, C_6D_6) of **9-Co**. Reprinted (adapted) with permission from Flowers, S.E and Cossairt, B. M. *Organometallics* **2014**, 33, 17, 4341–4344. Copyright 2014 American Chemical Society.

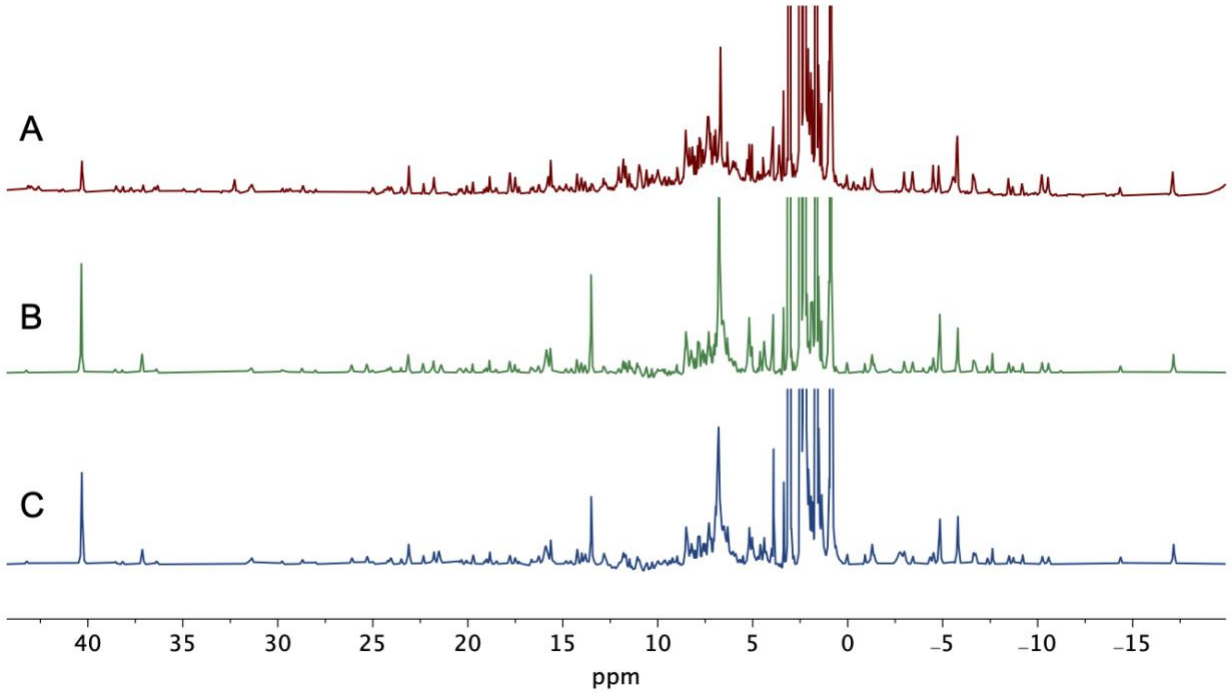

Figure 4.7. ^{1}H NMR (700 MHz, DMSO-d_6, 298 K) Reaction between **1** and $CoCl_2$ in 0.5 (A), 1 (B), and 2 (C) equivalents.

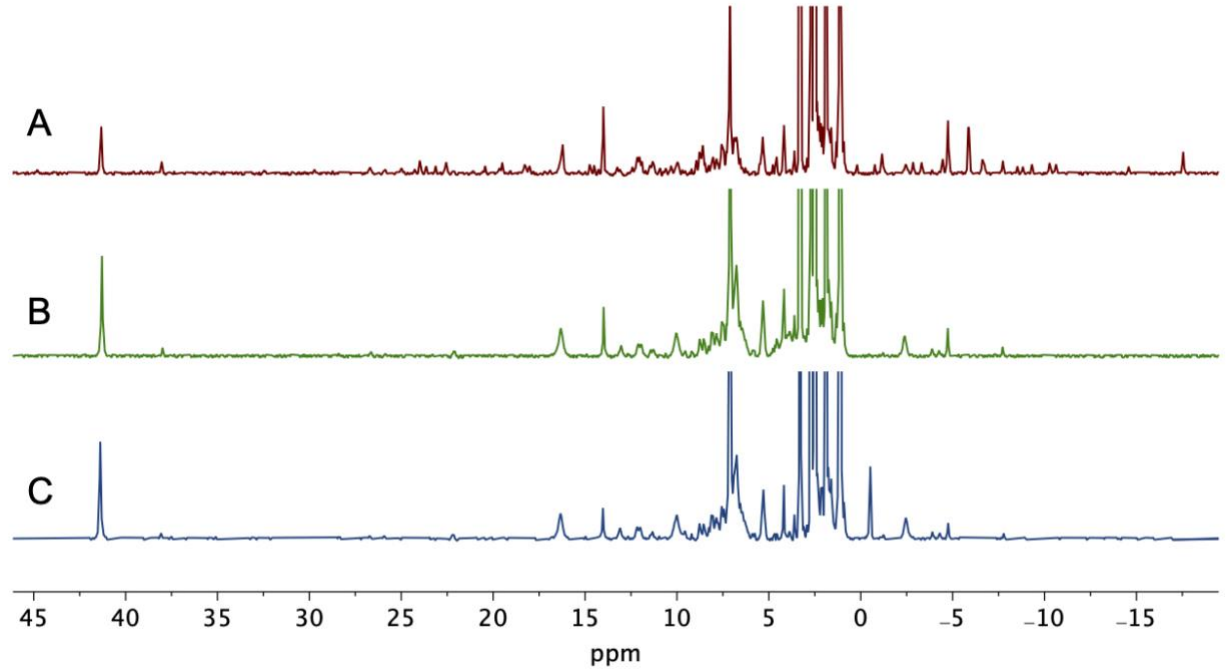

Figure 4.8. Complex **10** at room temperature for 10 minutes (A), after heating at 75 ºC for 90 minutes (B), and after heating at 75 ºC for 24 hrs (C).

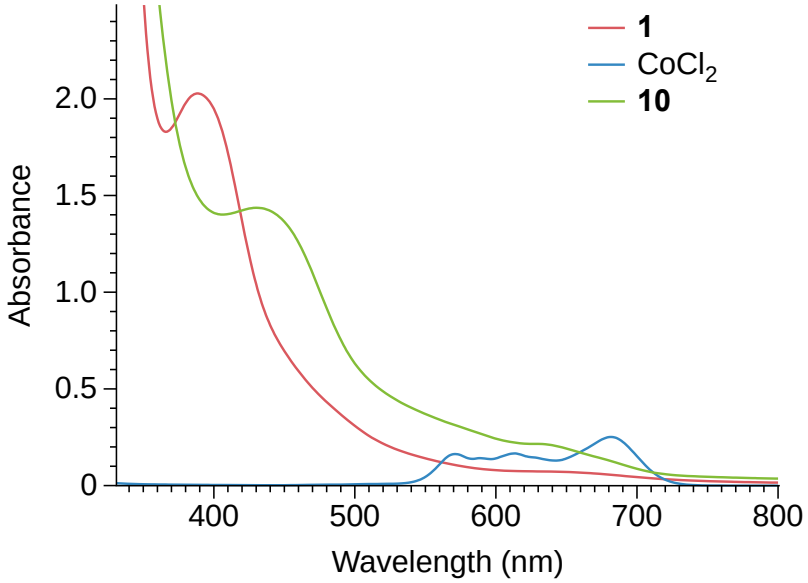

Figure 4.9. UV-vis of **1**, **10**, and $CoCl_2$

Further evidence supporting the formation of **10** are the shifts observed in both UV-vis, the FT-IR CO stretching frequency when **1-CO** is used as starting material, and elemental analysis. The UV-vis spectrum for **1** is dominated by the metal to ligand charge transfer (MLCT) band at 389 nm. The spectrum of **10** shows the MLCT band at 431 nm, as well as a new shoulder at 630 nm. The band at 630 nm is in a region that is consistent with the UV-vis spectrum of $CoCl_2$ in acetonitrile, however it is approximately 50 nm blue shifted, suggesting successful coordination of the cobalt (Figure 4.9). The MLCT for ruthenium bipyridine is well studied, and it is commonly accepted that the transition is occurring between the HOMO of predominantly Ru character and the LUMO of predominantly bipyridine π* character. Cyclic voltammetry can provide formal redox potentials for the metal center and bipyridine, which can support the HOMO/LUMO assignment. For complex **1** in acetonitrile, the $E_{1/2}(Ru^{II/III})$ = +0.72 V vs $Fc^{+/0}$ and the $E_{1/2}(bpy^{0/-})$ = -1.94 V vs $Fc^{+/0}$, thus corroborating the assignment of the HOMO/LUMO for the MLCT.[26] The red shift observed in the MLCT with the incorporation of Co(II) to form **10** indicates a narrowing of the HOMO/LUMO gap. While it is challenging to determine whether

this is due to a lowering of the LUMO or a rising of the HOMO, CO-labeling of the ruthenium and investigation of the CO stretching frequency by IR, as discussed below, suggests an increased electron density at the ruthenium in **10** versus **1**.

The addition of $CoCl_2$ to deprotonated **1** bound by a carbonyl ligand, **1-CO**, yielded a paramagnetic product **10-CO**, as is evident by the ^{1}H NMR showing peaks from -10 ppm to 42 ppm, including a sharp singlet at -6.9 ppm and nine distinct peaks downfield of 11 ppm. The ν_{CO} stretch for **1-CO** with an unlabeled CO was 2023 cm^{-1}, and after metalation with Co, the ν_{CO} was lowered to 1973 cm^{-1}. This indicates that additional electron density is residing on the ruthenium with the addition of cobalt. When comparing **1-^{13}CO** to its deprotonated form, a decrease of 38 cm^{-1} in the ν_{CO} stretch was observed, whereas a decrease of 50 cm^{-1} was observed from **1-CO** to **10**. This difference suggests cobalt is adding to the electron density at the NHC nitrogen which is then being donated to the ruthenium center.

Work up and solvent choice both influence the observed ^{1}H NMR spectrum, highlighting the sensitivity of the binding pocket to solvent coordination of the metal centers. While the major species changes, the number of peaks and integrations are consistent with one major paramagnetic product consistent with **10**. In some cases, the peak distribution and integrations may suggest dimerization. DOSY NMR was attempted following literature precedent for analysis of paramagnetic complexes[27], however the available probes lacked sufficient gradient strength to obtain meaningful data. Elemental analysis of the isolated product was in close agreement with the calculated H, N, and C percentages (H: 4.158% exp. vs 4.287% calc.; N: 6.096% exp. vs 6.499% calc.; C: 40.263% exp. vs 40.870% calc.) with the assumption of three coordinated DMSO solvent molecules and two PF_6 counter ions. This data supports the assignment of **10** as drawn (Scheme 4.2).

Scheme 4.3. Synthesis of **11**.

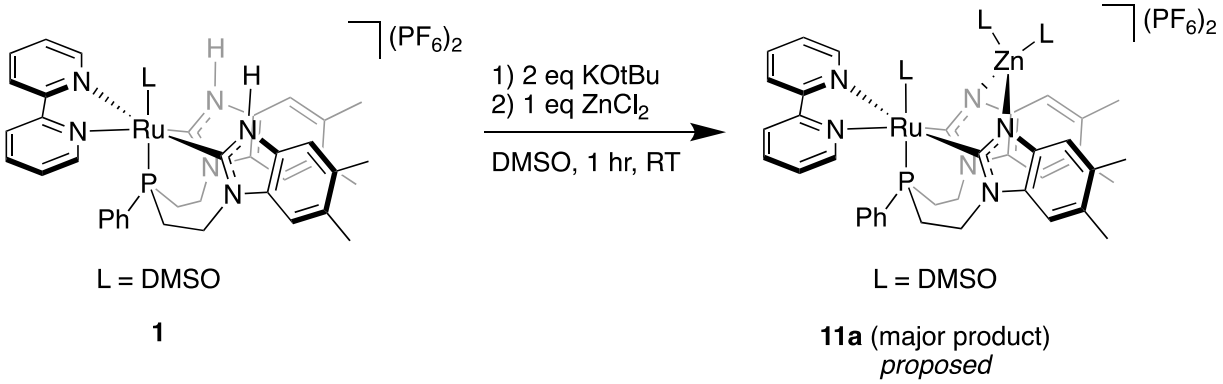

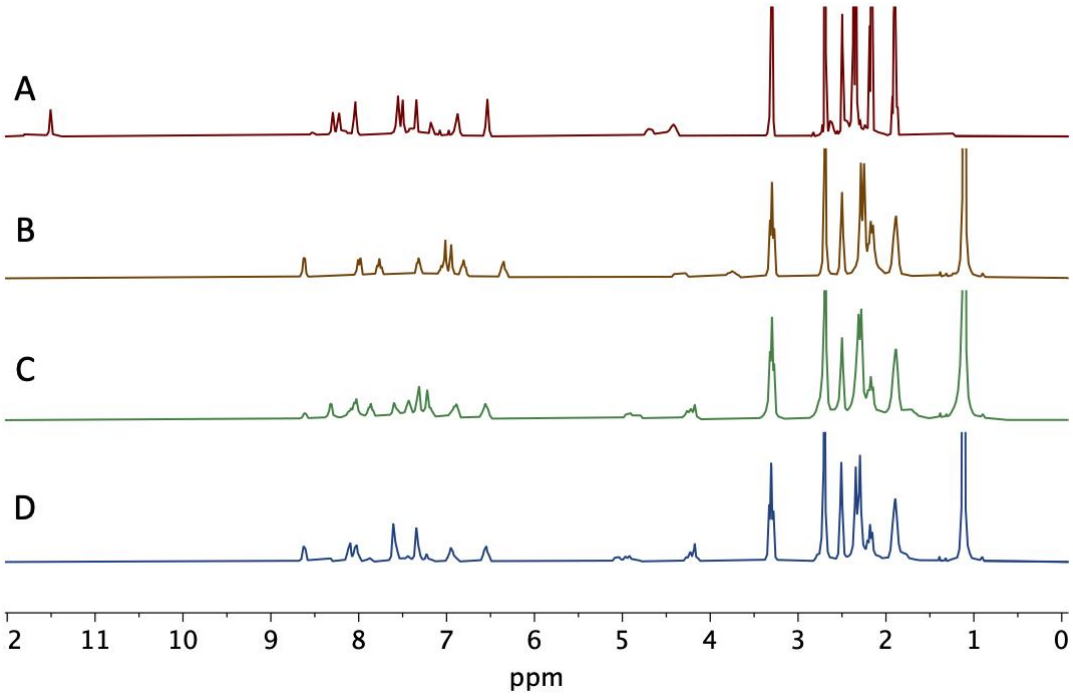

Figure 4.10. ^{1}H NMR (300 MHz, 298K, DMSO-d_6) of the reaction between **1** (A) deprotonated with 2 equivalents of KOtBu (B) followed by the addition of 1 equivalent (C) and 2 equivalents (D) of $ZnCl_2$.

The synthesis of the ruthenium-zinc bimetallic complex (**11**) was pursued following a similar procedure as for **10** (Scheme 4.3). Complex **1** is first deprotonated by 2 equivalents of KOtBu, followed by 1 addition of $ZnCl_2$. The diamagnetic product in the case of **11** allows for simple tracking of reaction progression by ^{1}H and ^{31}P NMR. With the addition of 1 equivalent of

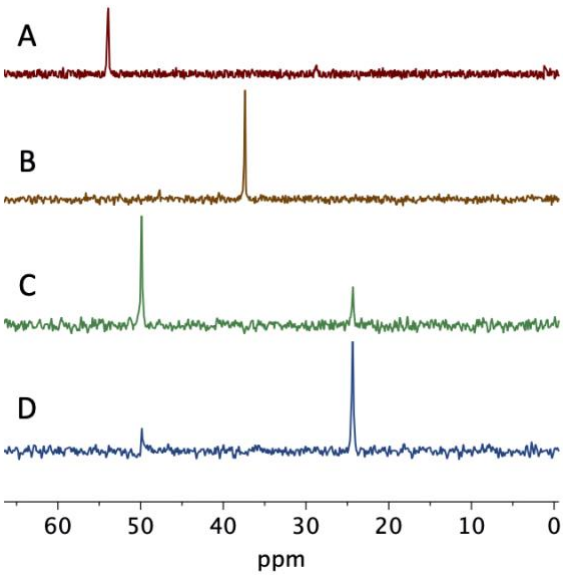

Figure 4.11. ^{31}P NMR (121.48 MHz, 298K, DMSO-d_6) of the reaction between **1** (A) deprotonated with 2 equivalents of KOtBu (B) followed by the addition of 1 equivalent, **11a**, (C) and 2 equivalents, **11b**, (D) of $ZnCl_2$.

$ZnCl_2$ two peaks are observed by ^{31}P NMR, with the major product (**11a**) at 49 ppm and the minor product at 24 ppm. The peak distribution was unaffected both by prolonged time at room temperature and by heating 75 ºC for 20 hours. The addition of a second equivalent of $ZnCl_2$ leads to the peak at 24 ppm being the major species, compound **11b** (Figures 4.10 and 4.11). The proposed structure of **11b** is an analog of the Ru-PR_3 complex previously characterized, which has **L** coordinated to the ruthenium through only the phosphine.[28] This structure has a similar ^{31}P NMR shift of 23.9 ppm. Another unique character of the Ru-PR_3 complex is its +4 charge. While the influence of geometry and charge are convoluted in predicting chemical shifts in ^{31}P NMR spectra, both may be relevant to **11b** with the possibility of incorporation two Zn(II) leading to a total +4 charge. Additionally, base promoted transmetalation of PNHCs has been observed from Mn(I) to Au(I), driven by the hard/soft character of the metals.[29,30]

Upon work up of **11b**, it is apparent that the PF_6^- has been displaced, as evidenced by its absence in the ^{31}P NMR spectrum. It is proposed that the second equivalent of $ZnCl_2$ provides

chlorides to the complex of interest, leading to the precipitation of $Zn(PF_6)_2$ salt. Additionally, the ^{31}P NMR resonance at 24 ppm is no longer the major species: additional peaks are present at 54 ppm and 51 ppm, with the peak at 54 ppm being the major species. One proposed explanation could be that in solution with two equivalents of $ZnCl_2$ transmetallation occurs, yielding the Ru-PR_3 analog with Zn(II) coordinated at each carbene. Under the work up conditions, concentrating under elevated temperatures and changing from DMSO to DCM, the Ru-PR_3 undergoes transmetallation back to **11a**. The two peaks at 54 ppm and 51 ppm can be explained by variation in coordination by Cl^- or solvent. Work up of **11a** yield did not yield any unexpected changes in product distribution, maintaining the compound with the ^{31}P NMR resonance at 49 ppm as the major species.

4.2.2 *Reactivity with Formate*

In addition to understanding metal-metal synergy, the ability to tune reactivity between the monometallic and bimetallic complexes is of interest. As previously reported by the Cossairt

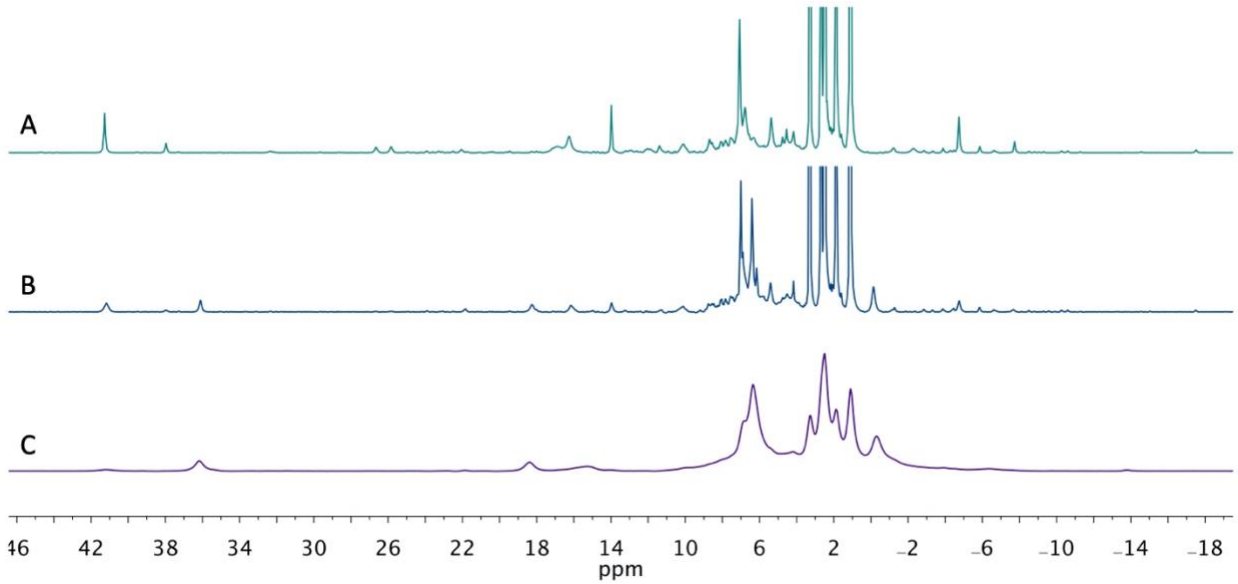

Figure 4.12. ^1H NMR (500 MHz, DMSO-d_6, 298K) of the reaction between **10** (A) and formate after 1 day at room temperature (B) and 4 days at room temperature (C).

group, complex **1** has been shown to facilitate the decomposition of formate to the CO_2 adduct, complex **6**, and liberate H_2 gas.[28] It is proposed that this proceeds through the elimination of the formate hydrogen atom with one of the PNHC NH-wingtips. By X-ray crystallography, the formate complex with **1** is shown to be a dimer, with formate bridging between two ruthenium atoms. With the installation of a second metal center occupying both nitrogen wingtip positions, it is anticipated that a different formate decomposition pathway would be observed.

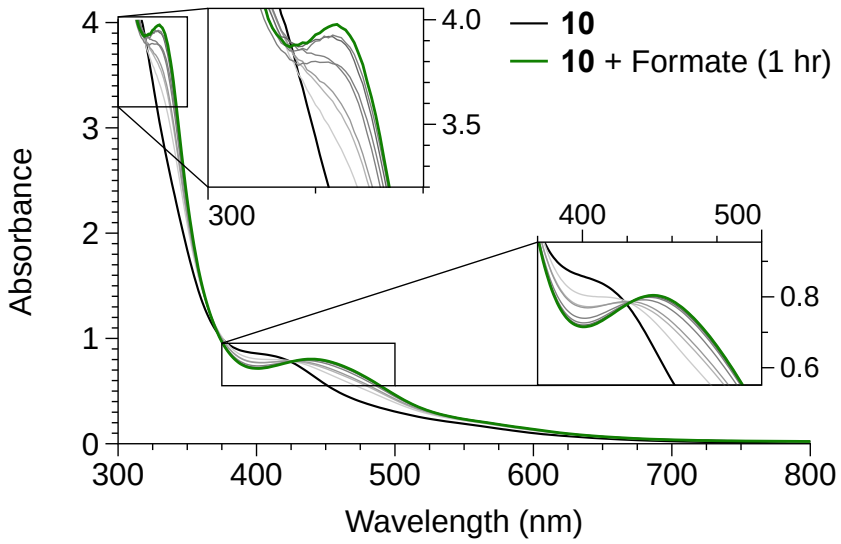

Figure 4.13. UV-vis spectrum showing the reaction progression between **1** and formate up to 60 minutes.

Both complexes **10** and **11** undergo reaction with formate. While **10** itself is challenging to isolate and sensitive to solvation, the addition of excess formate reliably yields one major product (Complex **12**) characterized by ^{1}H NMR and UV-vis. By ^{1}H NMR, the characteristic peaks are two singlets at 18.37 ppm and 36.19 ppm, as well as a lower intensity and broad peak at 41.17 ppm. These peaks are accompanied by a cluster of broad, stronger signal peaks in the diamagnetic range (Figure 4.12). The UV-vis spectrum tracking the reaction progress between **1** and formate shows a clean transformation, indicated by a red shift of the MLCT band from 431 nm to 445 nm as well as a new higher energy band at 330 nm (Figure 4.13). Characterization by

X-Ray crystallography has yielded inconsistent products, likely due to variability with solvent conditions (Figure 4.1, A and B).

Both **11a** and **11b** undergo reactivity with formate to yield the same product (Scheme 4.4). With the addition of 5 equivalents of $NaH^{13}CO_2$ separately to **11a** and **11b** in DMSO-d_6, there is conversion to a single product characterized by ^{31}P NMR with a peak at 53 ppm (Figure 4.14 and 4.15). The ^{1}H NMR also shows one major species accompanied by the resonance of the excess ^{13}C-formate with its characteristic $^{1}J_{CH}$ splitting pattern. Interestingly, while the formate appears unreacted it is slightly shifted and has a slightly smaller coupling constant compared to the control spectrum taken with just ^{13}C-formate and $ZnCl_2$ in DMSO-d_6 (Figure 4.16). By ^{13}C NMR there are two peaks at 166 ppm and 168 ppm. These are both close to the expected chemical shift for free formate.

After holding the reaction between **11a** and ^{13}C-formate at 75 ºC for 24 hours there is evidence in the ^{13}C NMR of free CO_2 evolution at 124 ppm, in addition to the formate peak at 166 ppm (Figure 4.17). There is also a very small amount of H_2 gas evident in the ^{1}H NMR appearing at 4.61 ppm (Figure 4.18). Interestingly, there is no change in the product **13** peaks in either the ^{1}H or the ^{31}P NMR spectra, which may indicate that this CO_2 and H_2 evolution is due to natural formate decomposition.

Scheme 4.4. Reactivity of **11a** and **11b** and Formate.

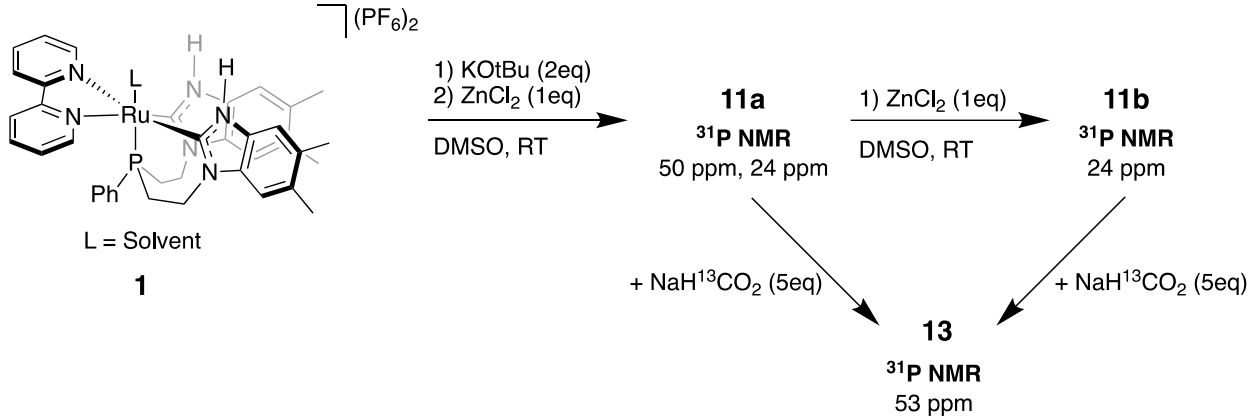

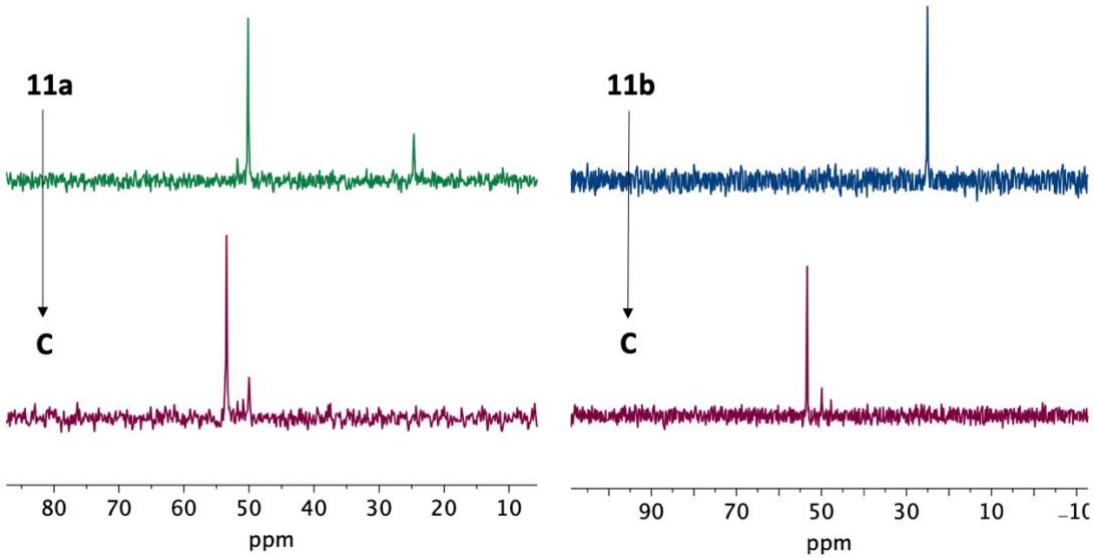

Figure 4.14. ^{31}P NMR (121 MHz, DMSO-d_6, 298K) of the reactions between **11a** and **11b** and 5 equivalents of $NaH^{13}CO_2$.

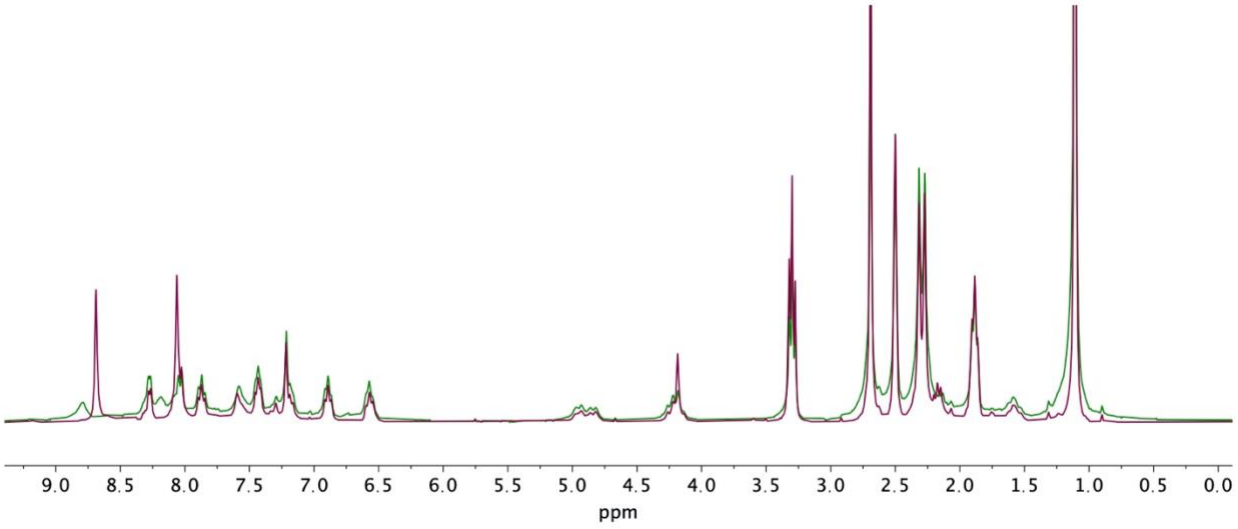

Figure 4.15. ^{1}H NMR (300 MHz, DMSO-d6, 298K) overlay of **13** synthesized from **11a** and **11b** with 5 equivalents of $NaH^{13}CO_2$.

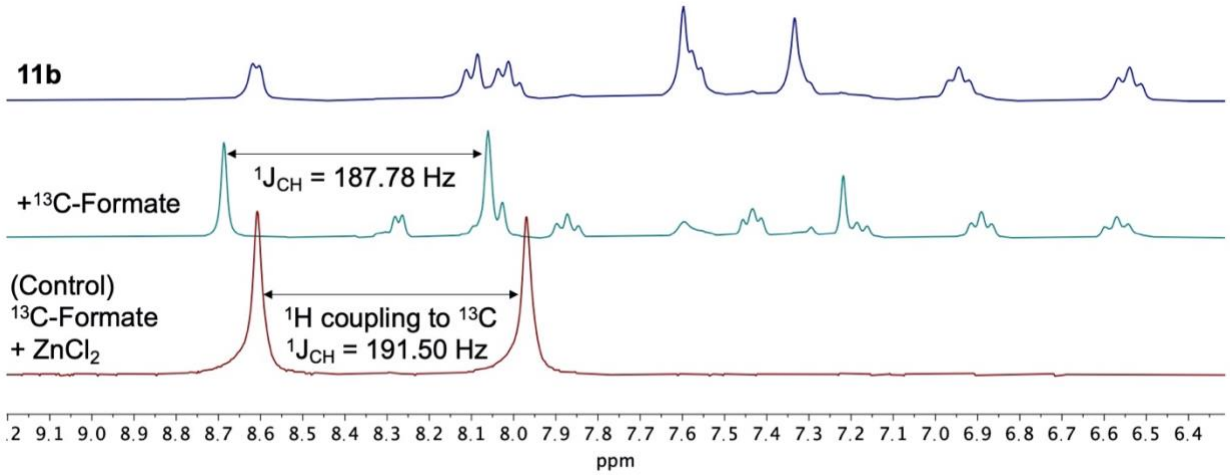

Figure 4.16. ^{1}H NMR (300 MHz, DMSO-d_6, 298K) illustrating the slight changes in chemical shift and $^{1}J_{CH}$ coupling for the excess formate between reaction with **11b** and $ZnCl_2$ alone.

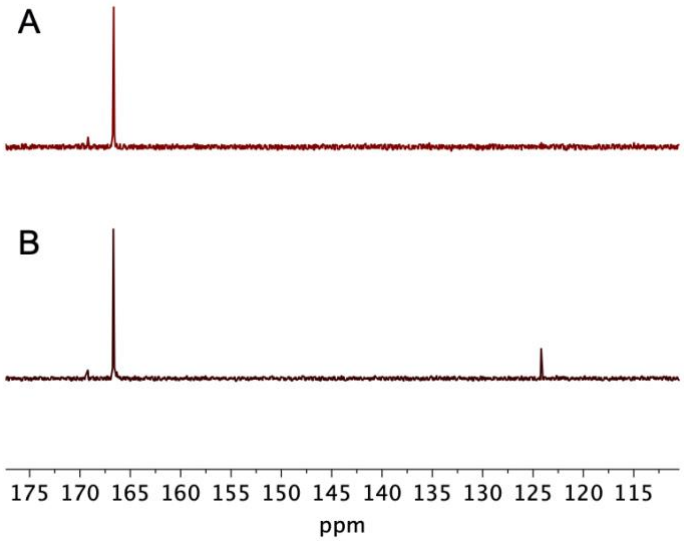

Figure 4.17. ^{13}C NMR (125 MH, 298K, DMSO-d_6) of **11b** with ^{13}C-formate before (A) and after heating at 75 ºC for 24 hr (B).

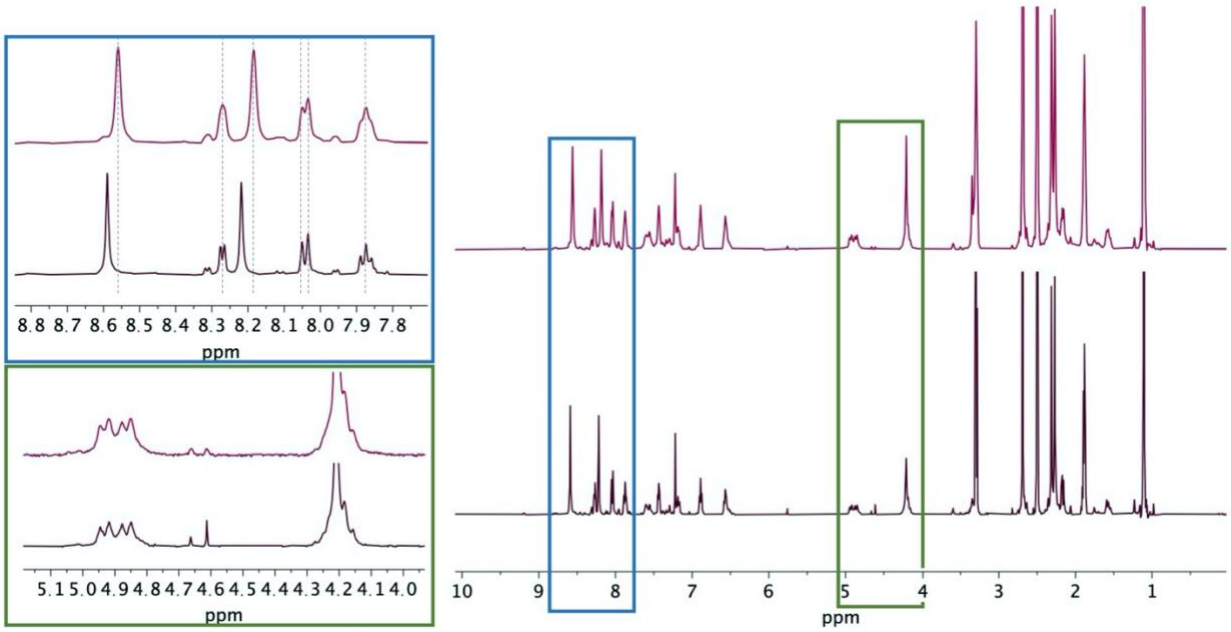

Figure 4.18. ^{1}H NMR (500 MHz, DMSO-d_6, 298 K) of **11a** with ^{13}C-formate (top) and after 24 hours at 75 ºC.

4.2.3 *Other Reactivity*

Among the initially stated observed coordination environments of cobalt within the PNHC coordination environment was the coordination of a μ-OH ligand, bridging between the ruthenium and the cobalt (Complex **10-dimer**, Figure 1C and Figure 4). This structure was obtained twice; first, after dissolving **10** in THF, which within minutes lead to the formation of blue/green crystals. Second was after synthesis of **10** in acetonitrile which was then recrystallized from a layered solution of DCM and benzene. This second structure was disordered, with a μ-OH^- ligand in 69% of the molecules and μ-Cl^- in 31%. It is hypothesized that the μ-OH ligand is a result of adventitious water. To study this type of bridging and the reactivity opportunities associated with it, 2 equivalents of tetrabutylammonium hydroxide (40wt%) in methanol were added to complex **10**. There was a clear transition in the ^{1}H NMR, showing a major species with broad peaks at 30 ppm, 14 ppm, 11 ppm, and a broad set of peaks in the typical diamagnetic region (Figure). This coordination environment appears to favor anionic oxygen containing

ligands (OH, formate) capable of bridging between two cobalt atoms and/or ruthenium-cobalt in the solid state.

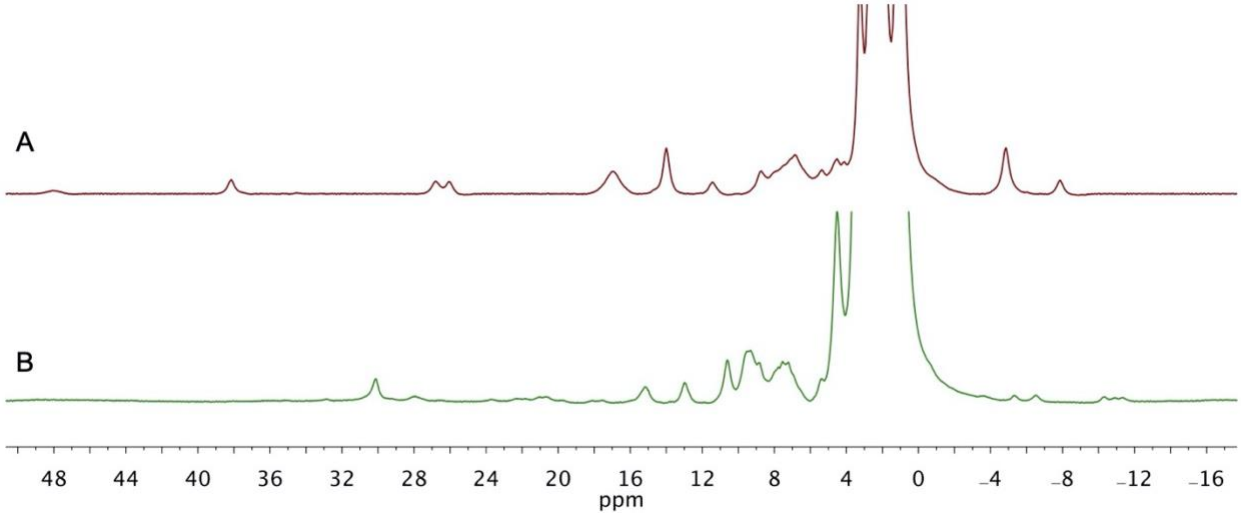

Figure 4.19. ^{1}H NMR (500 MHz, DMSO-d_6, 298 K) of **10** synthesized in situ (A) followed by the addition of 2 equivalents of tetrabutylammonium hydroxide (40wt%) in methanol (B).

4.3 CONCLUSIONS

The metalation of **1** to form heterobimetallic complexes with available coordination sites on both metals was pursued following prior work performed for the metalation of the Cp* analog, **2**.[7] While evidence of successful synthesis of both the Ru/Co (**10**) and Ru/Zn (**11**) is apparent, the coordination environment is far more dynamic and sensitive to conditions such as solvent and concentration relative to the Cp* system. This is likely due to the impact that the ancillary ligand has on the orientation of the PNHCs relative to one another, requiring more strain from the starting complex **1** to achieve κ^2N,N'-Co chelation binding motif. By X-ray crystallography we were able to confirm that the two metals are capable of coordinating a bridging ligand, specifically anionic oxygen containing ligands (OH-, formate) which form μ-O bonds between the Co and Ru in the solid state. This is promising for the pursuit of X–O or X=O bond activation reactivity with this complex.

4.4 EXPERIMENTAL

4.4.1 *General Considerations*

All manipulations were carried out under an N_2 atmosphere, either in a glovebox or using Schlenk technique, unless otherwise noted. THF, CH_2Cl_2, Et_2O, and CH_3CN were purchased from Fisher Scientific and dried on a solvent purification system. KOtBu, KHMDS, $CoCl_2$, $ZnCl_2$, ^{13}C-Sodium Formate were purchased from Sigma-Aldrich and dried as necessary. Deuterated NMR solvents were purchased from Cambridge Isotope Lab Inc. Unless manipulations were performed in air, all NMR solvents were dried over 4Å molecular sieves, vacuum transferred or vacuum distilled as necessary, and stored in the glovebox over 4Å molecular sieves. THF-d_8 was purchased in ampules and used without further purification. ^{1}H, ^{13}C, and ^{31}P NMR were recorded on either a Bruker AV300, Bruker AV301, Bruker AV 500, or Bruker AV700 spectrometer. [Ru(bpy)(H_2O)(P^{Ph}(PNHC)$_2$)](PF_6)$_2$ (**1**) was synthesized according to section 2.4.

Cyclic voltammetry was carried out using an Epsilon Potentiostat (BASi) in an N_2 glovebox. The electrolyte solution was 0.2 M tetrabutylammonium hexafluorophosphate in CH_3CN, with a glassy carbon working electrode, platinum counter electrode, and a Ag wire pseudo reference electrode in a Vycor-fritted compartment. The tetrabutylammonium hexafluorophosphate electrolyte was recrystallized two times in EtOH and dried overnight under vacuum at 100 ºC. Glass carbon electrodes with a diameter of 3.0 mm were polished using 1.0, 0.3, and 0.05 micron polishing powder followed by 5 minute sonication cycles in deionized water. All CVs were referenced to a ferrocene internal standard added after the experiment.

4.4.2 *Synthesis and Characterization*

[Ru(bpy)(DMSO)(P(Ph)(NHC)$_2$-κ^2-N,N'-Co(DMSO)$_2$)](PF$_6$)$_2$ (10). Complex **1** (50 mg, 0.0490 mmol, 1 eq), KOtBu (11 mg, 0.0980 mmol, 2 eq), and $CoCl_2$ (6.4 mg, 0.0490 mmol, 1 eq) separately in 2 mL, 1.5 mL, and 1.5 mL DMSO respectively and frozen. While thawing, the KOtBu solution is added to the thawing and stirring solution of **1**. The reaction mixture is stirred at room temperature for 10 minutes before freezing. The $CoCl_2$ solution is then added while thawing to the thawing and stirring reaction mixture, which is stirred together for 1 hour at room temperature. The solution was then concentrated under vacuum at 50 ºC, dissolved in DCM, filtered through a PTFE syringe filter, concentrated, stirred in Et_2O for 45 minutes, and collected as a pale brown powder on a frit. Crystals suitable for X-ray diffraction were grown from DCM layered with C_6H_6 and showed a structure in the solid state similar to **10-dimer**, with 69% of the molecules with bridging OH^- ligands and 31% with bridging Cl^- ligands (Complex **10-dimer$_{OH/Cl}$**, Figure 4.20). Elemental Analysis – Predicted (Actual): C: 40.870 (40.263); H: 4.287 (4.158); N: 6.499 (6.096).

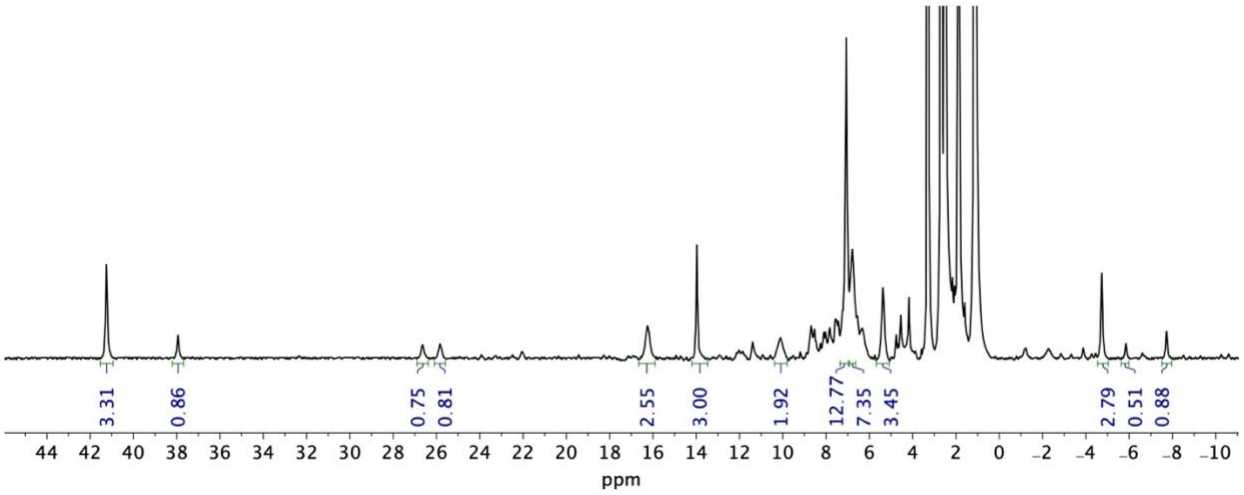

Figure 4.20. ^{1}H NMR (500 MHz, 298k, DMSO-d_6) of **10**.

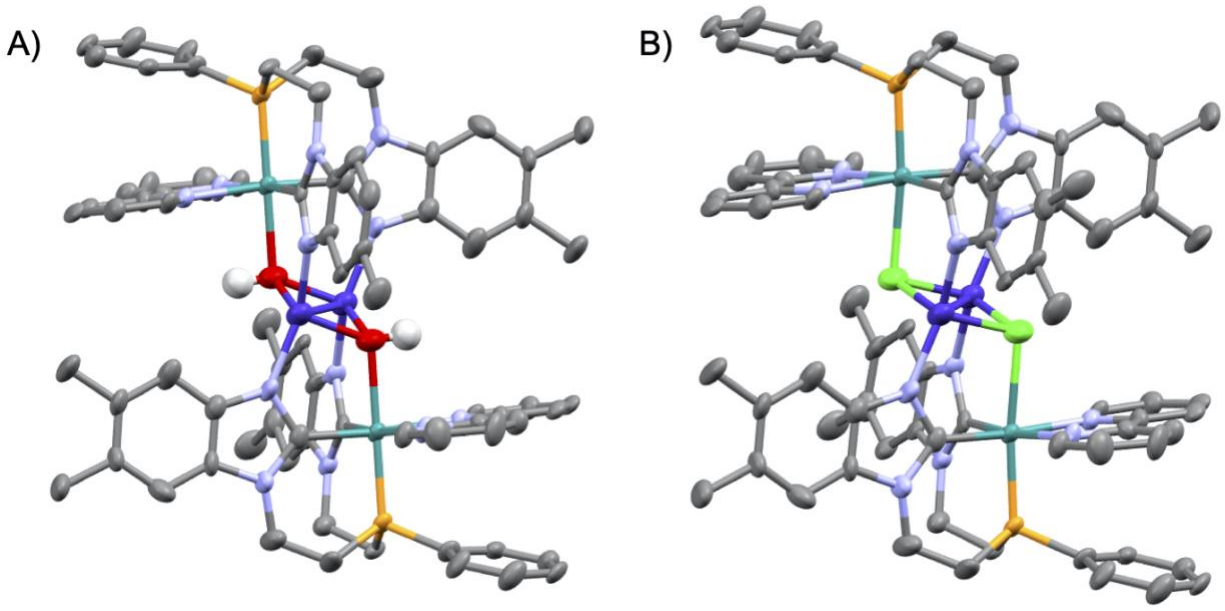

Figure 4.21. Crystal Structures obtained for **10-dimer$_{OH/Cl}$**, with 69% of the molecules with bridging OH^- ligands (A) and 31% with bridging Cl^- ligands (B). All hydrogen atoms, except for hydroxide protons, and one PF_6^- anions, one benzene, and one DMC solvent molecule were excluded for clarity.

[Ru(bpy)(DMSO)(P(Ph)(NHC)$_2$-κ^2-N,N'-Zn(DMSO)$_2$)](PF$_6$)$_2$ (11). Complex **11a**: Complex **1** (50 mg, 0.0490 mmol, 1 eq), KOtBu (11 mg, 0.0980 mmol, 2 eq), and $ZnCl_2$ (6.8 mg, 0.0490 mmol, 1 eq) separately in in 2 mL, 1.5 mL, and 1.5 mL DMSO respectively and frozen. While thawing, the KOtBu solution is added to the thawing and stirring solution of **1**. The reaction mixture is stirred at room temperature for 10 minutes before freezing. The $ZnCl_2$ solution is then added while thawing to the thawing and stirring reaction mixture, which is stirred together for 1 hour at room temperature. The solution was then concentrated under vacuum at 50 ºC, dissolved in DCM, filtered through a PTFE syringe filter, concentrated, stirred in Et_2O for 45 minutes, and collected as a pale brown powder on a frit. There remains approximately 20% impurity of **11b**. Isolated: 37 mg. ^{1}H NMR (DMSO-d_6, 300 MHz, 298 K): δ 8.31 (d, *J* = 4.80 Hz, 2H), 8.12–7.97 (m, 5H), 7.86 (t, *J* = 6.79 Hz, 2H), 7.48–7.38 (m, 2H), 7.31 (s, 2H), 7.22 (s, 2H), 7.00–6.84 (m,

2H), 6.64–6.48 (m, 2H), 5.00–4.74 (m, 2H), 4.37–4.10 (m, 2H), 2.31 (s, 6H), 2.28 (s, 2H). ^{31}P NMR (DMSO-d_6, 121 MHz, 298 K): δ 49.88.

Complex **11b**: Complex **1** (15 mg, 0.0147 mmol, 1 eq), KOtBu (3.3 mg, 0.0294 mmol, 2 eq), and $ZnCl_2$ (2 mg, 0.0147 mmol, 1 eq) separately in in 0.5 mL, 0.4 mL, and 0.4 mL of DMSO-d_6 respectively and frozen. While thawing, the KOtBu solution is added to the thawing and stirring solution of **1**. The reaction mixture is stirred at room temperature for 10 minutes before freezing. The $ZnCl_2$ solution is then added while thawing to the thawing and stirring reaction mixture, and the solution was transferred to a J Young tube. After collecting NMR data of the reaction mixture with 1 eq of ZnCl2 (11a), the mixture in the J Young tube was frozen and an additional 1 eq of ZnCl2 (2 mg, 0.0147 mmol) was added while thawing, inverting the J Young tube to mix. The resulting product, **11b**, was characterized by ^{1}H and ^{31}P NMR. ^{1}H NMR (DMSO-d_6, 300 MHz, 298 K): δ 8.62 (d, *J* = 4.68 Hz, 2H), 8.11 (d, *J* = 8.57 Hz, 2H), 8.02 (t, *J* = 7.60 Hz, 2H), 7.64–7.53 (m, 5H), 7.34 (m, 4H), 6.94 (t, *J* = 7.77 Hz, 2H), 6.54 (t, *J* = 7.65 Hz, 2H), 4.99 (dd, *J* = 36.099 Hz, 13.82 Hz, 2H), 4.34–4.09 (m, 4H), 2.34 (s, 6H), 2.29 (s, 6H). ^{31}P NMR (DMSO-d_6, 121 MHz, 298 K): δ 24.37.

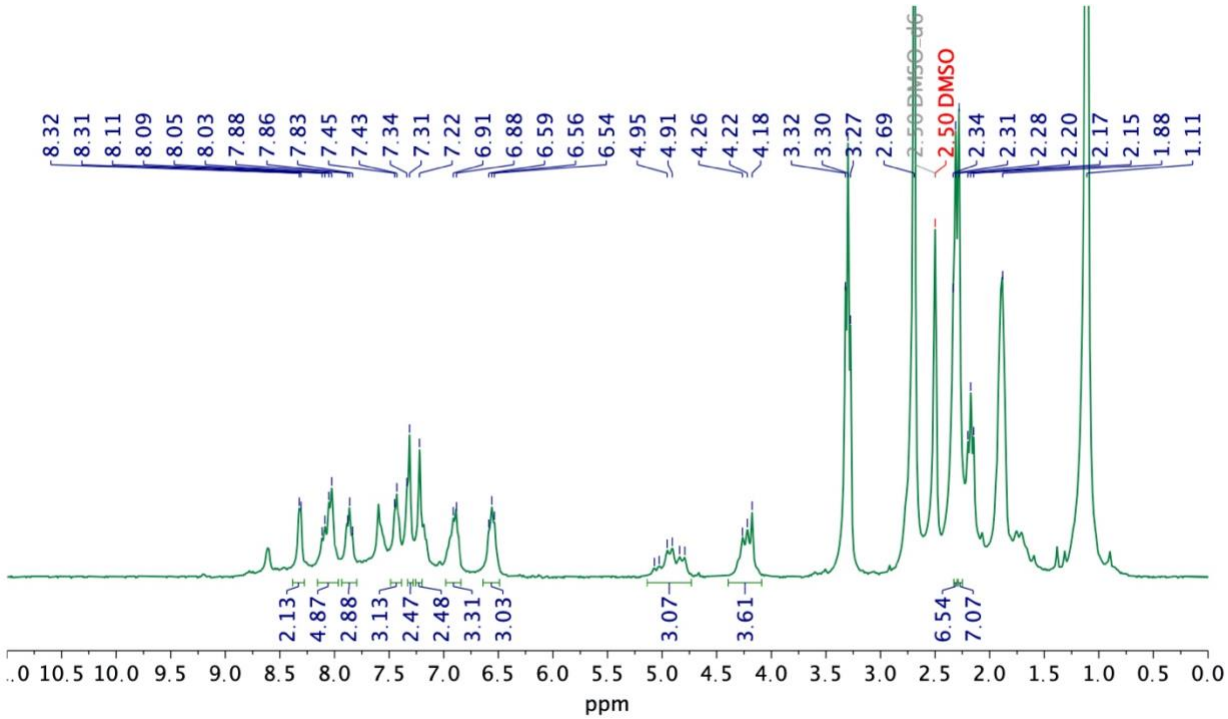

Figure 4.22. ^{1}H NMR (DMSO-d$_6$, 300 MHz, 298 K) of **11a** with **11b** impurity.

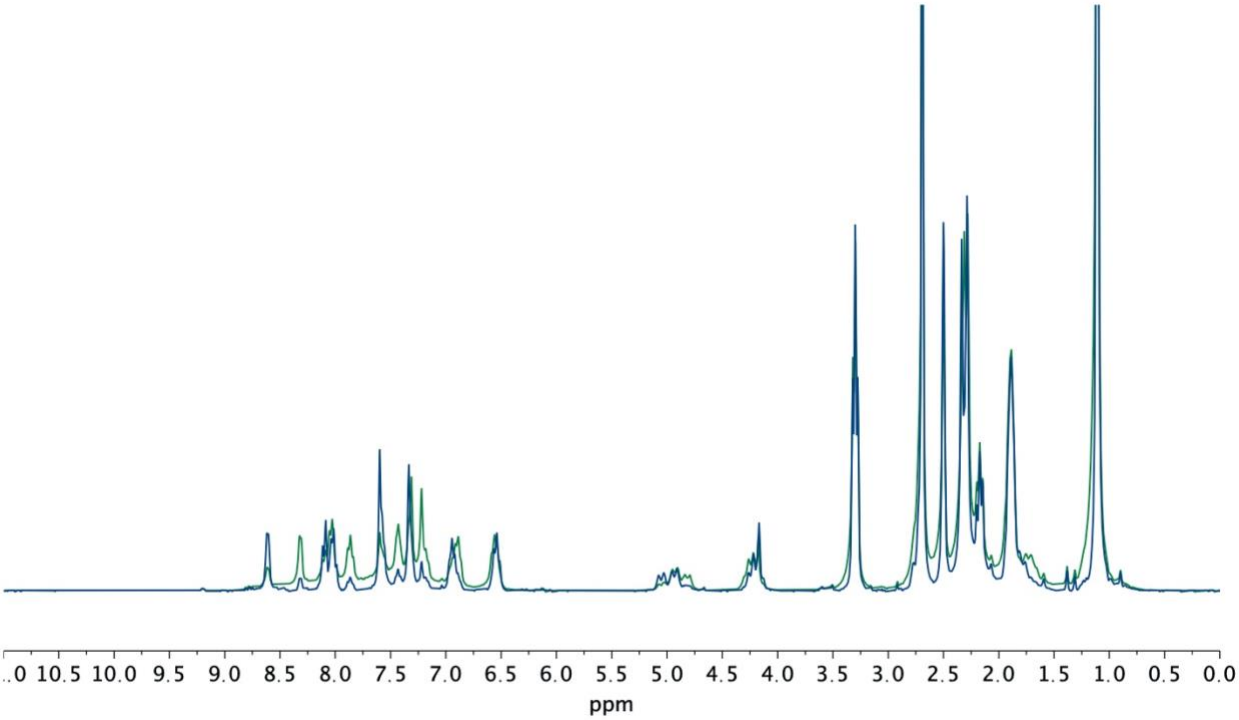

Figure 4.23. Stacked spectra of **11a** (green) and **11b** (blue) to illustrate changes in peak distribution.

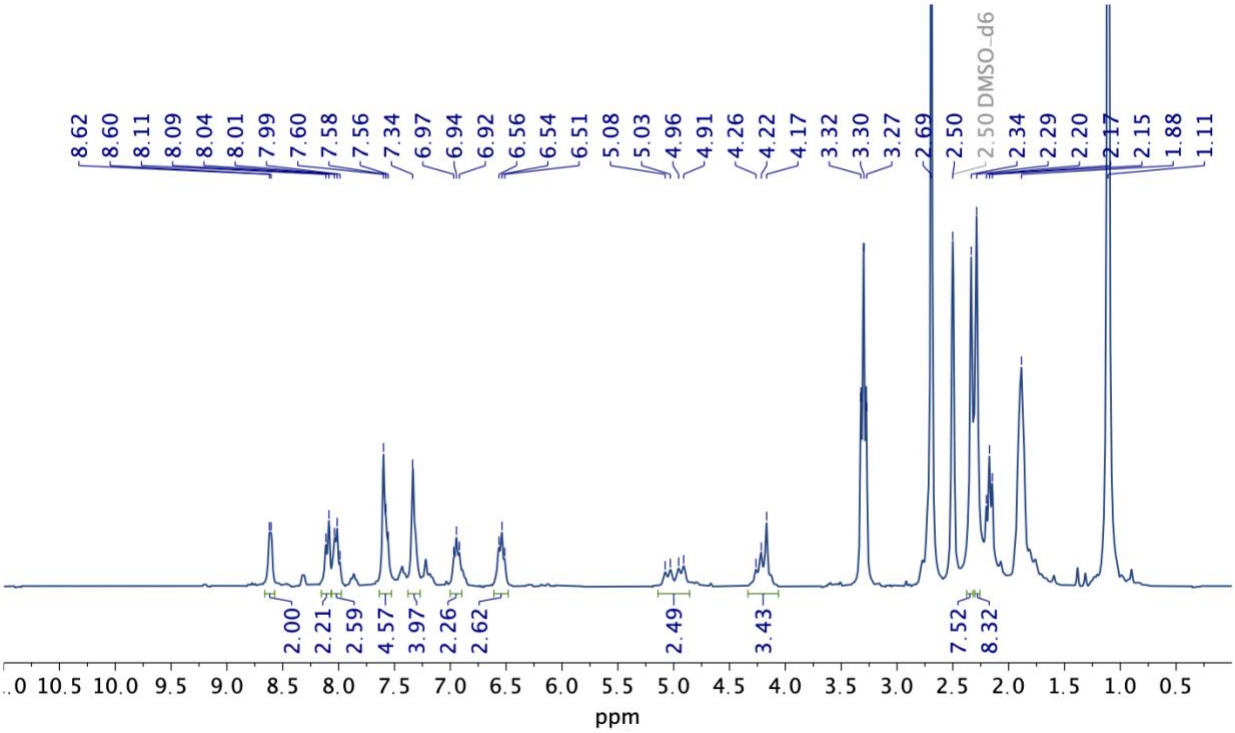

Figure 4.24. ^{1}H NMR (DMSO-d$_6$, 300 MHz, 298 K) of **11b** with **11a** impurity.

4.4.3 *Reactivity Studies*

Reactivity of complex 10 with ^{13}C-sodium formate (12). Complex **10** was synthesized in situ in a J Young tube. The solution in the J Young tube was frozen along side ^{13}C-sodium formate (5 equivalents relative to starting material complex **1**) in DMSO-d$_6$. The formate solution was added to the J Young tube while thawing, and the J Young tube was inverted to mix. The reaction was monitored by ^{1}H NMR (Figure 4.12) and UV-Vis (Figure 4.13).

Reactivity of complex 11 with ^{13}C-sodium formate (13). Complex **11a** and **11b** were synthesized in situ in J Young tubes. The solution in the J Young tube was frozen along side ^{13}C-sodium formate (5 equivalents relative to starting material complex **1**) in DMSO-d$_6$. The formate solution was added to the J Young tube while thawing, and the J Young tube was inverted to mix. The reaction was monitored by ^{1}H, ^{31}P, and ^{13}C NMR (Figures 4.14-4.18).

Reactivity of complex **10** with Hydroxide. Complex **10** was synthesized in situ and transferred to a standard NMR capped with an NMR tube septa. A solution of tetrabutylammonium (TBA) hydroxide 40wt% in MeOH was sparged with nitrogen for 30 minutes, and 2 equivalents of (TBA)(OH) (13.97 µL, 0.0490 mmol) were added through the septa via micro syringe. Reaction was monitored by ^{1}H NMR (Figure 4.19).

4.4.4 *Crystallographic Information*

Complexes **1**[28], **2**[7], and **9-Fe**[7] were reported previously in the literature.

Table 4.14. Crystallographic information for complex **10-dimer**.

Empirical formula	C116 H156 Co2 F12 N12 O12 P4 Ru2	
Formula weight	2582.40	
Temperature	100(2) K	
Wavelength	0.71073 Å	
Crystal system	Triclinic	
Space group	P -1	
Unit cell dimensions	a = 13.461(5) Å	α= 89.828(5)°.
	b = 15.519(5) Å	β= 70.798(5)°.
	c = 15.876(5) Å	γ = 69.376(5)°.
Volume	2907.3(17) Å^3	
Z	1	
Density (calculated)	1.475 Mg/m^3	
Absorption coefficient	0.675 mm^{-1}	
F(000)	1342	
Crystal size	0.250 x 0.200 x 0.070 mm^3	
Theta range for data collection	1.369 to 25.154°.	
Index ranges	-16<=h<=16, -18<=k<=18, -18<=l<=18	
Reflections collected	20166	
Independent reflections	10231 [R(int) = 0.0423]	
Completeness to theta = 25.000°	98.1 %	
Refinement method	Full-matrix least-squares on F^2	
Data / restraints / parameters	10231 / 421 / 760	
Goodness-of-fit on F^2	1.036	
Final R indices [I>2sigma(I)]	R1 = 0.0464, wR2 = 0.1057	
R indices (all data)	R1 = 0.0704, wR2 = 0.1195	
Largest diff. peak and hole	2.464 and -0.895 e.Å^{-3}	

Table 4.15.. Crystallographic information for complex **10-dimer$_{OH/Cl}$**.

Empirical formula	C90 H91.38 Cl4.62 Co2 F12 N12 O1.38 P4 Ru2
Formula weight	2198.86

Temperature	100(2) K	
Wavelength	0.71073 Å	
Crystal system	Triclinic	
Space group	P -1	
Unit cell dimensions	a = 11.2340(9) Å	α= 107.173(6)°.
	b = 13.2065(12) Å	β= 102.110(6)°.
	c = 16.3287(15) Å	γ = 92.743(6)°.
Volume	2247.4(4) $Å^3$	
Z	1	
Density (calculated)	1.625 Mg/m^3	
Absorption coefficient	0.982 mm^{-1}	
F(000)	1115	
Crystal size	0.100 x 0.070 x 0.050 mm^3	
Theta range for data collection	1.343 to 25.155°.	
Index ranges	-13<=h<=13, -15<=k<=15, -19<=l<=19	
Reflections collected	15864	
Independent reflections	8046 [R(int) = 0.1704]	
Completeness to theta = 25.000°	99.7 %	
Refinement method	Full-matrix least-squares on F^2	
Data / restraints / parameters	8046 / 65 / 625	
Goodness-of-fit on F^2	0.972	
Final R indices [I>2sigma(I)]	R1 = 0.0844, wR2 = 0.1859	
R indices (all data)	R1 = 0.2107, wR2 = 0.2490	
Largest diff. peak and hole	1.242 and -1.404 $e.Å^{-3}$	

Table 4.16. Crystallographic information for complex **12-dimer**.

Empirical formula	C82 H88 Co N12 O6 P2 Ru2 S2	
Formula weight	1724.77	
Temperature	100(2) K	
Wavelength	0.71073 Å	
Crystal system	Triclinic	
Space group	P -1	
Unit cell dimensions	a = 13.7721(13) Å	α= 113.666(4)°.
	b = 14.0309(13) Å	β= 100.266(4)°.
	c = 14.5174(14) Å	γ = 109.117(4)°.
Volume	2266.9(4) $Å^3$	
Z	1	
Density (calculated)	1.263 Mg/m^3	
Absorption coefficient	0.644 mm^{-1}	
F(000)	889	
Crystal size	0.080 x 0.070 x 0.050 mm^3	
Theta range for data collection	1.640 to 28.589°.	
Index ranges	-18<=h<=17, -18<=k<=18, -14<=l<=19	
Reflections collected	17846	
Independent reflections	11397 [R(int) = 0.0589]	
Completeness to theta = 25.000°	99.8 %	

Refinement method	Full-matrix least-squares on F^2
Data / restraints / parameters	11397 / 42 / 528
Goodness-of-fit on F^2	0.994
Final R indices [I>2sigma(I)]	R1 = 0.0506, wR2 = 0.0970
R indices (all data)	R1 = 0.0955, wR2 = 0.1122
Largest diff. peak and hole	0.581 and -0.792 e.Å^{-3}

Table 4.17. Crystallographic information for complex **12-trimer**.

Empirical formula	C129 H147 Cl Co3 N21 O7 P3 Ru3 S6	
Formula weight	2904.39	
Temperature	100(2) K	
Wavelength	0.71073 Å	
Crystal system	Trigonal	
Space group	P -3	
Unit cell dimensions	a = 26.0284(13) Å	α= 90°.
	b = 26.0284(13) Å	β= 90°.
	c = 15.0281(11) Å	γ = 120°.
Volume	8817.2(11) Å^3	
Z	2	
Density (calculated)	1.094 Mg/m^3	
Absorption coefficient	0.686 mm^{-1}	
F(000)	2990	
Crystal size	0.210 x 0.060 x 0.060 mm^3	
Theta range for data collection	1.355 to 25.432°.	
Index ranges	-31<=h<=31, -31<=k<=31, -18<=l<=18	
Reflections collected	150003	
Independent reflections	10786 [R(int) = 0.0623]	
Completeness to theta = 25.000°	99.7 %	
Refinement method	Full-matrix least-squares on F^2	
Data / restraints / parameters	10786 / 18 / 549	
Goodness-of-fit on F^2	1.055	
Final R indices [I>2sigma(I)]	R1 = 0.0371, wR2 = 0.0955	
R indices (all data)	R1 = 0.0586, wR2 = 0.1088	
Largest diff. peak and hole	1.332 and -1.156 e.Å^{-3}	

4.5 REFERENCES

(1) De, S.; Dokania, A.; Ramirez, A.; Gascon, J. Advances in the Design of Heterogeneous Catalysts and Thermocatalytic Processes for CO 2 Utilization. *ACS Catal.* **2020**, *10* (23), 14147–14185. https://doi.org/10.1021/acscatal.0c04273.

(2) Iglesia, E.; Soled, S. L.; Fiato, R. A.; Via, G. H. Bimetallic Synergy in Cobalt Ruthenium Fischer-Tropsch Synthesis Catalysts. *J. Catal.* **1993**, *143* (2), 345–368. https://doi.org/10.1006/jcat.1993.1281.

(3) Hidai, M.; Matsuzaka, H. Chemistry of Cobalt-Ruthenium Mixed Metal Complexes: Carbonylation and Metalloselective Substitution Reactions. *Polyhedron* **1988**, *7* (22–23), 2369–2374. https://doi.org/10.1016/S0277-5387(00)86354-8.

(4) Krogman, J. P.; Foxman, B. M.; Thomas, C. M. Activation of CO 2 by a Heterobimetallic Zr/Co Complex. *J. Am. Chem. Soc.* **2011**, *133* (37), 14582–14585. https://doi.org/10.1021/ja2071847.
(5) Krogman, J. P.; Bezpalko, M. W.; Foxman, B. M.; Thomas, C. M. Synthesis, Structure, and Reactivity of an Anionic Zr–Oxo Relevant to CO 2 Reduction by a Zr/Co Heterobimetallic Complex. *Inorg. Chem.* **2013**, *52* (6), 3022–3031. https://doi.org/10.1021/ic302473j.
(6) Walker, W. K.; Kay, B. M.; Michaelis, S. A.; Anderson, D. L.; Smith, S. J.; Ess, D. H.; Michaelis, D. J. Origin of Fast Catalysis in Allylic Amination Reactions Catalyzed by Pd–Ti Heterobimetallic Complexes. *J. Am. Chem. Soc.* **2015**, *137* (23), 7371–7378. https://doi.org/10.1021/jacs.5b02428.
(7) Flowers, S. E.; Cossairt, B. M. Mono- and Dimetalation of a Tridentate Bisimidazole-Phosphine Ligand. *Organometallics* **2014**, *33* (17), 4341–4344. https://doi.org/10.1021/om500592u.
(8) Kuwata, S.; Hahn, F. E. Complexes Bearing Protic N-Heterocyclic Carbene Ligands. *Chem. Rev.* **2018**. https://doi.org/10.1021/acs.chemrev.8b00176.
(9) Evans, K. J.; Mansell, S. M. Functionalised N-Heterocyclic Carbene Ligands in Bimetallic Architectures. *Chem. – Eur. J.* **2020**, *26* (27), 5927–5941. https://doi.org/10.1002/chem.201905510.
(10) Jin, H.; Kluth, P.; Hahn, F. E. Synthesis of Complexes with Protic NH,NR-NHC Ligands by Oxidative Addition of N-Alkyl-2-Iodoimidazoles to [M(PPh3)4] (M = Pd, Pt) Complexes. *Eur. J. Inorg. Chem.* **2017**, *2017* (20), 2774–2781. https://doi.org/10.1002/ejic.201700403.
(11) He, F.; Danopoulos, A. A.; Braunstein, P. Trifunctional PNHC, Imine, Pyridine Pincer-Type Iridium(III) Complexes: Synthetic, Structural, and Reactivity Studies. *Organometallics* **2016**, *35* (2), 198–206. https://doi.org/10.1021/acs.organomet.5b00926.
(12) Rong, M. K.; Chirila, A.; Franciolus, D.; Lutz, M.; Nieger, M.; Ehlers, A. W.; Slootweg, J. C.; Lammertsma, K. Protic NHC Iridium Complexes with β-H Reactivity–Synthesis, Acetonitrile Insertion, and Oxidative Self-Activation. *Organometallics* **2019**, acs.organomet.9b00584. https://doi.org/10.1021/acs.organomet.9b00584.
(13) Bente, S.; Kampert, F.; Tan, T. T. Y.; Hahn, F. E. Site-Selective Metallation of Dicarbene Precursors. *Chem. Commun.* **2018**, *54* (91), 12887–12890. https://doi.org/10.1039/C8CC08440H.
(14) Tegethoff, M.; Roelfes, F.; Schulte to Brinke, C.; Tan, T. T. Y.; Kampert, F.; Jin, G.-X.; Hahn, F. E. Synthesis of Heterobimetallic Complexes by Coordination of Rhodium(III) and Iridium(III) Poly-N,O-NHC Complexes to Silver(I), Copper(II), and Zinc(II). *Organometallics* **2018**. https://doi.org/10.1021/acs.organomet.8b00252.
(15) Hahn, F. E.; Hein, P.; Lügger, T. Synthesis of Heterobimetallic Metal Derivatives: A Carbene Complex as Chelate Ligand. *Z. Für Anorg. Allg. Chem.* **2003**, *629* (7–8), 1316–1321. https://doi.org/10.1002/zaac.200300078.
(16) Li, W.; Kim, C. K. Theoretical Investigations on the Methylation of N H Bond Using CO 2 and Hydrosilane Catalyzed by Zinc II Complexes: Mechanism and Ligand Effect. *J. CO2 Util.* **2017**, *20*, 178–189. https://doi.org/10.1016/j.jcou.2017.05.016.
(17) Miller, G. B. S.; Uggerud, E. C−C Bond Formation of Mg- and Zn-Activated Carbon Dioxide. *Chem. – Eur. J.* **2018**, *24* (18), 4710–4717. https://doi.org/10.1002/chem.201706069.
(18) Yang, Z.-Z.; Yu, B.; Zhang, H.; Zhao, Y.; Ji, G.; Liu, Z. Fluoro-Functionalized Polymeric N-Heterocyclic Carbene-Zinc Complexes: Efficient Catalyst for Formylation and Methylation of Amines with CO 2 as a C1-Building Block. *RSC Adv.* **2015**, *5* (25), 19613–19619. https://doi.org/10.1039/C5RA00380F.

(19) Cheng, M.; Lobkovsky, E. B.; Coates, G. W. Catalytic Reactions Involving C 1 Feedstocks: New High-Activity Zn(II)-Based Catalysts for the Alternating Copolymerization of Carbon Dioxide and Epoxides. *J. Am. Chem. Soc.* **1998**, *120* (42), 11018–11019. https://doi.org/10.1021/ja982601k.
(20) Garden, J. A.; White, A. J. P.; Williams, C. K. Heterodinuclear Titanium/Zinc Catalysis: Synthesis, Characterization and Activity for CO 2 /Epoxide Copolymerization and Cyclic Ester Polymerization. *Dalton Trans.* **2017**, *46* (8), 2532–2541. https://doi.org/10.1039/C6DT04193K.
(21) Deacy, A. C.; Kilpatrick, A. F. R.; Regoutz, A.; Williams, C. K. Understanding Metal Synergy in Heterodinuclear Catalysts for the Copolymerization of CO2 and Epoxides. *Nat. Chem.* **2020**, *12* (4), 372–380. https://doi.org/10.1038/s41557-020-0450-3.
(22) Lindeboom, W.; Fraser, D. A. X.; Durr, C. B.; Williams, C. K. Heterodinuclear Zn(II), Mg(II) or Co(III) with Na(I) Catalysts for Carbon Dioxide and Cyclohexene Oxide Ring Opening Copolymerizations. *Chem. – Eur. J.* **2021**, *27* (47), 12224–12231. https://doi.org/10.1002/chem.202101140.
(23) Vollmer, M. V.; Ye, J.; Linehan, J. C.; Graziano, B. J.; Preston, A.; Wiedner, E. S.; Lu, C. C. Cobalt-Group 13 Complexes Catalyze CO 2 Hydrogenation via a Co(−I)/Co(I) Redox Cycle. *ACS Catal.* **2020**, *10* (4), 2459–2470. https://doi.org/10.1021/acscatal.9b03534.
(24) Roy, L.; Al-Afyouni, M. H.; DeRosha, D. E.; Mondal, B.; DiMucci, I. M.; Lancaster, K. M.; Shearer, J.; Bill, E.; Brennessel, W. W.; Neese, F.; Ye, S.; Holland, P. L. Reduction of CO 2 by a Masked Two-Coordinate Cobalt(I) Complex and Characterization of a Proposed Oxodicobalt(II) Intermediate. *Chem. Sci.* **2019**. https://doi.org/10.1039/C8SC02599A.
(25) Hujon, F.; Lyngdoh, R. H. D.; Schaefer, H. F.; King, R. B. Binuclear Cobalt Paddlewheel-Type Complexes: Relating Metal–Metal Bond Lengths to Formal Bond Orders. *Inorg. Chem.* **2021**, *60* (2), 584–596. https://doi.org/10.1021/acs.inorgchem.0c02076.
(26) O'Donnell, R. M. METAL-TO-LIGAND CHARGE TRANSFER (MLCT) EXCITED STATES OF RUTHENIUM POLYPYRIDYL COMPOUNDS RELEVANT TO DYE-SENSITIZED SOLAR CELLS (DSSCs). 207.
(27) Crockett, M. P.; Zhang, H.; Thomas, C. M.; Byers, J. A. Adding Diffusion Ordered NMR Spectroscopy (DOSY) to the Arsenal for Characterizing Paramagnetic Complexes. *Chem. Commun.* **2019**, *55* (96), 14426–14429. https://doi.org/10.1039/C9CC08229H.
(28) Norris, M. R.; Flowers, S. E.; Mathews, A. M.; Cossairt, B. M. H 2 Production Mediated by CO 2 via Initial Reduction to Formate. *Organometallics* **2016**, *35* (17), 2778–2781. https://doi.org/10.1021/acs.organomet.6b00595.
(29) Ruiz, J.; Perandones, B. F. Base-Promoted Tautomerization of Imidazole Ligands to N-Heterocyclic Carbenes and Subsequent Transmetalation Reaction. *J. Am. Chem. Soc.* **2007**, *129* (30), 9298–9299. https://doi.org/10.1021/ja073144n.
(30) Ruiz, J.; Sol, D.; Van der Maelen, J. F.; Vivanco, M. Base-Promoted Transmetalation Reactions of Protic N-Heterocyclic Carbenes and Acyclic Diamino Carbenes from Mn I to Au I : A Mechanistic Study. *Organometallics* **2017**, *36* (5), 1035–1041. https://doi.org/10.1021/acs.organomet.7b00009.

VITA

Cecilia grew up in Benicia, California and attended Seattle University where she graduated in 2016 with a Bachelor's of Science in Chemistry and a minor in Mathematics. She performed undergraduate research with Professor P.J. Alaimo at Seattle University, studying enantioselective catalysis for the synthesis of dihydropyridinones, and with Professor Walter Leitner at the RWTH in Aachen, Germany, investigating the reduction of CO and CO_2 and their uses as C_1 building blocks. During graduate school, Cecilia participated in the Pacific Science Center Science Communication Fellowship and the Torrance Technology Due Diligence Fellowship, where she served as a technology due diligence analyst with the E8 Angel Investors. Outside of work Cecilia enjoys being outdoors, especially hiking and backpacking in the Pacific Northwest.

---

[i] While separation of oxidized byproducts from the ligand by chromatography and recrystallization have been unsuccessful, selective reduction of the phosphine oxide with silanes has shown promise for the isolation of clean ligand. Silanes have been shown to reduce a variously substituted phosphine oxides under a variety of conditions, such as solvent free[5,6] and with[7–9] or without[5,6,10,11] additives. In a procedure adapted from the literature,[5,6,8–10] a J. Young tube was charged with oxidized ligand, polymethylhydrosiloxane (PMHS), and a small amount of toluene to aid solubility. The J. Young tube was degassed and the tube was heated at 110 ºC. After two hours at 110 ºC roughly 33 % of the oxidized ligand had converted to the desired deoxygenated ligand, as evident by the appearance of the characteristic 31P NMR ligand peak at -33 ppm. After 16 hours at 110 ºC yielded no further change, the reaction temperature was increased to 175 ºC. After an additional six hours at 175 ºC, the ratio of oxidized to reduced ligand remained roughly unchanged.